UNIVERSITY OF SOUTHAMPTON

FACULTY OF ENGINEERING, SCIENCE AND MATHEMATICS

School of Geography

Shoreline Mapping Using Satellite Sensor Imagery

by

AIDY @ MOHAMED SHAWAL M MUSLIM

Thesis for the degree of Doctor of Philosophy

March 2004

UNIVERSITY OF SOUTHAMPTON

ABSTRACT

FACULTY OF ENGINEERING, SCIENCE AND MATHEMATICS
SCHOOL OF GEOGRAPHY

Doctor of Philosophy

SHORELINE MAPING USING SATELLITE SENSOR IMAGERY

By Aidy @ Mohamed Shawal M Muslim

Malaysia's shoreline is dynamic and constantly changing. Increased coastal population, rapid urbanization, oil and gas production, tourism development, large rainfall throughout the year and various economic activities have created numerous environmental and ecological problems in Malaysia's coastal areas. Malaysia's severe coastal erosion caused by a variety of natural and human-made processes has been a subject of major national concern. As the boundary between land and water surfaces the shoreline is one of the most basic and common features represented on maps. It can, however, be difficult to map accurately, particularly if the coast is dynamic. Remote sensing has been used widely to map the shoreline and offers the potential to update maps frequently. The shoreline could be mapped accurately from fine spatial resolution satellite sensor imagery. Utilizing fine spatial resolution satellite sensor imagery a shoreline prediction with an RMSE of 1.80 m was achieved. But this is an impractical approach for use over large areas. Alternative approaches using coarse spatial resolution satellite sensor imagery were examined.

A pilot study was conducted to examine the potential of these methods on a linear stretch of shoreline. Using a simulated 20 m spatial resolution imagery, a conventional hard classification yielded a shoreline prediction with an RMSE of 6.48 m. To increase the positional accuracy, methods of fitting a shoreline boundary at a sub-pixel scale were examined. Initially a soft classification was applied to predict the class composition of image pixels which were located geographically using sub-pixel mapping techniques. Several sup-pixel mapping methods were applied; contouring, wavelet interpolation and two-point histogram. In the pilot study, the two-point histogram method obtained the most accurate prediction with an RMSE of 2.25 m followed by wavelet interpolation and contouring with an RMSE of 2.82 m and 3.20 m, respectively. This work was extended by analysing effects of shoreline orientation on the prediction. Using a 16 m spatial resolution imagery as a basis for analysis the accuracy of the shoreline prediction varied with orientation. For example, result from the two-point histogram method varied from the RMSE from 1.20 m to 2.08 depending on the shoreline orientation.

To further increase the accuracy of the shoreline prediction, the method was revised by using localised training statistics in the derivation of the soft classification. Using the two-point histogram method, the use of the revised approach yielded shoreline prediction with RMSE ranging from 0.97 to 1.10 m. The result indicates that the accuracy of the shoreline prediction was positively related to the accuracy of the soft classification. This approach of shoreline mapping satisfied the requirement for mapping at a 1: 1,500 scale.

Contents

List of Figures

List of Table

Acknowledgments

There are a lot of people whose participation made the completion of this thesis possible. My primary thanks goes to Professor Giles M. Foody and Professor Peter M. Atkinson for their thorough, efficient and ongoing suggestions and support through this thesis. I am eternally, or at least forever, in their debt.

Thanks to the people at the School of Geography, University of Southampton and the Malaysian Centre for Remote Sensing (MACRES) for offering some excellent insights and comments towards my research.

Special thanks to the Director of MACRES, Y. Bhg Dato' Nik Nasruddin Mahmood for his continual support towards my career and the opportunity to pursue my Phd.

Great thanks to my parents, who always give me strengths and confidence. Not forgetting my wife, Zaleha and daughter, Aleeya Farzana, for their endless emotional support and encouragement.

Finally to the Malaysian Government for providing the scholarship and financial support towards this research.

A very heart felt thank you to all for helping me to achieve this goal!

1 Introduction

Coastal zones are the transition area between the terrestrial and marine environment. They provide various services and have become an important region of human activities. The large extent of human activities at these areas have caused various environmental problems. These problems include beach erosion, resource depletion, environmental degradation, and destruction of natural habitats (Cicin-Sain and Robert, 1998; Adams and Minor, 2002; Byrnes *et al.,* 2003; Bowman and Pranzini, 2003). Malaysia, being largely surrounded by sea, is not immune to these problems and to attempt to reduce them has made the management of coastal areas a priority.

Coastal erosion has been a major concern and during 1984-1985, the Malaysian government launched the National Coastal Erosion Study to quantify the effect of coastal erosion to the Malaysian shoreline. According to this, out of 4,800 km of the shoreline in Malaysia about 1,400 km were subjected to critical erosion. The severity of shoreline erosion was defined by several factors including its geomorphological properties and land use (Stanley consultants Inc. *et al.,* 1985). To help coastal managers make informed and responsible decisions, accurate shoreline maps are required.

To monitor shoreline changes, the Malaysian government has allocated a large amount of funds to survey coastal areas using conventional methods such as aerial photography and ground surveys. Due to the large extent of the Malaysian shoreline and limited resources the shoreline has only been mapped every 5 years. Aerial photography and ground survey techniques are expensive and require trained staff and

expensive equipment (Bohnestiehl, 2001). The time required for the post-processing of aerial photographs and ground surveys are also long resulting in outdated maps when completed (Zuzek *et al.,* 2003; McKenna *et al.,* 2003). Due to the time requirement needed to produce these maps aerial photography and ground surveys techniques are inadequate to efficiently monitor dynamic areas such as coastal areas. Therefore, there is a need to develop new techniques of shoreline mapping that are capable of producing shoreline maps quickly and cost effectively.

Remote sensing satellite sensor imagery has been used widely to monitor coastal areas and offer the potential of updating maps frequently (Clark, 1983; Balopoulos *et al.,* 1986; Dekker *et al.,* 1992; Elraey *et al.,* 1995; Cendrero and Fischer, 1997; LaValle and Lakhan, 2000; Lemmens, 2001; Stauble, 2003). Early research in the application of satellite sensor images for shoreline mapping relied on coarse spatial resolution satellite sensor images (Blodget and Taylor, 1990; Dwivedi, 1997; Frihy *et al.,* 1998; Byrnes *et al.,* 2003). Despite the coarse spatial resolution, satellite sensor imagery has assisted in understanding small cartographic scale coastal erosion in areas such as the Nile Delta (Blodget *et al.,* 1991; El Asmar, 2002). To observe more local scale changes, finer spatial resolution satellite sensor imagery are required. The new generation of fine spatial resolution sensors such as 1 m spatial resolution IKONOS panchromatic imagery provide the capability to resolve small changes (Li *et al.,* 2001). But to process fine spatial resolution satellite sensor imagery requires, among other things, computers with large hard disk capacity and processing power limiting the application of fine spatial resolution imagery to mapping small areas. Fine spatial resolution satellite sensor images are often inappropriate and expensive, particularly when mapping the shoreline of a whole country such as Malaysia. For practical reasons, therefore, mapping large stretches of shoreline can rarely make use of very

fine spatial resolution data. Approaches to map the small shoreline changes from coarse spatial resolution sensor data are required.

Mapping from satellite sensor imagery is commonly achieved through hard classification methods, where pixels are classified on the basis of their spectral similarity to a certain pre-defined class. However, this technique is unsuitable when using coarse spatial resolution imagery to monitor small (< 5 m) shoreline changes because the hard allocation process assigns a pixel to only one class thus forcing the shoreline boundary to lie between pixels (Richards, 1993; Mather and Tso, 2001). In reality, the shoreline should be positioned within pixels as pixels may have a mixed class composition (Foody, 1998).

Mixed pixels result when the area represented by a pixel contains two or more classes, which is common in coarse spatial resolution imagery. For these mixed pixels, soft-classifiers have been developed to allow a pixel to have multiple and partial class membership (Foody, 2002a). The conventional output of a soft classification is a set of fraction images which indicate the relative coverage of the class in the area represented by each pixel (Kanellopoulos *et al.,* 1992; Foody and Cox, 1994). These approaches, however, do not provide any indication of where the class proportions are located spatially within a pixel. But knowing these fraction values opens the possibility of positioning the shoreline within a pixel or at a sub-pixel scale. Several methods have been proposed to address mapping at a sub-pixel scale (Atkinson, 1997; Gavin and Jennison, 1997; Atkinson *et al.,* 1997; Tatem *et al.,* 2001; Aplin and Atkinson, 2001; Tatem *et al.,* 2003)

This thesis introduces techniques for accurately mapping the shoreline from satellite sensor imagery. For short stretches of shoreline (< 10 km) a method of mapping the shoreline using fine spatial resolution satellite sensor imagery was

evaluated. The method used topographic and bathymetric data generated from fine spatial resolution satellite sensor imagery to construct a 3-D terrain model of the coastal area. A shoreline was later delineated from this 3-D terrain by positioning the water level at a selected tide elevation by using the intersection of land and water as the shoreline position (Li *et al.,* 2001; Ruggiero *et al.,* 2003). But to map large areas, this method was impractical. Therefore this thesis evaluates techniques of mapping the shoreline from coarse spatial resolution satellite sensor image. Initially, a soft classification was applied to a coarse spatial resolution imagery producing an imagery of fraction values representing the thematic composition of image pixels. After assessing the accuracy of the soft classification, methods of mapping at a finer scale than the pixel's spatial resolution or sub-pixel/super-resolution mapping techniques were applied to the imagery to predict the actual shoreline position. In this way, the shoreline was mapped at a sub-pixel resolution.

The ability to map the shoreline accurately from satellite sensor imagery enables the continual monitoring of the shoreline at regular intervals. With this capability it is hoped coastal managers would be able to ensure better management of coastal areas.

2 Background

2.1 Introduction

Malaysia, located in Southeast Asia consists of two geographical regions: Peninsular Malaysia, which is part of mainland Asia, and the states of Sabah and Sarawak on the island of Borneo. A map of Malaysia is shown in Figure 2.1. The eastern coast of Peninsular Malaysia and the western coast of Sabah and Sarawak are characterized by sandy beaches with clay-composed soils and mudflats. Mangrove forest are found along the west coast of Peninsular Malaysia and are generally associated with mudflats and clay swamps (Harakunarak, 2000).

Figure 2.1: Map of Malaysia.

2.1.1 Environmental impact of coastal zone development

Increased coastal population, rapid urbanization, oil and gas production, tourism development, severe rainfalls throughout the year, and various economic activities have created numerous environmental and ecological problems in Malaysia's coastal areas. These problems include beach erosion, resource depletion, environmental degradation, and destruction of natural habitats (Cicin-Sain and Robert, 1998). Malaysia's severe coastal erosion caused by a variety of natural and human-made processes has been a subject of major national concern. During 1984-1985, the Malaysian government launched the National Coastal Erosion Study. According to this study completed in 1986, out of 4,800 km of shoreline in Malaysia about 1,400 km (47 sites) was subjected to critical erosion. This has since increased to 2,327 km totalling 74 sites in 2000 (Saw, 2000). An example is the Seberang Takir area illustrated by Figure 2.2.

Figure 2.2: Image shows destruction to properties at a critical erosion site in Seberang Takir, Terengganu, Malaysia

2.1.2 Measures taken by Malaysian government to reduce coastal erosion.

2.1.2.1 Short and long term measures.

In accordance with the National Environmental policy, the Malaysian government has since 1987 adopted a two-pronged strategy (short-term and long-term) to control coastal erosion. The short-term strategy is construction-focused and reactive in nature. This involves measures that require structural solutions such as the construction of revetments, breakwaters, sea walls and beach nourishment to protect existing facilities and properties in coastal areas (Ministry of Agriculture, 1997). These measures are illustrated by Figure 2.2 and Figure 2.3. The long-term strategy involves monitoring and management of coastal development by taking into account its consequences towards coastal erosion. This was achieved through an integrated and coordinated development plan and strategy.

Figure 2.3: Among measures to address coastal erosion are to build a concrete seawall (Kuala Terengganu).

Figure 2.4: Rock sea walls were build to address coastal erosion in Kuala Terenganu.

2.1.2.2 Establishment of government institutions

Following the recommendations of the coastal erosion study, two important institutions related to coastal zone management were established in 1987: the Coastal Engineering Technical Centre (CETC) and the National Coastal Erosion Control Council (NCECC) (Cicin-Sain and Robert, 1998). The CETC is presently known as the Coastal Engineering Division (CED), under the Department of Irrigation and Drainage (DID) in the Ministry of Agriculture. The DID's CED is responsible for implementing coastal erosion control, engineering works for critical erosion areas, providing technical support to the NCECC, providing technical advisory services to other government agencies, and collecting coastal engineering data.

2.1.2.3 Financial allocation for coastal programs

Under the CED, an erosion control program was implemented in 1987 with a budget allocation of £ 1.78 million[1] to protect the 47 critical erosion sites. This allocation was further increased to £ 22.6 million [1] in the Sixth Malaysian Plan (1991-1995) reflecting the growing concern of the Malaysian government towards coastal erosion. In the Seventh Malaysian Plan (1996-2000) a similar budget of £ 21.66 million [1] was allocated. With the coastal zone being subjected to increasing development, DID as the implementing agency has put forth a budget allocation of £ 113.83 million [1] for the Eighth Malaysian Plan (2001-2005). This amount would be used to continue previous programs, upgrade and restore coastal structures and implement new projects such as restoration and nourishment of tourist beaches (Saw, 2000).

2.1.2.4 Regulatory measures

Among the regulatory measures instituted by the Malaysian Government are the General Administrative Circular No. 5 of 1987 issued by the Prime Minister's Department, the Environmental Quality Act 1974, Environment Quality (Prescribed Activities) (Environmental Impact Assessment) Order 1987, and the Natural Resources and Environment Ordinance (Sarawak) 1949 (As Amended 1994). Circular No. 5 of 1987 requires all proposed development projects in the coastal zone to be referred to the CED of the DID for comments. The Environmental Impact Assessment (EIA) Order 1987 sets out a list of development activities, which require mandatory submission of EIA reports for prior approval of the Department of Environment

[1] Based on exchange rate of £ 1 pound sterling. = RM 5.29 Ringgit Malaysia (1st July 2001)

(DOE). The CED reviews and comments on EIA submissions for the DOE in relation to projects that affect the coastline (Ministry of Agriculture, 1997).

2.2 Shoreline mapping

Among the major tasks of the CED is the collection of coastal engineering data. These data include hydro-graphic profiles, wind information, wave dynamics and shoreline maps. Shoreline maps are important, as maps are a record of the coastal position at a certain moment of time. In 1998, DID established a memorandum of understanding with the Malaysian Centre for Remote Sensing (MACRES) to apply remote sensing and related technologies to its operation. One of the areas identified for this purpose was the production of satellite sensor based shoreline maps.

2.2.1 Definition of shoreline

The shoreline can be defined as the intersection of the land with the water surface at a selected tidal elevation level (Camfield and Morang, 1996; Parker, 2003). In Malaysia the tidal elevation chosen for shoreline maps is the mean high water springs (MHWS). MHWS is the average height of the high waters of the spring tides. Tide levels occur as a result of the moon's gravitational force based on a semi-monthly cycle (new or full moon). The spring range of tide is the average range occurring at the time of spring tides and is most conveniently computed from the harmonic constants (Ministry of Agriculture, 1997).

2.3 Conventional method of shoreline mapping

2.3.1 Line survey

Line survey is performed by taking regular measurements of the beach surface level relative to a reference datum along a line normal to the local shoreline. These measurements are repeated at regular intervals along the shoreline. Levelling and triangulation are later applied to obtain accurate values. Levelling is the operation of determining differences in elevation by measuring vertical distance directly on a graduated rod with the use of a levelling instrument such as transit or theodolite (Morton *et al.,* 1993; Simons and Hollingham, 2001; Gibsob and Dorothy, 2003; Langley *et al.,* 2003). To obtain accurate elevation, use of benchmarks is very important. Benchmarks are permanent objects of known elevation located where there is least likelihood of disturbance (Gibsob and Dorothy, 2003). By relating measurements to the benchmarks sub-metre positional accuracy are possible.

To obtain horizontal accuracy, the triangulation method is applied. Basically, triangulation consists of the measurement of the angles of a series of triangles. The principle of triangulation is based on simple trigonometry. If the distance along one side of a triangle and the angles at each end of the side are accurately measured, the other two sides adjacent to the remaining angle can be computed. Normally, all of the angles of every triangle are measured to minimize error and to furnish data for use in computing the precision of the measurements (Ruggiero *et al.,* 2003). Depending on the scale and accuracy requirement of the shoreline maps a large number of ground control points (GCPs) and line surveys may be needed. These line surveys are later interpolated to produce a 3-Dimensional model of the area. Shoreline position is then determined based on a selected tide elevation (Anon, 1984). Using conventional

surveying instruments, it is possible to achieve a fine precision; however the overall usefulness depends on the spatial density requirement of point measurements (Simons and Hollingham, 2001). Despite the possibility of increased accuracy, line surveying is a labour intensive and time-consuming process.

2.3.2 Photogrammetry

The conventional method of generating shoreline maps from aerial photography is through photogrammetry (Cromwell *et al.,* 1991; Shoshany and Degani, 1992; Cetin *et al.,* 1999; Adams and Minor, 2002; Norcross *et al.,* 2002; Friedman *et al.,* 2002; Leatherman, 2003; Fletcher *et al.,* 2003; Honeycutt and Krantz, 2003).
Photogrammetry has been used in Malaysia since the 1950s and has provided shoreline maps up to 1: 10,000 scale. Aerial photographs are acquired with a 60% overlap along a strip, which allows coverage to be viewed in stereo. These stereo images allow precise photogrammetric measurements to be made in order to locate features accurately. In photogrammetry, acquisition date and time are crucial as water level and therefore, shoreline position can show great variation (Lane *et al.,* 2000). Ideally photographs need to be collected during a selected tide elevation. By capturing a scene at two different vantage points an object with height will appear to have moved relative to the background. This effect is called stereoscopic parallax. This is a normal characteristic of aerial photography and is the basis of 3-D stereoscopic viewing. The difference in parallax in various objects of interest are analysed using a stereo plotter or digital photogrammetry application to remove photographic distortions and determine height. The shoreline is later extracted from the orthophoto produced. The planimetric accuracy obtained through orthophotos provides accurate shoreline maps. But the photogrammetic procedures involving data acquisition and processing are

costly and time consuming (Anon, 1993; Jensen, 2000). Due to this restriction DID have been able to map Malaysia's shoreline only every five years.

2.4 Potential of satellite remote sensing in coastal studies.

With the launch of satellite remote sensing systems a wide range of applications in coastal studies have been realised and several advantages have been discovered. Among the major advantages of remote sensing are that it provides the ability to monitor large areas without physically being there. Remote and inaccessible areas can be monitored from space. Remote sensing through passive sensors also provide the ability to unobtrusively monitor the environment with better general availability and a large ground coverage (Chevrel *et al.,* 1981; Jensen, 2000).

Under controlled conditions remote sensing can provide biogeophysical data such as, location X, Y, elevation or depth Z, biomass, temperature, *etc.* However unlike conventional methods, remote sensing data are collected systematically over a large geographical area rather than a single point observation. This systematic data collection can remove the sampling bias introduced in some in situ investigations (Jensen, 2000). Digital satellite sensor data are also easily manipulated through digital image analysis procedures to extract relevant features (Richards, 1993; Mather and Tso, 2001).

Remote sensing sensors cover a large spectral region that commonly ranges from the 0.3 μm to 1m. Covering a large spectral region, more geographical information can be extracted. Figure 2.5 depicts the electromagnetic spectrum used by common remote sensing sensors.

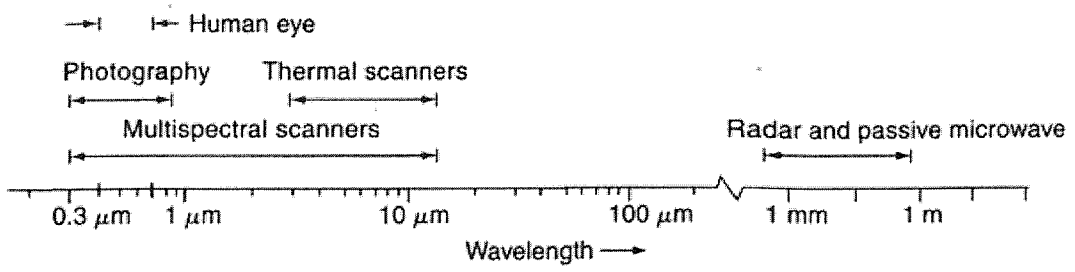

Figure 2.5: Spectrum range of common remote sensing systems (Jensen, 1996).

Research in shoreline mapping has been conducted using a variety of sensors such as Landsat Thematic Mapper (TM), Landsat Multi Spectral scanner (MSS) and SPOT HRV (Blodget and Taylor, 1990; Dwivedi, 1997; Cetin *et al.,* 1999; Dewidar and Frihy, 2003). Until recently the spatial resolution of these satellite sensors have been too coarse for shoreline mapping. But newer satellite sensors providing finer spatial resolution has increased remote sensing capability in shoreline mapping (Li, 1998; Malthus and Mumby, 2003). Table 2.1 summarizes commonly used remote sensing satellites and their sensors.

2.5 Electromagnetic interaction in remote sensing

When energy is recorded by a passive remote sensing sensor it undergoes fundamental interaction with different mediums. These mediums include the atmosphere and Earth's surface (water or land). To properly interpret remote sensing data an understanding of each interaction undergone by electromagnetic energy need to be understood.

As electromagnetic energy from the Sun propagates through the Earths atmosphere it encounters a difference in density when coming across air or water.

These differences will cause the electromagnetic energy to move at different speed and refracts. Refraction refers to the bending of light or energy when passing through one medium to the other. Another effect of atmosphere is the scattering of energy by atmospheric particles. Scattering differs from refraction as the direction of scattering is unpredictable. The effects of scattering depends on the relative size of wavelength of the incident energy, the diameter of gases, water vapor, water, and dust with which the energy interacts. Essentially there are three types of scattering: Raleigh, Mie and non-selective scattering.

Another interaction that occurs in the atmosphere is absorption. Absorption is the process by which energy is absorbed and converted into another form of energy. Absorption occurs at several range of wavelengths or frequency corresponding to various atmospheric gasses such as carbon dioxide, ozone, oxygen, water vapor and nitrous oxide. Absorption occurs when incident energy of the same frequency as the resonance frequency of an atom or molecule is absorbed, producing an excited state. If instead of reradiating a photon of the same wavelength, the energy is transformed into heat motion and is subsequently reradiated at a longer wavelength, absorption occurs (Jensen, 2000). When the energy from the Sun bounces of an object such as clouds and terrestrial Earth this process is called reflectance. When radiation is reflected from an object the incident radiation, the reflected radiation, and a vertical to a surface from the angle of incidence and reflection are measured all lie in the same plane. The angle of incidence and the angle of reflection are also approximately equal (Jensen 2001). Depending on the reflecting surface, reflectance occurs in many different ways and sometimes is diffused.

Table 2.1: Remote sensing satellites characteristics.

Platform	Owner	Launch Date	Revisit (days)	Sensor	Swath (km)	Total FOR (km)	Number of Bands / Pixel size (m)						Bits/ pixel
							PAN (~ 0.4 - 0.8μm)	VIS (~ 0.4 - .7μm)	NIR (~ 0.7 - 1.5μm)	SWIR (~ 1.5 - 3μm)	MWIR (~ 3 - 8μm)	LWIR (~ 8 - 15μm)	
ERS-1	ESA	Jul-91	3	ASTR/IRR	500	500				1 / 1000	1 / 1000	2 / 1000	
ERS-2	ESA	Apr-95	3	ASTR-2	500	500		2 / 1000	1 / 1000	1 / 1000	1 / 1000	2 / 1000	
IKONOS	USA	Oct-99	1.5 - 3		13	13	1 / 1	3 / 4	1 / 4				11
IRS-1B	India	Aug-91	24	LISS-1	148	148		3 / 73	1 / 73				
			24	LISS-2	131	131		3 / 36.5	1 / 36.5				
IRS-1C	India	Dec-95	24	LISS-3	142	142		2 / 23.5	1 / 23.5	1 / 70.5			7
			24	PAN	70	800	1 / 5.8						7
			5	WiFS	804	804		1 / 188	1 / 188				7
IRS-1D	India	Sep-97	24	LISS-3	142	142		2 / 23.5	1 / 23.5	1 / 70.5			7
			24	PAN	70	800	1 / 5.8						7
			5	WiFS	804	804		1 / 188	1 / 188				7
IRS-P2	India	Oct-94	24	LISS-2	131	131		3 / 36.5	1 / 36.5				7
IRS-P3	India	Mar-96		MOS	200	200		8 / 520	9 / 520	1 / 520			16
			5	WiFS	770	770		1 / 188	1 / 188	1 / 188			7
IRS-P4	India	May-99	2	OCS	1420	1420		5 / 250	3 / 250				12
JERS-1	Japan	Feb-92	44	OPS	75	75		2 / 20	1 / 20	4 / 20			8
Landsat 4	USA	Jul-82	16	MSS	185	185		2 / 78	2 / 78				8
			16	TM	185	185		3 / 30	1 / 30	2 / 30		1 / 120	8
Landsat 5	USA	Mar-84	16	MSS	185	185		2 / 78	2 / 78				8
			16	TM	185	185		3 / 30	1 / 30	2 / 30		1 / 120	8
Landsat 7	USA	Apr-99	16	ETM+	185	185	1 / 15	3 / 30	1 / 30	2 / 30		1 / 60	8
SPOT-2	France	Jan-90	26	HRV	60	850		2 / 20	1 / 20				8
			26	Pan	60	850	1 / 10						8
SPOT-4	France	Mar-98	26	HRVIR	60	850		2 / 20	1 / 20	1 / 20			8
			26	Pan	60	850	1 / 10						8
			1	Vegetation	2,200	2,200	1 / 1150	3 / 1150	1 / 1150	1 / 1150			10

2.5.1 Water penetration of electromagnetic energy.

When conducting remote sensing studies on water bodies one of the most important characteristics which needs to be determined is the wavelength with the least amount of absorption and scattering of light in the water column. Bakuta *et al.*, (1995) determined that these characteristics are found in the blue wavelength region from approximately 400-400nm, with the minimum located at approximately 460-480nm. Table 2.2 shows the optical properties of pure water.

Table 2.2: Optical Properties of Pure water (derived from various sources from Bukata *et. al.*,1995)

Wavelength (nm)	Absorption (m^{-1})	Scattering (m^{-1})	Total Attenuation (m^{-1})
250	0.19	0.032	0.220
300	0.040	0.015	0.0550
320	0.020	0.012	0.320
350	0.012	0.0082	0.0202
400	0.006	0.0048	0.0108
420	0.005	0.0040	0.0090
440	0.004	0.0032	0.0072
460	0.002	0.0027	0.0047
480	0.003	0.0022	0.0052
500	0.006	0.0019	0.0079
520	0.014	0.0016	0.0156
540	0.029	0.0014	0.0304
560	0.039	0.0012	0.0402
580	0.074	0.0011	0.0751
600	0.200	0.00093	0.2009
620	0.240	0.0082	0.2408
640	0.270	0.00072	0.2707
660	0.310	0.0064	0.3106
680	0.380	0.00056	0.3806
700	0.600	0.0005	0.6005
740	2.250	0.0004	2.2504
760	2.560	0.00035	2.5604
800	2.020	0.00029	2.0203

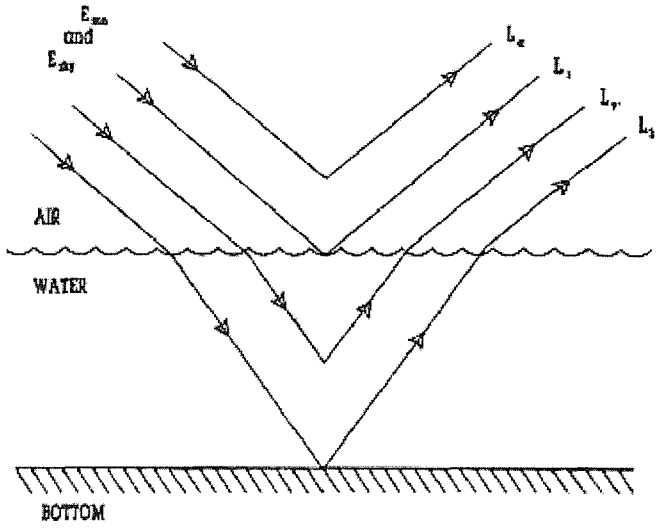

Figure 2.6: Components of radiance recorded by remote sensing over water (Source: Bukata *et. al.*, 1995)

For the best penetration, water bodies need to be free from organic and inorganic substance as these would cause scattering and absorption thus obscuring bottom topography. When conducting bathymetry studies using remote sensing data it is important to understand the interaction encountered by the energy or radiance recorded by the sensor. Figure 2.6 depicts the interaction between down-welling light with the atmosphere and aquatic media. Down welling solar and sky irradiance are labelled E_{sun} and E_{sky} respectively. Radiance recorded by a remote sensing sensor can compromise of four main components (Bukata *et al.*, 1995):

L_a: radiance that never reaches the air-water interface thus returning to the atmosphere.

L_s: radiance that reaches but does not penetrate the air-water interface. It, therefore, represents a reflection from the water surface.

L_v : radiance that penetrates the air-water interface and re-emerges from the water without reaching the bottom topography. It, therefore, represents a return from the volume of water.

L_b : radiance that penetrates the air-water interface and re-emerges from the water reaching the bottom topography. It, therefore, represents a return from the bed of water body.

These interactions need to be carefully studied in order to extract bathymetry data. To obtain bathymetry it is important to be able to extract L_b from all other radiance component. It has been determined that the total radiance observed by the sensor can be represented as the sum of the four radiance above:

$$L = L_a + L_s + L_v + L_b \qquad 2\text{-}1$$

Thus the basic starting point for extracting bathymetry information can be achieved by obtaining L_b. This can be represented by: -

$$L_b = L - (L_a + L_s + L_v) \qquad 2\text{-}2$$

2.5.2 Obtaining elevation information.

The ability to measure height (elevation) using remote sensing sensor have evolve from the use of stereo aerial photographs. Similar concepts of photogrammetry have been applied to remote sensing imagery for this purpose. To understand the process of obtaining elevation from stereo satellite sensor images it is important to understand the fundamental principle of stereoscopy. Stereoscopy is the science of perceiving depth using two eyes (or view point). When both eyes are focused on a certain point, the

optical axes of the eye converge on that point forming a parallactic angle (Φ) (Baltsavias, 1999). This angle will increase when the object is nearer and *vice versa*. By associating the responding parallactic angle with distance the depth of different objects could be differentiated. If both objects were exactly the same distance away, then the parallactic angle will be the same thus appear to be the same distance away. Figure 2.7 illustrates the concept of parallactic angles and its association with the perception of depth in various objects. When an object A is viewed from two points L and R it will produce a parallactic angle Φ_A, similarly angle Φ_b will be produced when an object B is viewed. By associating these angles with a known distance D_A, distance D_B could be determined.

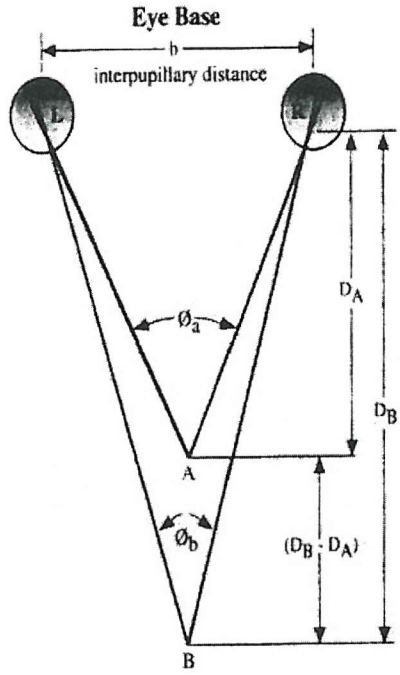

Figure 2.7: Parralactic angles and its association with the perception of depth in various objects (Jensen, 1996)

By applying the same concept to remote sensing imagery elevation of different objects are distinguishable. Stereo parallax is introduced to remotely sensed images when the same object is viewed from two different vantage points along a flight line. These overlapping satellite sensor images can be analysed to produce digital elevation models (Brokelbank and Tam, 1991; Giles and Franklin, 1996; Baldwin *et al.,* 1998; Vassilopoulou *et al.,* 2002). To extract elevation information from a satellite stereoscopic pair, a mathematical relationship needs to be developed to describe the geometric relationship between stereo satellite sensor images to object spaces. Other factors have to also be considered such as type of sensor and sensor motion during acquisition.

2.6 Remote sensing application in shoreline monitoring and bathymetry

Satellite sensors have been used for coastal studies in a variety of applications. A summary of satellite systems currently available are displayed in Table 2.1. Among the major satellite sensor used in coastal application are the Landsat MSS, Landsat TM and SPOT HRV. The Landsat series of satellites have carried a variety of sensors, among them are the MSS and TM. The MSS and TM sensors provides user with 79 m and 30 m spatial resolution satellite images respectively.

By pioneering the linear array push-broom technology the Centre National d'Etudes Spatiales (CNES) were able to provide satellite sensor images at 10 metres (PAN) and 20m (Multi spectral) for the SPOT HRV sensor. This provides increased spatial resolution over the Landsat series. The Linear Array Push-broom system acquires imagery with no mechanical scanning. Breaking tradition (in relation to Landsat sensors) the push-broom system allows accurate detection of spectral radiant

flux from the Earth. At 10 m and 20 m spatial resolution, SPOT HRV imagery provides increased capability in resolving objects than Landsat TM. since than, newer satellite sensors such as IRS-1D panchromatic, Landsat ETM+ and IKONOS have been operational providing spatial resolution up to 5.8 m, 15 m and 1 m respectively. On December 6th 2000, Space Imaging was awarded a license by the National Aeronautical and Space Administration (NASA) to operate a commercial remote sensing satellite capable of providing 0.5 m (panchromatic) and 2 m (multi-spectral) spatial resolution imagery. This new satellite is schedule for launch in 2004 (Space Imaging, 2001).

This review will examine how previous researchers have approached shoreline mapping and bathymetry from remotely sensed data.

2.6.1 Application of remote sensing in shoreline mapping

Researchers have used remotely sensed imagery to monitor the shoreline as an alternative to aerial photography and ground surveying (Bhat and Subrahmanya, 1993; Fanos, 1995; Chen and Rau, 1998; Pajak and Leatherman, 2002; Byrnes *et al.,* 2003; Shaghude *et al.,* 2003; Frihy and Dewidar, 2003; Frihy *et al.,* 2003; Dewidar and Frihy, 2003). Early research in the application of satellite sensor images for shoreline mapping relied on coarse spatial resolution satellite sensor images. The Landsat series of satellites have supplied satellite sensor imagery continuously since 1972 (Gibson, 2000). Landsat 1 through 3 were equipped with the MSS sensor providing a spatial resolution of 79 m. EL-Raey (1999) evaluated Landsat MSS data from 1978, 1983, 1990 to detect erosion and accretion patterns along Damietta-Port Said shoreline, Egypt. Due to the coarse spatial resolution of Landsat MSS it could only be applied for

regional and small scale mapping exercises. Precise aerial photogrammetry were still required in areas where critical measurements were need (Blodget and Taylor, 1990). In 1982 the Earth Observation Satellite Company (EOSAT) launched Landsat 4, its first satellite carrying the TM sensor. Landsat TM collects multi-spectral imagery that had finer spatial, temporal, spectral, and radiometric resolution than Landsat MSS (Jensen, 2000). With these capabilities the Landsat TM sensor was capable of deriving various geomorphologic features and efficiently monitor human activities such as land reclamation, building and aquaculture (Blodget *et al.,* 1991).

Initial studies in shoreline mapping have focused on methods to differentiate between land and water bodies. Basic remote sensing image analysis was applied to satellite sensor imagery for this purpose. Image processing systems are capable of analysing digital multi-band satellite sensor imagery in various ways to extract relevant information (Richards, 1993). Among methods applied to obtain coastal information are image differencing, image ratioing, principal component analysis (PCA), and change vector analysis (CVA) (Ceballos and Bottino, 1997; El Raey *et al.,* 1999). Image differencing is the process of subtracting values between 2 co-registered images of different dates. Its primary usage is for change detection. Another widely used technique is image ratioing. Image ratioing is an enhancement technique accomplished by dividing digital number (DN) values of one spectral band by corresponding DN of another band. One reason for this is to resolve differences in scene illumination due to cloud or topographic shadow. Ratio images also bring out spectral variation in different target materials.

Spectrally adjacent bands in a multi-spectral remotely sensed image are often highly correlated. The correlation among the bands of a multi-spectral image implies that there is redundancy in the data. The PCA technique aims to remove this

redundancy. PCA is related to another statistical technique called factor analysis and can be used to transform a set of image bands such that the new bands (called principal components) are uncorrelated with one another and are ordered in terms of the amount of image variation they explain. The components are thus a statistical abstraction of the variability inherent in the original band set.

False colour composite of various bands provide more detail and information in comparison with single band imagery. Frihy *et al.* 1998 used bands 4, 5, 3 of the Landsat TM to represent red, green, blue in a false colour composite to study coastal changes. This composition provided details and accurate visualization of land use or land cover (Frihy *et al.,* 1998). Satellite sensor images either colour composition or a single band can also be classified to separate different features and reduce redundancy (Richards, 1993). Frihy *et al.,* (1998) utilised unsupervised classification and applied clustering and minimum distance rule to Landsat TM and Landsat MSS images to detect shoreline.

Other approaches in satellite sensor imagery analysis have also been explored to increase positional accuracy. Among the method includes using sub-pixel methods to analyse coarse spatial resolution satellite sensor imagery, which includes interpolation and sub-pixel classification techniques (Mather and Tso, 2001). Several researchers have addressed this sub-pixel classification problem and developed methods to estimate class proportions within a pixel (Kanellopoulos *et al.,* 1992; Foody and Cox, 1994; Zhang and Foody, 1998). These approaches, however, do not provide any indication of where the class proportions are located within a pixel. To address this issue several approaches have been developed. Foody (1998) evaluated a fuzzy sharpening approach to predict boundaries with sub-pixel geometric accuracy. Atkinson (1997) proposed a sub-pixel mapping approach, which divides pixels into

sub-pixels and allocates the different class proportion into these sub-pixels. Gavin and Jennison (1997) adopted a Bayesian approach and incorporated prior knowledge about a reference image in a stochastic model that attaches higher probability to images with shorter total edge length. Mertens *et. al.* (2003) applied genetic algorithms combined with the assumption of spatial dependences to assign a location for each sub-pixel. Aplin and Atkinson (2001) segmented pixels using vector boundaries to achieve a sub-pixel land cover mapping, while Tatem *et al.* (2001; 2003) introduced a Hopfield neural network optimisation algorithm to obtain a sharpened image.

Methods of image interpolation includes kriging and Thiessen interpolation (Doucette and Beard, 2000). Another method of image interpolation is the usage of wavelet transforms, wavelets are mathematical functions that cut up data into different frequency components and then study each component with a resolution matched to its scale (Donoho, 1992).

In mapping the shoreline most early researchers took a 2 dimensional approach concentrating only in differences in position (X, Y). Elevation and variations in sea water height were neglected (Frihy and Dewidar 1998, El Raey, El Din *et al.,* 1999). These approaches resulted in positional error in the shoreline up to 10 m. But as spatial resolution of Landsat MSS and TM sensors were 79 m and 30 m respectively, the positional error of the shoreline due to variation to sea water height were acceptable. To predict the shoreline position the spectral characteristics of coastal areas were analysed statistically and used to train classification algorithm. This algorithm was then used to analyse the whole image and classify land and water bodies.

2.6.2 Three-dimensional approach to shoreline mapping.

2.6.2.1 Satellite stereo images for deriving DEM of coastal areas

Tidal variation plays a significant role in estimating shoreline change over a long period of time as tidal elevation between different acquisition dates are rarely the same (Chen and Rau, 1998). As it is unlikely any satellite sensor data acquisition could be programmed to place during a specific tidal elevation, shoreline derived from these images need to be corrected. To do so a 3-D model of the inter-tidal zone is necessary.

Photogrammetry has been the main method of producing DEM (Hancock and Willgoose, 2001; Judge and Overton, 2001). The evolution of photogrammetry can be categorized into 4 main development cycles that are plane table photogrammetry (1850-1900), analogue photogrammetry (1900-1960), analytical photogrammetry (1960-present) and softcopy photogrammetry (late 1980's- present) (Bohnestiehl, 2001). With the availability of digital sensor data input from airborne and satellite platforms, softcopy photogrammetry has become a significant process for generating DEM. The availability of satellite sensors with stereo capabilities such as SPOT HRV, RADARSAT SAR and IKONOS sensor has been a major step in mapping science as it is possible to map large areas with very few images. On the other hand, photogrammetry requires a large number of photographs, which need to be processed individually.

With its stereo imaging capability and 10 m (PAN) spatial resolution, SPOT HRV provides the ability to incorporate elevation and tidal variation in modelling or detecting shoreline position (Chen and Rau, 1998). At this 10 m spatial resolution tidal elevation effects are more prominent thus changes in tidal height during acquisition can be modelled to increase positional accuracy of the shoreline position.

The SPOT HRV sensors are capable of acquiring cross-track stereoscopic pair images on successive days. Around the equator the ratio between the observation base (distance between the two satellite positions) and satellite height is approximate 0.75. This base to height ratio has been found to be sufficient for topographic mapping up to 1: 50,000 scale (Jensen, 2000). When detecting shoreline, a DEM of the area has to be established. The DEM, tidal height information and shoreline position during satellite sensor image acquisition will be used to correct the shoreline to a selected tidal elevation. Ideally DEM of the inter-tidal zone need to be established from SPOT HRV images taken during the lowest possible tide elevation. Only then can the shoreline position can be corrected to other tidal elevation (*i.e* Mean Low water Spring (MLWS) and Mean high water spring (MHWS)). By acquiring and processing satellite images from several dates, changes between each shoreline position can be accurately determine as they have been normalise to a common tidal elevation (Chen and Rau, 1998).

2.6.2.2 Water line method for creating DEM of coastal areas

Another approach to establish a DEM of the tidal zone is the water line method. The waterline is defined as the position of land water boundary at the time of satellite data acquisition also known as an instantaneous shoreline. The method regards the sea as an altimeter, the height of which is determined using a hydrodynamic tidal model (Lohani and Mason, 1999). In this method satellite sensor images are acquired during different stages of tide elevation and processed to delineate the position of the shoreline. The geometrically corrected shorelines would then be assigned elevation values determined by a hydrodynamic model. A model commonly used is the simplified harmonic method (SHM). These shorelines were then interpolated to produce a DEM of the area. An advantage of this method over generation of DEM using stereoscopic satellite

sensor imagery is that it is sensor independent. Chen (1998) applied this method to SPOT HRV images to study shoreline change for tideland areas in Taiwan. Similar research was conducted in Sumatra utilizing SPOT HRV and ERS sensor data (Leow *et al.,* 2000). This method has also been used with Airborne Thematic Mapper data (Lohani and Mason, 1999). One major disadvantage of this method is it requires several images at different tide elevation and this is not easily available. Acquisition of the satellite sensor images also needs to be temporally close to ensure elevation of tidal areas has not changed

2.6.3 Application of remote sensing in bathymetry studies

Several methods can be used to derive data of bathymetry. These include conventional sounding techniques and application of remotely sensed data.

2.6.3.1 Sounding techniques for obtaining bathymetry

Sounding techniques can generally be divided into 4 categories, which are single beam echo sounding, Multi-beam forming sonar, multi-beam interferometric sonar and side scan sonar (Atanu and Saxena, 1999). Deriving bathymetry data for shallow water areas by conventional shipboard sounding techniques can be slow, hazardous and expensive especially for large areas (Lyzenga, 1985). As a result development in the application of remote sensing techniques to solve this problem has been explored.

2.6.3.2 Application of remote sensing for bathymetry

The use of passive remote sensing data was first demonstrated in the late 1960. The blue region of the electromagnetic spectrum (0.45-0.52 μm) provides minimum absorption thus maximum penetration of water. In this region water is penetrable up to 30 m depending on the water quality (Bierwirth *et al.,* 1993; Jensen, 2000).

Essentially the water depth calculation technique depends on finding a relationship between water depth and the reflected radiance of a wavelength band. Bathymetry can be obtained indirectly from its relationship to the electromagnetic radiation reflected from the water medium. The interaction between downwelling light with the atmosphere and aquatic media has been explained previously.

2.6.3.3 Difficulties in using remotely sensed data in water research.

When measuring detailed information from remotely sensed measurements in water there are three main problems. First the atmospheric path between the object and the sensor affects the characteristics of the radiation signal received by the sensor. The amount of energy transmitted into the sea versus that reflected off the surface also depends on the sea surface state, wind speed and Sun angle, which create inconsistent light interactions at the air-sea interface. Shallow water substrates also create difficulty in separating the water column signal from that of the substrate. These problems are addressed to some degree using a simple radiative transfer model for optically shallow water in the general form (Philpot, 1989):

$$L_d = L_b \exp(-gz) + L_w \qquad 2\text{-}3$$

Where :

L_d = radiance observed at remote detector (mwcm^{-2} μ^{-1} sr^{-1})

L_b = radiance term which is sensitive to bottom reflectance (mwcm^{-2} μ^{-1} sr^{-1})

g = effective attenuation coefficient of water (m^{-1})

z = Depth of water column (m)

L_w = remotely observed radiance over optically deep water (mwcm^{-2} μ^{-1} sr^{-1})

Under ideal conditions both depth and effective attenuation coefficient of water over several bottom types can be obtained from passive satellite sensor imagery (Philpot, 1989). These conditions apply that the water quality and atmospheric conditions are similar throughout the imagery. Thus, the simplest method of extracting water depth information from multi-spectral sensor data is to invert equation 2-3 for a single wavelength (Lyzenga, 1978). As these conditions are not easily met, researchers have expanded equation 2-3 to take the atmospheric and water conditions into account. An expansion to the first method assumes that a pair of wavelength bands can be found such that the ratio of the bottom reflectance in the two bands is the same in the imagery. If these assumptions are correct an equation can be derived so that the depths calculated are not affected by changes in bottom composition (Lyzenga, 1978). Several other methods have also been proposed to deal with less than ideal conditions such as changes in water type and variables atmospheric conditions. These methods are based on three case scenarios that are 1) variable depth, all other parameters constant 2) Variable depth, and bottom reflectance, 3) Variable depth, bottom type and water type (Philpot, 1989).

2.6.4 Modelling Shoreline data and GIS analysis

Geographical Information Systems (GIS) have become an important tool in resource management. Factors affecting shoreline position such as wave dynamics, geomorphology, littoral transport and sand supply can be incorporated into a GIS for analysis. Incorporating historical shoreline maps, recession rate data and time series data into a GIS, shoreline position and its movement can be predicted (Li *et al.,* 2001). To predict shoreline movement and beach loss as a function of time several approaches

have been explored. Among the most commonly used is the End Point Rate (EPR). It is an ~~emphatically~~ empirical technique where no knowledge of sand transport system is required. Instead, the cumulative effect of all underlying process is assumed to be captured in the position history (Li *et al.,* 2001). Prediction of erosion hazard areas can also be preformed using predicted shoreline model and relevant GIS layers. The integration of modelling capability in GIS has been determined to be an integral part of shoreline modelling.

2.7 Limitations of remote sensing

Although many researchers have explored the potential of remote sensing in coastal application numerous limitations still exist. One of the primary limitations of remote sensing is the spatial resolution (Malthus and Mumby, 2003). The spatial resolutions of SPOT HRV and Landsat TM have not been sufficient for shoreline mapping. Currently the finest spatial resolution available commercially is 1 m (IKONOS satellite sensor), this would increase the capability of remote sensing to match the use of aerial photograph for shoreline mapping (Clark *et al.,* 1997; Mumby and Edwards, 2002; Malthus and Mumby, 2003).

Another limitation is the availability of data. Passive remote sensing sensors are very susceptible to atmospheric conditions such as cloud cover, haze and rain. As Landsat and SPOT satellites only have a revisit time of 16 and 26 days respectively, selection of cloud free days for data acquisition would be limited. Due to problems with these atmospheric conditions several researchers have also explored the use of radar or active sensors in shoreline mapping. But success has been limited and results were not as good as using passive sensors (Lyzenga and Tanis , 1981).

Radiometric resolution determines the amount of tonal variation a sensor can capture. Most satellite sensors collect data in 8 bit providing a total of 256 tonal variations. Although this radiometric resolution might be sufficient in medium scale application, a finer radiometric resolution is required in order to discriminate between features in small-scale mapping (small areas). With finer radiometric resolution continuous tone satellite sensor images are produced making it easier to detect different types of features.

2.8 Potential of IKONOS for shoreline mapping

2.8.1 IKONOS sensor system

Space Imaging Corporation launched the IKONOS satellite from Vandenburg Air Force Base, California, USA on the 24th September 1999 (Space Imaging, 1999). IKONOS was built with an agile, body-scanning configuration allowing for short revisit times and flexibility in data collection. A rigid satellite platform was built to reduce the vibration of platform and to contribute to the integrity of the line-of-sight determination (Lillesand and Kiefer, 2000). The system is based on a new optical system: a push-broom camera with a 10 m focal length, which has been folded into two through the use of a mirror. The IKONOS push broom sensor includes a panchromatic band (450-900 nm) at a nominal spatial resolution of 1 m, and a four-band multi-spectral with a spatial resolution of 4 m (Jensen, 2000). Image data are quantised to a radiometric resolution of 11-bits/pixel (0-2,047), thus providing an increment by a factor of 8 in the range of grey levels to represent target brightness, when compared to 8- bits/pixel systems (Space Imaging, 1999). This enhanced radiometric resolution can increase target discrimination and classification ability,

particularly for low light conditions that are typical of underwater environments (Jill , 2001).

The entire satellite is able to pivot in orbit to collect cross-track imagery covering a distance of 725 km at either side of the ground track. Due to the satellite's 680 km altitude, imagery will maintain at least a 1 m ground sample distance (GSD) for 350 km to either side of nadir, or a 700 km swath of at least one-metre imagery (Space Imaging, 1999). The system is designed to carry three GPS antennas and three digital star trackers to maintain precisely camera station's position and attitude. The satellite is rotating around the Earth in a Sun synchronous polar orbit, which allows it to traverse the planet every 98 minutes, crossing the equator at the same time (10.30 am) in every orbit (Zhou and Li, 2000).

2.8.2 Geometric accuracy of IKONOS sensor imagery

2.8.2.1 Mapping standards

Geometric accuracy is very importance if satellite sensor imagery is to be used to produce topographic map for shoreline monitoring. According to the United States National Map Accuracy Standards, horizontal accuracy for maps on publication scales larger than 1: 20,000, not more than 10 percent of the points tested shall be in error by more than 1/30 inch (0.8466667 cm), measured on the publication scale; for maps on publication scales of 1: 20,000 or smaller, 1/50 inch (0.0508 cm) (U.S.Geological Survey, 1999). These limits of accuracy shall apply to positions of well-defined points only for other points any error is possible. Well-defined points are those that are easily visible or recoverable on the ground (U.S.Geological Survey, 1999).

2.8.2.2 Application of satellite imagery for mapping

Aerial photography is still the primary technique for large-scale mapping. But in spite of its advantages, the need of special flight planning and scheduling limits its application (Mikhail, 1999; Jensen, 2000). Due to these limitations several countries have used satellite sensor imagery for national mapping projects. SPOT HRV images have been used to produce national mapping products in Saudi Arabia, France, Ethiopia and Yemen. Despite its advantage over aerial photography, SPOT HRV imagery can only meet the requirement for small scale mapping at 1:50,000 and 1: 100,000 scale (Al-Rousan *et al.,* 1997). It is expected that fine spatial resolution satellite sensors such as IKONOS have the potential to acquire geographic information at a medium to large scale (1:24,000 and 1:10,000) (Li, 1998).

2.8.2.3 IKONOS stereo mapping capabilities

The CCD linear array of IKONOS is capable of imaging the same ground profile at three angles, which are fore, nadir and aft. This is illustrated in Figure 2.8. In attaining stereo pairs three types of combination can be obtained. They are fore-nadir (F-N), nadir-aft (N-A) and fore-aft (F-A). The base to ratio is a critical factor in 3-D mapping. For 1: 24,000 scale topographic maps aerial photography with a base-height ratio of 0.63 have been used. This base-height ratio could be obtained through IKONOS by forming a stereo pair using F-A or N-A combination (Li, 1998). At this scale DEM accuracy need to be less than 15 m and this is also attainable from IKONOS even without GCPs. Although GCPs are not required, it is recommended that GCPs be used to increase accuracy.

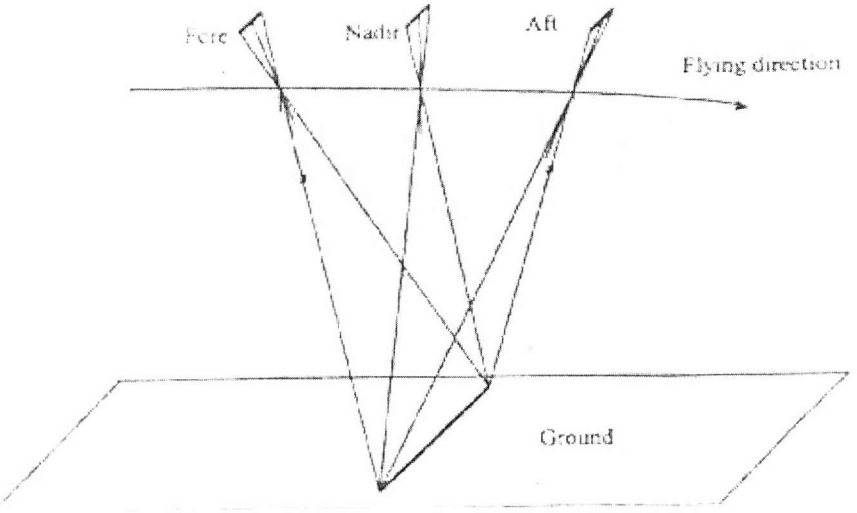

Figure 2.8: Fore-, Nadir-, and Aft-looking CCD liner array and their look angle (Li, 1998)

Li *et al.,* (2000) evaluated the attainable accuracy of GCPs derived from integrated global positioning system (GPS) and fine-resolution stereo IKONOS data. Simulated IKONOS imagery was generated from aerial photograph based on the principle of "projection" and "back-projection". Projection is the processing of the data from aerial images to the surface of the DEM, and back-projection is the same processing from the surface of the DEM to a satellite sensor image at a fore, nadir, or aft-look. Using these simulated satellite sensor images several accuracy test such as geometric accuracy versus the number and distribution of GCP, accuracy versus image measurement errors of GCP and checkpoints were conducted. It was concluded that accuracy can reach 3 m horizontally and 2 m in height with 4 GCP. Therefore, they suggested that only 4 GCP be used to maintain accuracy and minimize cost. An increased number of GCP but poorly distributed would be less beneficial than a few GCP well spread. They also determined that the 1 m spatial resolution satellite sensor imagery would meet mapping accuracy for medium scale maps from 1 : 24,000 to 1 : 10,000 scales. So, the fine-resolution imagery has potential for shoreline mapping and

erosion monitoring. This thesis would examine the accuracy attainable by fine spatial resolution satellite sensor imagery to monitor the shoreline.

2.8.3 Application of IKONOS sensor imagery for shoreline mapping

The spatial resolution of 30 m and 10 m of Landsat TM sensor and SPOT HRV sensor respectively are insufficient for 1: 24,000 and 1: 10,000 scale mapping using standard method of image processing. This has been the primary impediment for the application of remote sensing in shoreline mapping. With the availability of fine spatial resolution satellite sensors researchers have achieved increased capabilities for surface and subsurface feature delineation. The IKONOS sensor with a spatial resolution of 1 m provides a feasible alternative to aerial photogrammetry. IKONOS multi spectral is also capable of extracting a range of geographical features as its sensors spectral range is larger in comparison to aerial photography.

A shoreline is the intersection between the DEM and near-shore bathymetry. This intersection changes as the water surfaces increase and decrease due to tide elevation. Therefore, a tide-coordinated shoreline should be based on a certain water datum. The DID produces shoreline map based on the MHWS (Ministry of Agriculture, 1997; Li *et al.*, 1998). Because satellites have a prescribed orbit, it is not possible to image an area at the required water level (MHWS). To correct the captured shoreline to a MHWS shoreline, an accurate elevation model of the inter-tidal zone need to be constructed. Inter-tidal zone can be defined as the coastal transition region between the permanently exposed land surface on one side and the submerged region on the other side (Leow *et al.*, 2000). The elevation model of the Inter-tidal zone could be constructed by combining the DEM and near-shore bathymetry.

2.8.3.1 Deriving DEM from IKONOS sensor imagery.

SPOT HRV has been the most widely used stereo sensor. Using SPOT HRV imagery DEM and ortho-images can be produced with accuracy up to 10 m horizontally and vertically (Krupnik, 2000). But even at this spatial resolution its utilization in coastal mapping is limited (Cracknell, 1999).

The IKONOS sensor and SPOT HRV are similar as both are push-broom sensors. In the case of IKONOS and most other satellite sensors, the perspective centre is constantly changing, as the satellite is moving. This is in contrast to vertical aerial photography as the perspective centre is constant in each photograph (Anon, 1993). A number of researchers have examined methods of determining elevation from stereo SPOT HRV imagery. Early research utilized SPOT HRV imagery and analytical plotters in conjunction with film transparency and operator controlled measurements (Al-Rousan *et al.,* 1997). Recently remote sensing image processing systems have incorporated programs for digital or softcopy photogrammetry. To extract elevation information from satellite sensor stereoscopic pairs, mathematical models need to be developed to describe the geometric relationship between stereo satellite sensor images to object spaces through the perspective centre of the imaging sensor. Beside this relationship it is also necessary to take into account the dynamic motion of the satellite and sensor over the time period of image acquisition. Several researchers have developed models to explain this relationship including Brokelbank and Tam (1991), Al-Rousan *et al.,* (1997), Kim (2000) and Kim *et al.,* (2001).

IKONOS has a very complex sensor model. To generate ortho-rectified images from IKONOS imagery Space Imaging has developed a Rational Polynomial Camera (RPC) model, which is a header file that expresses the camera model as a ratio of two cubic polynomials. It is derived from the physical camera model during on orbit

calibration of the sensor (Bohnestiehl, 2001). Space Imaging has kept this information secretive and only releases them to selected customers. In lieu of the RPC model three methods can be used to geo-rectify these images, which are the simple polynomial method, rational polynomial method and the rigorous (or parametric) model method (Toutin, 2004). The simple polynomial method only corrects planimetric (X and Y) distortion of GCPs and does not take elevation into consideration. The rational polynomial method is similar to the simple polynomial method but it also takes into account the ratio of polynomial transformation and elevation of GCPs. This method is useful for areas with gentle terrain. As both method do not require satellite and sensor information they require many GCPs and distortion between GCPs are not eliminated (Toutin and Cheng, 2000). Rigorous model reflects the physical reality of the complete viewing geometry and correct distortion due to sensor, Earth and deformation due to cartographic projection. It then takes into consideration the satellite sensor information (Toutin and Cheng, 2000). Despite not having detailed sensor information, Toutin *et al.,* (2001) had successfully developed a rigorous IKONOS model using basic information of metadata and image files. Using this model the exterior orientation parameter of each image and the interior orientation parameters can be determined. Using these, DEM can be generated using pixel matching between adjacent stereo pairs (Bohnestiehl, 2001). In this process an elevation will be calculated from the stereoscopic parallax between the same pixel between two stereo pairs. This allows for the creation of very dense points clouds reflecting minute variations in terrain.

To produce an accurate DEM accurate GCPs are required. These points must be precisely surveyed features that are visible in the satellite sensor imagery. Non-natural and natural features would be carefully selected in a well-distributed grid. The GCPs would be surveyed using differential global positioning system (DGPS) for

accurate measurements. Several companies offer wide-area differential GPS service, using satellite broadcast techniques. Using DGPS resultant GCP will have sub-metre accuracy in the X and Y direction. Accuracy in the Z direction will be less than 2 m (Omnistar, 2001).

2.8.3.2 Deriving bathymetry from IKONOS sensor imagery.

As previously discussed researchers have used passive remote sensing sensor imagery to obtain bathymetry data (Lyzenga, 1985; Clark *et al.,* 1987; Cracknell and Ibrahim, 1988; Ji *et al.,* 1992; Sandidge and Holyer, 1998; Bagheri *et al.,* 1998; Roberts and Anderson, 1999; Stumpf *et al.,* 2003). Studies have concentrated on the blue region of the electromagnetic spectrum (0.45-0.52 μm) due to its ability to penetrate of water. Landsat TM has been used extensively for this purpose and several researchers have extensively developed models to extract bathymetry information (Lyzenga, 1979; Philpot, 1989). As the IKONOS multi-spectral bands are spectrally similar to bands 1-4 of the Landsat TM (Table 2.4) they could be applied in bathymetric applications.

IKONOS with its spatial resolution of 4 m (MS) and radiometric resolution of 11 bit provides the capability to extract accurate bathymetry information better than Landsat TM.

Table 2.3: IKONOS multi-spectral sensor bandwidth specifications

Band	Wavelength
1	445-516 nm
2	506-595 nm
3	632-698 nm
4	757-853 nm

Table 2.4: Landsat TM multi-spectral sensor bandwidth specifications

Band	Wavelength
1	445– 520 nm
2	520 – 600 nm
3	630 – 690 nm
4	760 – 900 nm
5	1550 – 1750 nm
6	10400 – 12500 nm
7	2080 – 2350 nm

2.9 Aim of study

The aim of this thesis is to develop methods to accurately map the shoreline from satellite sensor imagery. Methods of mapping the shoreline from fine and coarse spatial resolution satellite sensor imagery would be explained.

In this thesis a method of generating a 3-D terrain model of coastal areas using fine spatial resolution satellite sensor imagery would be examined. Using the 3-D terrain model of the coastal area the shoreline could be determined by the water land boundary.

Methods of mapping the shoreline from coarse spatial resolution satellite sensor imagery would also be explored. Sub-pixel mapping methods would be examined and compared with method such as hard classification. This thesis would examine sub-

pixel mapping methods to accurately predict the shoreline position at a sub-pixel scale based on coarse spatial resolution satellite sensor imagery.

2.10 Conclusion

Coastal Information is valuable for the management and future planning of coastal areas. Coastal areas are dynamic environments, constantly changing in response to human and natural forces. As a result coastal maps rapidly become outdated, resulting in a need for quicker method of producing coastal map (Dorota and Charles, 1999). Remotely sensed imagery provides a means of promptly extracting geographical features and coastal maps.

By processing multi temporal satellite sensor images and extracting 3-D model of the coastal zone, the data would be useful to effectively quantify accretion and erosion patterns, predict shoreline positions, sand transport patterns and other useful geographical information. With this information, it is hoped the coastal areas would be managed and monitored accordingly.

3 Study Area and Data

3.1 Study Area

The study area for this research is located in the state of Terengganu, Malaysia. Terengganu is located in the east coast of peninsular Malaysia and its shoreline is generally categorised as white sandy beaches (Figure 2.1) (Gobbett and Hutchison, 1973). The main economic activity of the population is fishing, tourism, and cottage industries. In the 1980s with the discovery of petroleum in the South China Sea off Terengganu, petroleum based industries have become an important contributor to the local economy.

3.1.1 Climate

The climate of Malaysia is generally characterized by the northeast monsoon and the southwest monsoon (Figure 3.1). The Northeast monsoon starts in November and lasts until March. It brings substantial rain and severe winds to the east coast of peninsular Malaysia. The Southwest monsoon, which starts in May and lasts to September causes substantial rainfall and severe winds along the west coast of peninsular Malaysia but the sheltering effects of Sumatra dampens the dynamics of the monsoon. The east coast of peninsular Malaysia is not drastically affected by the Southwest monsoon (Ooi, 1974). Figure 3.1 illustrates the monsoons effecting Malaysia.

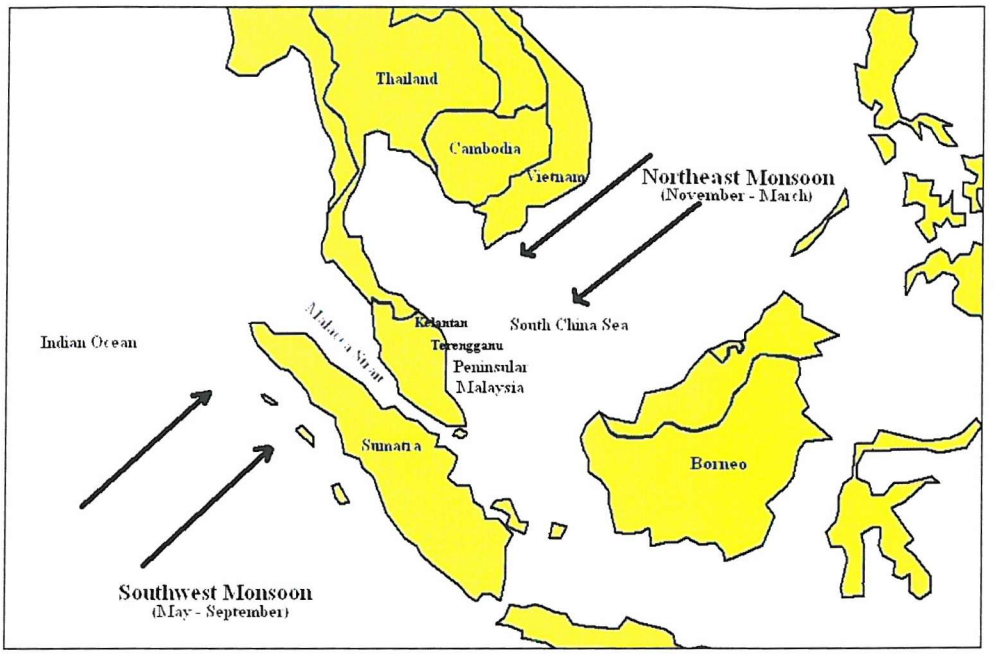

Figure 3.1: The two monsoon affecting the climate of Malaysia.

Air temperatures in peninsular Malaysia vary throughout the year. Monthly mean air temperature varies from 24.4 to 27.9 ° C along coastal areas. The warmest month is usually April along the northern part of west coast and May along the east coast and southern part of the west coast (Malaysian Meteorological Service, 2001).

Relative humidity is high throughout Malaysia with a monthly mean ranging from 80 to 87 percent. The seasonal variation of relative humidity conforms to the rainfall pattern of the area. Typically, the highest occurs in November and lowest in February (Malaysian Meteorological Service, 2002).

The average annual rainfall in peninsular Malaysia is about 2400 mm. The average monthly rainfall along the east coast of peninsular varies from about 120 mm in April to 615 mm in December. On the west coast, the minimum and maximum average monthly rainfall is approximately 80 mm in January and February and 260 mm in October and November (Malaysian Meteorological Service, 2001).

3.1.2 Winds

The wind from the Northeast monsoon blows mainly from the northeast and north direction. On the northern part of the east coast of peninsular Malaysia, the prevailing Northeastern monsoon winds are more north-eastern to east. Winds of 15 ms^{-1} and more occur less than once a month in January and February and very seldom during the rest of the monsoon period. Gusts of up to 20 ms^{-1} have been recorded.

The Southwest monsoon winds rarely exceed 15 ms^{-1}. Gusts of up to 30 ms^{-1} have been recorded. Prevailing wind directions are south to west with an average speed of about 4 metres per second (Malaysian Meteorological Service, 2002).

3.1.3 Tides, Water Elevation and Datums.

Water levels along the coast of peninsular Malaysia are mainly influenced by astronomical tides. These tides are co-oscillating tides of the Indian and Pacific Ocean basins causing this region to have a variation of tide types. In Malaysia the common type of tide are diurnal, semi-diurnal and mixed. The east coast of peninsular Malaysia particularly the state of Terengganu is characterized by diurnal tides. The west coast of peninsular Malaysia is more characterized by mixed tides. Currently there are no long-term records of water elevation along the coast. Due to this the Directorate of National Mapping has established a network of tide gauges along the coast for recording water elevation.

Tidal ranges are in the order of 1.0 to 2.0 m along the east coast of peninsular Malaysia. The spring tidal range on the west is generally 2.0 to 2.5 m but spring range of 4.1 m has been recorded in Port Kelang, Selangor. Storm surges and wave setup can significantly affect the water surface elevation at the Malaysian shoreline. Storm surges are caused by the wind stress and the moving atmospheric pressure jumps

accompanying moving storm systems. Wind stress is responsible for the largest part of storm systems. The wind exerts a horizontal force on the water surface, which induces a surface current in the general direction of the wind. The current is impeded in the shallow water near the shore causing the water level to rise down wind (Ooi, 1974).

Observations along the Malaysian coast indicate that there is generally little variation between the predicted tides and observed tides (Stanley consultants Inc. *et al.*, 1985). However, the tidal prediction tables indicate that the highest astronomical tides may be as much as 1 m above mean higher high water and mean high water spring.

Datum's used in Malaysia are the admiralty chart datum (ACD) and the land Survey datum (LSD). Typically all published nautical chart and tide tables follow the ACD while all topographic and other land based survey follow the LSD. Relationships between the ACD and LSD have been established and at specific sites in Malaysia and have been published (Ministry of Agriculture, 1997).

3.1.4 Waves

The Northeast monsoon causes prominent wave along the east coast of peninsular Malaysia. The predominant wave approach direction offshore of Kelantan and the northern part of Terengganu is more easterly due to the limited fetch caused by the Vietnam and Cambodia peninsular (Figure 3.1).

Wave height on the east coast of peninsular Malaysia during the Northeastern monsoon period are generally less than 1.8 m with a period of less than 6 s, but can vary greatly due to the periods of strong winds and calm. Hindcast predictions of significant deepwater characteristics for 18 severe storms between 1960 to 1976 were made by Oceanographic services, Inc. for the offshore of Terengganu (Angkasa-Ghd

Engineers Sdn Bhd., 1981). Waves of 2.7 and 4.8 m with an average period of 6 to 9 s were indicated offshore Terengganu during severe monsoons. A 5.33 m deepwater significant wave height was determined to have a 100-recurrence interval in this area.

The Southwest monsoon causes predominant wave condition on the southern part of the west coast of peninsular Malaysia. However, the island of Sumatra shelters the west coast from the Indian Ocean, limiting the fetch length to approximately 40 to 130 km in the Malacca straits (Forbes, 1998). Wave height during the monsoon usually ranges from 0.5 to 1.0 m with a maximum height of 2.0 to 3.0 m. Wave periods are usually less than 3 s but may have a maximum of 6 to 9 s (Angkasa-Ghd Engineers Sdn Bhd., 1981).

3.2 Map projection

The application of a basic mapping projection is not suitable for a country such as Malaysia due to its orientation. Due to this, the Directorate of Colonial Surveys in Teddington, England prepared the rectified skew orthomorphic (RSO) Projection Tables for Malaya in 1947 (Hotine, 1947) . Since then, Directorate of National Mapping of Malaysia has used it for the Malayan Revised Triangulation (MRT) and topographical surveys. The characteristic of RSO are a constant minimum scale error along a great circle passing obliquely through the area, with scale increasing with distance from this great circle (Hotine, 1947). A basic diagram displaying the projection is shown in Figure 3.2. Therefore, it is suitable for areas like Peninsular Malaysia and Italy. The maps used and produced in this thesis were geo-rectified to the RSO based on the Modified Everest reference ellipsoid. This projection is the standard mapping projection used in Malaysia and used primary for topographic mapping.

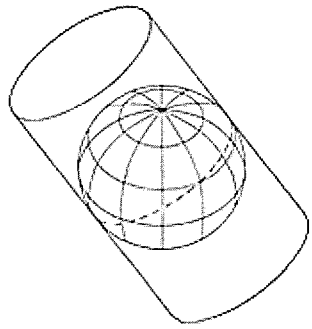

Figure 3.2: Diagram shows how the RSO projection projects the earth surface based on an oblique cylindrical surface.

The geodetic information regarding the RSO projection is given below:

Geodetic Data

Spheroid	:	Modified Everest 1948
Semi-major axis (a)	:	6 377 304.063m
Semi-minor axis (b)	:	6 356 103.039
Ecentricity Squared (e2)	:	0.006 637 846 6302
Reciprocal of flattening (l/f)	:	300.8017

Origin of Meridian of reference

Projection	:	Malaysian RSO
Longitude of Origin (CM)	:	E 102° 15' 00.00"
Latitude of Origin	:	N 004° 00' 00.00"
False Easting	:	804671.30m
False Northing	:	0.00m
Scale Factor on CM	:	0.99984
Skew Azimuth	:	323° 07' 48.37"

Satellite Datum

Spheroid	:	WGS-84
Semi-major axis (a)	:	6 378 137.000m
Semi-minor axis (b)	:	6 356 752.314m
Eccentricity Squared (e2)	:	0.006 694 380 023
Reciprocal of flattening (l/f)	:	298.2572

Datum transformation parameters from WGS-84 TO Malaysia Revised Everest, Kertau are as follows:

dx	=	+ 379.78m
dy	=	- 775.38m
dz	=	+ 86.61m
Rx	=	0° 00' 02.60"
Ry	=	0° 00' 02.10"
Rx	=	-0° 00' 12.11"
Scale	=	1.00000

3.3 Data

This section describes the main data used in this thesis.

3.3.1 Satellite sensor data

3.3.1.1 IKONOS Sensor Imagery

This research utilizes Space Imaging IKONOS sensor imagery. Several data sets were acquired of the study area on the 1st July 2000, 10 April 2002 and 28 August 2002. The three data sets are described bellow:

Table 3.1: IKONOS sensor data used in this thesis.

Data	1st July 2000	10th April 2002	28th August 2002
Product Type :	1-metre Pan-Sharpened Multispectral	Geo 1m + 4m bundle (Multi Spectral + Pan) + IGM	1-metre Stereo Pan-Sharpened Multispectral + IGM
Acquisition Date/Time	2000-07-01 03:14 GMT	2002-04-10 03:42 GMT	2002-08-28 03:45 GMT

Further details about the data including header information are given in Appendix 2

3.3.2 Bathymetric Ground data

Two field trips to the study area were conducted to obtain bathymetric ground data. Ideally these field trips should coincide with the date of satellite sensor data acquisition but as Space Imaging does not inform customers of the data acquisition dates before hand this was unlikely. Therefore the field trips were conducted on dates within the data delivery period assigned by Space Imaging. These field trips were conducted on 15th June 2000 and 6th July 2002. These dates are still close to the image acquisition dates and no major changes to the bathymetry were expected due to the difference.

To ensure the water depth obtained were accurate all depth values were made to an accuracy of 0.1 m and all echo-sounding equipment were calibrated before and after each day's sounding operations. In order to used these values for mapping purposes the water depth values were related to the latest published values of the Malaysian Land survey datum (LSD). This was done by establishing a Temporary Bench Mark (TBM), TBM are benchmark used to monitor water level variation during sounding operations. The TBM was setup at the Marine jetty located at Chendering harbour, Kuala Terengganu. The depth values were calibrated and standardise to a selected water level based on the TBM values. These values were later adjusted to the Malaysian LSD by a close levelling net to the government bench mark. This process ensures the data were corrected based on mapping standard setup by the Government. Data were collected at 200 m intervals along the shoreline up to 8 m depth seawards.

3.3.3 Shoreline survey

A shoreline survey was conducted on 6th of July 2002 to accurately map the shoreline at the Mean sea level tide elevation. The surveying work was contracted to the Sky-

Shine Corporation. Sky-Shine Corporation is a multi-disciplinary geographic based company dealing in surveying and positioning system, sea and land environmental system, hydrography and other mapping related disciplines. The shoreline map was produced at sub-metre accuracy.

3.3.4 Tide Table

The establishment of the Tidal Observation Network (TON) in Malaysia commenced in 1983. This project was initialized and carried out by Jabatan Ukur dan Pemetaan Malaysia (JUPEM) with the cooperation of the Japan International Cooperation Agency (JICA). Twenty-one (21) tide stations were established by the end of 1995, in which twelve (12) were located in Peninsular Malaysia and the rest in Sarawak and Sabah (Department of Survey and Mapping Malaysia, 2001). The observed tidal data and other related values are published annually in two reports, namely The Tidal Observation Record and The Tidal Prediction Table. This research utilises the tidal prediction table specifically the tide station located at Chendering Kuala Terengganu, Terengganu.

3.3.6 GPS Control Points

A field trip was conducted in November 2001 to obtained ground control points (GCPs) within the study area. The GCPs were collected using the OmniStar DGPS system which was capable of collecting GCP at sub-metre accuracy (Omnistar, 2001). A total of 62 GCPs were collected based on points, which were distinguishable from IKONOS satellite imagery. Figure 3.3 shows a sample GPS report:

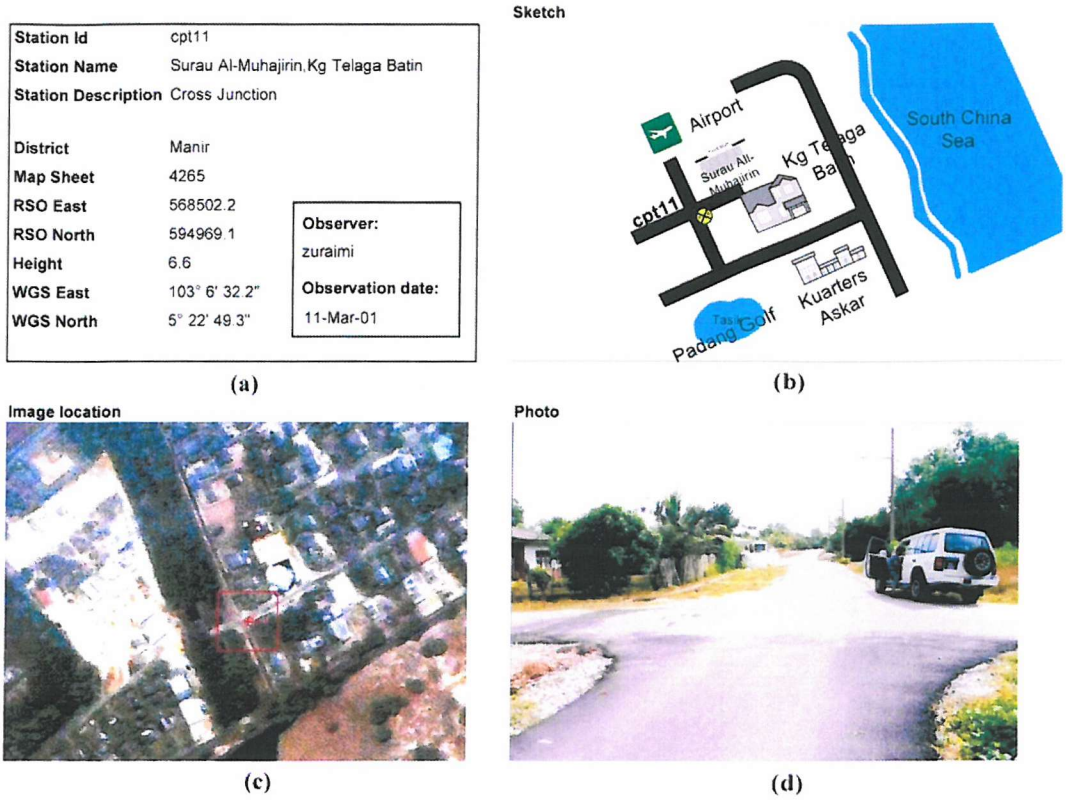

Figure 3.3: Sample GPS report for a point in Kg. Telaga batin. The report includes details about the (a) GCP point, (b) a sketch of the GCP point, (c) Location of the GCP point on an IKONOS sensor imagery and (d) a photograph of the location.

3.4 Conclusion

This chapter has given details of the study area and data used throughout this thesis. Characteristics of the study area are explained to give an understanding of condition attributing to problems related to the coastal area. Data used throughout this thesis were also explained and all spatial data sets were standardised to a single mapping standard, the RSO.

4 Sub–Pixel Analysis to Determine Shoreline Position.

Using coarse spatial resolution satellite sensor imagery for shoreline mapping is difficult. This is due to the fact that the actual shoreline could be located within the pixels. This chapter is a pilot study with the aims to examine shoreline positional errors due to different classification methods and increase its accuracy by mapping the shoreline at the sub-pixel level.

4.1 Introduction

The pilot study investigates the effects of utilizing coarse spatial resolution satellite sensor imagery to produce shoreline maps. Thematic mapping from remotely sensed data is commonly achieved through the application of a conventional hard image classification analysis. With hard classification, each pixel is allocated to the class with which it has the greatest similarity. The effect of this allocation process is to constrain the boundary between classes to lie between pixels. In reality, the boundary between classes will generally run through the area represented by a pixel, with the pixel having a mixed class composition. Since a hard classification can allocate a pixel to only one class its application will have the effect of mis-locating the boundary. Typically, the size of the mis-location error will increase with a coarsening of the spatial resolution of the data used. This pilot study analyses the shoreline positional accuracy achieved by a hard classification using coarse spatial resolution satellite sensor imagery similar to commonly used satellite sensor imagery such as Landsat TM, Landat ETM+ and

SPOT HRV. But these satellite sensor data sets are not suitable for mapping local changes in the shoreline as discussed in chapter 2. Therefore the potential of approaches to shoreline mapping based on sub-pixel level information derived from a soft classification is evaluated.

Soft classification allows a pixel to have multiple and partial class membership and so can accommodate for the effects of mixed pixels. The conventional output of a soft classification is a set of fraction images which indicate the relative coverage of the class as in the area represented by the pixel. If the predicted class coverages could be located geographically within the area represented by the pixel it would allow the boundary between classes to be plotted at a sub-pixel scale. The main aim of this research is to investigate a series of approaches for fitting the shoreline to a soft classification derived from remotely sensed data. A flowchart of the whole pilot study is given in Figure 4.1.

In this chapter a linear stretch of the beach measuring 500 m in length was used as the study area. The orientation of the particular shoreline is 45 degrees in the north-east direction and located in Kg. Seberang Takir, Terengganu (Figure 4.2). This stretch of shoreline was chosen as its a simple pattern and avoids simple pixel mixing due to its orientation. Since the aim was to investigate the accuracy of sub-pixel scale mapping of the shoreline, the study used a fine spatial resolution image to locate the actual position of the boundary with the analysis undertaken on a spatially degraded version of this image. Although imperfect, this approach removes problems of mis-registration between the image to be classified and the reference data on shoreline position.

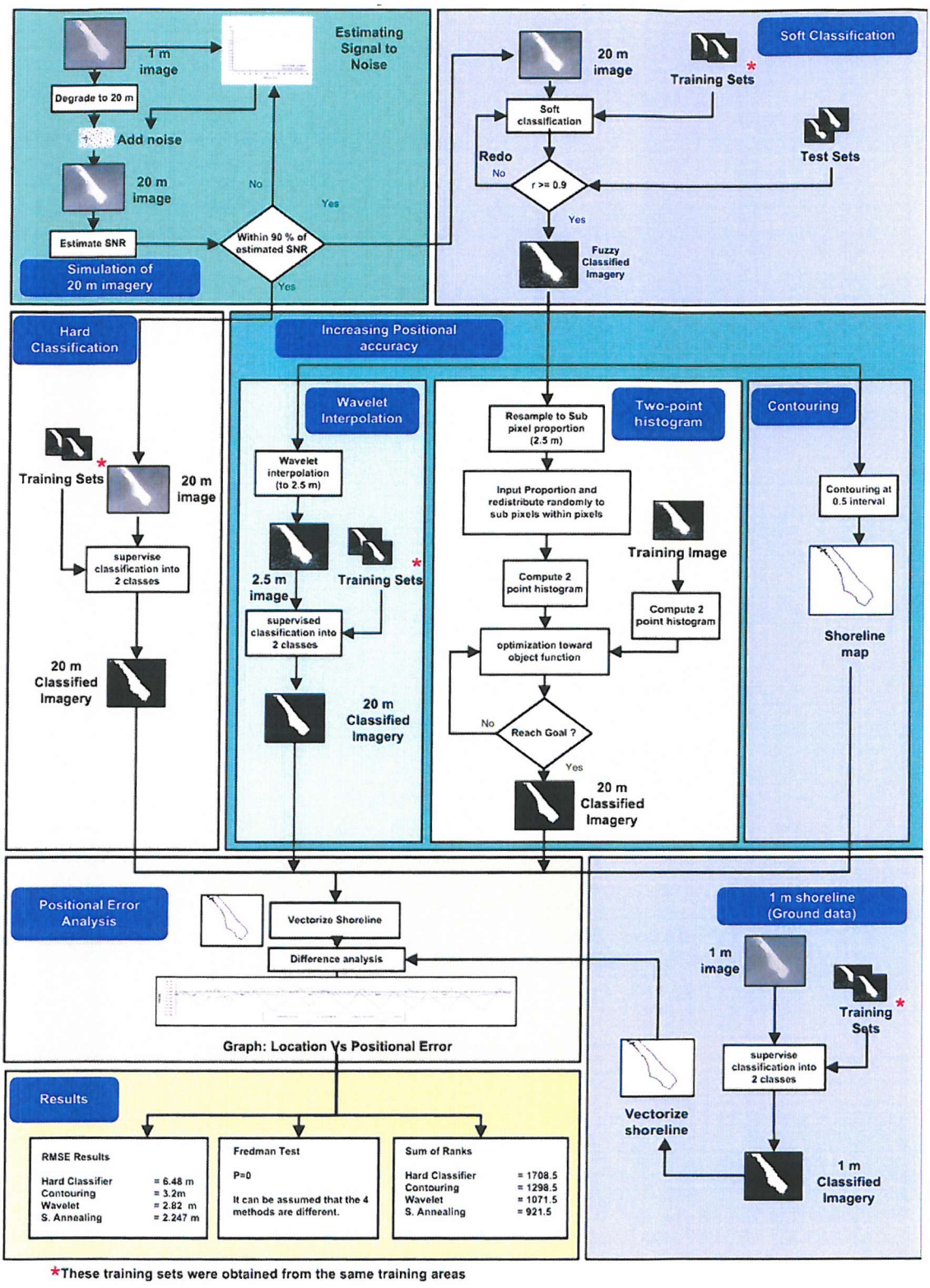

Figure 4.1: Flow chart of pilot study showing the different methods used in the pilot study.

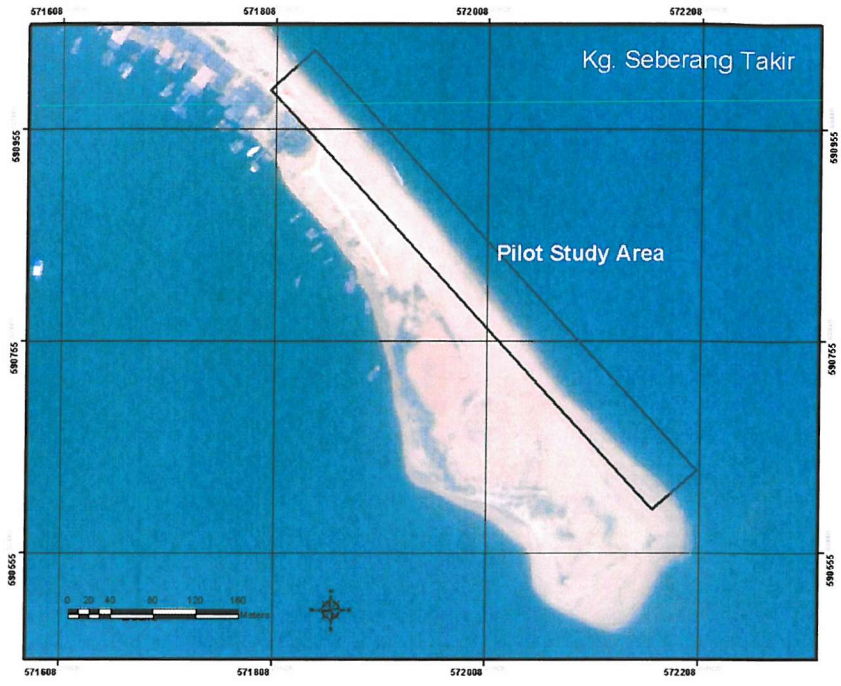

Figure 4.2: A colour composite of Kg. Seberang Takir (study area).

A 1 m spatial resolution IKONOS sensor image was acquired on 1st July 2000 and was geo-referenced to the Rectified Skew Orthomorphic (RSO) projection (Figure 4.2). The image was degraded spatially by aggregating pixels to 20 m spatial resolution.

4.2 Methodology

The methodology used in this chapter can be divided into several main sections. Initially a 20 m imagery was simulated from 1 m satellite sensor imagery. Several classification methods were used to analyze and effects on positional accuracy was determined. Methods to increase positional accuracy were explored and finally a positional error analysis was conducted to compare the different methods.

4.2.1 Simulation of 20m imagery

To ensure the actual shoreline position is known and minimize mis-registration problems, coarse resolution satellite imagery was simulated from fine resolution satellite data. This approach has the advantage that positional errors normally introduced during image geo-rectification of satellite imagery are not evident. Therefore the positional errors obtained in this chapter are solely because of the spatial resolution differences between the images. The fine spatial resolution satellite imagery used was acquired on 1st July 2000. To simulate coarse resolution satellite data the 1m IKONOS sensor imagery was sampled down to 20m. This resolution simulates spatial resolution comparable to widely used civilian system such as SPOT HRV sensor. A problem with resampling the imagery to a coarse spatial resolution is that it reduces the noise levels within the imagery produced. This eliminates errors normally evident in satellite sensor imagery such as internal sensor errors and effects of atmospheric condition (Duggin *et al.*, 1985). To properly simulate satellite imagery these errors need to be maintained. The noise in the original 1m imagery was determined and reapplied to the coarse resolution image to make the noise level comparable.

Several factors affecting the scene and the sensor were not considered when simulating the images. Of those affecting the scene, the adjacency effect is caused by complicated multiple scattering interactions, resulting in pixels with high DN values being lowered and pixels with low DN values being increased in a particular image. These pixel value changes largely depend on its contrast with neighbouring pixel values and are evident over large heterogeneous areas causing images to lack contrast and at edges, causing sharp lines to be blurred (Liang *et al.*, 2001). The adjacency affect could be simulated by modelling the point spread function (PSF) of the IKONOS sensor and affects of the atmosphere (Borel and Gerstl, 1992). To address

these issues further information such as IKONOS sensor information and atmospheric condition during image acquisition are required. As these information were not readily available, the adjacency affect were not considered when simulating the coarse spatial resolution imagery.

4.2.1.1 Satellite sensor noise

In satellite sensor imagery noise can be divided into 2 types : coherent and random. Coherent or system noise in most cases can be removed as its source is known within a particular sensor system (Wrigley *et al.,* 1984). Random noise on the other hand can not be removed easily as its source it not generally known (Smith and Curran, 1999).

The 1 m satellite sensor imagery used in this study was already corrected for coherent or system noise thus random noise is the primary concern. Even though random noise can't be removed easily, it can be measured by repeated measurement of a particular area then the average of these measurements will be the estimate of the true measurement (Shanmugan and Breipohl, 1988). The variation of each individual measurement is therefore an estimate of the random noise (Duggin *et al.,* 1985). Therefore, on a particular sensor system the signal strength could be used to estimate noise. Here noise will be defined as signal to noise ratio (SNR) (Smith and Curran, 1999), given by the equation :

$$\text{SNR} = \frac{\text{Signal}}{\text{Noise}} \qquad 4.1$$

SNR is proportional to data quality; therefore with a larger SNR it would be easier to distinguish useful information. The SNR of a satellite sensor is a function of the

spectral, spatial and radiometric resolution (Lillesand and Kiefer, 2000) and can be described as :

$$SNR(\lambda) = D(\lambda)\beta^2\left(\frac{H'}{v}\right)^{0.5} \Delta\lambda L(\lambda) \qquad 4.2$$

where:

SNR (λ) is the SNR at wavelength λ, D = detector quality,

β = instantaneous field of view of the sensor, H' =height of sensor platform

v = Plaform velocity $\Delta\lambda$ =Sensor spectral resolution

L = Radiance of target area.

The SNR of the sensor is also related to the quality of the optics and electronics within the sensor and the attenuation of the atmosphere at acquisition time.

4.2.1.2 Methods of estimating SNR of satellite sensor imagery

Several methods have been developed to estimate SNR. The simplest method, the homogenous area uses small windows of pixels within large homogenous image areas (Smith and Curran, 1999). The signal at a certain point is estimated by averaging the pixel response in the window. The noise is then estimated by calculating the standard deviation of the pixel responses within the windows. Another method, the nearly homogenous method addresses the issue of finding large homogenous areas within satellite sensor images. This method proposed by Yuhas *et al.*, (1993) allows for some natural variation within areas selected for analysis. As with the homogenous method, this method calculated the standard deviation of small groups of pixels. The pixels in the nearly homogenous area are then averaged in groups of increasing size and the standard deviation calculated against each group. The standard deviation is then plotted against the reciprocal of the square root of the number of pixels used in the group. This method assumed that as pixels are averaged in increasing larger group of

pixels the component of standard deviation due to sensor noise should decrease. The intercept from the vertical axis of this plot represents the standard deviation for an infinite number of sample. This value is assumed to be made up of only spatial variation. Therefore, the SNR can be estimated by dividing the average pixel values with the difference in standard deviation.

Geostatistics has also been used to estimate noise. Curran and Dungan (1989) developed a method to estimate the within pixel variation attributable to noise. The method used pixels along a traverse. The method employed the variogram, a plot of the semivariances $\overline{S_h^2}$ of the responses of the pixels pairs from the traverse against their separation of lag *(h)* (Curran and Atkinson, 1998). The semi-variance is estimated using:

$$\overline{S_h^2} = \left(\frac{1}{2m_h}\right)\sum_{i=1}^{m_h}\left[R(x_i) - R(x_i + h)\right]^2 \qquad 4.3$$

Where

M = number of pixel pairs h = lag

R = response of pixel. x_i = location of the first pixel of the i th pair

To determine the variance within a pixel that can be attributed to noise it is necessary to estimate the values of the semi-variance at lags less than one. This can be done by extrapolating the variogram model below one lag until it reaches lag zero. The semi-variance of the model when lag reaches zero is known as the nugget variance. The nugget variance is an unbiased estimate of the aspatial variation within each pixel. It has be shown that the square root of this nugget variance can be used as an estimate of the standard deviation and, therefore, the noise component of the pixel response within the traverse (Curran and Dungan, 1989). Therefore, the SNR can be estimated

by dividing the average pixel response along a traverse by the square root of the nugget variance. This method makes several assumptions. First it assumes that the spatial variation in the pixel response is related to the lag between pixels and not their location. It also assumes that the orientation of the traverse does not affect the variogram but dependant on the sensor operation.

4.2.1.3 SNR estimation of 1 m IKONOS satellite imagery

This chapter uses the geo-statistical method to estimate SNR value of the IKONOS sensor imagery. A traverse of 100 pixels was selected from the 1 m satellite imagery and a spherical model was used to fit the data. By extrapolating the semi variogram an intercept of 56.10 was determined. The square root of this value or the nugget variance was used as an estimate of the standard deviation along the traverse. Therefore the standard deviation was estimated as 7.48. To estimate the SNR the average the pixel response along a traverse (determined to be 233) was divided by the square root of the nugget variance. The resulting SNR for the 1 m IKONOS imagery was 31.14. Figure 4.3 shows the variogram used.

4.2.1.4 Generating Simulated 20 m IKONOS sensor imagery.

To generate the 20 m simulated imagery, the 1 m IKONOS sensor imagery was resampled to a spatial resolution of 20 m by aggregating the pixels. To counter effect the reduction of noise within the imagery due to resampling, the SNR of the resulting imagery need to be similar to the initial 1 m imagery. This was done by adding random noise to the 20 m imagery so that the resulting imagery has a similar SNR. As SNR can only be estimated and it is impossible to exactly obtain the same SNR between both images, it was decided that the resulting imagery needs to have a SNR

value to within 90 % of the SNR in the 1 m imagery. The resulting image is shown in Figure 4.4.

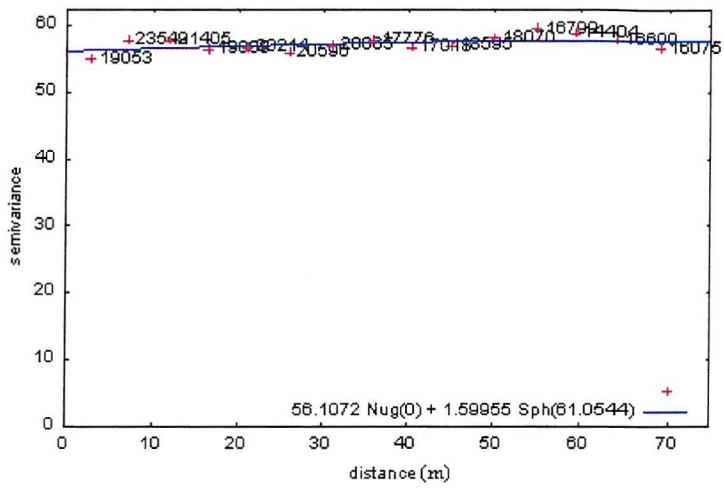

Figure 4.3: Variogram used to model 1 m imagery.

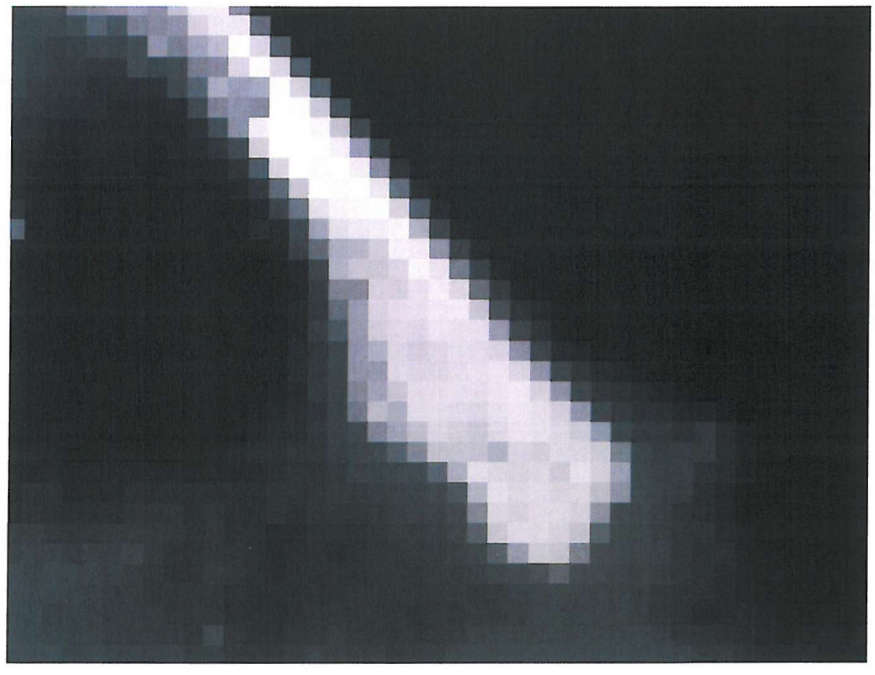

Figure 4.4: Simulated 20 m spatial resolution imagery

4.2.2 Generation of Ground Data from 1 m imagery.

To analyse positional errors generated from coarse resolution satellite imagery a shoreline map needed to be generated to represent ground data. This shoreline map was generated from 1 m IKONOS satellite sensor imagery. To differentiate between land and water body a supervised hard classifier was applied. Hard classifiers can be defined as a classifier that evaluate pixels and assigns them to only one class, based on the class of which it has the highest similarity of being a member, such as maximum likelihood (Richards, 1993; Jensen, 1996). Five homogenous land and five homogenous water sites were chosen to define pure land and water classes (Figure 4.5). These areas are determined from visual interpretation and field work and were used throughout this chapter in other classification methods to provide a consistency.

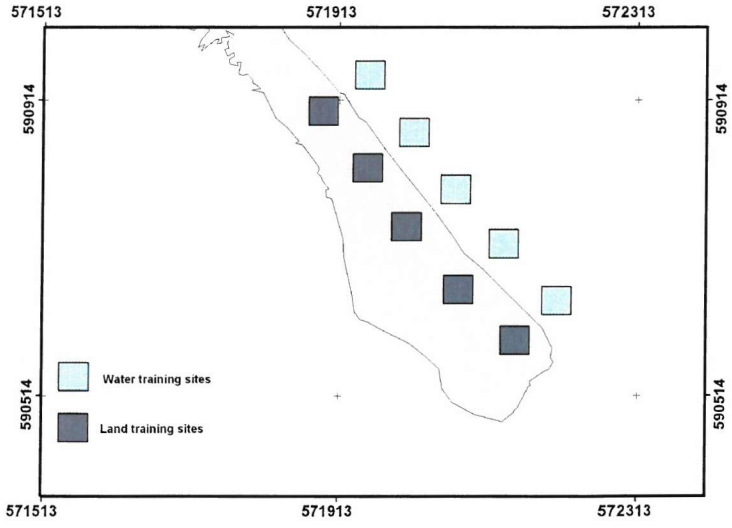

Figure 4.5: Training sites used in classification methods throughout this chapter.

Using these training sites to define pure land and water classes, the 1 m imagery was classified to 2 classes (land and water) using a maximum likelihood classifier. The resulting imagery was used to calculate the positional accuracy of the different classification method applied to the simulated 20 m imagery (Figure 4.6). Using the coarse 20 m simulated satellite sensor imagery several methods were used to map the shoreline. These include approaches based on hard and soft classifiers.

Figure 4.6: 1 m spatial resolution classified imagery (used as ground data in analysis)

4.2.3 Hard Classifier

To differentiate between land and water body a hard classifier was applied to the simulated coarse spatial resolution satellite sensor imagery. The maximum likelihood hard classifier used to classify the coarse spatial resolution imagery was similar to the one used to classify the 1 m imagery. The same training sites used in classifying the fine spatial resolution image were used (Figure 4.5). Using these training sets the 20 m imagery was classified to 2 classes (land and water). The resulting image (Figure 4.7) would later be analysed to determine the positional error between the predicted shoreline location and the actual location based on the ground data.

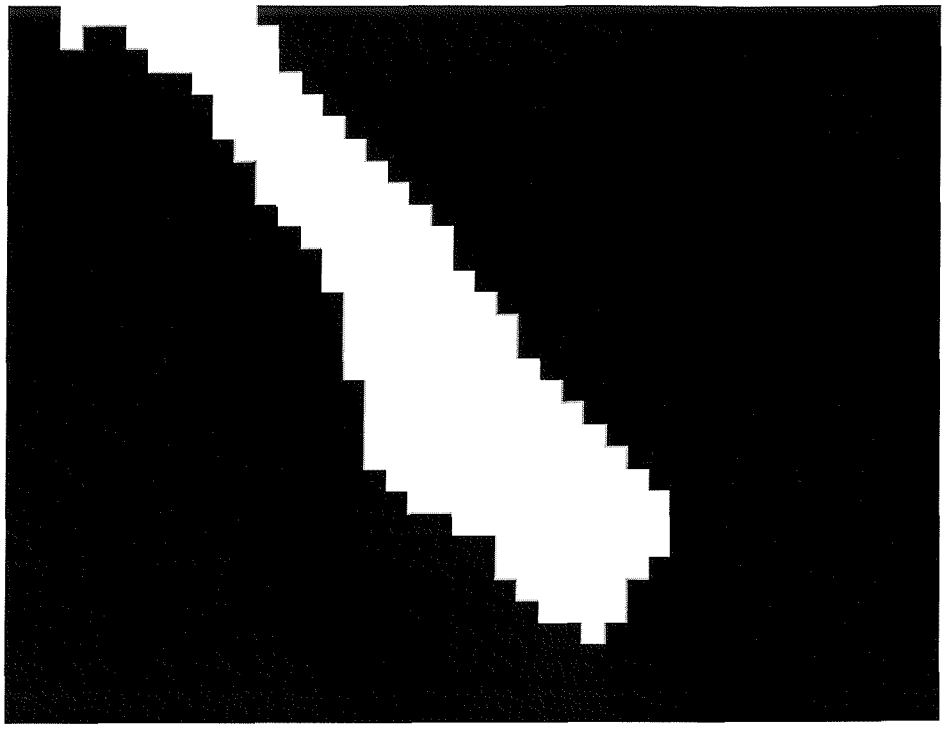

Figure 4.7: Imagery generated from hard classifying the 20 m spatial resolution imagery.

4.2.4 Soft Classification

Hard classification techniques have been popular in remote sensing but they only assign one class to a certain pixel (Richards, 1993; Jensen, 1996). As shoreline pixels usually contain a mixture of land and water classes, information within a pixel is lost. A major problem for accurate interpretation of remote sensing data is related to the fact that pixels may contain more than 2 classes which would only be realised from ground activities (Foody, 1992). This is due to the complex relationship of land cover types and their spectral reflectance (Richards, 1993). To address this problem researchers have developed methods to derive estimates of the sub-pixel class composition through the use of techniques such as mixture modelling and soft or fuzzy classifications (Foody, 1996). Soft classifiers allow pixels to have variable degrees of membership to

multiple classes. Soft classifiers assign a membership grade between 0 and 1 to each class in a pixel. This allows a pixel to be associated to multiple classes rather than just to one class as in conventional hard classifiers.

In this pilot study a sigmoidal function was chosen to classify between land and water. The function would classify pixels, based on a gradual transition between membership and non-membership to a class (Zadeh, 1965). The sigmoidal function was chosen because it models the gradual transition between land and water in coastal areas. For the function to be applied it requires that 2 pure classes be defined. These classes are pure land and water classes. The average DN value from the water and land training sites were used to define these classes (Figure 4.5). The soft classifier then classified each pixel in the study area to proportion values representing proportion of land within a pixel. For example if the value is 0.3 this means that the pixel contains 30 % land and 70 % water.

Since this soft classification was the basis of all the later analyses, its accuracy was evaluated. This evaluation was based on a comparison of the predicted coverage of a class with that derived from the ground data, the 1 m spatial resolution image. The correlation was calculated based on the Pearson correlation coefficient. The Pearson's correlation coefficient, denoted by r is a measure of linear association between two variables (Siegel and Castellan, 1988). The resulting classified imagery has a r value of 0.904 ($p < 0.05$). This result shows that the predicted and actual data are correlated significantly. Figure 4.8 shows the relationship between the predicted proportion of land and actual proportion of land. The output from the soft classification is shown in Figure 4.9.

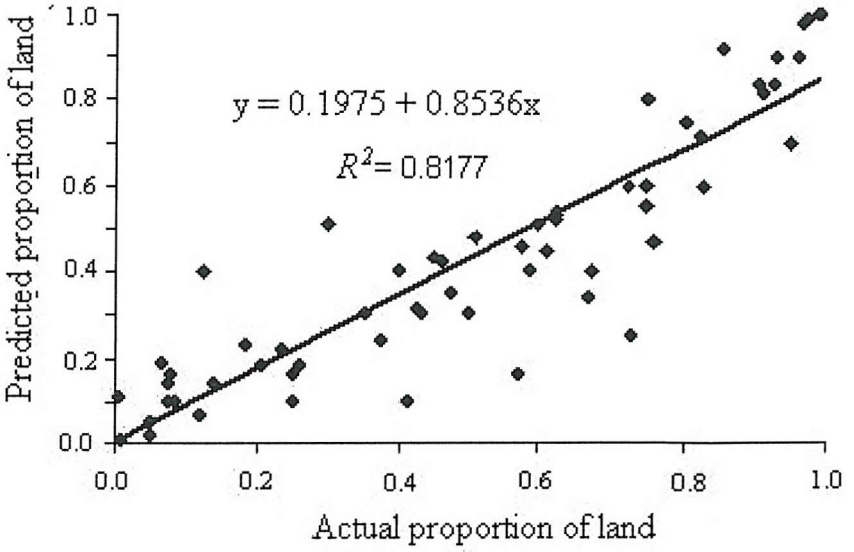

Figure 4.8: The relationship between the predicted proportion of land and actual proportion of land.

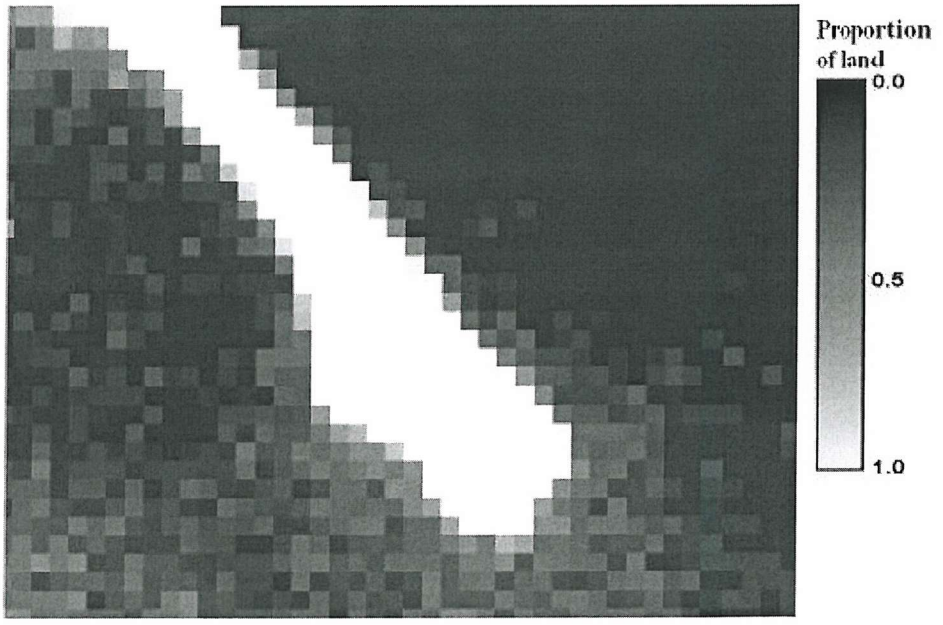

Figure 4.9: Output of the soft classification. The grey level represents the proportion of land class in each pixel.

With a r value of 0.904 ($P < 0.05$) it was determined that the output of the soft classification accurately represented the actual proportion of classes within each pixel. This was important as further analysis in increasing spatial accuracy depends on the accuracy of the soft classification. Though the soft classifier accurately predicted the class proportion of each pixel it did not indicate where these proportions were located geographically within a pixel. This issue was undertaken in the next section.

4.2.5 Methods of Increasing Positional Accuracy.

Output from a soft classification produces images with pixels values representing the proportion of a certain class within pixels. But it does not indicate where within a pixel these classes are located. To address this problem, methods of distributing the proportion within each pixel to different classes were explored. This section explains the methods undertaken which were wavelet interpolation, contouring and two-point histogram.

4.2.5.1 Wavelet interpolation

Shoreline position maps would be more accurate with fine spatial resolution data. Wavelets are a relatively new tool for generating hierarchical or multi-scale representations of images and could be used to increase the spatial resolution of the 20 m spatial resolution simulated imagery. This technique has been used for remote sensing applications such as digital change analysis (Carvalho *et al.,* 2001), spectral fusion (Horgan, 1998), feature extraction (Simhadri *et al.,* 1998). By increasing the spatial resolution of the simulated imagery and applying a hard classification the shoreline could be positioned within the pixel boundary thus increasing the positional accuracy of the shoreline prediction.

Wavelets are mathematical functions that cut up data into different frequency components and then study each component with a resolution matched to its scale (Donoho, 1992). This pilot study implements the 2-D wavelet refinement method based on average–interpolation method to increase the spatial resolution of the soft classified imagery (Donoho, 1993). The basic idea is to use data at coarser scales to predict data at finer scales, and to record the prediction errors as coefficients associated with the finer scales. Average interpolation can be described as the following. "Given a function f on an interval J defined by, $ave(f|I) = |I|^{-1} \int_I f(t)dt$ for an average value of f over the interval I. With a given triadic interval of $\{a_{j,k}\}_{k=0}^{3^j-1}$ of numbers representing the average of f on the triadic intervals $I_{j,k}$. Average-interpolation refinement uses the data at scale j to impute behaviour at the finer scale $j+1$, obtaining the (pseudo-) averages of f on intervals $I_{j+1,k.}$ " (Donoho, 1993). When a even interger D is defined, it runs as follow ;

(Interpolation) for each interval $I_{j,k}$, find a polynomial $\pi_{j,k}$ of degree $D = 2A$ satisfying the average –interpolation condition :

$$ave\left(\pi_{j,k} \middle| I_{j,k+1}\right) = a_{j,k+1} \quad for \quad -A < I < A \tag{4.4}$$

(Imputation) Obtain (pseudo-) cell averages at the finer scale by setting

$$\bar{a}_{j+1,3k-1} = ave\left(\pi_j, k \middle| I_{j,3k-1}\right) \quad \text{for I =0, 1, 2} \tag{4.5}$$

for any degree D one can find coefficient $C_{h,l}^{(D)}$ for which

$$\bar{a}_{j+1,3k+l} = \sum_{h=-A}^{A} c_{h,l}^{(D)} a_{j,k+h}, \; l = 0, 1, 2, \tag{4.6}$$

Exhibiting the fine-scale imputed average $\bar{a}_{j+1,k}$'s as linear functionals of the coarse-scale average $a_{j,k}$.

The soft classified imagery was interpolated from 20 m to 2.5 m based on the average-interpolation using a Haar wavelet function (Donoho, 1992). This resolution was chosen as at this resolution it provides a balance between computing time of the process and shoreline detection capability. The average-interpolating scheme was used to refine boxcar averages on a grid of n x n points, imputing averages on a finer grid of $2^L n$ x $2^L n$ points. To obtain a finer resolution of 2.5 m from 20 m requires that a L value of 3 and D value of 2 were given. Further detail to the algorithm used can be referred to Donoho (1993).

To determine the land/water boundary a supervised maximum likelihood hard classification was applied to the wavelet interpolated imagery. The method applied was similar to the one used in classifying the 1 m classified imagery (4.2.2) using the same training sites (Figure 4.5). The resulting wavelet interpolated imagery and its classified imagery is shown in Figure 4.10.

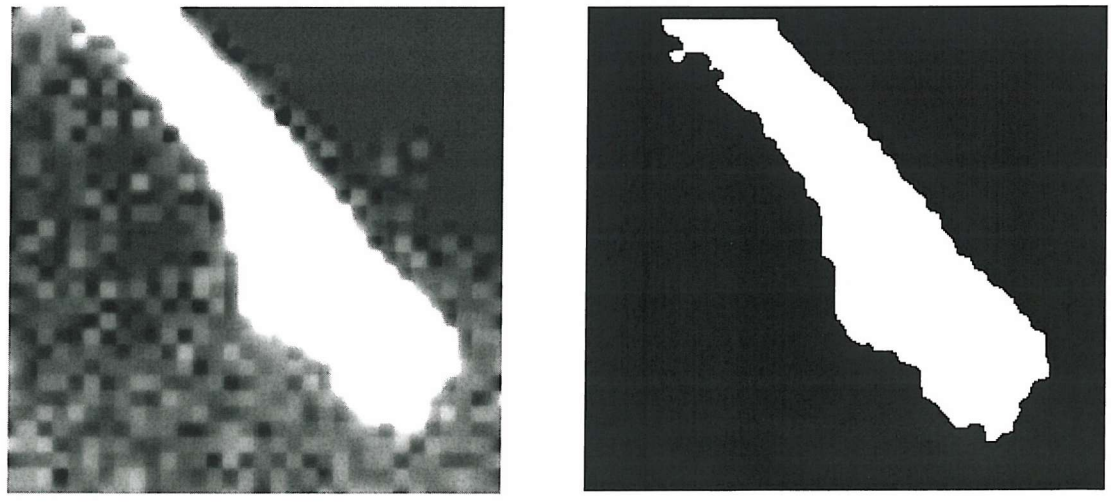

(a) (b)

Figure 4.10: (a) Wavelet interpolated imagery and (b) its classified imagery

4.2.5.2 Contouring soft classified imagery

Contouring could be used to increase the shoreline positional accuracy prediction from the 20 m spatial resolution simulated imagery. The soft classified image was contoured at 0.5 interval to produce a shoreline. This value was chosen as it could be assumed that at this point a pixel contains 50 % water and 50% land, therefore, the position of the shoreline. This represents a first step in increasing the positional accuracy as the generated shoreline crosses within a pixel thus increasing its accuracy in comparison to hard classifiers that produces shoreline that follows the edges of pixels (Foody *et al.*, 2003). The shoreline generated from contouring the soft classification output is shown in Figure 4.11.

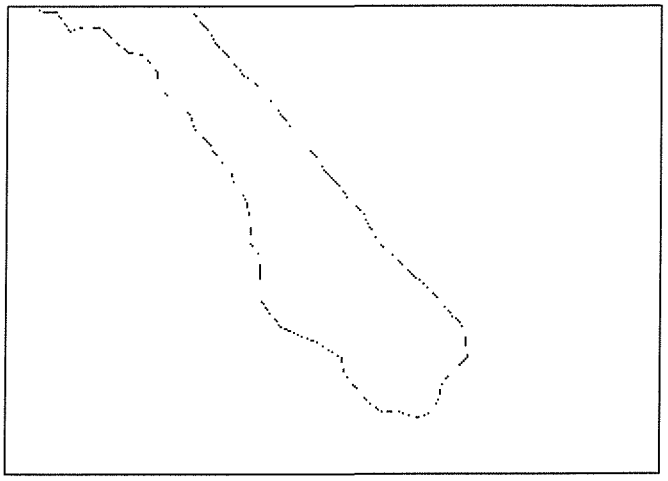

Figure 4.11: Shoreline generated from contouring output of the soft classification.

4.2.5.3 Two-point histogram

Interpolation provides a method to infer the distribution of classes at a sub-pixel level but this is often too simplistic (Atkinson, 1997). Another method used to predict class boundary within each pixel is by using geostatistical methods such as simulated annealing (Kirkpatrick *et al.*, 1983; Jeroen and Gerard, 2002). The concept of

annealing in combinatorial optimization was introduced by Kirkpatrick *et al.,* (1983). The concept is based on the analogy between combinatorial optimization and the physical process of crystallization. Inspired by this the Metropolis algorithm proposes a numerical optimization procedure which works as follows (Metropolis *et al.,* 1953). "Starting from an initial situation with energy level *f(0)*, a small perturbation in the state of the system is brought about. This brings the system in to a new state with energy level *f(1)*. If *f(1)* is smaller than *f(0)*, then the state change is accepted. If *f(1)* is greater than *f(0),* then the change is accepted with a certain probability" (Metropolis *et al.,* 1953). A movement to a state with a higher energy level is sometimes allowed to be able to escape from local minima (Jeroen and Gerard, 2002). The probability of acceptance is given by the metropolis criterion:

$$p \text{ (accept changes)} = \exp\left(\frac{f(0) - F(1)}{S_0}\right) \qquad 4.7$$

Where S_o is a control or freezing parameter. Next, the freezing parameter is decreased and a new perturbation is made. The energy levels are again compared and it is decided whether the state change is accepted. This iterative procedure is repeated until a maximum number of iteration is reached of until change occurrence have become very rare (Geman and Geman, 1984). Two important perturbation methods normally used are swapping two randomly selected pixels in the grid (Deutsch *et al.,* 1998) and generating a new pixel value from a local conditional distribution (Deutsch and Wen, 1998). Examples of studies that use simulated annealing for spatial optimization can be found in areas ecological research (Church *et al.,* 1996), of spatial resource allocation (Jeroen and Gerard, 2002) and forestry research (Lockwood and Moore, 1993).

The spatial optimization used in this pilot study is based on a geostatistical method inspired by simulated annealing as defined and used in the program Anneal.f, apart of the GSLIB library (Deutsch *et al.*, 1998). The method calculates a two-point histogram or grey level co-occurrence matrix (GLCM) statistics to analyse similarity between two images. A two-point histogram is a two-dimensional histogram of grey levels for a pair of pixels which are separated by a fixed spatial relationship (lag) (Haralick *et al.*, 1973). The two-point histogram approximates the joint probability distribution of a pair of pixels within an imagery. A sample two-point histogram calculation is shown in Figure 4.12 . The calculation is based on a horizontal direction with a lag of 2. For example to calculate the two point histogram value for the relationship between grey level value 2 and 3 at a distance of 2 pixels, the total amount of relationship is added up and inserted into the table (calculated as 4).

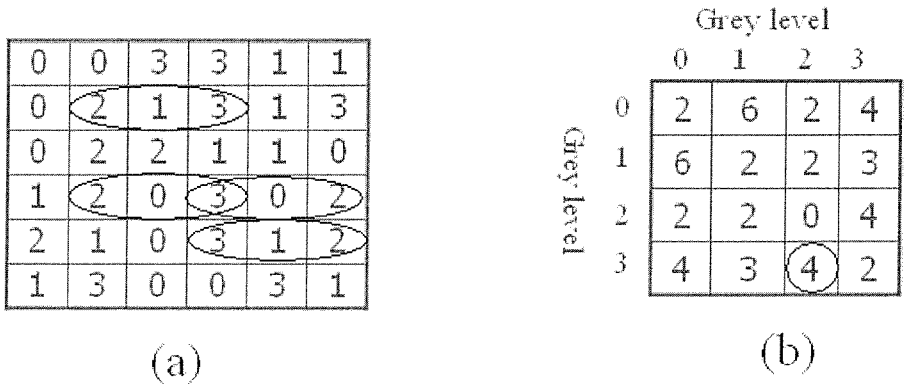

Figure 4.12: Sample calculation of the two-point histogram for a horizontal direction with a lag of 2. (a) The relationships between grey level 2 and 3 at lag 2 and (b) the corresponding two-point histogram are shown.

Details of the optimization method used are describes as follows. Given a random variable Z that can take one of $k = 1,.....,K$ outcomes (i.e., categorical variable)

the two-point histogram for a particular lag (distance and direction of separation) h is the set of all bivariate transition probabilities:

$$p_{k,k'(h)} = Pr\begin{Bmatrix} z(u) \in \text{ category } k, \\ z(u+h) \in \text{ category } k' \end{Bmatrix} \quad 4.8$$

Independent of u, for all k, $k' = 1,....,K$. The objective function corresponding to the two-point histogram control statistic is as follow:

$$O = \sum_{h}\left(\sum_{k=1}^{K}\sum_{k=1}^{K}\left[p_{k,k'}^{training}(h) - p_{k,k'}^{realization}(h)\right]^2\right) \quad 4.9$$

Where $p_{k,k'}^{training}(h)$ are the target transition probabilities calculated from a training image and realization $p_{k,k'}^{realization}(h)$ are the corresponding transition probabilities of the realization image.

To increase spatial resolution the two point histogram alone was insufficient. A scheme must be devised to alter the sub-pixel values. This could be done by a change in attribute (as in Anneal.f) or via a swap in sub-pixel location. Here a swap in sub-pixel location was used. This was chosen as in classifying land and water boundary (shoreline), the proportion of land and water within a pixel has to be maintained to correctly identify the division within it. The optimization goal also needs to be constrained so that the sub-pixels are swapped within pixels (Atkinson, 2003).

The algorithm used in this study was developed for super resolution land cover classification (Atkinson, 2003). Two point histograms of the training and satellite sensor imagery were calculated and evaluated toward an objective function. If a pixel swap results in a smaller objective function, the swap is retained and updated on the other hand if it results in a larger objective function the swap is discarded.

To increase efficiency two checks were added to the algorithm (Atkinson, 2003). First when pixels are found to contain only one cover class they are ignored. However, sub-pixels within these pixels may still be used in comparison between sub-pixels within adjacent pixel because the two-point histograms are calculated for eight directions and at different lags. Second, sub-pixels were compared only if their classes were different. Initially the 20 m soft classified imagery was resampled to a sub-pixel spatial resolution of 2.5 m and the class proportion was redistributed randomly within the pixel. Two proportion images were created, one for land and one for water. Basically they are the inverse of each other (Figure 4.13). A training image of the training site was prepared using the 1 m hard classified satellite sensor imagery. The imagery was resampled down to a spatial resolution of 2.5 m to match the algorithm target spatial resolution (Figure 4.14). The soft classified imagery was processed with a lag of 5 m until 50 iteration. It was discovered that on this particular imagery no increase in positional accuracy was obtained if the algorithm was run for 50 iteration. The imagery before and after the 50 iteration are shown in Figure 4.15 and Figure 4.16, respectively.

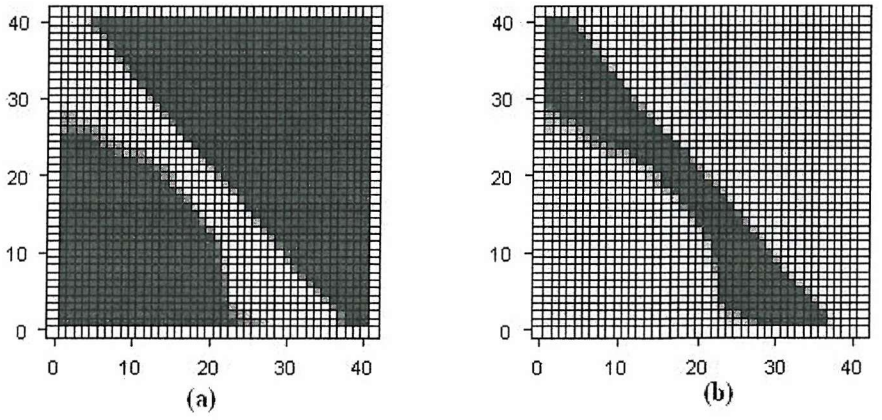

Figure 4.13: (a) Water and (b) land proportional images. The X and Y axis represent the location in pixels while the grid represents the pixel size of 20 m. The grey scale (from white to black) indicates the class proportion within the pixels.

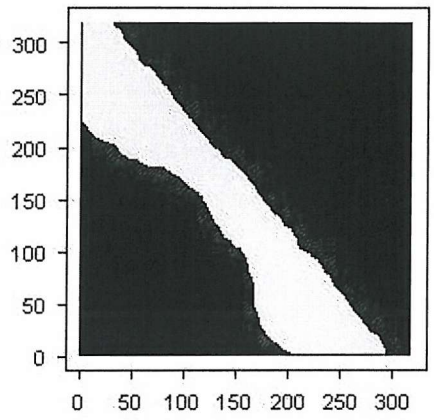

Figure 4.14: Training imagery used in the two-point histogram process. The X and Y axis represent the location in pixels (2.5 m)

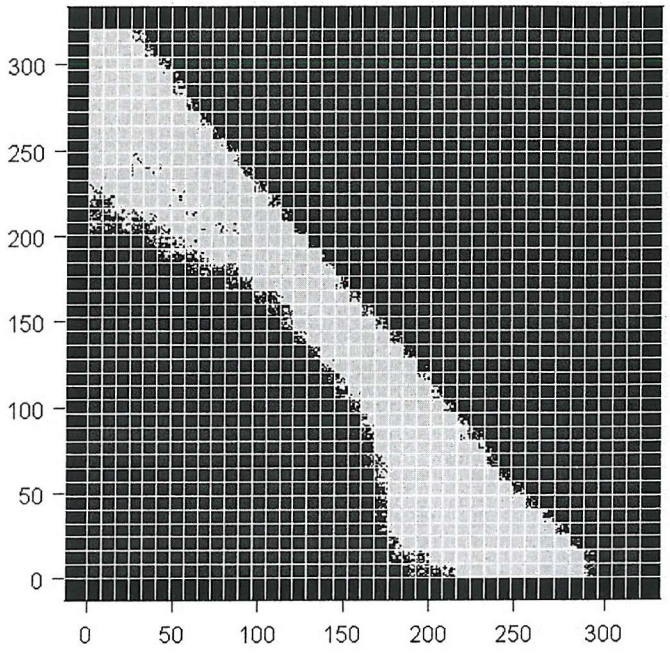

Figure 4.15: Initial Two-point histogram imagery with randomly distributed sub-pixels (2.5 m spatial resolution). The grid represents the original pixel size (20 m)

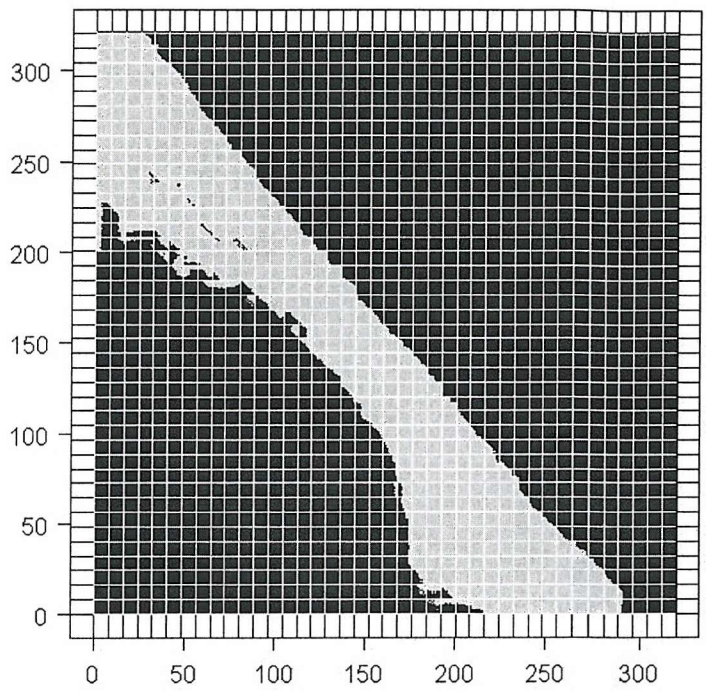

Figure 4.16: Two-point histogram imagery after 50 iterations. The grid represents the original pixel size (20 m).

4.2.6 Positional Error Analysis

To compare the various methods used in obtaining shoreline position a positional error analysis was conducted. A standardized method was chosen to extract the shoreline position from the output of each method used. With the exception of output from contouring, which produces a vector representing the land water boundary, output from the other methods are classified imagery with water and land classes. Therefore, to generate a shoreline position from these images (output from wavelet interpolation and two-point histogram), the images were vectorised along the boundary between the land and water classes. The basic operation is to generate lines which outline the boundaries of these areas.

By comparing these shoreline positions to the actual/ground data (from 1 m imagery) the positional accuracy could be evaluated. Shoreline maps generated from these images are shown in Figure 4.17 to Figure 4.20

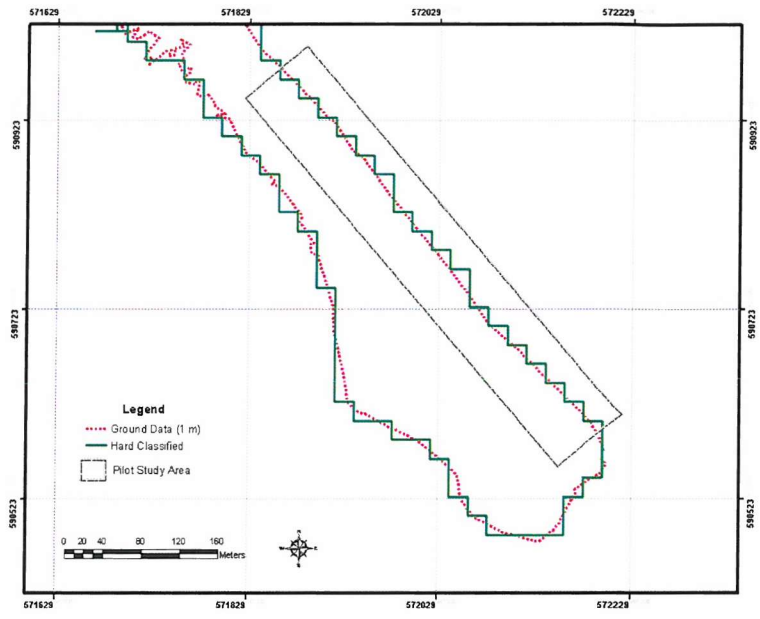

Figure 4.17: Shoreline map generated from output of a hard classification.

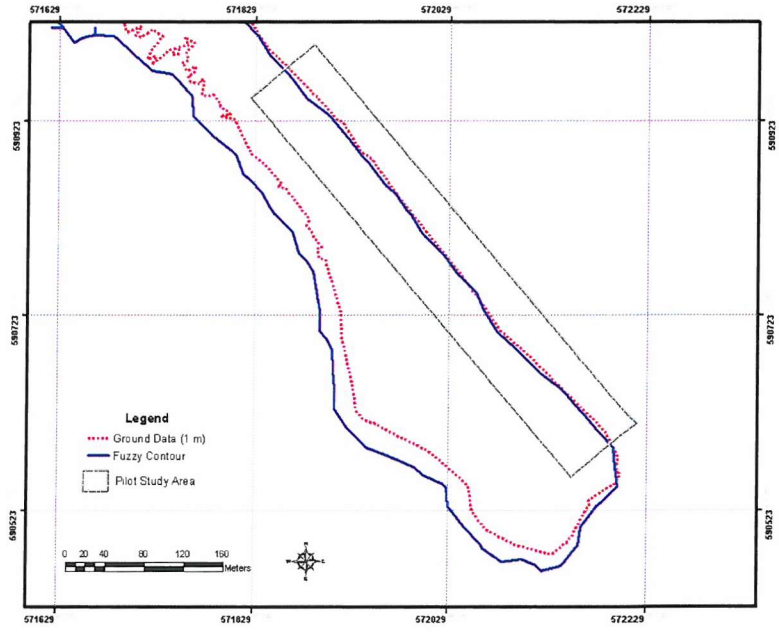

Figure 4.18: Shoreline map generated from contouring of the soft classification output.

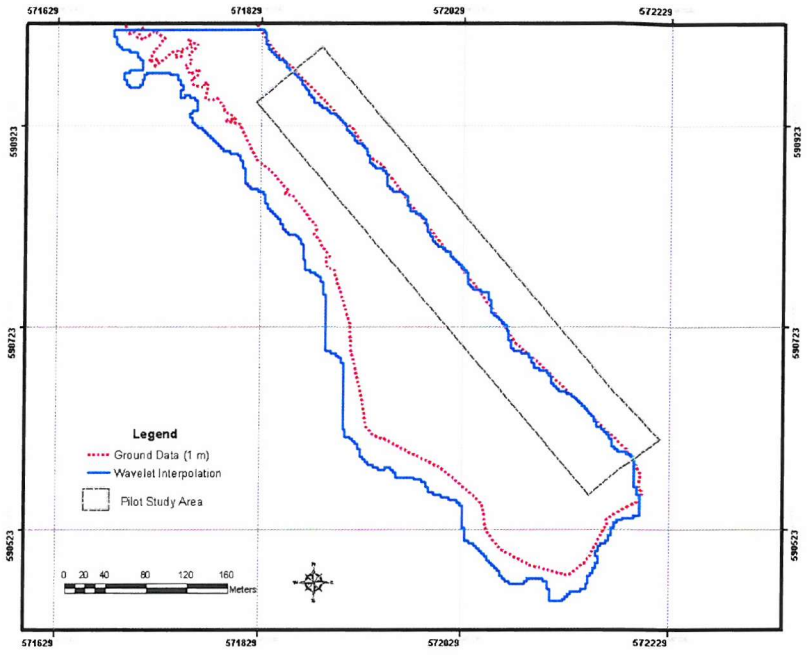

Figure 4.19: Shoreline map generated from wavelet interpolation.

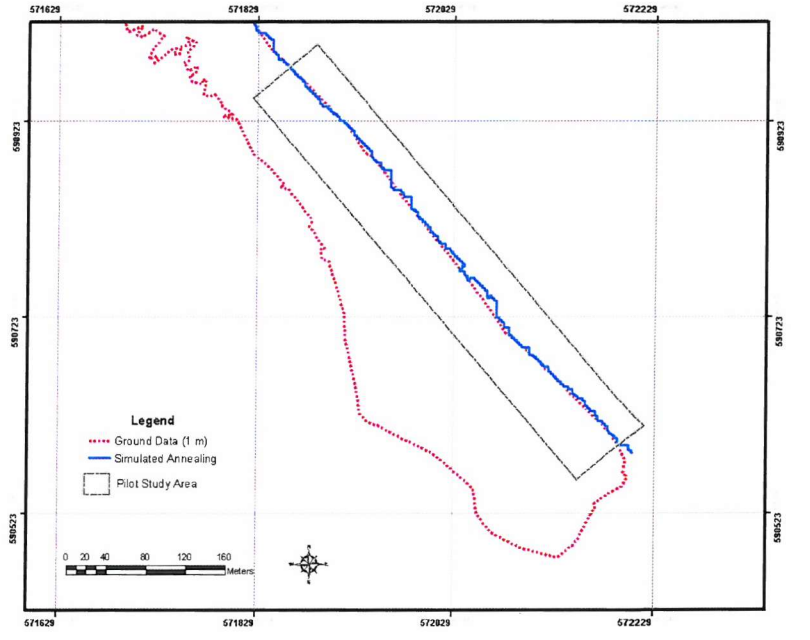

Figure 4.20: Shoreline map generated from the Two-point histogram output imagery

(Only areas where comparison is conducted)

The shoreline maps contain detailed positional information, but when looking at the maps produced, this information was not clearly obvious. Even though the shoreline maps were created at a scale of 1: 3,000 this information seems lost and all the shorelines look similar with the exception of the shoreline generated from hard classification. Output from the hard classification method was the worst with the shoreline having jagged edges. To make the differences obvious the map of the shoreline needed to be at a finer scale but doing so limits the portion of shoreline that would be displayed. To address this issue a graphing method was used to display the shoreline positional information. Therefore, graphs were produces with the shoreline position on the X axis and the shoreline changes on the Y axis (Duffy and Dickson, 1998). By adapting this methodology subtle changes in shoreline can be displayed by stretching the X axis. Shoreline errors between each classification method and ground data along each metre of the shoreline are graphed. Having these values quantitative analysis could be done. These values were graphed to analyse positional accuracy between the different classification methods. Due to the length, the shoreline was divided into two shoreline graphs based on 250 m of the shoreline. Areas for each graph are shown in Figure 4.21 and the two graph depicting the errors along the shoreline are shown in Figure 4.22 and Figure 4.23.

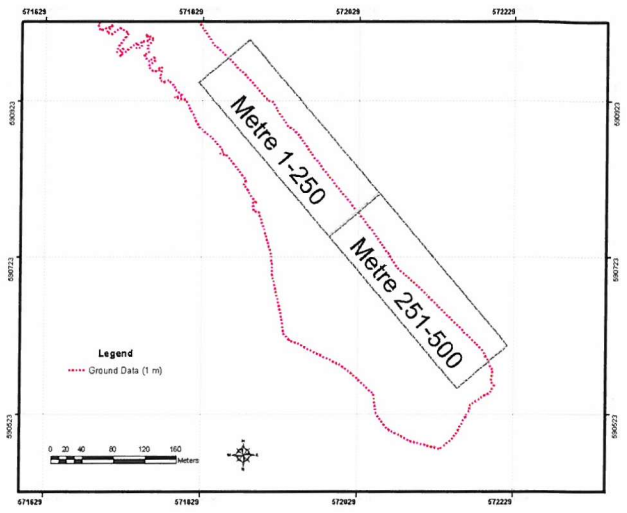

Figure 4.21: Shoreline position of the generated positional error graphs

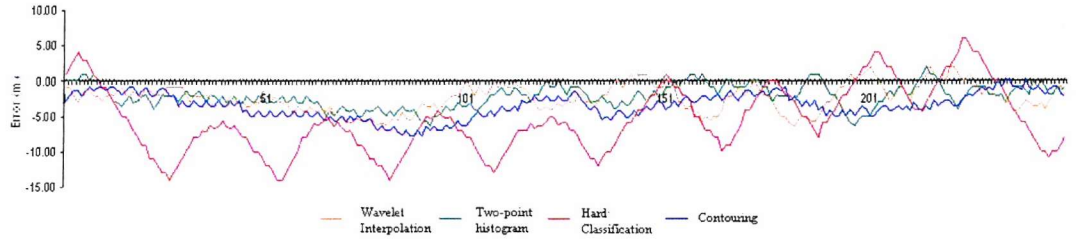

Figure 4.22: The positional errors along the shoreline (Metre 1-250)

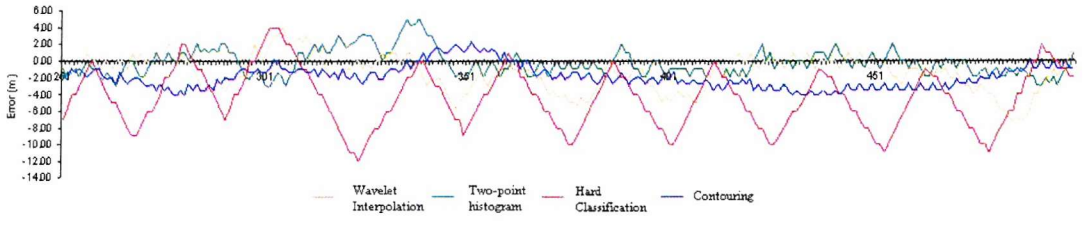

Figure 4.23: The positional errors along the shoreline (Metre 251-500)

4.3 Results and analysis.

4.3.1 Results

Using this graphing method the positional error along the shoreline of each method could be seen more clearly in comparison to displaying conventional shoreline maps (*i.e* Figure 4.18). Using this method quantitative analysis was done as errors at each metre of the shoreline are displayed. From analysis the root mean square error (RMSE) of each classification method were calculated. The results are shown in Table 4.1.

Another test to verify the result was to rank each method based on the lowest error at each metre of the shoreline. The sums of the ranks reaffirm the results obtained from RMSE (Table 4.1). The result shows that the two-point histogram method is again the most accurate with a sum of ranks value of 921.5, followed by wavelet interpolation, contouring and hard classification.

Table 4.1: RMSE of the 4 classification methods used.

Classification method	RMSE
Hard Classification	6.48 m
Contouring Soft classification	3.20 m
Wavelet interpolation	2.82 m
Two-point histogram	2.25 m

Table 4.2: Sum of Ranks of the 4 different methods

Classification method	Sum of ranks
Hard Classification	1708.5
Contouring Soft Classification	1298.5
Wavelet Interpolation	1071.5
Two-point histogram	921.5

Another statistical test applied to the data was the Friedman test. The Friedman test is a non-parametric test that compares three or more paired groups (Siegel and Castellan, 1988). The Friedman test first ranks the values in each matched set (each row) from low to high. Each row is ranked separately. It then sums the ranks in each group (column). If the sums are very different, the *P* value will be small. Results from the Friedman test the *P* value was determined to be 0 thus it could be assume that the output from the 4 methods used in this pilot study are not equal to each other.

The statistical test shows that the two-point histogram method provided the most accurate representation of the shoreline followed by wavelet interpolating, contouring soft classification and lastly hard classifier.

4.3.2 Analysis

Analysis was done to evaluate the four methods used. The analyses were limited to shoreline position within the 500 m stretch as defined in Figure 4.2.

4.3.2.1 Hard classifier

The hard classifier was found to produce the least accurate representation of the shoreline with an RMSE of 6.48 m and sum of rank of 1708.5. Only 26 % of the shoreline was within 2 m of the actual shoreline and 42 % within 4 m. This poor representation of the shoreline was expected as the hard classification method was reliant on the pixel size as the shoreline was generated according to the edges of pixels and not through the pixels such as in the other methods. The hard classifier assigns pixels to only one class, based on the class of which it has the most similarity. Therefore, pixels with 49% land would still normally be classified as water. This

introduces errors to the shoreline position. Due to these restraints and the orientation of the shoreline, the shoreline produced was jagged and errors up to 15 m distance were observed in several areas (Figure 4.22 and Figure 4.23). Errors also tend to be in the negative direction (landwards), this was again due to the nature of the shoreline direction.

4.3.2.2 Wavelet interpolation

To increase the positional accuracy of the shoreline the soft classification output was interpolated using an average interpolator. This produces a shoreline with an RMSE of 2.82 m. Although the shoreline was more accurate it was still affected by the orientation of the shoreline. The wavelet interpolator tries to smooth the peaks that were so evident in the hard classification output. The shoreline was still jagged at similar areas as the shoreline generated from the hard classification although the peaks were smoother. Although this method produces a jagged shoreline 35 % of the shoreline was within 2 m from the actual shoreline and 84 % within 4 m, producing less error than the smoother soft classified imagery. About 40 % of the shoreline was also within 1 m from the actual shoreline. Similarly to contouring, a drawback of this method was that it modified the pixel proportion of each pixel. As the wavelet interpolator did not maintain the proportion of each pixel it produced fewer errors at positions where the soft classification was not accurate. An example could be seen from metres 310 – 350 of the shoreline (Figure 4.23). Again as in the result from the hard classification the shoreline tend to be in the negative direction or landwards.

4.3.2.3 Contouring soft classification output.

Outputs from a soft classification are class proportion values representing the proportion of a class within a pixel. Using these proportion values a shoreline position

could be generated at the position where the proportion values are 0.5 thus, providing a method of positioning the shoreline location within a pixel. This increased the shoreline mapping accuracy and produces a shoreline with an RMSE of 3.2 m. Only 35 % of the shoreline was within 2 m from the actual shoreline and 42.8 % within 4 m. The shoreline generated from this method was visually the smoothest among the 4 methods used. The positional error from this method was within 2 to 5 m, 62.8 % of the time and very seldom (16 %) within 1 m to the actual shoreline position. This method does not suffer from the orientation of the shoreline as it does not reveal any jagged areas. A drawback of this method was that it modified the proportion values when fitting the contour. Again the results show that errors tend to be in the negative direction or landwards, this was again due to the nature of the shoreline direction.

4.3.2.4 Two-point histogram

Among the 4 methods used, the two-point histogram approach produced the most accurate result with an RMSE of 2.25 m with 57 % of the shoreline within 2 m from the actual shoreline and 84 % within 4 m. The output from this method was also more accurate than the output from the wavelet interpolation method with 46.6 % of the shoreline within 1 m of the actual shoreline. The two-point histogram approach was very dependant to the initial soft classification output as the proportion of each pixel was maintained. This explains why in certain portion of the shoreline sharps peaks are visible. These peaks can be seen at metre 335 and 380 of the shoreline (Figure 4.23). Although the shoreline was not as smooth as the contouring method it was consistently close to the actual shoreline despite the peaks.

4.4 Conclusion

This chapter examined the effects of spatial resolution on generating shoreline position maps and methods of accurately predicting the shoreline accurately. For this purpose a 20 m satellite sensor imagery was simulated from a 1 m satellite sensor imagery. Using a hard classifier the 20 m imagery was classified to produce 2 classes, land and water. The shoreline generated by the hard classifier had large positional errors as the shoreline was generated along pixel boundaries and not through the pixels. To increase accuracy of the shoreline prediction the 20 m imagery was soft classified and several methods were applied to position the shoreline within the pixels. These methods were contouring, wavelet interpolation and two-point histogram.

Using a graphing method the accuracy of shoreline generated by these methods were compared. From the result it was determined that two-point histogram method produced the most accurate representation of a shoreline followed by wavelet interpolation and contouring. As these results were obtained from a linear shoreline, the results are only valid for linear shoreline characterized by a simple linear pattern. For shorelines that are more complicated with different orientations, it could be assume that the results will be different.

This chapter provides a starting point on sub-pixel methods of generating accurate shoreline maps from coarse spatial resolution satellite sensor imagery. For linear shoreline it has been shown that two-point histogram and wavelet interpolation were able to produce shoreline maps with an RMSE of fewer than 3 m. This should satisfy the requirements for a 1 : 10,000 scaled map (U.S.Geological Survey, 1999). But shorelines are generally more complicatedly shaped and further research needs to be done to develop methodologies to map these shorelines. Chapter 6 will address these

issues and look into methods of producing accurate shoreline maps from shoreline with different orientations.

This chapter has revealed the potential of using coarse spatial resolution satellite sensor imagery to map the shoreline, even so, fine spatial resolution imagery are still useful to produce local shoreline maps. The following chapter examines the application of using fine spatial resolution satellite sensor imagery to accurately position the shoreline.

5 Shoreline Mapping From Fine Spatial Resolution Satellite Sensor Imagery.

5.1 Introduction

The shoreline is defined as the intersection of land and water surfaces. Due to the dynamic nature of the water body, the shoreline is constantly changing in location (Davis *et al.*, 2000; Fletcher *et al.*, 2003). When a shoreline position is captured by satellite sensors the resulting shoreline position is categorised as an instantaneous shoreline. This instantaneous shoreline could not directly be used for mapping purposes, nor be employed for quantifying shoreline changes as it is not based on a reference datum (Li *et al.*, 2002). For these purposes a reference shoreline is required. A reference shoreline is defined based on a stable vertical datum or is the linear intersection between water and land at a desired water level. These shorelines are also known as tide-coordinated shoreline such as, the shoreline normally shown on a topographic map of Malaysia.

Conventionally shoreline maps are derived from aerial photography by acquiring the images during a selected tide elevation level (Camfield and Morang, 1996; Gorman *et al.*, 1998). This requires coordination between a tide gauge reading (to determine tide level) and aerial photography (to acquire images at a particular time) to ensure that the shoreline acquired was based on a selected tide level (Li *et al.*, 2002; Parker, 2003). This type of tide coordinated shoreline is called a physical tide coordinated shoreline.

The spatial resolution of satellite sensors has increased so that the spatial resolutions are comparable to that of aerial photography. These sensors also have stereo mapping capabilities. However, to acquire a tide coordinated shoreline based on a satellite sensor image is unrealistic as the acquisition times of satellite sensor are not flexible and are based on the orbit of a particular satellites (Jensen, 2000). Therefore to establish a tide coordinated shoreline from satellite sensor imagery, a relationship needs to be established between the instantaneous shoreline and the tide coordinated shoreline. Knowing this relationship the requirement for field coordination between gauge reading and aerial photography/satellite sensor imagery would no longer be necessary. This provides a new method of digitally establishing a tide coordinated shoreline.

The idea of digitally establishing a tide coordinated shoreline comes from the definition of a shoreline as the contact or intersection line between water and the land surfaces. This is intuitive to people's perception of a shoreline. A shoreline profile or side view explaining this concept is shown in Figure 5.1. To generate a digital tide–coordinated shoreline the intersection between land and water surface needs to be established, by combining topographic and bathymetric information. The water surface could later be repositioned based on a selected tide elevation as a boundary condition. Therefore the shoreline position at a selected water level could be derived.

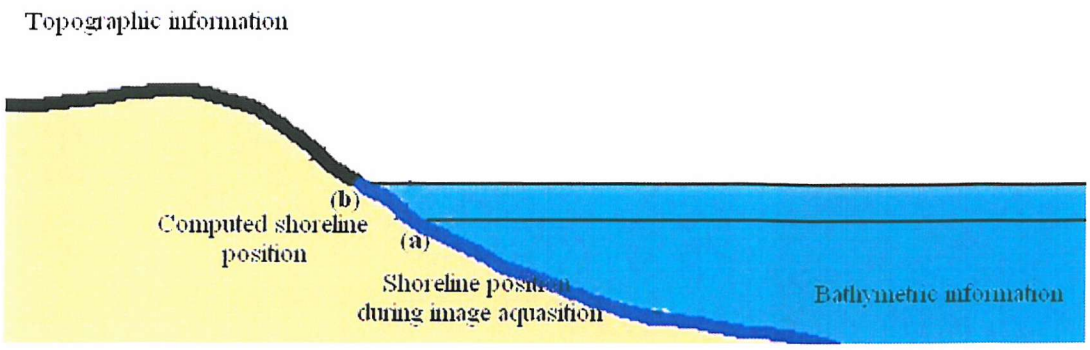

Figure 5.1: Profile showing the combination of topographic and bathymetric information. The figure gives an example of the shoreline position (a) during satellite sensor image acquisition and (b) a computed shoreline position based on a selected tide elevation

Li *et al.*,(2002) digitally established a tide coordinated shoreline for a portion of Lake Eire, USA. A terrain model was used to define the elevation for areas above the water and bathymetric information to define the elevation below the water level. By combining these two data sets a 3-D model of the shoreline was established. The terrain model was derived from aerial photographs and integrated with bathymetric data acquired by the Ohio Department of Natural Resources to form a 3-D terrain model of the coastal area. By modelling the water surface to a selected tide elevation, a tide coordinated shoreline was generated with an overall accuracy ranging from 2.1 m to 13.4 m. Li *et al.*,(2002) concluded that the major error source came from the 3-D terrain model and increased accuracy was achievable with accurate terrain information of the study area.

In Malaysia, shoreline maps are generally derived from the intersection between land and water body at the Mean High Water Springs (MHWS) tide. MHWS is defined as the 19 year average height of high water mark occurring on spring tides. Spring tides are defines as the average tide during new and full moon days and the 2

days following each (John, 1983). As the MHWS information at the Kuala Terengganu tide station was not available to the author, the shoreline was mapped based on Mean Sea level (MSL). MSL is defines as the average height of the sea surface, based upon hourly observation of the tide height on the open coast or in adjacent waters that have free access to the sea (Clark, 1983). Even though MSL was used, the method employed in this research would work with any reference level. To digitally establish a tide coordinated shoreline based on the MSL a 3-D representation of the study area was required. By doing so the shoreline could be repositioned from its instantaneous location (satellite sensor imagery) to its reference position (MSL). Figure 5.2 shows the relationship between shoreline positions at different tide levels.

This thesis proposes the use of IKONOS imagery to produce a 3-D elevation model of the area. The process was two fold involving the generation of elevation information for land and depth information for water areas. For land the elevation information was derived by utilizing stereo IKONOS sensor imagery, on the other hand, depth for water areas are derived from multi-spectral IKONOS sensor imagery based on spectral reflectance values. These two processes are explained in detail in the following sections.

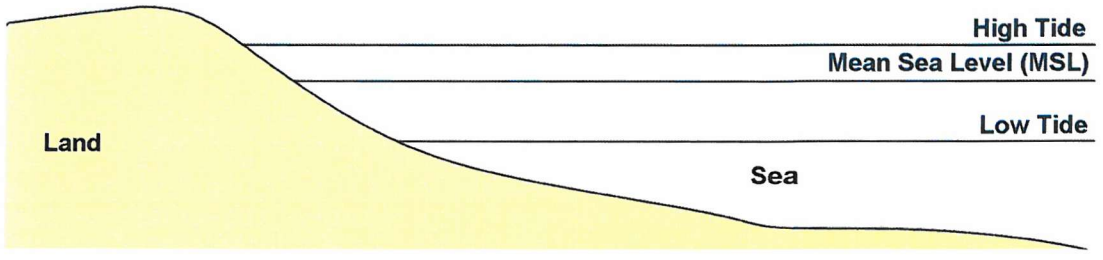

Figure 5.2: Shoreline positions at different tide levels

Li *et al.,* (2002) establish a methodology for deriving a digital tide coordinated shoreline utilising a terrain model of an area by correcting the tide level to a selected datum to determine the shoreline position. Li *et al.,* (2002) work utilizes aerial photographs and available bathymetry data to establish a terrain model of an area. But to map shorelines in Malaysia, similar data sets would not be suitable as the coastal area is dynamic and would change from year to year (Ministry of Agriculture, 1997). This research aimed to develop a method of producing shoreline maps quickly by utilizing mainly satellite sensor imagery to derive both topographic and bathymetric information. This not only provided a faster but also a cheaper alternative to mapping the shoreline (Rao *et al.,* 1985). These two factors are very important to a country like Malaysia which has limited resources and requires the monitoring of long shorelines. A 3-D terrain model of the shoreline would also be useful in other coastal research studies such ecosystem management, coastal engineering, sediment movement and erosion studies (Clark, 1983; Balopoulos *et al.,* 1986; Cromwell *et al.,* 1991; Bhat and Subrahmanya, 1993; Cendrero and Fischer, 1997; Chauvaud *et al.,* 1998; Lane *et al.,* 2000; Davis *et al.,* 2000; Honeycutt *et al.,* 2001; Adams and Minor, 2002; Friedman *et al.,* 2002; Byrnes *et al.,* 2003; Leatherman, 2003; Fletcher *et al.,* 2003; Honeycutt and Krantz, 2003; Dewidar and Frihy, 2003).

5.2 Coordinate system

Before producing the DEM and bathymetry maps it was important to first select an established coordinate system (Kenward *et al.,* 2000; Ruggiero *et al.,* 2003). The use of a common coordinate system on a defined horizontal and vertical datum allowed data to be combined easily without the need for coordinate transformation. For this thesis, the horizontal and vertical datum used was based on the RSO projection. The

RSO projection is the mapping standard used in Malaysia. Details of the RSO projection could be found in section 2.2.

5.3 Deriving bathymetry and DEM information utilizing IKONOS sensor data.

Research in deriving DEM using satellite sensor imagery has grown enormously since the launch of stereo capable satellites such as SPOT HRV but its capability was limited due to its coarse spatial resolution (Giles and Franklin, 1996; Al-Rousan *et al.,* 1997). Newly developed sensors such as IKONOS and Earlybird with a fine spatial resolution (under 1 m) have spawned new research in their capability to produce accurate and detailed elevation information (Zhou and Li, 2000; Ganas *et al.,* 2002). Research conducted in topographic mapping and feature extractions has shown promise producing accuracy similar to aerial photography (Grodecki and Dial, 2001; McCarthy *et al.,* 2001; Ganas *et al.,* 2002; Fraser *et al.,* 2002a; Malthus and Karpouzli, 2003).

Satellite sensor imagery has been used to derive bathymetry information since the launch of Landsat MSS in the 1980s (Benny and Dawson, 1983; Lyzenga, 1985; Philpot, 1989; Ibrahim and Cracknell, 1990; Bierwirth *et al.,* 1993; Roberts and Anderson, 1999). Even so, satellite sensor imagery has not been widely used as the spatial resolutions of these satellites were too coarse for practical marine surveying such as mapping bathymetry. IKONOS with a fine spatial resolution of 4 m (Multi-spectral) provides a new avenue to utilize satellite sensors imagery to produce accurate bathymetric data. IKONOS sensor also has a larger radiometric resolution of 11-bit (2048 grey levels) in comparison to previous sensor such as SPOT HRV and Landsat TM which have a radiometric resolution of 8-bit (256 grey levels).

5.3.1 Bathymetry mapping

Hydrographic surveying by conventional ship borne sounding techniques is slow, hazardous and expensive (Cracknell, 1999; Brock *et al.,* 2002). As a result, interest has been generated in the application of remote sensing techniques for bathymetry mapping. Satellite sensor imagery provides an alternative to conventional hydrographical surveys for measuring water depth. The application of passive satellite sensor imagery to derive bathymetry maps have concentrated on the blue region of the electromagnetic spectrum (0.45-0.52 μm) due to its penetration of water (Bukata *et al.,* 1995; Jensen, 2000). Landsat TM has been used extensively for this purpose and several researchers have extensively developed models to extract bathymetry information (Lyzenga, 1985; Philpot, 1989). The IKONOS multi-spectral bands are spectrally similar to bands 1-4 of the Landsat TM, but provide data with a spatial resolution of 4 m (Multi-spectral) and radiometric resolution of 11 bit in comparison to Landsat TM 30 m spatial resolution and 8-bit radiometric resolution. The radiometric resolution of IKONOS of 11- bit with 2048 grey levels provides the ability to provide increased tonal and intensity variation in comparison to the Landsat TM (8-bit; 256 grey levels). With these capabilities IKONOS is capable of producing accurate bathymetric predictions in comparison to Landsat TM.

5.3.1.1 Techniques for bathymetry extraction from remote sensing imagery

This section reviews several techniques developed for the estimation of bathymetry from satellite sensor imagery.

5.3.1.1.1 Single band method

This is the simplest method of bathymetry extraction in which the water depth extraction techniques were developed on the basis of a simple water reflectance model which accounts for a major part of the signal received by a multi-spectral scanner but neglects the effects due to scattering in the water and internal reflection at the water surface. According to the single band method, the reflectance in a single wavelength band can be written as,

$$R(\lambda) = R_d(\lambda) + R_c(\lambda) r_b(\lambda) \exp^{-[\alpha(\lambda) \cdot f \cdot Z)]} \qquad 5.1$$

Where $R_d(\lambda)$ represents the sum of the radiance from the atmosphere and the reflection at the sea surface and is therefore equal to the radiance observed over deep water; $R_c(\lambda)$ is a constant which includes solar irradiance, the transmittance of the atmosphere and the water surface; $r_b(\lambda)$ is the bottom reflectance; $\alpha(\lambda)$ is the effective attenuation coefficient (m^{-1}) of the water; f is a geometric factor to account for path length through the water and Z is the water depth (m) (Lyzenga, 1978).

The single-band method assumes that the bottom reflectance is constant throughout the test site and that the water attenuation coefficient is constant and independent of water depth. It also assumes that the atmosphere and sea state are uniform and that the effects of multiple scattering between the water surface and the

bottom can be ignored or assumed constant throughout the image. Further, it assumes that the angular distribution of light does not change with depth and that there is no contribution to the upwelling radiance by the reflected sky radiance from the water surface.

The simplest method of extracting water depth information from multi-spectral scanner data is to invert equation 5.1 for a single wavelength band. An extension of this method would be to calculate the depth from two or more bands and average the results. Despite the crudeness of the model, it accounts quite well for the signals recorded by a multi-spectral scanner over shallow water (Lyzenga, 1979). The difficulty with this method is that changes in the bottom reflectance or water attenuation will cause errors in the depth calculation.

5.3.1.1.2 Ratio Method

Commonly the attenuation coefficient of water and the bottom reflectance change from one location to another within the same scene. However, the difference between the attenuation coefficients in two appropriately chosen bands does not vary much from point to point and from time to time. The same is true of the ratio of the bottom reflectance in the two bands. The following algorithm developed by Polcyn *et al.* (1970) relies on the assumption that a pair of wavelength bands can be found such that the ratio of the bottom reflectance's in these two bands is the same for all the bottom types within a given scene,

$$Z = \frac{1}{(\alpha_2 - \alpha_1)f}\left[in\left(\frac{R_{c2}}{R_{c1}}\right) + in\left\{\frac{r_{b2}}{r_{b1}}(R_1 - R_{d1})\right\} - in(R_2 - R_{d2})\right] \qquad 5.2$$

Where r_{b2} / r_{b1} is the ratio of bottom reflectance in bands 1 and 2 and α_1 and α_2 are the attenuation coefficients in bands 1 and 2 respectively. R_1 and R_2 are the observed radiances, R_{d1} and R_{d2} are the radiances observed over deep water and R_{c1} and R_{c2} are the constants which include solar irradiance, the transmittance of the atmosphere and the water surface in bands 1 and 2 respectively. Thus, if the assumption that the ratio of bottom reflectance in the two bands is constant within a given scene is correct, the depth calculated by this method is not affected by changes in bottom composition in the scene. The estimation of water depth is also insensitive to changes in water quality if the difference between the attenuation coefficients, remains constant (Gould and Arnone, 1997). In many cases, a pair of wavelengths can be found where an approximately constant value can be obtained for the ratio of the bottom reflectance and for which difference between the attenuation coefficients remains relatively constant. However, the wavelengths which satisfy one criterion are in general not the same as those which satisfy the other; moreover, if changes in bottom composition or water quality are too large, a pair of wavelengths may not exist which satisfies either criterion.

5.3.1.2 Evaluation of methods

The methods described in this section essentially depend upon finding a relationship between water depth and the reflected radiance in one or more wavelength bands. If the water's optical properties and the bottom reflectance are uniform and a large correlation exists between the water depth and the radiance in a single wavelength band then single-band method may give accurate results. If the optical properties and bottom reflectance are not uniform then more than one wavelength band must be used in the depth calculation. In deeper waters, using the band with maximum penetration will give increased accuracy when compared to

using multi-bands with insufficient depth penetration. Ratio methods give accurate results in areas of non uniform bottom reflectance and optical properties. The selection of method would, therefore, depend on the type of data available, the spectral channels available, the water and bottom characteristics and the range of depth in a particular area.

5.3.1.3 Method of depth determination and algorithm used in this thesis.

Knowledge of the study area played a vital part in deciding the method used to obtain water depth. By utilizing information such as bottom type and water quality of the study areas a suitable method could be selected. Since the study area was small (4 km length) and the area had a consistent bottom type of white carbonated sand, it was assumed that the albedo or reflective properties of the bottom type was constant. Water quality in this area was also consistent and hence the water attenuation coefficient, k did not vary within the imagery. Field visits to the study site validated this assumption. As these assumptions are implicit to the Benny and Dawson (1983) method, this method was chosen to estimate water depth. An in-depth explanation of the method is given below.

The fundamental principle of using remote sensing imagery to estimate water depth information is that different wavelength of radiation will penetrate water at varying degrees. As radiation passes through water it is attenuated by the interaction with the water column, its intensity I_d,remaining after the passage length p through water, is given by :

$$I_d = I_o.e^{-pk} \qquad 5.3$$

Where I_o = intensity of radiation and k is the attenuation coefficient, which varies with wavelength. If a vertical pathway of radiation from surface to bottom and back is assumed, p maybe substituted by the term $2d$, where d = water depth. The Benny and Dawson (1983) method assumes that for a certain water depth d, the length of the path is equal to $d + d.\text{cosec}\ (E')$, which can be rewritten as $d(1+ \text{cosec}(E')$. The cosec function corrects for the fact that the Sun is not vertically overhead at the time of image acquisition. Therefore, the amount of radiation remaining after passage through the water column to depth d and back upwards (I_d) will be :

$$I_d = R.\ I_o.e^{-k.d(1+\text{cosec}(E'))} \qquad 5.4$$

Where R is the proportion scattered upwards from seabed and I_o is the amount of incident light. Figure 5.3 displays the light path from the Sun to satellite sensor assumed by this method.

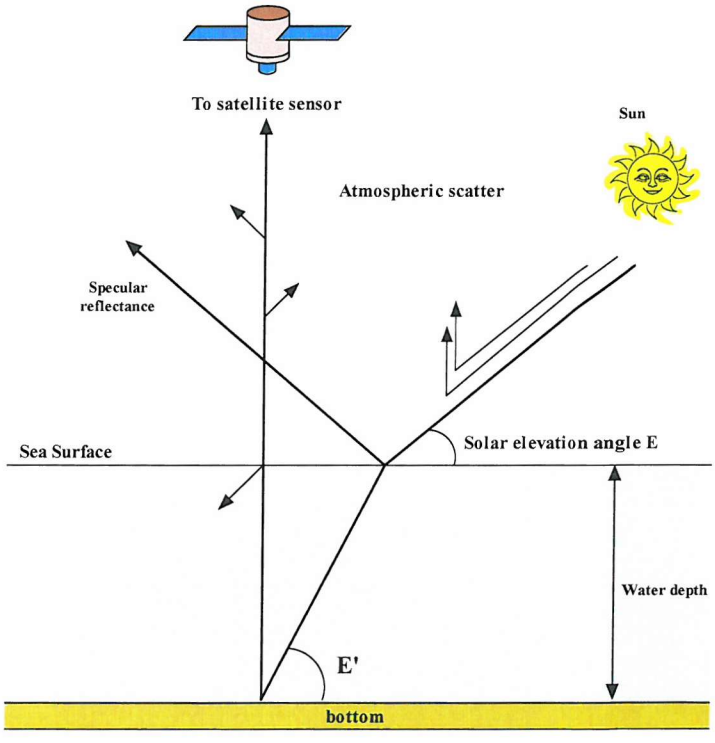

Figure 5.3: The light paths from Sun to satellite sensor modified from Benny and Dawson (1983))

Assuming that the radiation returned to the sensor by specular reflection and atmospheric scatter is the same for deep and shallow water, the total radiance (L) recorded by the sensor is :

$$L = L_d + R.\ I_o.e^{-k.d(1+cosec(E'))} \quad 5.5$$

Where L_d = deep-water radiance. The ratio of the radiance from the two different depths, x and y, is therefore:

$$\frac{L_x - L_d}{L_y - L_d} = \frac{R.I_o.e^{-k.x(1+\cos ec(E'))}}{R.I_o.e^{-k.y(1+\cos ec(E'))}} \quad 5.6$$

As the albedo or reflective properties of the bottom type in this study area is constant, the equation simplifies to:

$$\frac{L_x - L_d}{L_y - L_d} = \frac{e^{-k.x(1+\cos ec(E'))}}{e^{-k.y(1+\cos ec(E'))}} \quad 5.7$$

Hence :

$$x - y = \frac{ln(L_x - L_d) - ln(L_y - L_d)}{-k(1 + Co\sec(E'))} \quad 5.8$$

In very shallow water (< 1 cm), $y = 0$, and the equation reduces to:

$$\text{Depth } x = \frac{ln(L_x - L_d) - ln(L_o - L_d)}{-k(1 + \text{Cosec}(E'))} \quad 5.9$$

Where L_o is the signal strength for shallow water. This formula was applied to the IKONOS multi-spectral sensor imagery to derive a bathymetry map.

5.3.1.4 Data

This section describes the data used to estimate bathymetry.

5.3.1.4.1 Satellite sensor imagery

This study utilizes multi-spectral IKONOS satellite sensor imagery with a spatial resolution of 4 m to estimate bathymetry. The data was acquired on the 10th of April

2002 over Kuala Terengganu. Further details regarding the data can be obtained in section 3.3.1.1. The imagery was geo-rectified to the Malaysian Mapping standard based on the RSO map projection utilizing 20 carefully selected control points with an accuracy RMSE 5.4 m.

The IKONOS sensor imagery acquired for this purpose was contaminated by sun-glint. This was evident especially in band 1 but was less apparent in band 2 and 3. This occurs as the satellite sensor was in the opposite direction of the Sun during imagery acquisition. It was expected that this phenomena would affect the ability to derive depth information as it interferes with the radiation water interaction essential in determining bathymetry. Details of this phenomenon will be given in the discussion section.

5.3.1.4.2 Ground data

The data used were obtained from a field trip conducted within 3 months of the date of satellite sensor data acquisition. The field trip was conducted from the 6th July till 10th July 2002 to obtain bathymetry information. The bathymetry was obtained by collecting X, Y and water depth along a several profiles starting from land towards the sea. Further details on the data can be found in section 3.3.2. From this field trip a selection of 115 points were selected as ground data. The points were selected based on their location to form an evenly distributed network of points. The points were also selected evenly between depth values of 0.5 m and 7.5 m. From these 115 points 90 points were used as training data to estimate k, L_d, L_o *and* E', while the remaining 25 as check points to access the accuracy of the estimated depth (Figure 5.5).

Figure 5.4: Colour composite of Band 1, 2 and 3 of IKONOS satellite sensor imagery of study area.

Figure 5.5: Ground data and check point used to estimate bathymetry. Training data was used to estimate the parameter necessary to estimate bathymetry while check points were used to determine the accuracy of the derived bathymetry map.

5.3.1.5 Image processing

5.3.1.5.1 Converting image DN to planetary reflectance

In order to convert DN values from IKONOS satellite sensor imagery to Top of Atmosphere (TOA) or planetary reflectance the following formula was used (NASA, 2003):

$$\rho_p = \frac{\pi L_\lambda d^2}{ESUN_\lambda Cos(\theta_s)} \quad 5.10$$

Where ρ_p is the planetary reflectance, L_λ is the spectral radiance at sensor's aperture, $ESUN_\lambda$ is the band average solar Spectral Irradiances, θs is the solar zenith angle and d is the Earth-Sun distance, in astronomical units.

To utilize this formula the IKONOS sensor spectral radiance at sensor's aperture need to be determined. This parameter could be determined by the equation (Space Imaging, 2003b) :

$$L_\lambda \text{ (mW cm}^{-2} \text{ sr}^{-1}\text{)} = DN / CalCoef_\lambda \quad 5.11$$

or

$$L_\lambda \text{ (W m}^{-2} \text{ sr}^{-1}\text{)} = DN / (CalCoef_\lambda/10) \quad 5.12$$

Where the value of $CalCoef_\lambda$ was be obtained from Table 5-1.

Table 5.1: IKONOS satellite sensor calibration values (Source: Space Imaging Document Number SE-REF-016, Rev. A)

Spectral Band	$CalCoef_k$ DN*[mW cm^{-2}-sr]$^{-1}$	Full Scale Dynamic Range (mW cm^{-2}-sr)	$ESUN_\lambda$ values (Wm^{-2} μm^{-1})
MS-1 (Blue)	728	2.98	1939.429
MS-2 (Green)	727	3.32	1847.400
MS-3 (Red)	949	2.87	1536.408
MS-4 (VNIR)	843	3.75	1147.856

However, in order to use the values in Table 5.1 in the conversion formula, the values must be in units of W m^{-2} sr^{-1} μm^{-1}. This can be accomplished by dividing the wavelength dependent $CalCoef_\lambda$ by 10 and dividing this number by the bandwidth for each band (Fleming, 2003). Thus, spectral radiance in units of W m^{-2} sr^{-1} μm^{-1} now becomes:

$$L_\lambda \text{ (W m}^{-2}\text{ sr}^{-1}\text{ }\mu\text{m}^{-1}\text{)} = \text{DN}/((CalCoef/10)/\text{Bandwidth}) \quad 5.13$$

The final formula that incorporates the spectral radiance and band pass conversions for IKONOS DN values now becomes:

$$\rho_p = \frac{\pi DN_\lambda / ((CalCoef_\lambda / 10) / Bandwidth)_\lambda d^2}{ESUN_\lambda cos(\theta_s)} \quad 5.14$$

Equation 5.14 calculates the top of the atmosphere reflectance for IKONOS sensor imagery without considering atmospheric affects. Several radiative transfer codes (RTCs) based on radiative transfer theory have been developed to correct the atmospheric affect on satellite sensor images, among them 6S and Lowtran (Song *et al.*, 2001). However, these RTCs require accurate atmospheric optical properties at the time of image acquisition to calculate the surface reflectance. As these measurements were not available, the planetary reflectance was used to derive bathymetry. Therefore, equation 5.14 was applied to band 1 and 2 of the IKONOS satellite sensor imagery to produce reflectance images.

5.3.1.5.2 Estimation of k, L_d, L_o and E'

To utilize equation 5.9 and generate bathymetry, several parameters need be determined from the satellite sensor imagery. These values are k, L_d , L_o and E'

To estimate k of the satellite sensor images, field data were required. Data of 90 training sites (Figure 5.5) of known and varying depth with the same bottom type were used in estimating k. Based on the Benny and Dawson (1983) method the reflectance in each band were logarithmically transformed and regressed against depth. The regression line will have a negative gradient whose value is equal to k. From the analysis it was determined that a linear correlation could be. Figure 5.6 shows IKONOS satellite sensor band data regressed against logged depth (band 1 and 2).

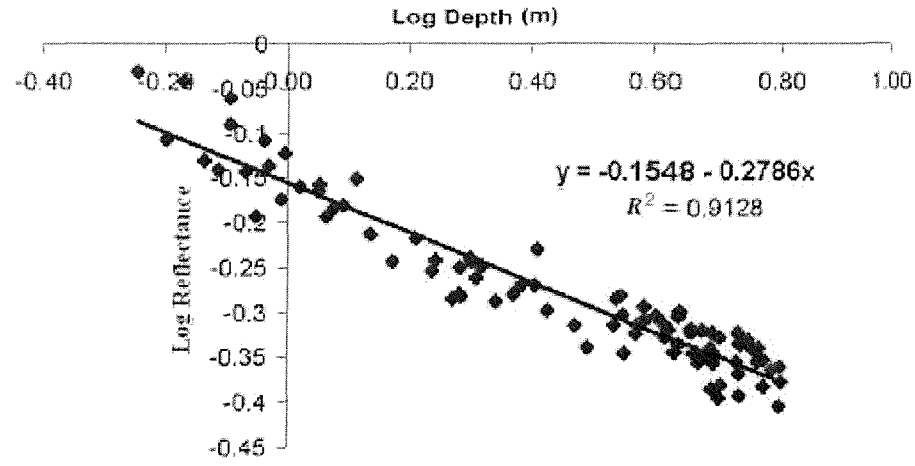

(a)

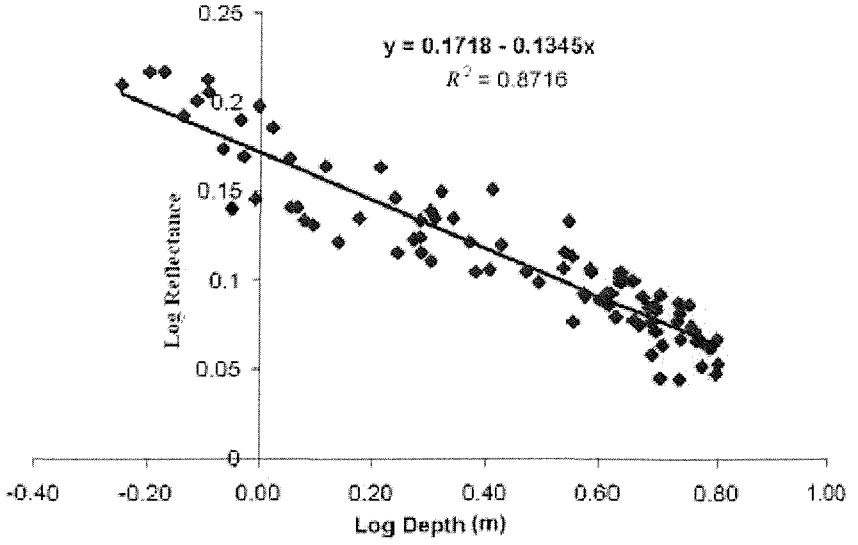

(b)

Figure 5.6: Reflectance values from IKONOS sensor reflectance regressed against logged depth from 90 sites in Pantai Batu Buruk and Seberang Takir for (a) band 1and (b) Band 2.

From the relationship between reflectance and depth in Figure 5.6 it was determined that the negative gradient for bands 1 and 2 were -0.2786 and -0.1345 respectively. Therefore, k was estimated to be 0.2876 and 0.1345 for band 1 and 2 respectively. As no data (from the 90 points) used in estimating these values were over 7.5 m, these k values could be assumed to be valid in estimating depth up to 7.5 m. An estimation of L_d and L_o, the pixel reflectance value for deep and shallow water for the two bands were calculated by producing a histogram of pixel values for the water area of the imagery, masking out land. The reflectance values for the lower part or the histogram is an approximate value for L_d while the upper end is an approximate value for L_o. This is illustrated in Figure 5.7.

The estimated values for L_d and L_o were verified by comparing them to location of known shallow and deep water in the satellite sensor imagery. By this means an

approximation were made for the of L_d and L_o for band 1 and 2 . These values are given in Table 5.2. *E'* could be calculated from its relationship with solar elevation angle (*E*) and through knowledge of the refractive index of water. Figure 5.8 show this relationship.

Table 5.2: Average deep-water (L_d) and shallow water (L_o) reflectance values calculated from IKONOS satellite sensor data of study area.

Band	L_d	L_o
1	1.513	0.431
2	2.026	1.081

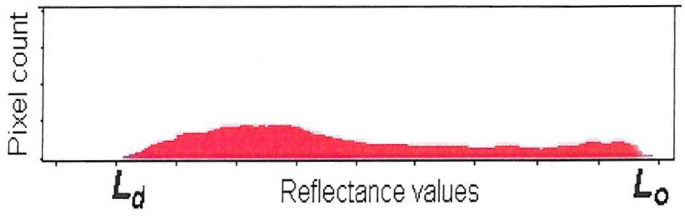

Figure 5.7: Histogram of reflectance values.

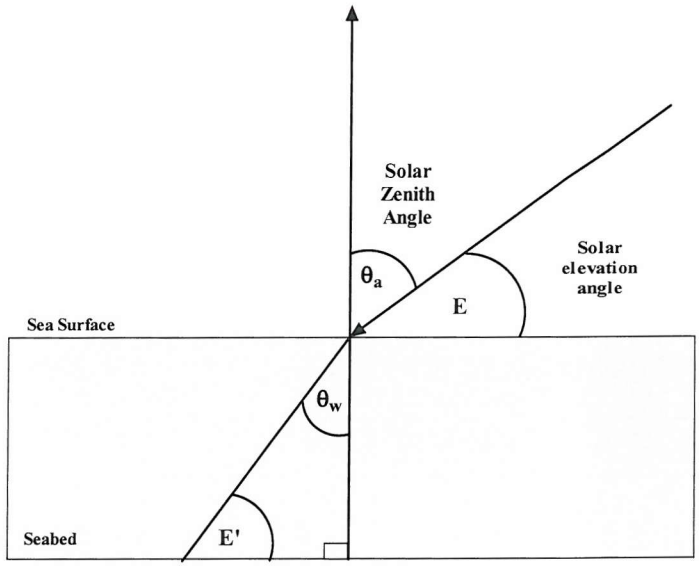

Figure 5.8: Relationship between Solar elevation angle (*E*) and *E'*

From Figure 5.8 it is apparent that $E' = 90 - \theta_w.\sin\theta_w$ could be calculated from the following equation :

$$\frac{\sin\theta_a}{\sin\theta_w} = \frac{n_w}{n_a} \qquad 5.15$$

Where n_w is the refractive index of water and n_a, the refractive index of air. Knowing the refractive index of air = 1 , the refractive index of sea water = 1.339 (Bukata *et al.,* 1995) and the Solar elevation angle of 68.13° (from header file), E' was calculated to be 41.14 °.

5.3.1.5.3 Depth estimation

The selection of the most appropriate band to predict water depth was very important. Several considerations were taken into account when choosing the band to use. These considerations were mainly based on the bottom type, purpose of bathymetry extraction and water penetration properties of the radiation (Nanu and Robertson, 1993). Other factors such as Sun glint were also considered.

The purpose of bathymetry extraction in this thesis was mainly to accurately extract depth values of shallow water close to the shoreline as outlined in section 5.1. These values would be combined with DEM values to form a 3-D terrain model of the area. Therefore, the selection of the appropriate band to use for the purpose of this thesis was based on these factors in mind. As radiation in band 1 is more penetrative in water than band 2, due to its spectral properties, it was expected that band 1 would be capable of estimating bathymetry more accurately. But as the study area mainly comprises of reflective sand and accurate bathymetry values close to the shoreline are

needed, band 2 was considered to be more appropriate. In band 1 the combination of its penetrative capability and reflective property of the substrate (white sand) in the study area causes the reflectance values in band 1 to be very saturated, resulting in less variation in L. Although band 2 was not as penetrative as band 1, resulting in an incapability to map deep water (more than 10 m) the results near the shoreline are better. As this thesis emphasis the mapping of coastal areas which are affected by tide levels depth more than 5 m were insignificant. As mention previously in section 5.3.1.4.1 the satellite sensor imagery was affected by sun-glint. Here at certain angles the water reflects sunlight and causes reflections of waves and ripples in the sea to be visible. This effect could be seen in Figure 5.9 was more apparent in band 1 in comparison to band 2.

Therefore band 2 was more suitable as reflectance values were less saturated while still capable of penetrating the water column. Utilizing the k, L_d, L_o and E' derived in section 4.2.6.2 and equation 5.9 a bathymetric map was derived from band 2 of the IKONOS satellite sensor imagery. The resulting map is shown in Figure 5.10

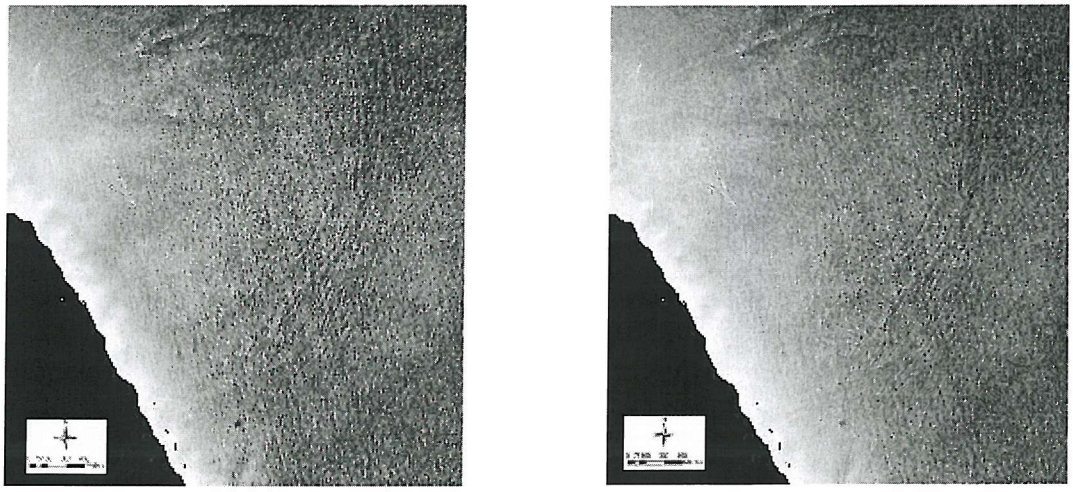

(a) (b)

Figure 5.9: The effects of Sun-glint in (a) band 1 and (b) band 2 of the IKONOS sensor imagery.

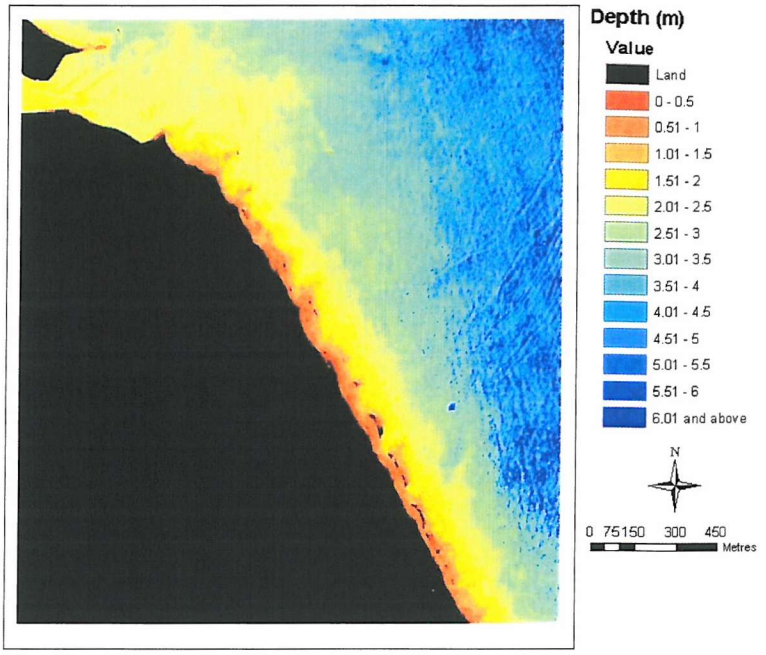

Figure 5.10: Bathymetry map generated from IKONOS sensor imagery.

5.3.1.6 Results

The accuracy of the bathymetry map produced from the IKONOS sensor imagery was determined by comparing depth values estimated from IKONOS imagery and actual depth from the 25 well distributed independent check points. These points are shown in Figure 5.5. It was determined that there was a significant correlation between the estimated depth and actual depth with a r value of 0.92 and an RMSE of 0.87 m. A graph of the relationship between the predicted and actual depth in metres is shown in Figure 5.11

5.3.1.7 Discussion

The method applied in this research has been tested in the Kuala Terengganu area with an RMSE value of below 1 m. The linear correlation coefficient of 0.92, shows a significant linear correlation ($p < 0.05$) between actual depth and estimated water depth achieved by utilising this methodology. Although there was a significant

correlation, a perfect correlation was not achieved because in this method k was assume to be constant and determined by regressing known bathymetry data against IKONOS radiance but it actually decreases in deeper water (Jerlov, 1976).

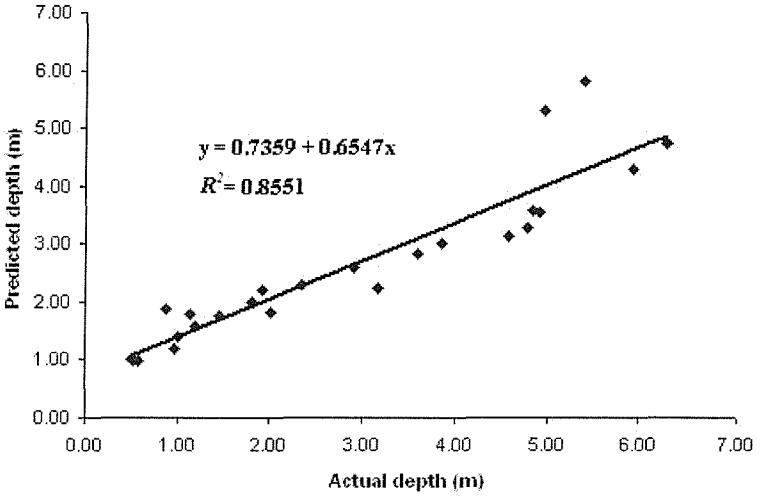

Figure 5.11: Relationship between predicted depth (m) and actual depth (m).

Utilizing IKONOS sensor imagery, the Benny and Dawson (1983) method was able to accurately estimate depth up to a depth of 7.5 m (section 5.3.1.5.2). But under optimum conditions, IKONOS sensor imagery should be able to predict water depth up to 21m, as in the case of Landsat TM imagery (Ibrahim and Cracknell, 1990). But this was expected as the IKONOS sensor imagery used was affected by sun glint which interferes with the reflectance values and limits its depth penetration. The sun-glint problem could be minimized by making a special request to Space imaging to capture the satellite sensor imagery at certain angles but this requires a special agreement. Under optimal conditions it was expected that with IKONOS sensor imagery it would be possible to estimate depth more accurately than with Landsat TM data. However, for the purpose of this thesis a depth penetration of less than 5 m is sufficient as the main interest was to accurately derive bathymetry maps of areas affected by tide levels.

This thesis used the Benny and Dawson (1983) method to extract water depth utilizing IKONOS sensor imagery. Even though this method makes several assumption mainly that the bottom type and water quality of the area was constant, accurate results were still obtained. Other more complicated methods developed to tackle different bottom type and water quality depend on obtaining substantial information of the study area. This required substantially more field data making the methods less appealing.

5.3.2 DEM extraction from stereo satellite sensor imagery

The process of DEM extraction is made possible by comparing two images acquired of the same area at different viewing angles. Ground point or interest points are then identified within the overlapped area of the two images. This process is termed digital image matching and is based on grey scale and contrast variations of points occurring on neighbouring images (Jensen, 2000). Automated DEM extraction can be achieved from stereo imagery, however sensor model information such as interior and exterior orientation associated with the imagery are required. Sensor models are a mathematical function explaining the relationship between the imagery acquired and their ground location. This sensor model information needs to be calculated through a process of aerial triangulation before it can be used. Once established the process of DEM extraction could begin (Toutin *et al.,* 2002).

The recent introduction of fine spatial resolution satellite sensor imagery has initiated a new era in Earth observation and digital mapping (Li *et al.,* 1998; Tanaka and Sugimura, 2001; Mumby and Edwards, 2002). Satellite sensor imagery from IKONOS and Quickbird offer fine spatial resolution satellite sensor imagery, with spatial resolution of 1 m and less. These sensors provide multi-spectral and panchromatic satellite sensor imagery and the capability of providing stereo imaging. In particular, IKONOS is capable of acquiring stereo imagery in near real time due to a very flexible pointing mechanism. These characteristics makes IKONOS sensor imagery suitable for generating DEM (Lee *et al.,* 2002; Fraser *et al.,* 2002a; Chen *et al.,* 2003). The aim of this section was to generate a DEM of the study area utilizing IKONOS 1 m pan sharpened geo stereo product.

5.3.2.1 Image data

The imagery comprised a stereo pair of Pan sharpened IKONOS satellite sensor imagery of Kuala Terengganu, Malaysia. Pan sharpened product was chosen as it provided a finer spatial resolution of 1 m in comparison to multi-spectral imagery used for bathymetry generation which was 4 m. For bathymetry generation spectral data was needed to relate the reflectance to water depth but for DEM generation a finer spatial resolution is important, to be able to resolve smaller objects in the imagery. When acquiring stereo imagery, two sets of data are acquired, one looking sideways to the left and the other to the right. Details of imagery are given in Table 5.3. In addition Figure 5.12 shows the left and right stereo images of the study area.

The stereo imagery were supplied with Image Geometry Model (IGM) or generally known as Rational polynomial camera (RPC) which provide a mechanism for object to image space transformation and 3-D point determination (Grodecki, 2001). The left imagery was collected at a low sensor elevation angle while the right imagery was taken at a higher sensor elevation angle providing a base to height ratio between 0.54 and 0.83 (according to IKONOS stereo imagery specification). These images have a horizontal accuracy of within 25 metres CE90 and a vertical accuracy of 22 metres LE90 (Space Imaging, 2003a).

Table 5.3: Acquisition parameters of IKONOS pan sharpen Images

	Left	Right
File name	po_103939_rgb_0000000.tif	po_103939_rgb_0020000.tif
Date , Time (GMT)	2002-08-28 03:45	2002-08-28 03:44
Sensor Azimuth (deg)	177.5195	52.4229
Sensor elevation (deg)	65.66296	80.21711
Sun azimuth (deg)	76.4012	76.5092
Sun elevation (deg)	68.81210	68.60580

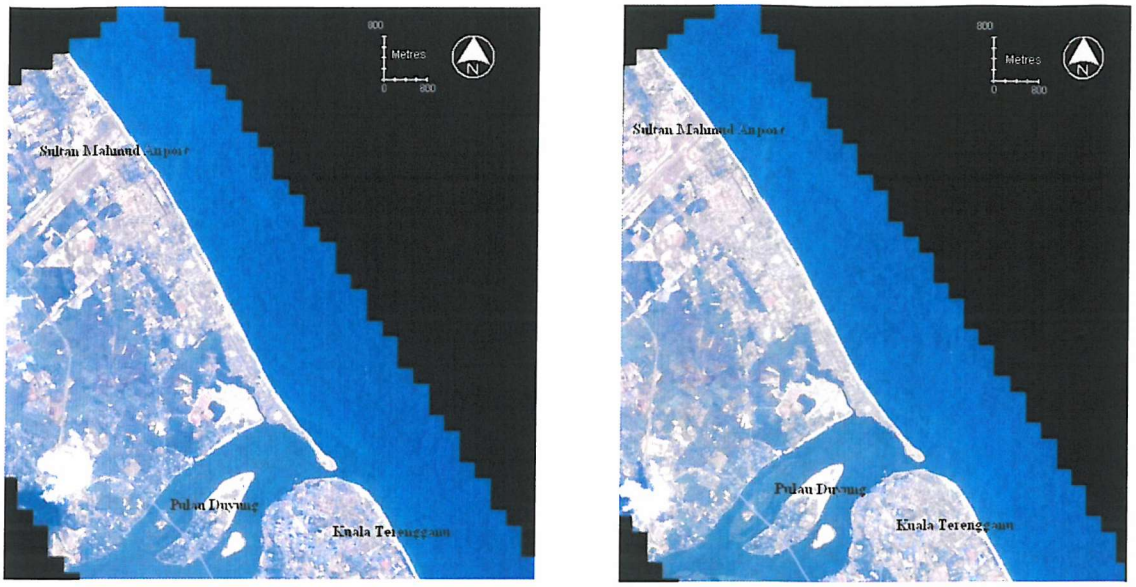

Figure 5.12: Left and right IKONOS satellite sensor image.

5.3.2.2 Study area and GCP collection.

The study area covers a 10 km by 7.5 km area with an elevation range less than 70 m. The area comprise Kuala Terengganu town in the south, adjacent to the Terengganu river mouth. Pulau Duyung a partly reclaimed island could also be found in this area. Several fishing villages could be located along the shoreline towards the north. The area is comprised of white sandy beaches facing the South China Sea to the east. The Sultan Mahmud airport is located in the north of this area.

To accurately generate a DEM of this area, a compilation of 62 high precision GPS control point was surveyed by performing Differential Geo-positioning system (DGPS) measurement under normal weather condition over this area. The GCPs were collected using the OmniStar DGPS system, capable of collecting GCPs at sub-metre accuracy. OmniSTAR is a wide-area differential GPS service, using satellite broadcast techniques. Data from many widely-spaced reference stations was used in a multi-site solution to overcome the influence of errors and biases (Omnistar, 2001). These points were simultaneously converted and collected in the RSO projection. The control

points were collected based on points which were identifiable on the IKONOS satellite sensor imagery.

5.3.2.3 Image Distortion and Correction Models.

Fine spatial resolution satellite sensor imagery contains geometric distortions that need to be corrected for it to be used for the generation of maps. This geometric distortion could be modelled and applied to the satellite sensor imagery to produce accurate satellite sensor maps. The source of distortion in satellite sensor imagery could be related to two general categories: satellite sensor (observer) and Earth (observed). The distortion caused by the acquisition system includes calibration parameters such as the focal length and the instantaneous filed of view (IFOV) of the sensor imaging system. Distortion from the Earth includes the effect of the Earth curvature which creates variation in the image pixel spacing and topographic relief which generates a parallax in the sensor scanning azimuth (Toutin *et al.,* 2002). To correct these geometric distortions requires models and mathematical functions. Several methods have been proposed to correct these distortions which include 3-D non-parametric models or rigorous parametric models, 3-D polynomial models and RPC models (Lee *et al.,* 1992; Clavet *et al.,* 1993; Bolstad and Stowe, 1994; Giles and Franklin, 1996; Clarke and Fryer, 1998; Vassilopoulou *et al.,* 2002; Ganas *et al.,* 2002; Toutin, 2003a).

To utilize the rigorous parametric model, it should mathematically model all distortions arising from the platform (position and velocity), the sensor (panoramic effect, viewing angles), the Earth (Ellipsoid and relief) and the cartographic projection. As most of these parameters (for IKONOS sensor) are not made available to the general public, utilization of the rigorous model has been limited. However, several researchers have been able to develop rigorous models that do not require the sensor model but utilize basic information of the meta-data and celestial mechanics laws

(Toutin *et al.,* 2001). Even though these models approximate physical characteristics of the sensor, they have been shown to be robust and able to achieve consistent results over different study sites and environments (Davies and Wang, 2001; Hoffman *et al.,* 2001; McCarthy *et al.,* 2001; Ganas *et al.,* 2002; Toutin, 2003a; Toutin, 2003b).

The 3-D polynomial model can be used when the parameters of the acquisition system or a rigorous 3-D physical model are not available. The 3-D polynomial model does not require any prior information on any component of the acquisition system and is based on polynomial function and are an extension of the 2D polynomial function by adding an elevation (Z) term relating to the third dimension of the terrain. However, this model requires a large number of GCPs that cover the whole planimetric and height range to produce accurate results. Results from this method are correct locally at GCPs and very sensitive to input error (Tao and Hu, 2002). Due to these limitations this method is suitable for small images where all systematic distortion except terrain were corrected. This method has been applied to geo-reference images, such as SPOT HRV (Pala and Pons, 1995) and IKONOS geo-products (Hanley and Fraser, 2001).

The final approach, RPC model is a method used by satellite sensor imagery suppliers to provide a relationship between image space (line, sample) to object space (latitude, longitude, height) without disclosing the sensor model. This relationship is revealed as the ratio of two polynomials derived from sensor model and the corresponding terrain information. Space imaging provides IKONOS sensor Geo products which have been corrected for systematic distortion. This corrects distortion caused by the sensor and provides increased accuracy when processing the images. Test cases comparing the rigorous camera model approach to the resultant RPC method under a diverse set of acquisition condition yield a worse case scenario error of

0.04 pixels (Grodecki, 2001). Therefore, the RPC model provides an accurate alternative to rigorous camera model approach.

Due to the unavailability of IKONOS satellite sensor model, this research utilizes the RPC method to obtain a DEM of the study area. The RPC method has also been shown as an accurate replacement for complex camera models providing information to establish the interior and exterior orientation parameters required to extract DEM (Grodecki, 2001).

5.3.2.4 Rational polynomial camera (RPC)

In order to relate image space coordinates on satellite sensor imagery to the object space coordinate on the Earth, a sensor model is required. Physical sensor models are based on the interior and the exterior geometry and physical properties of the sensor. When acquiring imagery, each IKONOS sensor image line is taken at a different instance of time and, therefore, from a different orbital position and satellite orientation. Owing to this dynamic nature, the physical IKONOS sensor model is extremely complex (Grodecki and Dial, 2001). The implementation of the RPC model provides a simplistic method of representing the relationship between the object-image relationship of the physical sensor model with near-perfect accuracy. Furthermore, it contains enough degrees of freedom to describe IKONOS physical sensor model with 0.05 pixel accuracy (Grodecki and Dial, 2001).

The RPC model relates the object space coordinates to image space coordinates and is of the form of a ratio of two cubic functions of object space coordinates (Figure 5.13). Separate rational functions are used to express the object space to line, and the object space to sample coordinates relationship (Grodecki, 2001). The image coordinates (X,Y) and the ground coordinates (X,Y,Z) are normalized to the range

from -1.0 to 1.0 by their image size and geometric extent, respectively, for computational stability and to minimise computational errors. The line RPC model is given as (Madani, 1999; Grodecki, 2001):

$$X = \frac{P_1(X,Y,Z)}{P_2(X,Y,Z)}, \quad Y = \frac{P_3(X,Y,Z)}{P_4(X,Y,Z)} \tag{5.16}$$

Polynomials P_i *(i=1,2,3* and *4)* have the general form :

$$P(X,Y,Z) = \sum_{i=0}^{m_1}\sum_{j=0}^{m_2}\sum_{k=0}^{m_3} a_{jik} X^i Y^j Z^k \tag{5.17}$$

In normal use, the order of the polynomials is limited to $0 \le m_1 \le 3$, $0 \le m_2 \le 3$, $0 \le m_3 \le 3$ and $m_1 + m_2 + m_3 \le 3$. Each *P (X,Y,Z)* is then a third-order, 20 term polynomial:

$$\begin{aligned} P(X,Y,Z) = {} & a_1 + a_2 \cdot X + a_3 \cdot Y + a_4 \cdot Z + a_5 \cdot X \cdot Y + a_6 \cdot X \cdot Z + a_7 \cdot Y \cdot Z + a_8 \cdot X^2 \\ & + a_9 \cdot Y^2 + a_{10} \cdot Z^2 + a_{11} Y \cdot X \cdot Z + a_{12} \cdot X^2 + a_{13} \cdot X \cdot Y^2 + a_{14} \cdot X \cdot Z^2 \\ & + a_{15} \cdot X^2 \cdot Y + a_{16} \cdot Y^3 + a_{17} \cdot Y \cdot Z^2 + a_{18} \cdot X^2 \cdot Z + a_{19} \cdot Y^2 \cdot Z + a_{20} \cdot Z^3 \end{aligned} \tag{5.18}$$

The RPC coefficient in IKONOS products are calculated based on virtual points generated from rigorous sensor model. These virtual points are created based on the full extent of the image and the range of elevation variation. RPC coefficients are supplied with the IKONOS satellite sensor imagery with the Geo-ortho kit (Space Imaging, 2003a).

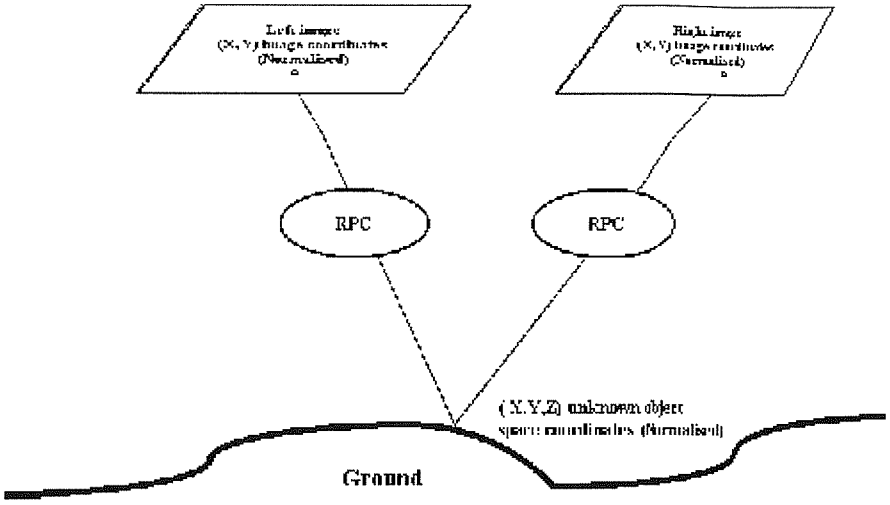

Figure 5.13: Relationship between RPC, object space and image space.

The RPC model of the IKONOS-2 satellite used in this research had 59 coefficients and 10 parameter values for object and image space offset and scale factors. Therefore, there are a total of 118 coefficients for the stereo pair image, which has a left and right image. The RPC coefficients for both images used in this research are listed in Appendix 1.

Even though RPC provides a translation between the space and image coordinates, positional biases may still exist. It has been shown that these positional errors are very systematic and could be reduced to sub-metre accuracy by post processing with few precise GCPs (Fraser *et al.*, 2002a) or the original RPC coefficients could be refined with a linear equation requesting precise GCPs (Lee *et al.*, 2002). Results from applying RPC model without any GCP refinement are not expected to be accurate with an accuracy of 6.2m CE90 horizontal and 10.1m LE90 vertical (Grodecki and Dial, 2001). This research applies a 3-D polynomial correction to refine the mathematical solution of the RPC model.

5.3.2.5 Control point selection

Control points used in this research are divided into 3 main categories:

1. GCP: measurements taken at distinct locations that are used to correctly position and rectify satellite sensor imagery.
2. Independent control points (ICP): measurements taken at distinct locations that are used to asses the accuracy of the rectification process which were independent from the rectification process.
3. Tie points: A point whose ground coordinates is not known, but is visually recognizable in the overlap area between the two images.

A survey of the study area was conducted in November 2001 to collect GPS ground coordinates of the study area. Details of the survey are given in section 3.3.6. The GPS coordinates were collected at an accuracy of less than 1 m according to RSO projection. The survey was successful in collecting 62 points but only 47 were located within both stereo images. Out of these 47 only 29 points were used in this study based on their location and the ability to accurately identify their position within the stereo IKONOS sensor Imagery. Out of the 29 points, 4 evenly distributed points were used as GCPs and the remaining 25 as ICP. In this research 25 additional tie-points between the left and right stereo imagery were collected to assist in the refinement of the RPC model. The corresponding image position coordinates of tie points appearing on the overlap areas of multiple images were identified and measured. Figure 5.14 shows the GCPs, ICP and tie-point used in this study. A main problem with this imagery is that on the north-east of the imagery 50 percent of the imagery is the sea thus no GCPs are available in this area. The effects of the distribution of control point would be analysed later.

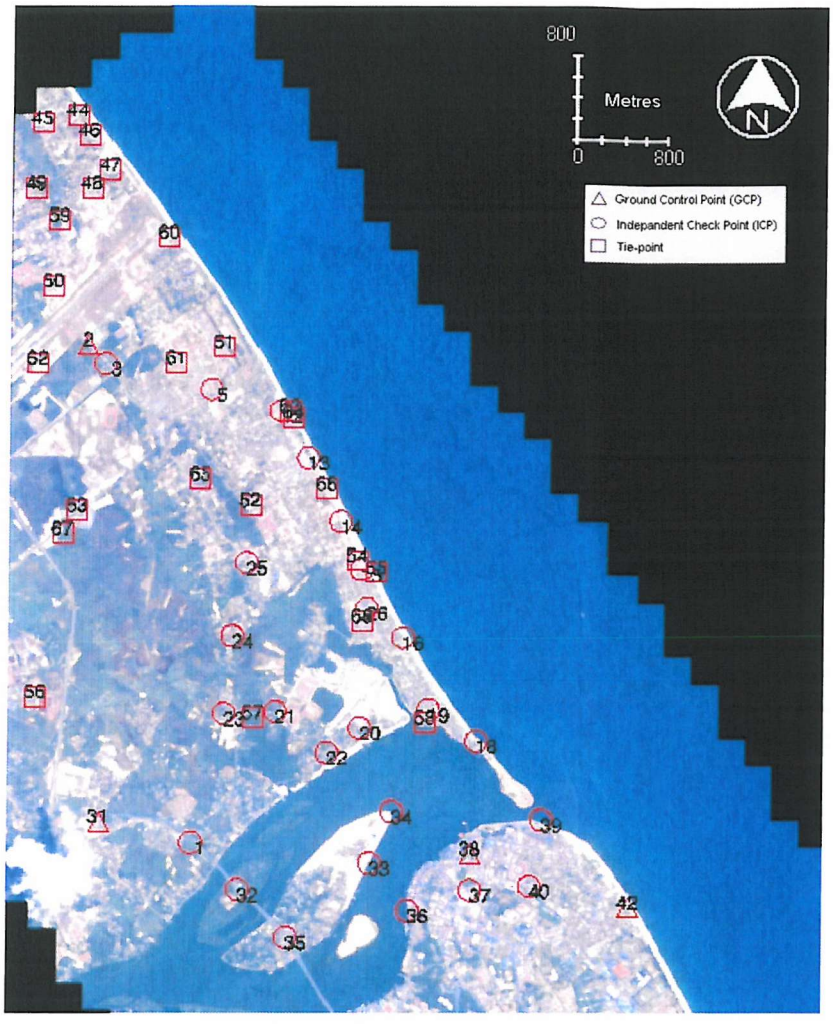

Figure 5.14: Distribution of GCPs, ICP and tie points used in research.

5.3.2.6 Derivation of DEM

As Space imaging does not publish the IKONOS sensor model and ephemeris data related to a particular satellite sensor imagery, this research utilises RPC coefficient to generate the DEM. The RPC coefficient was provided concurrently with the stereo IKONOS satellite sensor data. It has been shown when applying the RPC model without GCPs it results in large systematic positional errors due to a large bias. These systematic errors could be reduced to sub-metre accuracy by employing GCPs (Baltsavias *et al.,* 2001; Chen *et al.,* 2003; Di *et al.,* 2003). In this research the RPC model was refined using 4 evenly distributed GCPs and 25 tie points. Only 4 evenly

distributed GCPs were used as a larger number of GCPs would reduce the accuracy (Lee *et al.,* 2002; Fraser *et al.,* 2002b; Fraser and Hanley, 2003). The effect of refining the RPC model is described in the result and discussion sections.

The process of automatic DEM generation is shown in Figure 5.15. The utilization of digital image correlation has been widely used in remote sensing and GIS applications to find similarities between two images that overlap or share a common geographical area. The correlation coefficient is used to represent the measure of similarity between a set of image pixels appearing within the overlapping portions of an image pair. A large correlation coefficient value (i.e., 0.80 -1.0) indicates that the set of image points are more similar than a set of image points which have a lower correlation coefficient value.

The process starts with the selection of a point of interest which displays sufficient grey level variation and contrast to be ambiguously identified in the imagery. A corresponding point was later selected from the adjacent imagery based on similarities in ground features and the correlation coefficient was computed between the points. Several strategy parameters are set to influence the success and accuracy of the matching process. These include the search window size used to locate points specific to a topographic type and a correlation window size that establishes the accuracy of the correlation between matching points.

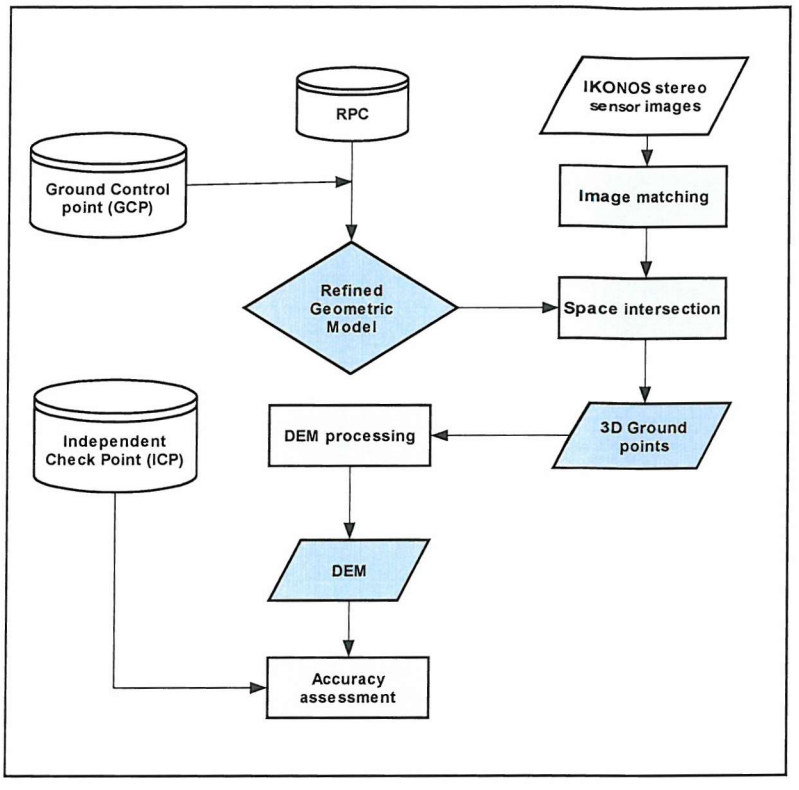

Figure 5.15: DEM generation overview.

IKONOS stereo images provided by Space Imaging have been resampled so that a pixel in both imagery and the two imagery centres lies on the same plane. This means that given a pixel in one image, its correspondent must lie on a known line in the second image (Kim, 2000). Images with these characteristics are known as epipolar images. As the stereo images are epipolar, the apparent displacement of conjugate points/pixels between the two images in the Y direction (Y- parallax) are very small, with most values being 0 or 1 pixel (Wolf, 1983). Figure 5.16 illustrates an image point on an image being located along the epipolar line of an adjacent overlapping image.

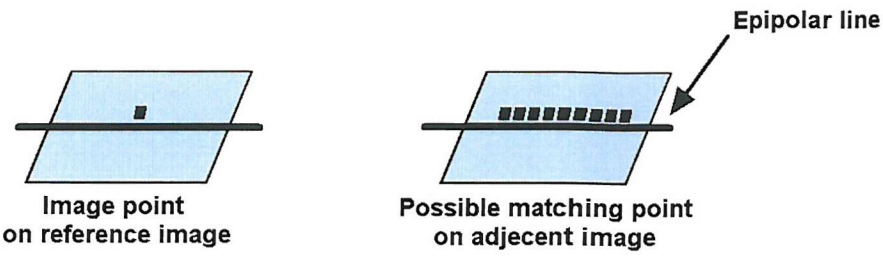

Figure 5.16: The process of locating a matching image point on a reference image on an adjacent image for two images that area epipolar to each other.

To make the process more accurate and efficient the search area used to establish a pair of matching image points was constrained. The search range in the Y direction was constrained to 3 pixels (as the images were epipolar) while in the X direction the matching windows size and search range were changed adaptively depending on the statistical analysis of an area. Initially a small window size and narrow search range were used. If the correlation coefficient of the point was lower than a selected threshold of 0.8 a larger window size was used. The approximate position of the conjugate point was estimated by the previous matched point in a neighbour. The correlation coefficient was calculated on each set of possible matching points along the epipolar line.

After the correlation coefficient was calculated from each image point within a search window, the points with the largest correlation coefficient were recorded and its row and column coordinates associated with a ground point on the Earth's surface. These interest points are then assigned 3-D (X, Y, and Z) coordinates based on the refined RPC model. The technique used to calculate these 3-D ground points, otherwise known as mass points, is known as space forward intersection. Space forward intersection is a technique that is commonly used to determine the ground

coordinates X, Y, and Z of points that appear in the overlapping areas of two or more images based on known interior and exterior parameters (Chen *et al.,* 2003). It is based on the collinearity condition, which states that the corresponding light rays from the sensors pass through the corresponding image points on the two images, and intersect at the same ground point. These ground points or mass points are discrete points located within the overlap portion of an image pair, and whose 3-D ground coordinates are known. These were automatically extracted and calculated mass points are then used as a basis for constructing a DEM.

5.3.2.7 Results

The accuracy of ground points computed from the RPC method was affected by systematic errors with a total RMSE of 5.23 m (X = 2.24 m, Y = 3.07 m and Z = 14.51 m). By applying a 3-D polynomial transformation supported by 4 evenly distributed GCPs, the RMS errors at 25 ICPs were reduced to 0.921 m, 0.782 m and 1.349 m for X, Y and Z coordinates. Using the carefully selected ground point, stereo image pair and refined RPC model a DEM of the study area was generated. A subset of the resulting DEM and its corresponding imagery is shown in Figure 5.17. The DEM shows the Kuala Terengganu town with the South China Sea to the east.

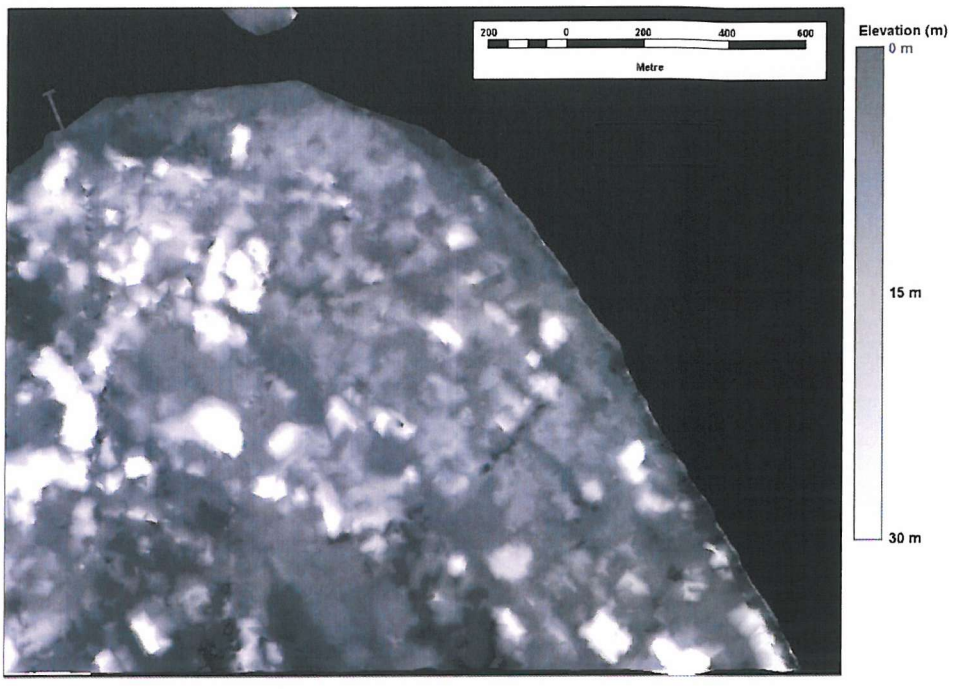

(a)

(b)

Figure 5.17: (a) Subset DEM for Kuala Terengganu and (b) it corresponding satellite sensor imagery.

The DEM generated had a spatial resolution of 1 m vertically and horizontally, this area represents the area of overlap between the left and right image. The correlation coefficient calculated for each mass point in the DEM provides a means of quantifying the quality of a DEM. DEM mass quality were categorised into several categories as defined in Table 5.4.

The general mass point quality describes the percentage of DEM mass point that could be categorised into the 4 categories given in Table 5.4 (Wolf, 1983). From the DEM generated 61.48 % was categories as excellent, 22.29 % as good, 16.21 % as suspicious and the remaining 0.0038% as isolated.

Several indices have been used to describe the accuracy of a DEM. The simplest are standard statistical indices such as minimum, maximum and mean mass point errors (Wolf, 1983). A similar method used is the mean absolute error of the DEM. Unlike the mean error, mean absolute error takes into consideration the positive and negative value associated with an error, where all negative values were made positive. The mean absolute error is useful to determine the average accuracy of an extracted DEM. RMSE is another widely used accuracy indicator. RMSE indicates the magnitude of error associated with all the DEM based on 3-D reference points used.

Table 5.4: Categories of mass points

Category	Definition
Excellent	Mass points with Correlation coefficient between 1 and 0.85.
Good	Mass points with Correlation coefficient between 0.85 and 0.70
Suspicious	Mass points where the standard deviation for it (within a 3 x 3 window) is three times of its neighbouring pixels
Isolated	Mass points with no immediate neighbour

Another index normally used to describe DEM errors is the Absolute LE90 (Linear error 90%). LE90 is the error range which would include 90 % of the pixels within the DEM. Thus, an LE90 of 4 m indicates that 90 % of the pixels within the DEM vary from the actual DEM by 4 m or less. Absolute LE90 is defined herein as the LE90 calculation for the DEM with no corrections applied. The error thus includes the effects of positional and elevation inaccuracies.

The National Imagery and Mapping Agency (NIMA) LE90 statistic is based on the assumption that a normal distribution of data exist with the set of observation. In this case the set of observation is the DEM errors computed using the 3-D reference points using the following equation (Department of Defense, 1990). :

$$\text{NIMA LE90} = \pm 1.646\sigma$$

Where,

$$\sigma = \sqrt{\frac{\sum\left(|e_i| - \overline{|e_i|}\right)^2}{n}} \qquad 5\text{-}1$$

Where,

σ = standard deviation
$|e_i|$ = absolute error of reference point i
$\overline{|e_i|}$ = mean absolute error for the entire set of refefence points
n = total number of 3D reference points used

Therefore, for example, if a value of ±4.5 m was computed for NIMA LE90, it is safe to state that at a 90 % confidence level, the DEM accuracy is within ±4.5 m.

Table 5.5: Accuracy of DEM

	Global Accuracy (m)	ICP Accuracy (m)	GCP Accuracy (m)
Number of 3-D Reference Points Used:	54	25	4
Minimum Error:	-1.5102	-1.0398	-0.3049
Maximum Error:	3.9192	3.9192	0.6570
Mean Error:	0.6180	1.4731	0.0617
Mean Absolute Error:	1.0821	1.8076	0.2667
Root Mean Square Error (RMSE):	1.5675	2.2171	0.3654
Absolute Linear Error 90 (LE90):	3.2076	3.5953	0.6570
NIMA Absolute Linear Error 90:	± 1.8667	± 2.1131	± 0.4112

As mentioned previously in section 5.3.2.5 the reference points used in this study were from 4 GCPs, 25 ICPs and 25 tie-points. Errors calculated at GCPs were typically smaller because they were employed in the refinement of the RPC model. A more objective assessment is provided by utilizing ICP, as they were not involved in refining the RPC model. Summaries of global (accuracy calculated based on all 54 points - GCP, tie point and ICP), ICP and GCPs vertical accuracies are shown in Table 5.5.

5.3.2.8 Discussion

The accuracy of the generated DEM computed by using the RPC method was affected by systematic errors; these errors were reduced by utilizing several GCPs. Even though the imagery had a large area of sea to the north east of the imagery the image was able to be positional corrected to within an RMSE of < 1.0 m for the X and Y coordinated and 1.5 m for the Z coordinates based on ICP (section 5.3.2.7). For the IKONOS sensor relative to other spaceborne satellite sensor, distribution of GCPs are less important due to the sensors small field of view (FOV), while GCPs positional accuracy becomes more important, due to the small pixel size (Lee *et al.*, 2000; Fraser and Hanley, 2003). By applying the RPC method with a simple first level polynomial

transformation the accuracy was increased comparable to the more expensive IKONOS Precision product which has an RMSE of 1.9 m (Space Imaging, 2003a). Therefore the selection of accurate GCPs was very important irrespective of location or distribution. Several papers have also emphasized that utilizing more than 4 GCPs does not further increase accuracy but may in fact reduce accuracy by introducing more errors (Lee *et al.,* 2002; Fraser *et al.,* 2002a).

Another factor that has to be considered was the accuracy of the GCP used and its position on the imagery. As IKONOS imagery has a spatial resolution of 1m, positioning sub-metre accurate ground point within a pixel is difficult and subject to errors. This again introduces positional errors. Therefore it is advisable that the person responsible for collecting ground point location at the field is also responsible for identifying position on the ground point within the imagery. The equipment also needs to be standardized where only the same set of equipment is used for a particular area. To generate the DEM the vertical accuracy of a ground point was very important as the vertical accuracy produced by GPS are usually double the horizontal accuracy of a ground point; this again introduces errors in generating DEM (Omnistar, 2001).

DEM extracted by utilizing the RPC model and stereo imagery has shown to be accurate with an RMSE of below 2.2 m at ICP. This was encouraging considering the terrain of the study area was quite flat. When visually comparing the DEM generated with satellite sensor imagery, high elevation values do correspond to high objects such as buildings (Figure 4.10 and 4.11). As the IKONOS stereo imagery was taken on the same orbital pass, one in forward and the other in backward direction, this was ideal for DEM generation as both images have similar reflectance values. The images are only a minute apart thus factors such as lighting condition and cloud cover are the same. The similarity between the images assist in the image matching process as the

spectral or grey scale variation between the left and right imagery are similar. This results in 83.77 % of the DEM mass points that have a correlation coefficient of 0.70 or above.

5.3.2.9 Conclusion

Stereo IKONOS sensor imagery has been shown to be able to produce accurate DEM. By utilizing vendor provided RPC and a limited number of GCP, accuracy within 1 m in X and Y and 2.5 m in elevation was achievable. But this accuracy is directly dependant upon the quality of the GCPs used. With accurate GCPs, the DEM produced from IKONOS sensor imagery was capable of satisfying the requirement of the US National mapping standard at a scale of 1:4,800. The output DEM generated in this research would be combined with bathymetry generated from multi spectral IKONOS sensor data generated in section 5.3.1. This would provide a coastal elevation model that would assist in determining shoreline position based on mean sea level.

5.4 Combination of DEM and bathymetry data

The IKONOS sensor images used in deriving the DEM and bathymetry of the study areas were acquired at different dates. Ideally the images should have been captured on the same orbital pass. The requirement for both IKONOS sensor imagery to be captured simultaneously was put forth to Space Imaging but for unspecified reasons this was not fulfilled. The images used were acquired on 10th April 2002 for bathymetry and 28th August 2002 for DEM generation. Even though there is a 4 month difference between the two dates the changes in bathymetry and DEM are expected to be minimal as the Northeast monsoon which brings severe rain to this area only starts in November and end in March. Details of the climate and wind condition of this area

were given in section 3.1. During this period the sea was considered calm and the changes to shoreline position and bathymetry were expected to be minimal.

After generating both the DEM and bathymetry of the study area, these two data sets were combined to form a 3-D terrain model representing the land and water areas. To ensure that both data sets were compatible geographically both were generated utilizing the same planimetric and vertical datum. The projection used was the RSO, details of the projection were explained in section 2.2. An overview of the process of combining DEM and bathymetry information to derive a shoreline map based on MSL is given in Figure 5.18

Before combining both DEM and bathymetry a decision had to be made on the spatial resolution of the final imagery. This was because the spatial resolution of the DEM was 1 m and for bathymetry 4 m. If the spatial resolution of the DEM was reduced to 4 m to match the bathymetry important positional information would be lost. It was decided that the pixels spatial resolution in the bathymetry map be reduced to 1 m. This was done by dividing the 4 m pixels into four 1 m pixels. This process does not increase the spatial resolution of the bathymetry but only its pixel size to accommodate the combination process.

To generate a 3-D representation of the shoreline, the bathymetry and DEM data need to be combined. But before doing so both data sets needed to be standardised as DEM was given in height and bathymetry was given depth. Therefore, both data sets were converted to elevation value where DEM values are positive and bathymetry values are negative. Both data were than combined at the position where the elevation value was 0. Ideally both data should fit nicely at the position where the elevation was zero but factors such as breaking of waves during satellite sensor acquisition causes several areas to have no data. These areas of no data are, for the DEM imagery areas

where the DEM was classified as isolated and suspicious (section 5.3.2.6) and for the bathymetry areas where land and breaking waves was masked out (section 5.3.1.5.2). Even so these areas of no data only represent less than 2 percent of the total imagery and less than 1 percent of the shoreline. The value for such area had to be interpolated from surrounding pixels. The resulting 3-D terrain model of the study area is shown in Figure 5.19.

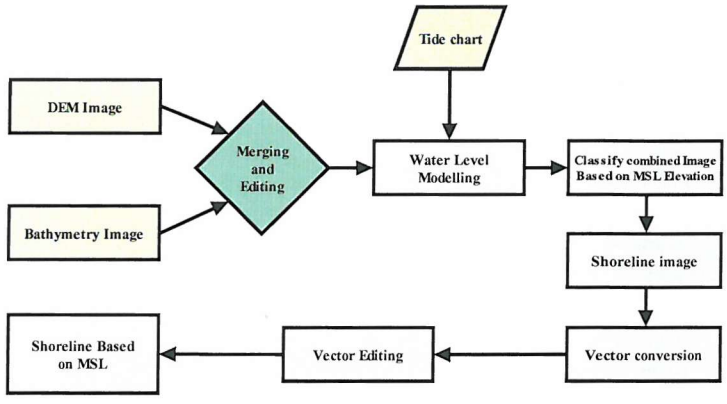

Figure 5.18: Overview of generating Shoreline position map at MSL

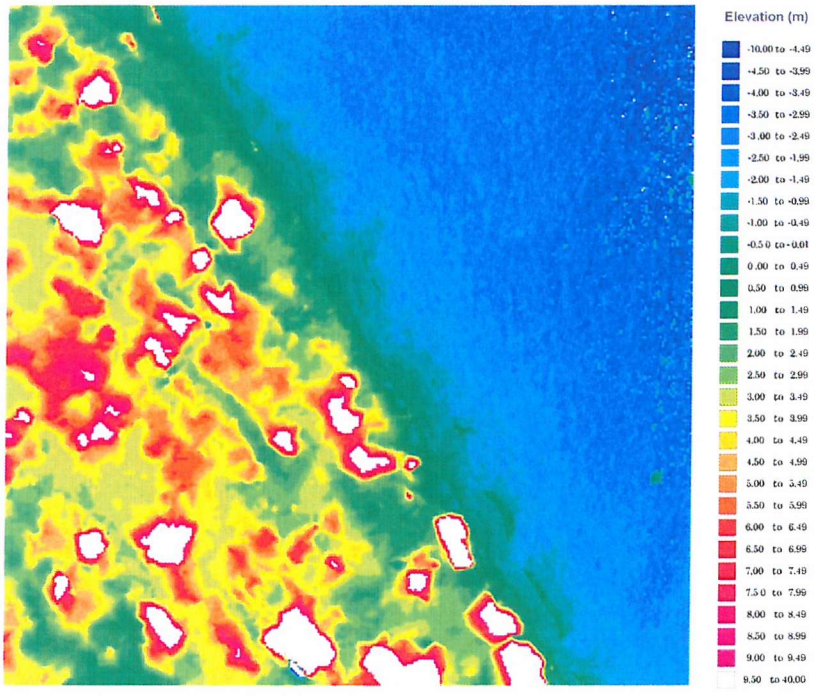

Figure 5.19: 3-D terrain model of the study area.

To accurately position the shoreline based on the MSL, the water elevation level during satellite acquisition needed to be determined. This could be determined by analysing its position base on the time the imagery was acquired. Ideally this would have been the date the satellite sensor imagery used for bathymetry and DEM was captured, but in this study the two dates were different so a choice needed to be made between them. The date selected was 10th April 2002, the date the bathymetry imagery was acquired. It was chosen as only bathymetry was affected by tide levels and not DEM. Another factor was that DEM are fairly constant and not as dynamic as bathymetry.

To determine the water elevation level during satellite sensor acquisition the harmonic constituent at the Kuala Terengganu tide station needed to be analysed. Harmonic constituent are mathematical expressions for the tide-producing force and in corresponding formulas for the tide or tidal current. Each constituent represents a periodic change or variation in the relative positions of the Earth, Moon, and Sun. (National Ocean Service, 1982). Utilizing the harmonic constituent, a tide chart for the Kuala Terengganu station was prepared for the 10th of April 2002 (Figure 5.20). A tide chart generally shows the tide elevation throughout a certain period. Zero elevation shown on the chart refers to the chart datum. The chart datum is a local variable, defined as 'a level so low that the tide will not frequently fall below it', and which is very close to the Lowest Astronomical Tide (LAT) (National Ocean Service, 1982).

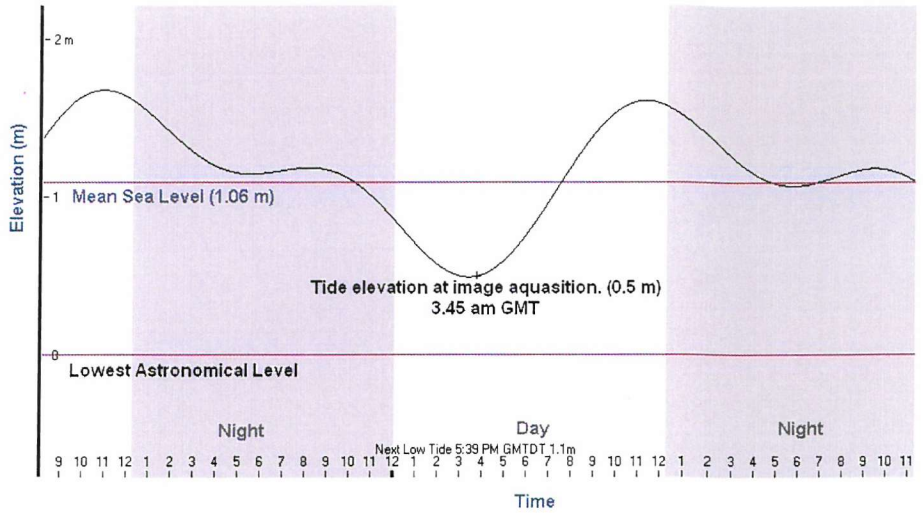

Figure 5.20: Tide chart of Kuala Terengganu station on 10th April 2002. The tide elevation (0.5m) at the time of satellite sensor imagery acquisition (3.45 GMT, 11.45 local solar time) is shown. The red lines represent the elevation of LAT and MSL. The tide level is shown as the black line running through the chart.

Referring to the tide chart at the Kuala Terengganu tide station, the tide level during satellite acquisition (10th April 2002 – 3.45 GMT, 11.45 local time) was at 0.5 m above the lowest astronomical level. To properly map the shoreline the water level at MSL needed to be determined and the water level remodelled accordingly, utilizing the 3-D coastal terrain model. From the same chart MSL was determined to be 1.06 m above the chart datum thus the water level was increased by 0.56 m. By increasing the water level on the 3-D terrain model, the shoreline position during MSL could be identified as the position where land and water meet.

The shoreline positions were later determined by classifying elevation values below 1.06 m into water class and 1.06 and above as land class. This imagery was later vectorised to produce a shoreline position map. During the conversation from raster to vector, errors occur resulting in lines along the shoreline which is not part of the shoreline (Dangles). These errors are a by-product of the automated raster to vector conversion and are not errors in shoreline position. These errors were removed through

visual inspection. Figure 5.21 and Figure 5.22 shows the shoreline position at satellite sensor acquisition time and MSL.

Figure 5.21: Instantaneous shoreline position at satellite sensor acquisition time is shown in blue (3.45 GMT on the 10th April 2002). The 3-D terrain model was overlaid with a RGB imagery of the study area

Figure 5.22: Shoreline position based on MSL is shown in red. The 3-D terrain model was overlaid with a RGB imagery of the study area.

By modelling the water elevation level on a 3-D terrain model of the study area, a shoreline map based on MSL was produced. To asses the accuracy of the generated shoreline map a GPS survey was conducted at the study area to map the shoreline position at MSL. Details of the survey are given in section 3.3.3. A subset map of the study area displaying the instantaneous shoreline (shoreline at satellite sensor acquisition), shoreline at MSL and actual shoreline (based on GPS survey) is shown in Figure 5.23

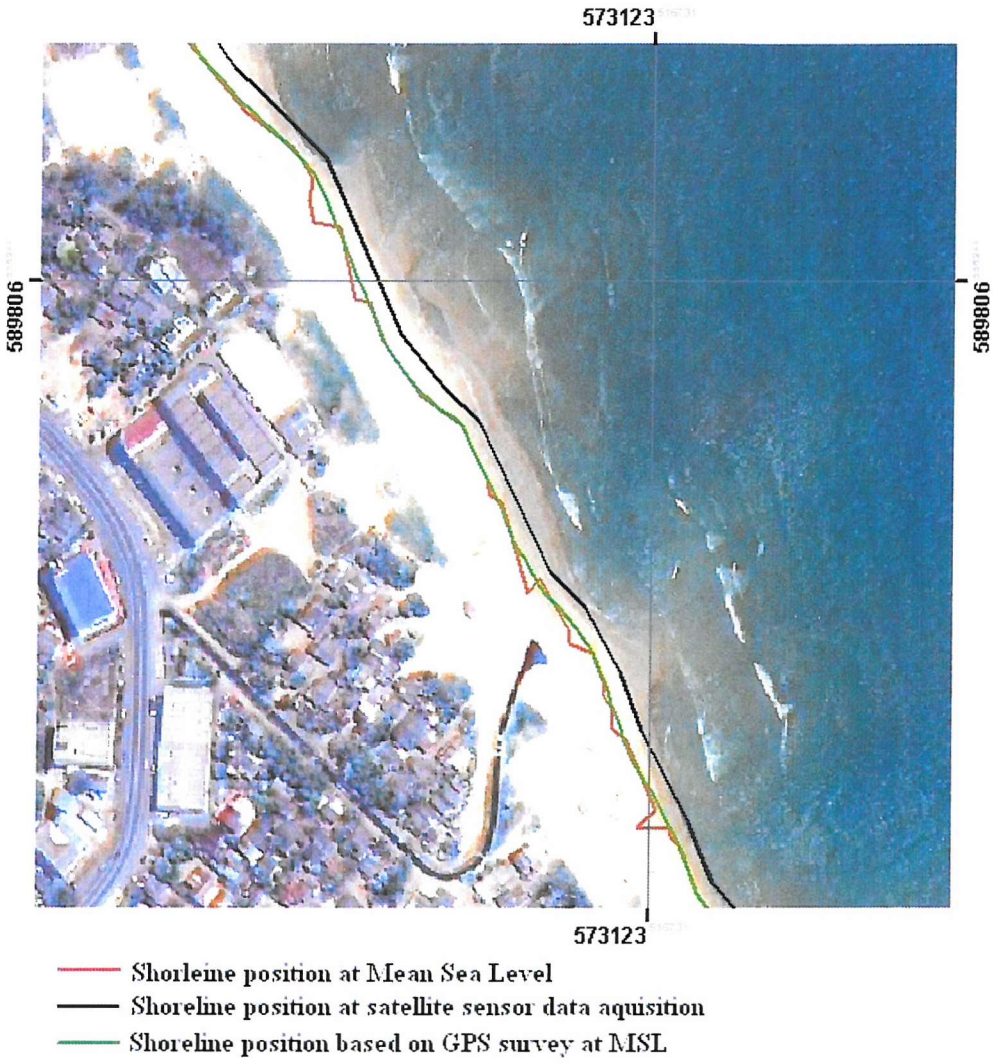

Figure 5.23: Shoreline position map based on different water elevations and GPS survey.

5.5 Accuracy assessment of shoreline position

The accuracy of the shoreline predicted by modelling the water level on a 3-D terrain model of the study area was determined by comparing its position to positions mapped by a DGPS survey of the shoreline at MSL. Details of the DGPS survey could be found in section 3.3.3. The length of the shoreline in the study area was 1.3 km. the positional errors for each metre of the shoreline determined and its RMSE was calculated. The results show that the shoreline predicted from modelling the water level on a 3-D terrain model of the study areas has an RMSE of 1.80 m with 90 % of the errors within 2.8 m. Figure 5.24 shows the shoreline positional error for each metre of the shoreline (a 500 m portion).

The shoreline generated had a jagged (zigzag) pattern this could be attributed to the pixel size of the combined bathymetry (4 m) and DEM (1 m). The shoreline was delineated by threading it between pixels allocated to land and water classes determined by elevation value of 1.06 m. Therefore, the shoreline was constrained to lie between pixels and resulting in a jagged shape shoreline.

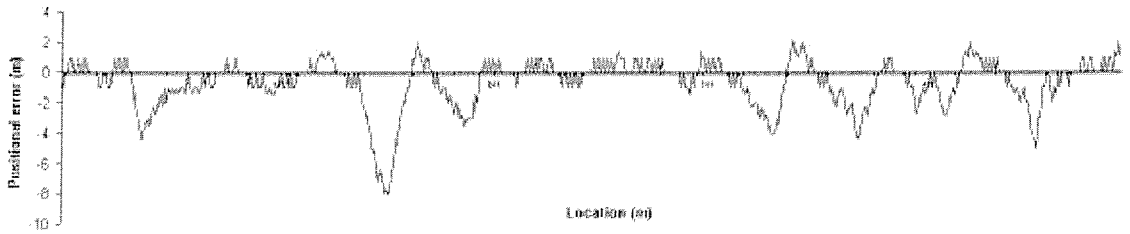

Figure 5.24: The positional accuracy of a 500m portion of the shoreline mapped against its location.

5.6 Discussion and conclusion

The coastal areas are dynamic in nature; therefore any coastal related data such as shoreline maps need to be current and easily updateable. This chapter introduced a method of generating such information using fine spatial resolution satellite sensor imagery. The method introduced used satellite sensor imagery as the primary data, as satellite imagery are widely available at regular interval.

The new generation of commercial satellites such as IKONOS and QuickBird offer users fine spatial resolution multi-spectral data as well as stereo imaging capabilities. Fine spatial resolution satellite imagery provides the potential to play a major role in coastal applications where currently mainly aerial photography is used. This chapter looked at utilizing IKONOS sensor imagery to generate the 3-D terrain of a coastal area. 3-D terrain information could be utilized in applications such as erosion studies, coastal management, sediment transport and shoreline mapping.

The 3-D terrain was generated by combining accurate DEM and bathymetry maps produced from IKONOS sensor images. Utilizing the 3-D terrain model, accurate tide-coordinated maps were produced by modelling the water level. The shoreline maps produced were accurate within an RMSE of 1.80 m. The accuracy of predicted shoreline could also be viewed from a perspective of mapping standards. According to the US national mapping standard for maps with a cartographic scale of 1:20,000 or larger, at least 90 % of a sample of well defined points plotted should lie within $1/30^{th}$ inch of the correct position when plotted on a map. Taking the shoreline positions as such a sample, the shoreline prediction satisfies the requirement of a 1: 2,500 scale map.

The accuracy of the shoreline produced was affected by the pixel size of the bathymetry and DEM used resulting in a jagged shaped shoreline. Though these jagged shapes were small (1 m and 4 m) they still contribute to errors in the shoreline prediction. To address such issues, methods of prediction the shoreline within a pixel or at a sub-pixel level were explored in the following chapters.

6 Sub-Pixel Analysis in Shoreline Mapping.

6.1 Introduction

This chapter aims to further advance and revise the techniques applied in chapter 4 and analyse the effect of shoreline orientation on the accuracy of the prediction. The four methods of predicting the shoreline location used in chapter 4 were revisited and applied to 4 different portions of the shoreline representing different shoreline orientation.

The methods examined in chapter 4 were hard classification, wavelet interpolation, contouring soft classification and two-point histogram. The hard classification (conventional remote sensing approach) and wavelet interpolation (interpolation approach) method were used as a benchmark for comparison with the approaches introduced in this thesis.

A Space Imaging 1 m Pan-Sharpen multi-spectral IKONOS satellite sensor imagery acquired of the study area on the 1st July 2000 was used (Figure 6.1). The imagery was geo-rectified to the Malaysian Mapping standard based on the RSO map projection with an accuracy RMSE 2.1 m.

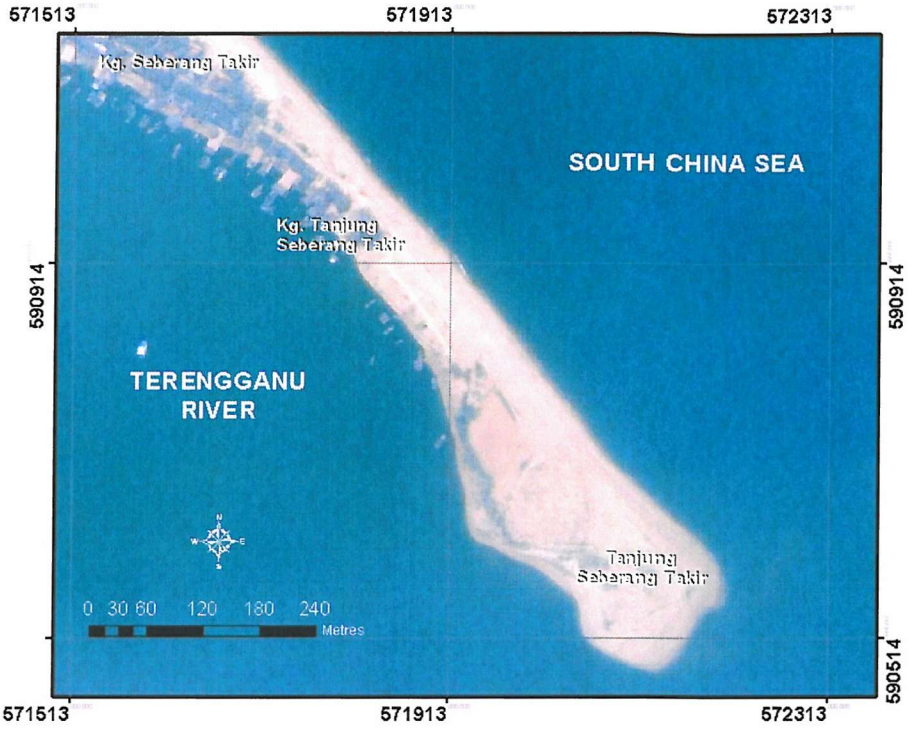

Figure 6.1: A RGB colour composite imagery of the study area.

6.2 Test sites

The work focused on a 1 km stretch of coast in Kampung Seberang Takir, Terengganu, Malaysia. The shoreline was characterized by sandy beaches facing the South China Sea to the northeast and the Terengganu River to the southwest. This research intent to look at the effect of differently shaped coast on accuracy of the shoreline prediction. Therefore, attention was focused on four 125 m long extracts of shoreline, each differently shaped. These were (Figure 6.2): I. Linear (across pixel orientation), II. Linear (along pixel orientation), III. Slightly curved and IV. Sharply curved.

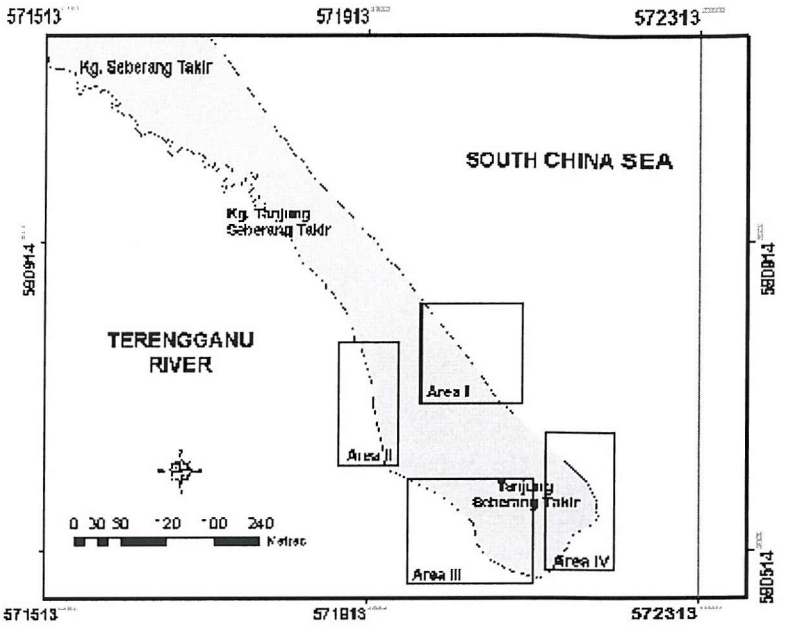

Figure 6.2: Location of the 4 shoreline extracts selected for analysis.

6.3 Methodology

The methodologies applied in this chapter are similar to the one applied in chapter 4. These methods are refined to produce accurate results. Here two set of simulated imagery was generated from the 1 m IKONOS sensor imagery. The imagery was generated at spatial resolutions of 16 m and 32 m to simulate commonly used satellite sensor imagery such as SPOT HRV and Landsat TM data.

6.3.1 Simulation of satellite imagery

The 1 m IKONOS sensor imagery was resampled to spatial resolutions of 16 m and 32 m. This was achieved by aggregating the original 1 m pixel to the target sizes. Since a simulated coarse spatial resolution image was to be used to predict shoreline location using classification analyses which may be evaluated against that derived from the original image, the effect of noise reduction in the spatial degradation need to be addressed. To address the impact of noise on the classification process, the SNR was

determined from the 1 m spatial resolution imagery and added to the 16 and 32 m imagery.

The SNR was estimated from a variogram derived from the imagery (Curran and Dungan, 1989); (Curran and Atkinson, 1998). The SNR for the 1 m imagery was already determined in section 4.2.1.3 and estimated to be 31.14. To counter effect of the reduction of noise, random noise was added to the resulting 16 and 32 m imagery so that the resulting imagery has a similar SNR to the 1 m imagery. As SNR can only be estimated and it was impossible to exactly obtain the same SNR between both images, it was decided that the resulting imagery needed to have a SNR of 90 % within the 1 m imagery. The resulting images are shown in Figure 6.3. Although issues such as the point spread function are not considered this provides a reasonable approach for the simulation of data with coarser spatial resolution.

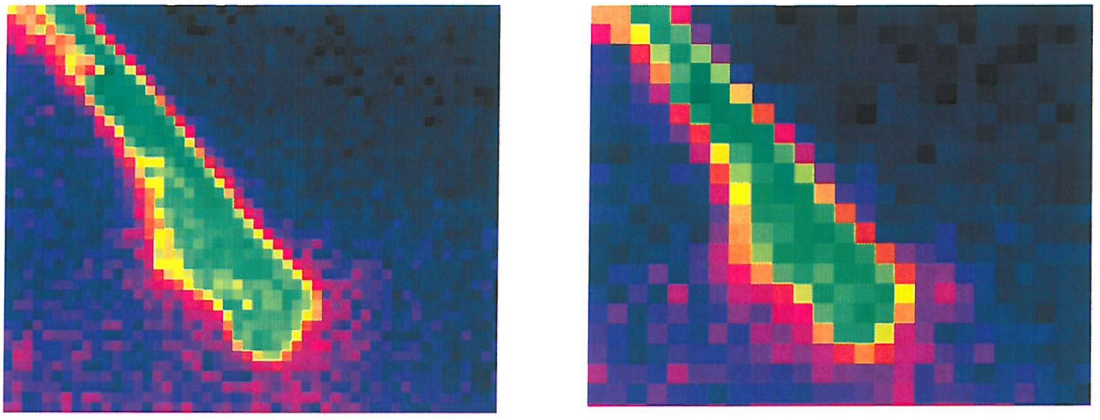

(a) (b)

Figure 6.3: Simulated satellite sensor images with spatial resolutions of (a) 16 m and (b) 32 m.

6.3.2 Generation of Ground Data from 1 m imagery

To analyse positional errors, an accuracy assessment needs to be done by comparing the shorelines generated from the coarse spatial resolution imagery with ground data. The ground data was generated from a 1 m fine spatial resolution imagery of the study area. To differentiate between land and water a supervised hard classifier was applied. Eight training sites were selected from the satellite sensor imagery, out of these 4 were defined as pure land and 4 as pure water (Figure 6.4). These sites were determined from visual interpretation and fieldwork of the study area. In all classification analysis undertaken in this chapter, these training sites were also used to provide consistency.

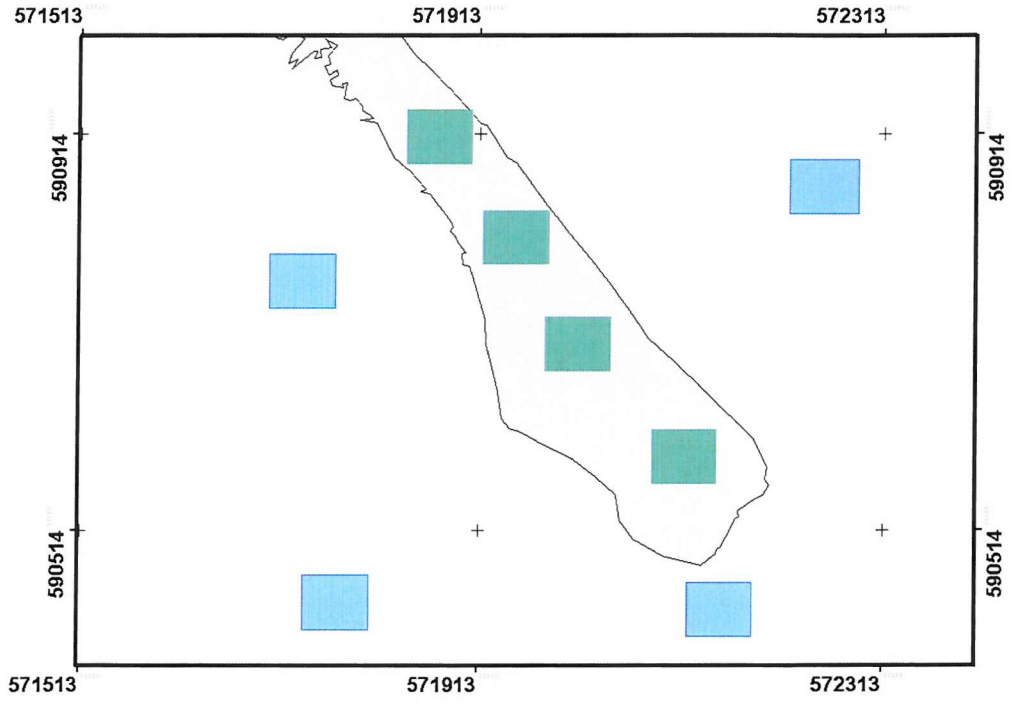

Figure 6.4: Training sites used throughout this chapter. Areas in blue were defined as water while green as land. The black line represents the classified shoreline.

Using these training sites a supervised hard classification was applied to the imagery classifying the imagery into land and water classes. The process assigns pixels to either land or water based on similarities to the training sites. The boundary between these two classes was later vectorised to represent the shoreline position. The classified shoreline is also shown in Figure 6.4.

6.3.3 Hard classification

As a benchmark, a conventional hard classification was used to predict the shoreline from the coarse spatial resolution images. The coarse spatial resolution images were classified using a supervised maximum likelihood classification (Richards, 1993). Initially training sets are selected from imagery by selecting areas of known homogenous water and land cover types. These sites were defined in Figure 6.4 and were determined from visual interpretation and fieldwork. The shoreline was fitted to the derived output of this classification by threading it between pixels allocated to different classes. The classified images are given in Figure 6.5.

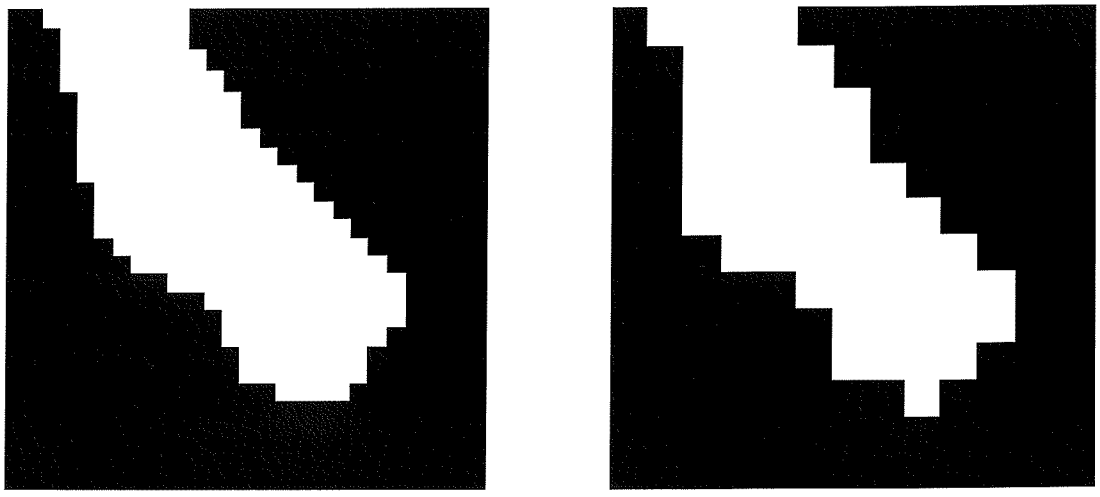

(a) (b)

Figure 6.5: Hard classified satellite sensor imagery showing land in white and water in black. (a) 16 m spatial resolution. (b) 32 m spatial resolution.

6.3.4 Wavelet interpolation

Since mapping a feature such as the shoreline may generally be expected to become more accurate as the spatial resolution of the imagery used becomes finer, a wavelet approach was used to interpolate the simulated images (Zhu and Yang, 1998; Simhadri *et al.,* 1998; Carvalho *et al.,* 2001; Tebbens *et al.,* 2002).

The spatial resolution of the coarse imagery was increased by using a 2-D wavelet refinement method based on average–interpolation. Wavelets are mathematical functions that cut up data into different frequency component and then study each component with a resolution matched to its scale (Donoho, 1992). The basic approach is to use pixel values of coarse spatial resolution imagery to estimate the sub-pixel values based on a wavelet transform. An average-interpolation refinement scheme was used to increase the spatial resolution of both coarse spatial resolution simulated imagery to a target resolution of 1 m. Initially average interpolating filters were calculated from the simulated images, these filters form the basis in predicting fine resolution imagery. Using these filters a 2-D refinement function was applied to simulated images to refine boxcar averages, imputing averages on a finer grid. For the 16 m simulated imagery, 16 m pixels were refined to 1 m pixels. Similarly for 32m simulated imagery, 32 m pixels were refined to 1 m pixels. Further details on this method was already explained in section 4.2.5.1

To map the shoreline a maximum likelihood classification using training sites defined in section 6.3.2 was applied to the interpolated images to derive an estimate of the shoreline location. The wavelet interpolated images and corresponding classified images are given shown in Figure 6.6.

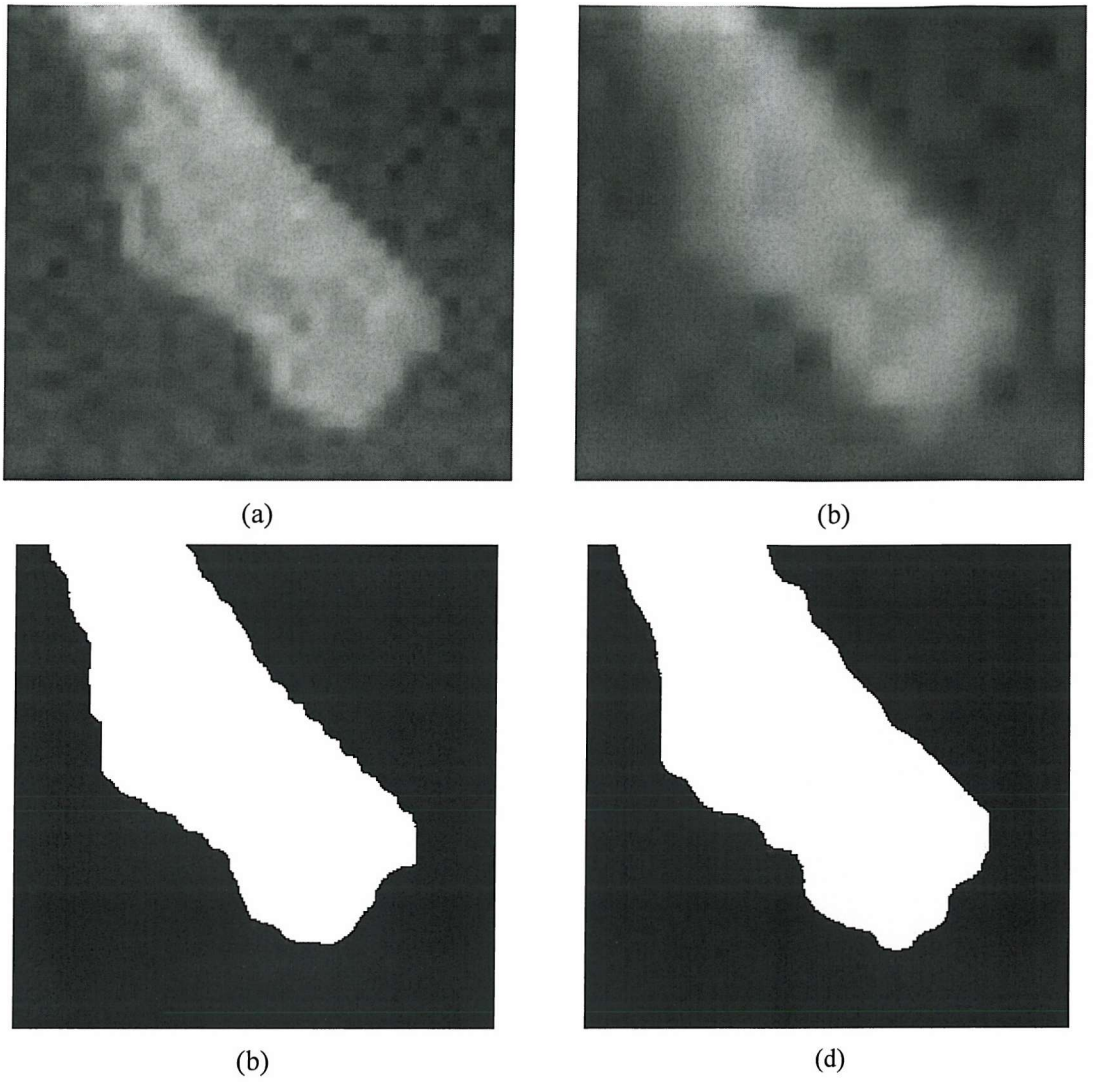

Figure 6.6: Imagery derived from wavelet interpolation and associated hard classified imagery. (a) 16 m spatial resolution, (b) 32 m spatial resolution, (c) hard classification output of 16 m imagery and (d) hard classification output of 32 m imagery. Black areas representing water while white represents land.

6.3.5 Soft classification

This chapter utilises two classification techniques, hard classification and soft classification. The hard classification used represents the conventional method of classifying water and land areas in order to delineate the shoreline position. It has been shown previously in chapter 4 that it was unable to accurately predict the shoreline position (section 4.3.2.1). To analyse and position the shoreline within a pixel and

produce a more accurate representation of the shoreline a soft classification was applied.

Soft classification provides a first step in analysing the content of a pixel allowing pixels to be classified as fraction values representing the proportion of a certain class. Both coarse spatial resolution images were soft classified using a sigmodial function with a Z score of 7. This function was selected as it models a profile of a typical shoreline (Figure 5.1). The sigmodial function used is shown in Figure 6.7. The resulting images gave the fraction prediction for land within a pixel. The resulting soft classification is shown in Figure 6.8.

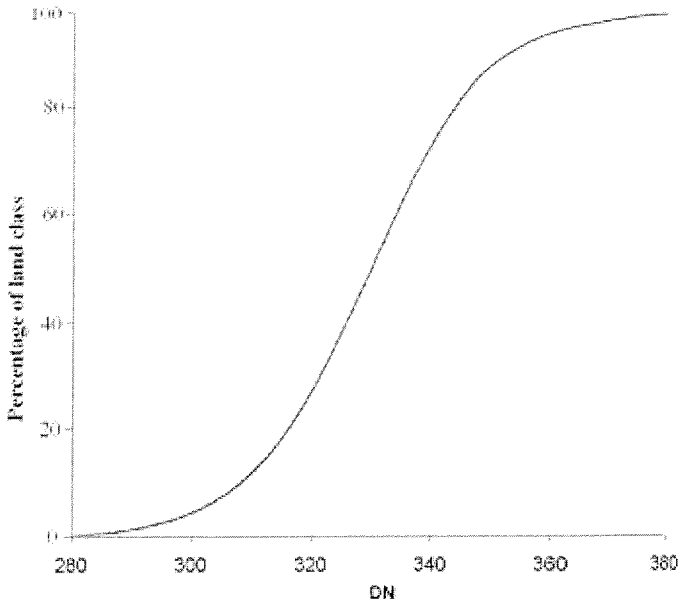

Figure 6.7: Sigmodial function used to soft classify the images.

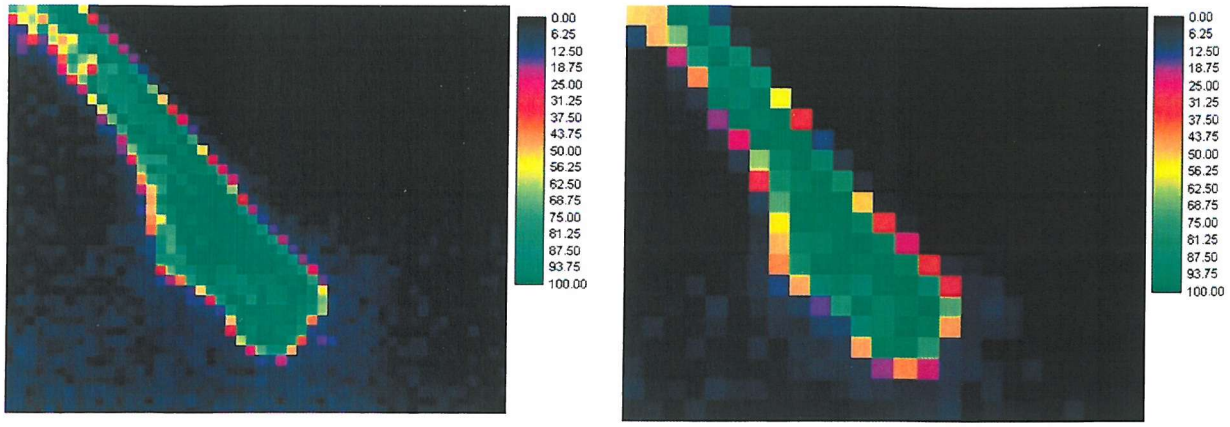

(a) (b)

Figure 6.8: The figures show the percentage of land class within the (a) 16 m imagery and (b) 32 m imagery as indicated by the colour scale.

Since these soft classifications were the basis of all the later analyses, their accuracy was evaluated. This evaluation was based on a comparison of the predicted coverage of a class with that derived from the reference data, the 1 m spatial resolution image. The comparisons were done based on pixels located along the shoreline. Figure 6.9 and Figure 6.10 shows the actual class percentage of land in the 16 and 32 m images respectively. Based on these values and the predicted coverage both coarse spatial resolution images was found to be significantly correlated ($p < 0.05$) to the actual, $r = 0.958$ (16 m Imagery) and $r = 0.946$ (32m imagery). Therefore, the soft classification results were taken to be an appropriate base for the work (Figure 6.8) as they accurately represent the sub-pixel level class composition.

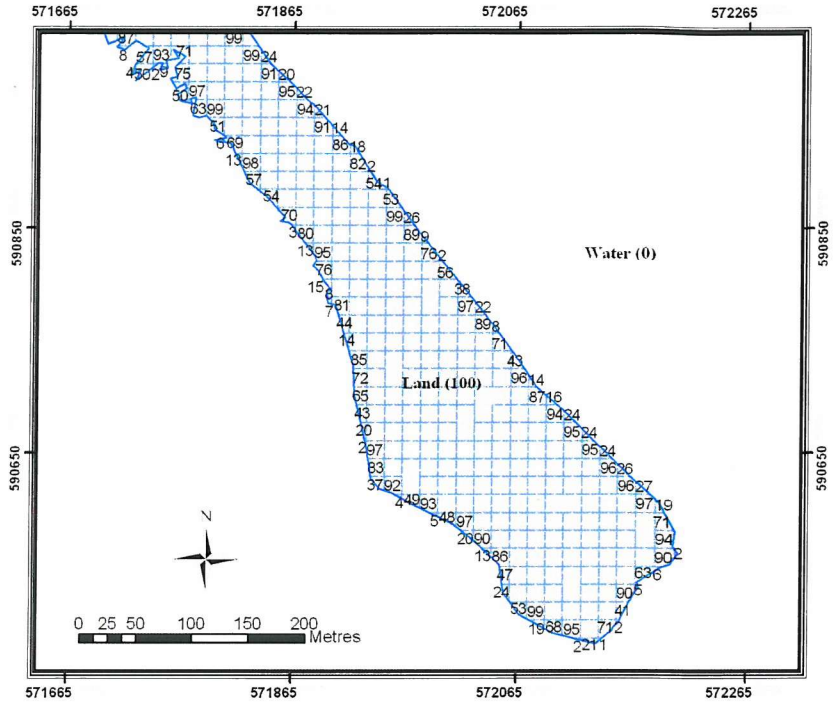

Figure 6.9: The map shows the actual percentage of land class within 16 m pixels. The grids shown are 16 m pixels, numbered by the percentage of land class within them.

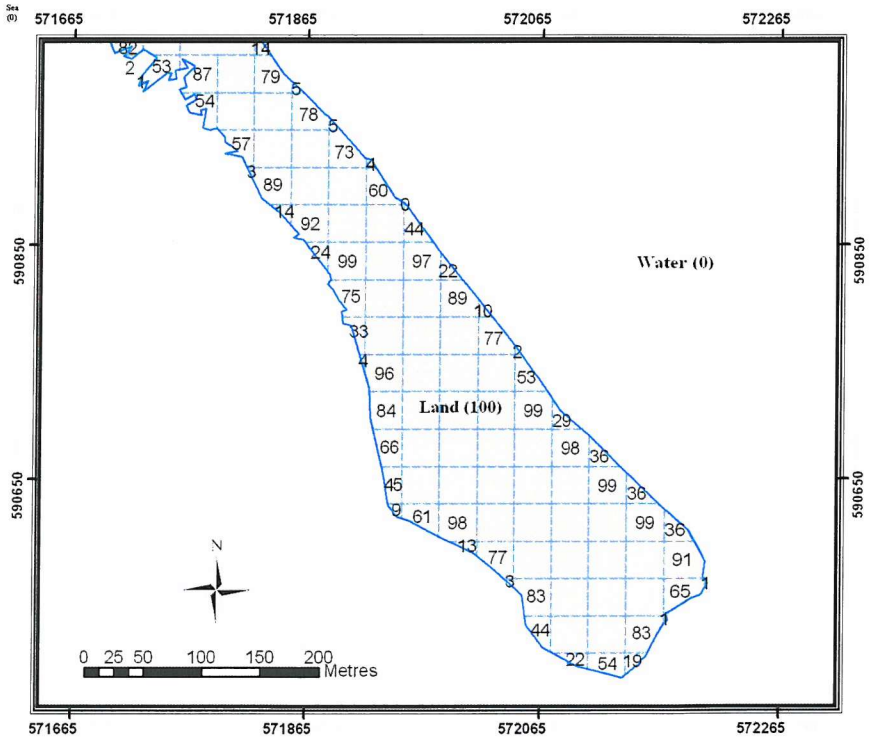

Figure 6.10: The map shows the actual percentage of land class within 32 m pixels. The grids shown are 32 m pixels, numbered by the percentage of land class within them.

6.3.6 Methods for mapping the shoreline from the soft classification

The output of the soft classification for each pixel was an estimate of the percentage cover of the component classes. This does not indicate where the sub-pixel component covers were located within the area represented by image pixel, information that is required in order to fit a class boundary at a sub-pixel scale.

Initially the soft classification outputs were converted from percentage values to fraction or proportion values to facilitate the shoreline mapping prediction process. Here, two approaches for locating the sub-pixel components were investigated. Before applying these techniques the fraction images need to be filtered to remove fraction information attributed to noise. These were removed using a specially designed filter.

6.3.6.1 Filtering the Soft classified imagery

Previously the soft classification result was determined to be highly correlated to the actual proportion values (r= 0.95). But these correlations were based on fraction values located close to the shoreline (section 6.3.5). Fraction values at pure pixels (0 and 1) still contained noise and may affect the sub-pixel mapping process. Therefore, before utilizing the soft classified imagery a filter had to be applied to remove noise from the imagery.

The aim of this process was to remove noise located in pure land and pure water classes while maintaining proportion information at pixels adjacent to the shoreline. Noise in the soft classified imagery causes pure classes (proportion 0 and 1) to be classified as pixels with small (near 0) or large (near 1) fraction values. This could be seen in Figure 6.8, where areas of pure land and water for both images still contains fraction values. Here pixels with estimated fraction values higher than 0.85

were classified as 1 and below 0.15 classified as 0. To ensure these fraction values were noise and not part of the shoreline the filter reclassifies these pixels only when summation of the surrounding pixels (within a 3 x 3 window) is smaller than 1.0.

An example of how this filter works is given in Figure 6.11. The example shows how the fraction value 0.02 (located in the centre of the selected 3 x 3 window) was reclassified as 0, because the summation of the surrounding pixels amounts to only 0.14. Removing noise from the soft classification helps the sub-pixel / super-resolution methods used in the following section produce accurate shoreline prediction.

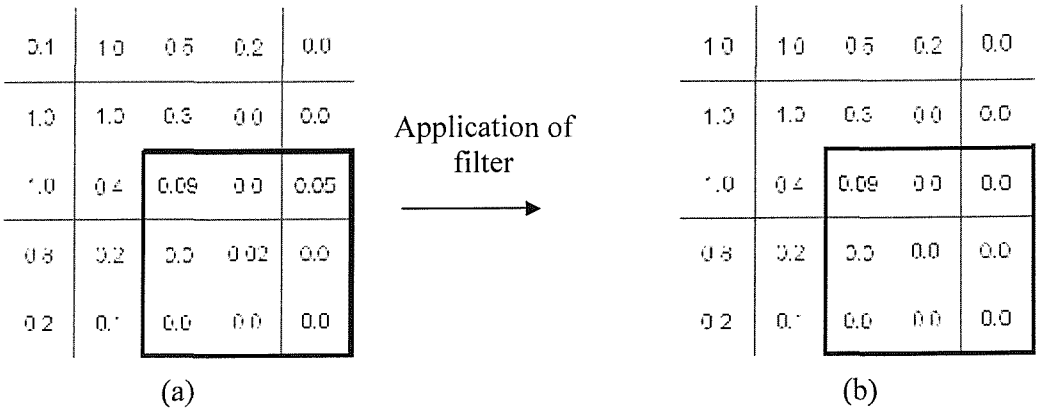

Figure 6.11: Example of filtering the fraction imagery to remove fraction information attributed to noise.

6.3.6.2 Contouring soft classified imagery

The filtering process removes noise that contaminates fraction values of the pure pixels. This allows the possibility of applying a contouring process to locate the shoreline with more accuracy. Since there was a simple geometrical arrangement of the two classes, the possibility of representing the shoreline by fitting a class membership contour through the soft classification was evaluated (Foody, 2002b). Specifically the shoreline was represented by fitting to the soft classification a contour of 0.5 membership to the land class, representing the 50% membership to land and 50% membership to water. An example of the process in shown in Figure 6.12. Result from contouring the soft classification is shown in Figure 6.13.

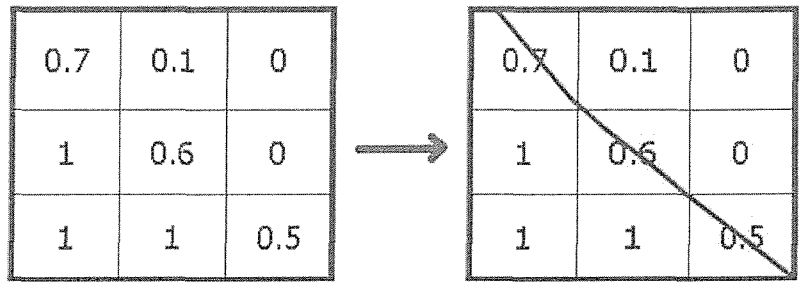

(a) (b)

Figure 6.12: The figure show the (a) initial fraction value and (b) contouring output

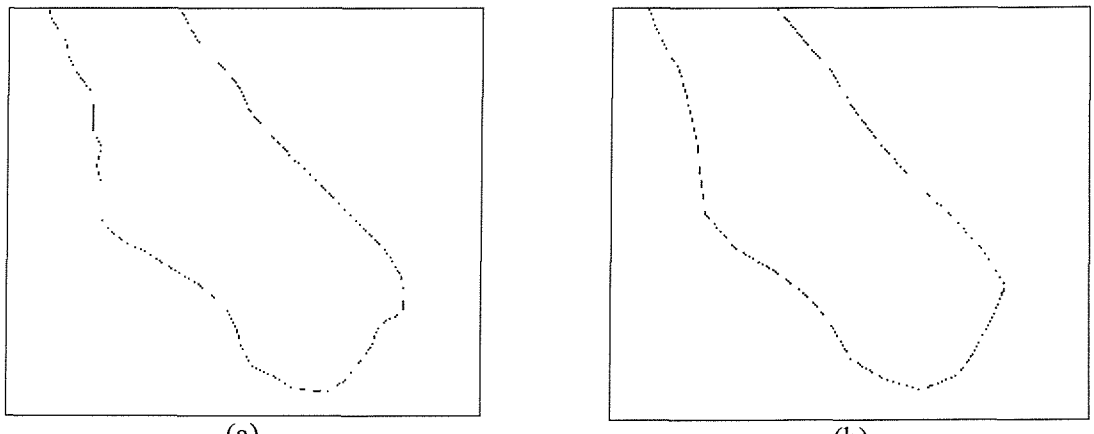

(a) (b)

Figure 6.13: Shoreline generated from contouring soft classification from the (a) 16 m spatial resolution imagery and (b) 32 m spatial resolution imagery.

6.3.6.3 Two-point histogram

Contouring the soft classification provides a first step into mapping the shoreline within pixel boundaries. But this method does not maintain the proportion information of the soft classification when designating the shoreline. For example in Figure 6.12, the proportion values were modified to in order to fit the contour. That is, the contour fitted to the soft classification was guided by the proportion information conveyed by the soft classification but the proportion either side of the fitted shoreline may not match those depicted in the soft classification as a result of the generalisation process involved in fitting the contour (Foody *et al.,* 2003). A refinement, therefore, was to use the contouring result to direct an approach in which the class proportion information contained in the soft classification is maintained. The final approach to estimating the shoreline was based on two-point histogram using a pixel swapping algorithm that was developed for super resolution land cover classification (Atkinson, 2003). The geo-statistical technique adopted here was designed to post-process a soft classification imagery and position the classes geographically at a sub-pixel scale.

The two-point histogram based approach was used to adjust iteratively the sub-pixel class composition estimates in the soft classification output to provide a super-resolution representation of the shoreline. This approach requires two sets of imagery, a soft classification output, to generate the representation of the shoreline and a training image (at a finer spatial resolution), as a target for the process. For this analysis the soft classified imagery was initially converted to hard classified sub-pixels, with the number of sub-pixels per class determined in proportion to the class proportion, maintaining the relative proportion of the class. Here, the analysis was undertaken using sub-pixels with a spatial resolution of 1 m. Thus for the 32 m simulated imagery, 32 x 32 m sub-pixels were created. As an example for a land pixel

value 0.25, 256 of the 1024 pixel are hard classified as land. These sub-pixels were initially distributed randomly throughout the area of the pixel that they are associated with. The training images used were based on the contouring of the soft classification outputs which were generated in section 6.3.6.2. The spatial resolution of these training images were 1 m similar to the target spatial resolution.

The optimization algorithm begins by comparing two-point histogram statistics between the initial imagery and its training image. A sub-pixel swap was then initialized, if the swap allocates the sub-pixel so that the initial imagery becomes closer to the training imagery it was maintained and the two-point histogram was updated. This process was repeated for every pixel and every sub-pixel until 70 iterations. An example of this process is shown in Figure 6.14.

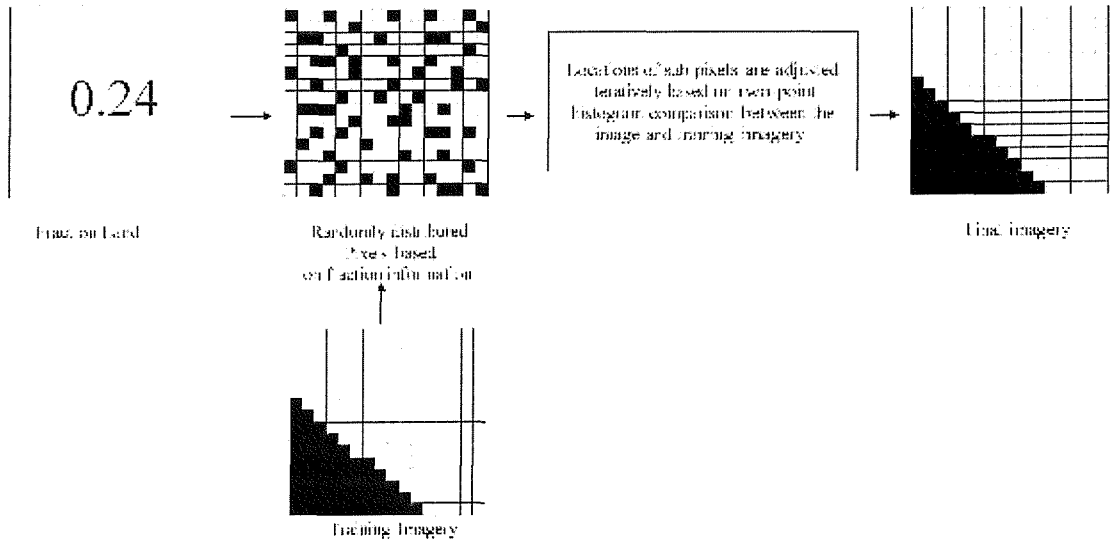

Figure 6.14: Illustration of the operation of the two point histogram method. The training imagery was generated from the contouring output.

This method ensures that the proportions of land and water predicted by the soft classifier were maintained while geographically locating sub-pixel regions of the classes in the area represented by a pixel (Atkinson, 2003). The outputs were later vectorised to produce shoreline map of the area. Figure 6.15 - Figure 6.18 shows the images involved in processing the coarse spatial resolution images to predict the shoreline location.

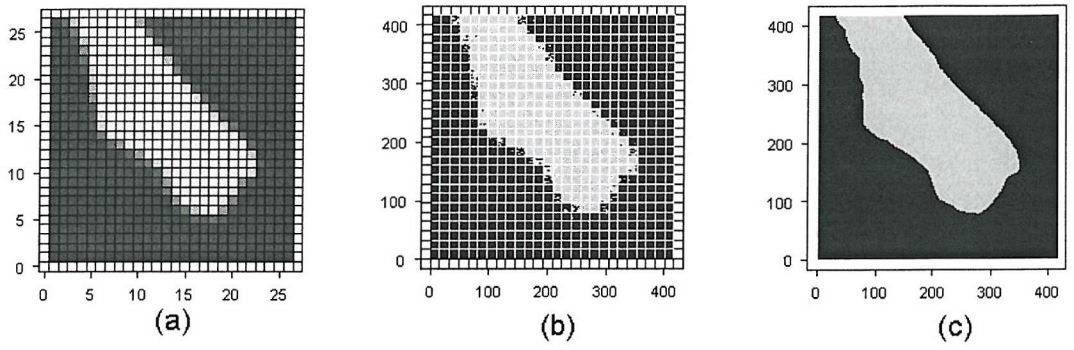

Figure 6.15 : (a) Soft classified imagery with proportion values, (b) imagery with randomly distributed 1 m sub-pixels, (c) Training Image. The grid represents the pixel spatial resolution of 16 m.

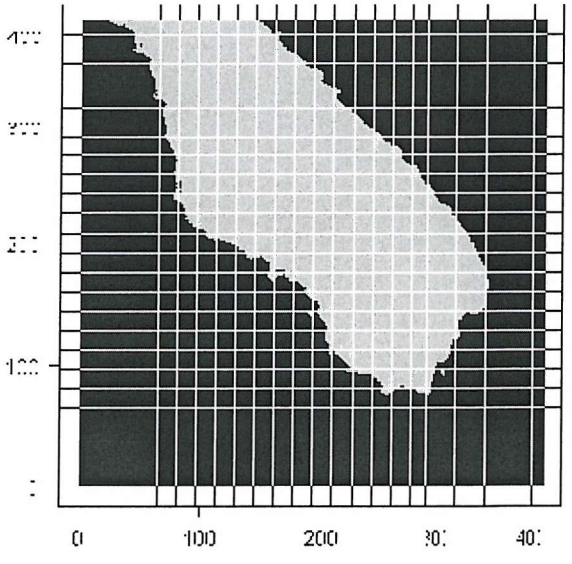

Figure 6.16: Shoreline prediction from the two-point histogram method based on the 16 m imagery. The grid represents the pixel spatial resolution of 16 m.

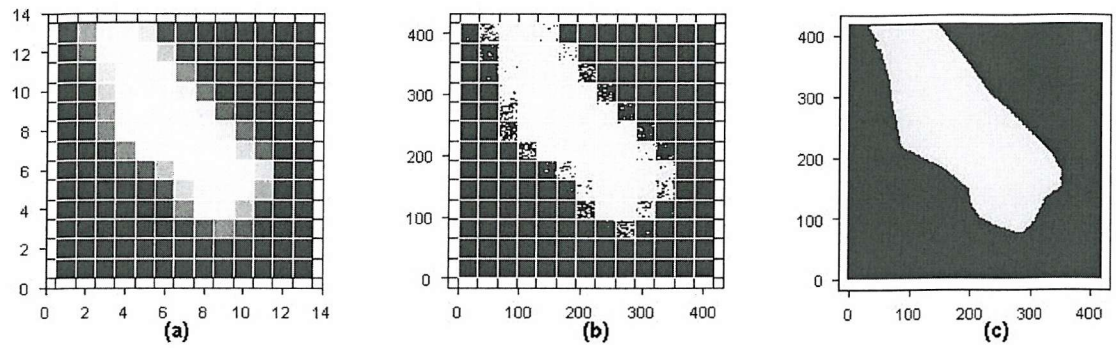

Figure 6.17: (a) Soft classified imagery with proportion values, (b) imagery with randomly distributed 1 m sub-pixels, (c) Training Image. The grid represents the pixel spatial resolution of 32m.

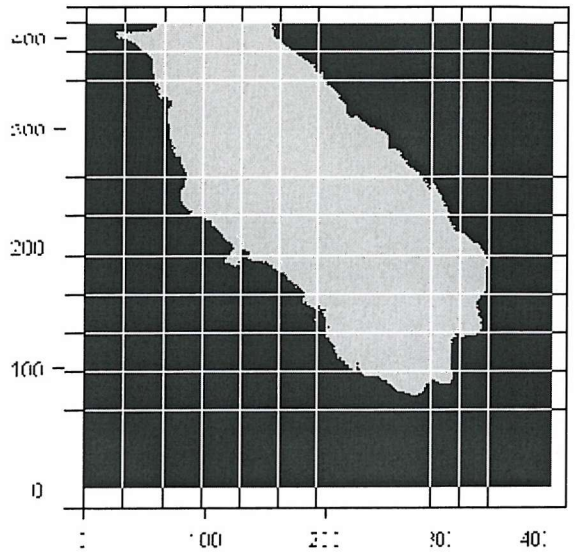

Figure 6.18: Shoreline prediction from the two-point histogram method based on the 32 m imagery. The grid represents the pixel spatial resolution of 32 m.

6.4 Positional error analysis in shoreline prediction

To analyse the positional accuracy at the 4 sites (Figure 6.2), the accuracy of the 4 methods were determined by comparing their positional location to the actual location determined by hard classifying 1 m imagery of the areas. An overlay of the predicted shoreline over the actual shoreline and a graph representing the errors in position along the shoreline (for the 4 test sites) are given in Figure 6.19 to Figure 6.26. Information

regarding the graphing technique used to display errors along the shoreline were given in section 4.2.6.

6.5 Results and analysis.

This section shows the accuracy of shoreline prediction obtained by the 4 methods. The results are divided based on the 4 test sites defined in section 6.2.

6.5.1 Results

This research examined 4 different methods in predicting the shoreline location from coarse spatial resolution imagery. The 4 methods were applied at 4 portions of shoreline with 2 different spatial resolutions (16 and 32 m). Due to the amount of results generated a standardise method of calculation positional errors needed to be established. This was done but determining the positional errors along every metre of the shoreline and calculating the RMSE. The results for the 16 and 32 m images are shown in Table 6.1 and 6.2 respectively.

Table 6.1: RMSE (m) in shoreline mapping from the four methods using 16 m spatial resolution simulated imagery.

	RMSE (m)			
Location	Hard Classified	Contouring	Two point Histogram	Wavelet Interpolation
Area I	3.16	1.17	1.20	1.74
Area II	4.25	4.72	1.34	2.53
Area III	3.67	1.29	1.15	2.97
Area IV	3.49	2.82	2.08	1.32

Table 6.2: RMSE (m) in shoreline mapping from the four methods using 32 m spatial resolution simulated imagery.

	RMSE (m)			
Location	Hard Classified	Contouring	Two point Histogram	Wavelet Interpolation
Area I	6.71 m	0.98 m	1.71 m	5.72 m
Area II	8.67 m	6.42 m	2.62 m	6.13 m
Area III	8.13 m	4.83 m	2.46 m	6.15 m
Area IV	5.73 m	6.75 m	5.11 m	4.32 m

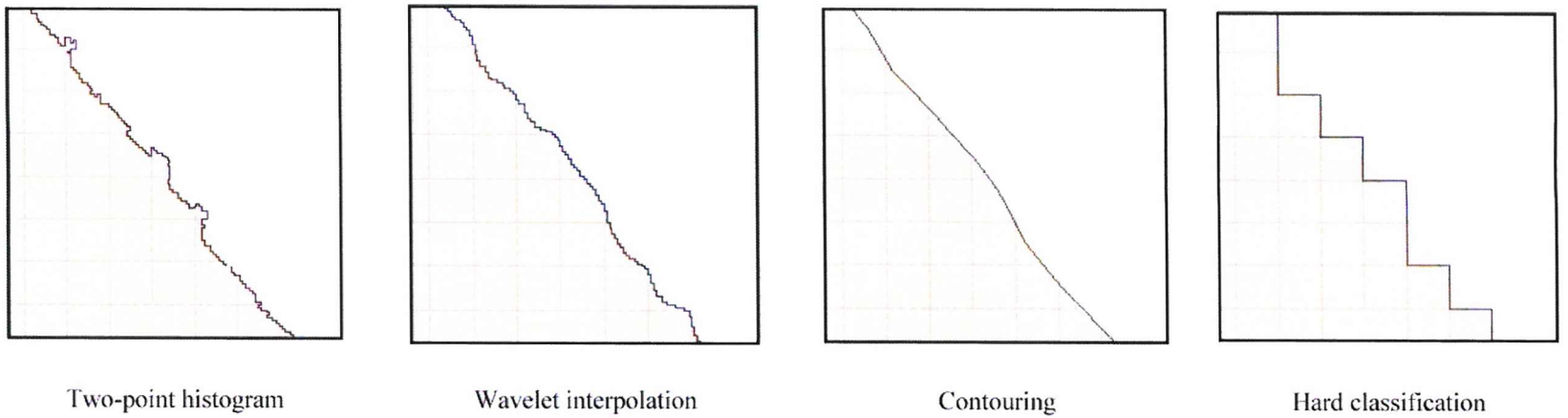

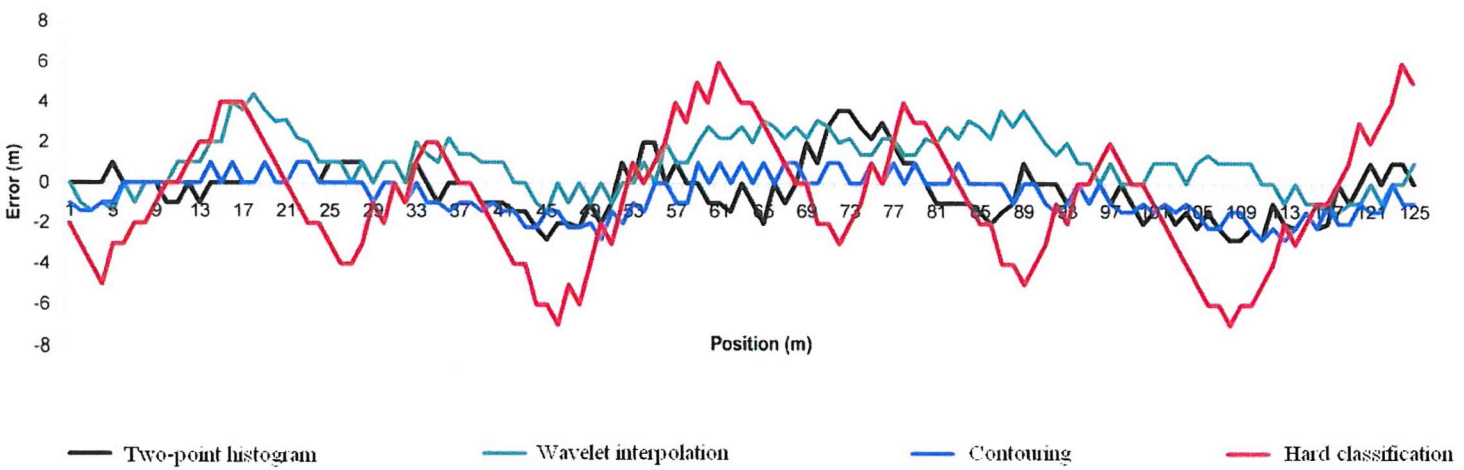

Figure 6.19: Shorelines generated from 16 m imagery of Area I. Actual land area is shown in orange with the pixel spatial resolution represented by the square grid. Shorelines generated by the 4 methods are shown in red. A graph showing positional errors along the shoreline is shown below the prediction. Positive errors represent error seawards while negative errors represent errors landwards.

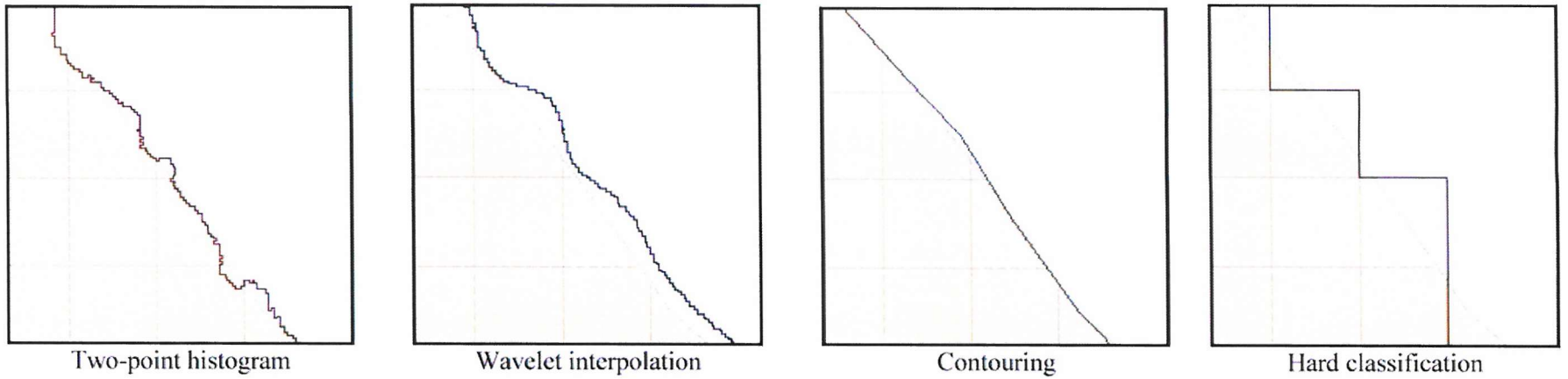

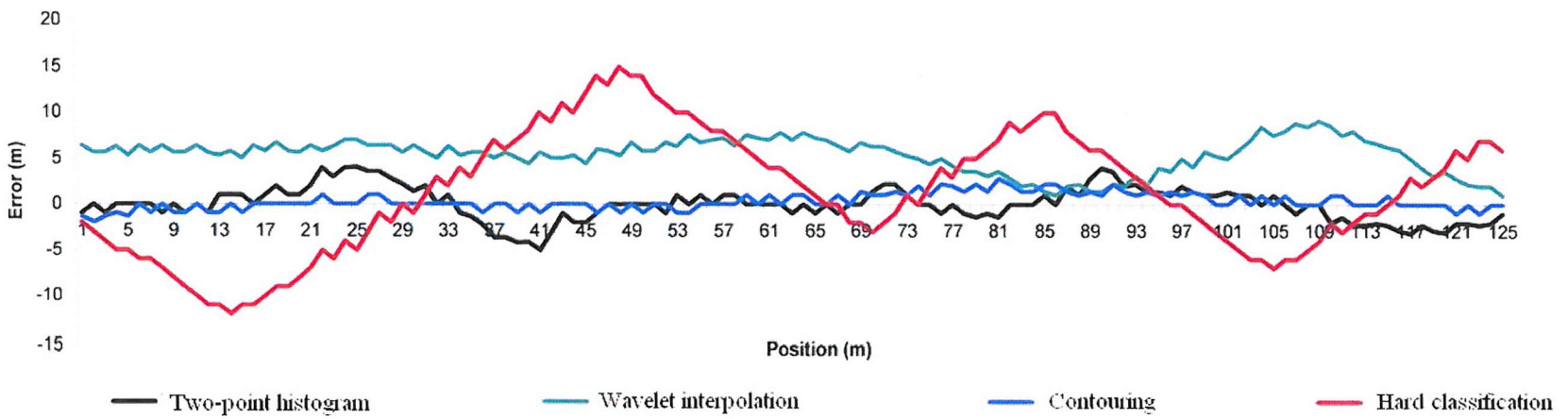

Figure 6.20: Shorelines generated from 32 m imagery of Area I. Actual land area is shown in oarnge with the pixel spatial resolution represented by the square grid. Shorelines generated by the 4 methods are shown in red. A graph showing positional errors along the shoreline is shown below the prediction. Positive errors represent error seawards while negative errors represent errors landwards.

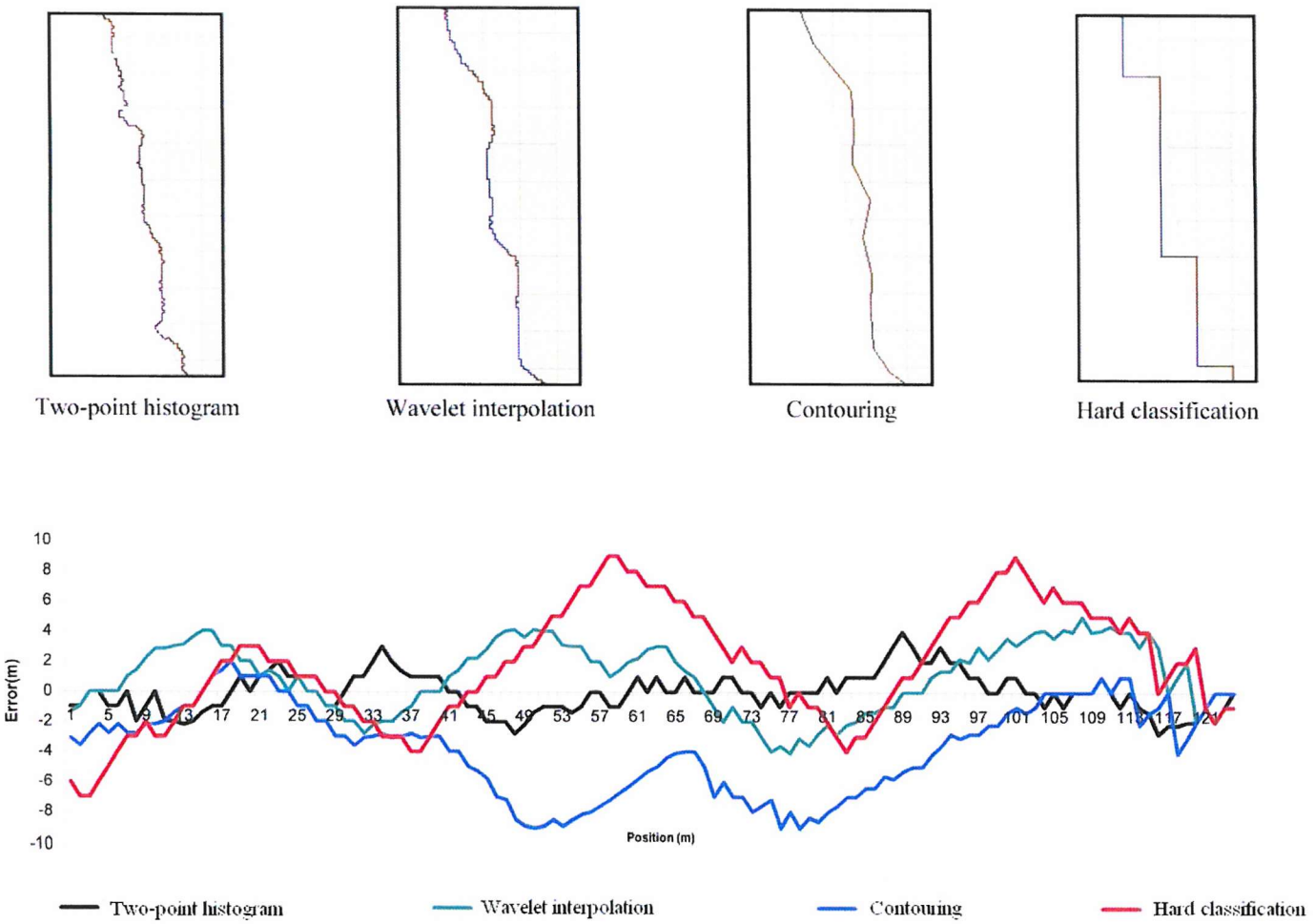

Figure 6.21: Shorelines generated from 16 m imagery of Area II. Actual land area is shown in orange with the pixel spatial resolution represented by the square grid. Shorelines generated by the 4 methods are shown in red. A graph showing positional errors along the shoreline is shown below the prediction. Positive errors represent error seawards while negative errors represent errors landwards.

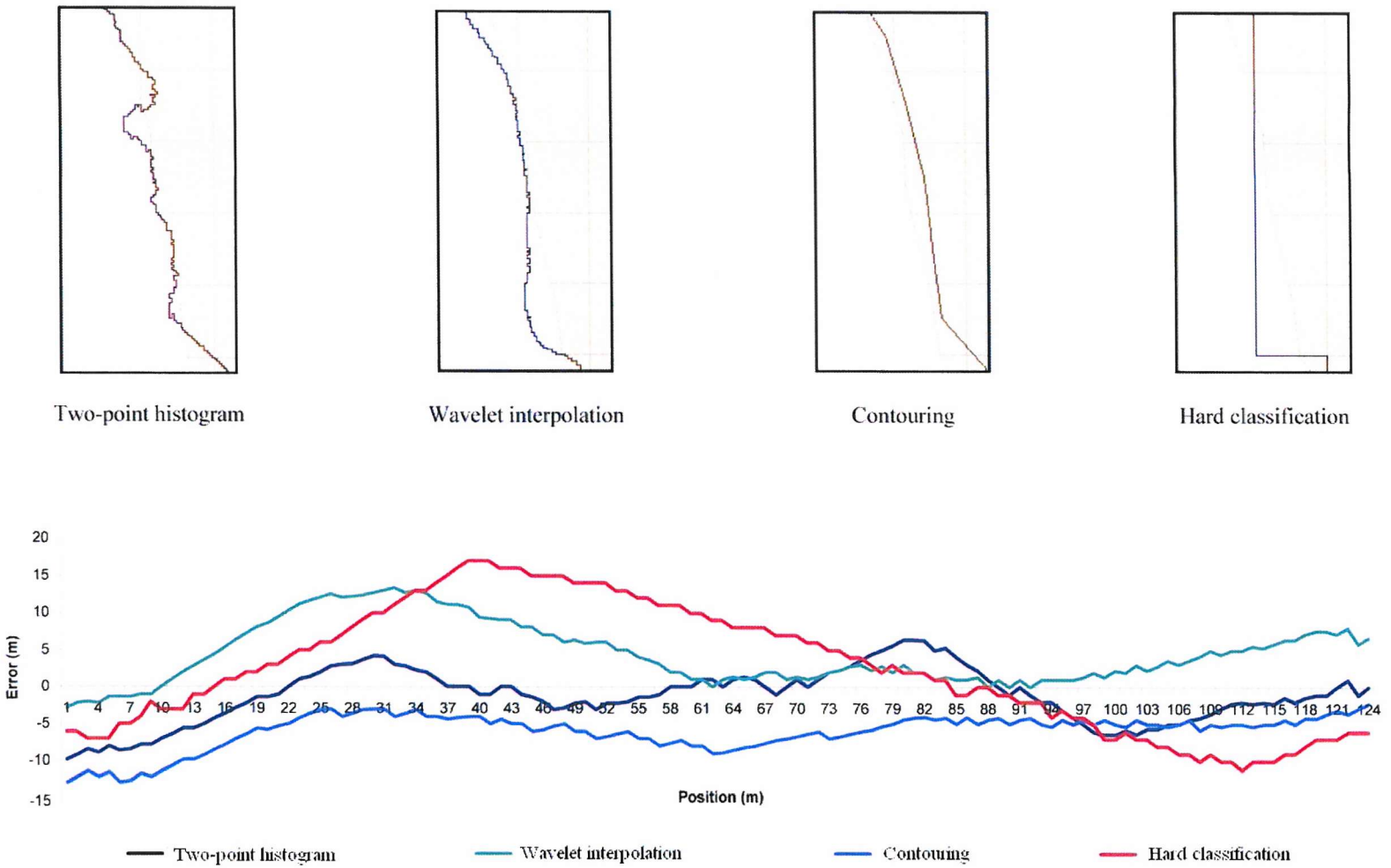

Figure 6.22: Shorelines generated from 32 m imagery of Area II. Actual land area is shown in orange with the pixel spatial resolution represented by the square grid. Shorelines generated by the 4 methods are shown in red. A graph showing positional errors along the shoreline is shown below the prediction

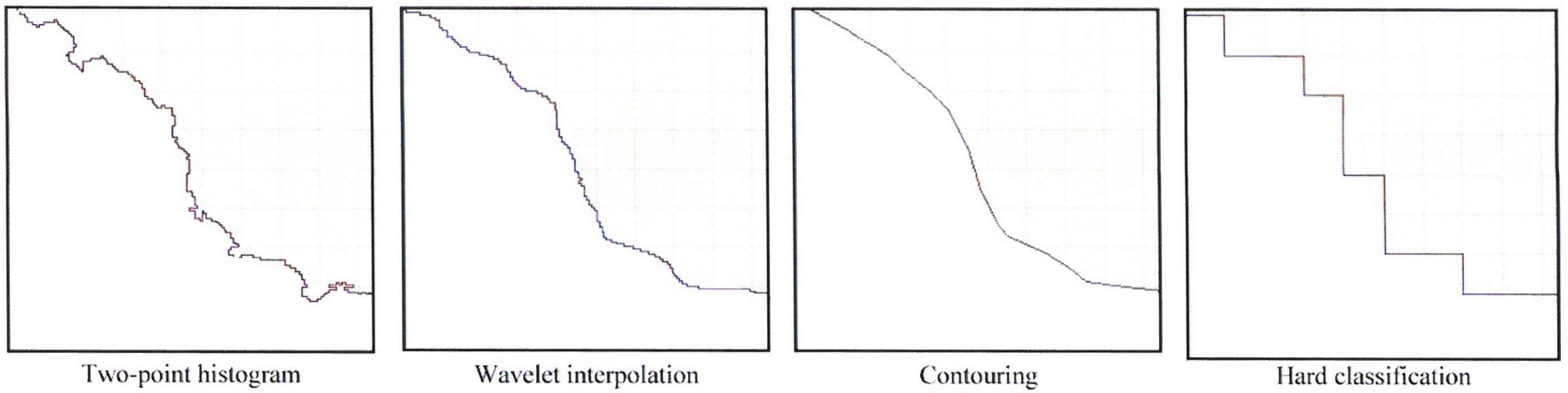

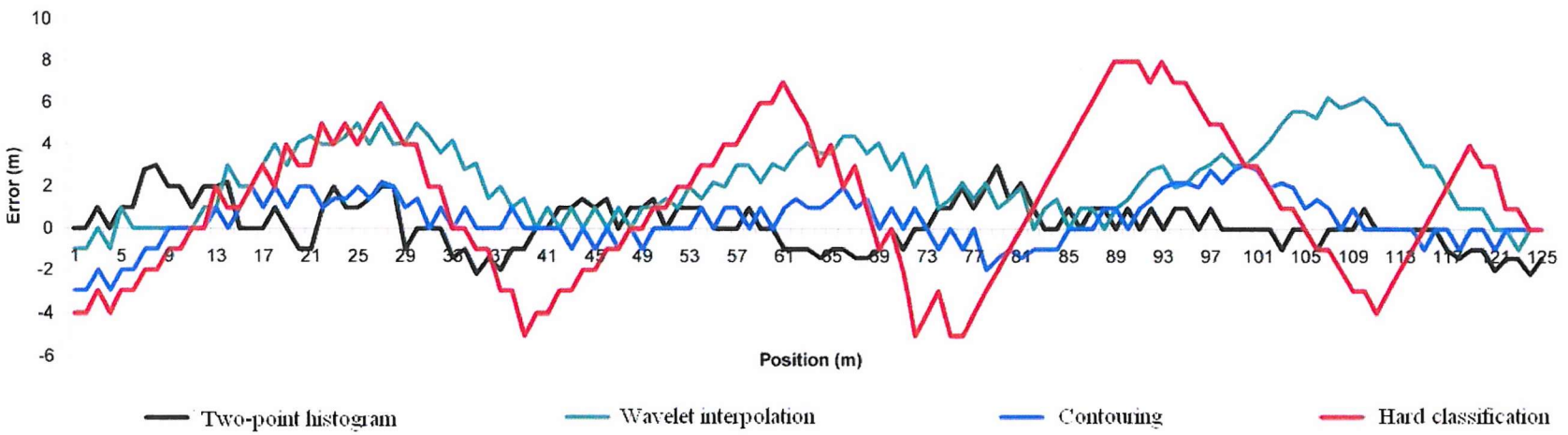

Figure 6.23: Shorelines generated from 16 m imagery of Area III. Actual land area is shown in orange with the pixel spatial resolution represented by the square grid. Shorelines generated by the 4 methods are shown in red. A graph showing positional errors along the shoreline is shown below the prediction. Positive errors represent error seawards while negative errors represent errors landwards.

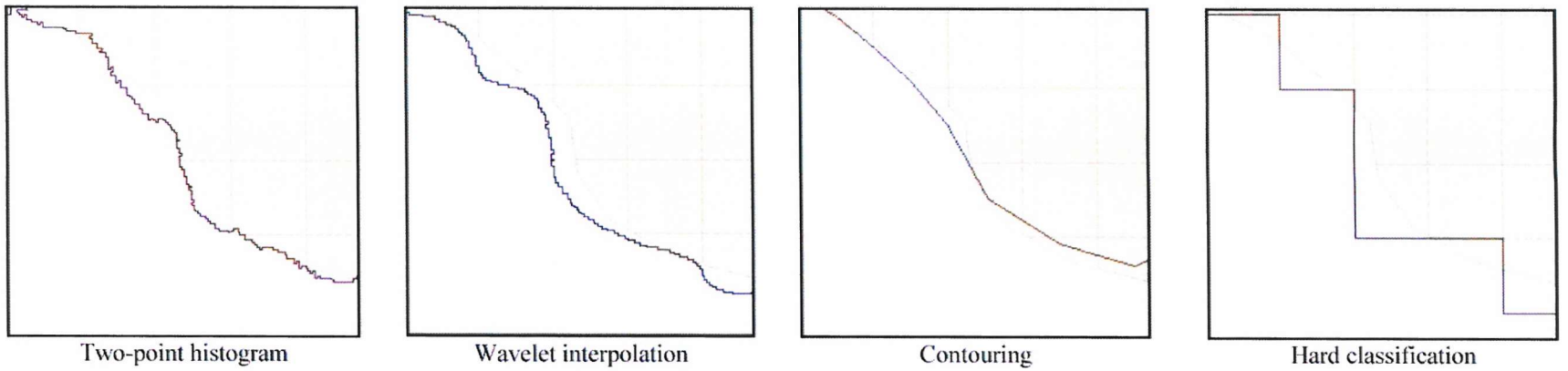

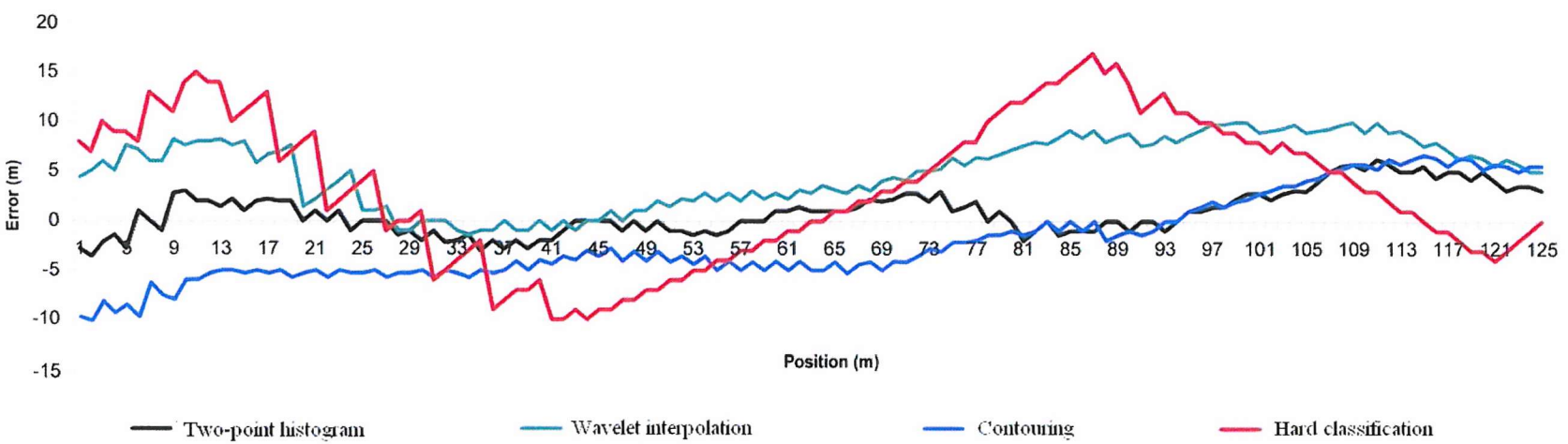

Figure 6.24: Shorelines generated from 32 m imagery of Area III. Actual land area is shown in orange with the pixel spatial resolution represented by the square grid. Shorelines generated by the 4 methods are shown in red. A graph showing positional errors along the shoreline is shown below the prediction. Positive errors represent error seawards while negative errors represent errors landwards.

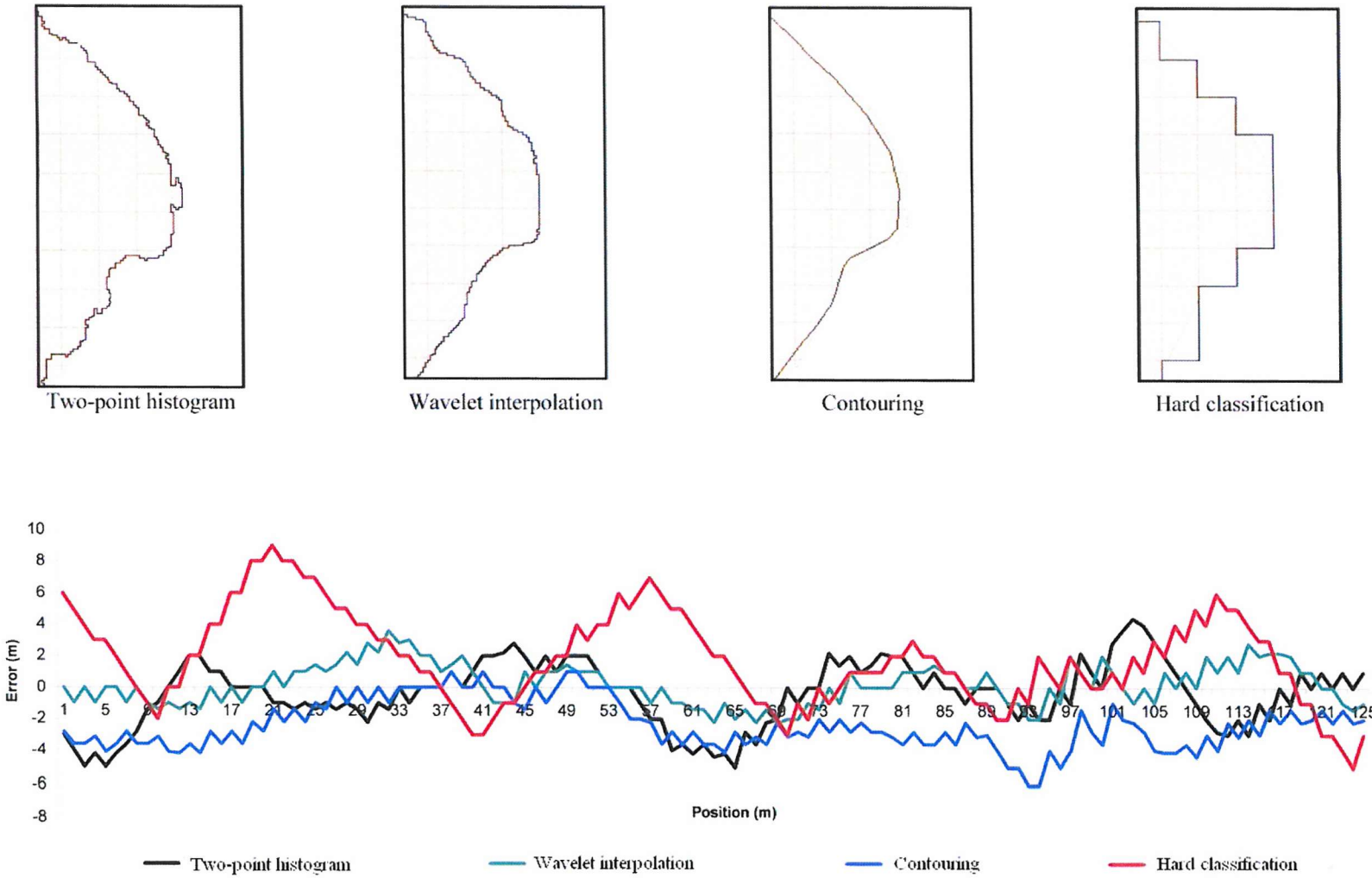

Figure 6.25: Shorelines generated from 16 m imagery of Area IV. Actual land area is shown in orange with the pixel spatial resolution represented by the square grid. Shorelines generated by the 4 methods are shown in red. A graph showing positional errors along the shoreline is shown below the prediction. Positive errors represent error seawards while negative errors represent errors landwards.

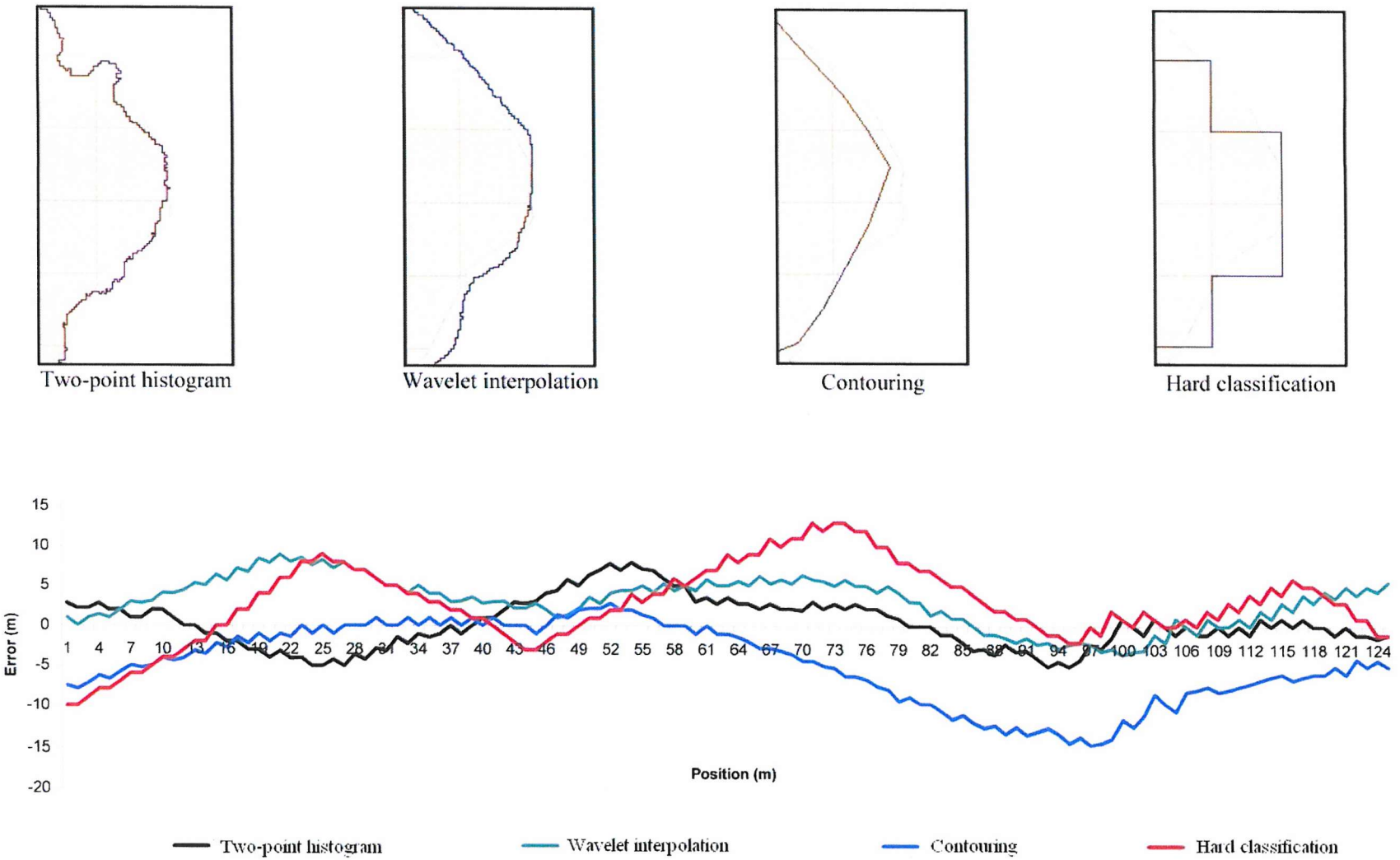

Figure 6.26: Shoreline generated from 32 m imagery of Area IV. Actual land area is shown in orange with the pixel spatial resolution represented by the square grid. Shoreline generated by the 4 methods are shown in red. A graph showing positional errors along the shoreline is shown below the prediction. Positive errors represent error seawards while negative errors represent errors landwards.

6.5.2 Analysis

This section analysed the effects of different types of shoreline orientation and spatial resolution on predicting the shoreline location. Generally, shoreline prediction from the 4 methods were the most accurate when predicting linear shoreline (Area I). While in other areas the results were mixed with the shoreline prediction derived from contouring and hard classification the least accurate in Area II and the prediction derived from wavelet interpolation were the least accurate in Area III. An analysis on the accuracy of the shoreline prediction derived from the 4 methods based on the 4 test sites are given in the following section.

Results show that when the methods are ranked from the best to worst based on accuracy of their predictions there is a similar order for both the 16 and 32 m spatial resolution. For example in Area 1, the prediction derived from contouring method was the most accurate at both the 16 and 32 m spatial resolution. Therefore, these analyses emphasised the result from the 16 m spatial resolution imagery, taking into account that an analysis for the 32 m spatial resolution imagery would be similar. Analyses on the effects of spatial resolution (between 16 m and 32 m images) are explained in a later section.

6.5.2.1 Area I (Linear across pixel orientation)

For linear shorelines that are positioned across pixel orientation (Area I), all of the methods used were able to predict the shoreline position to within an RMSE of 3.16 m for the imagery simulated to a spatial resolution of 16 m and 6.71 m for the imagery simulated to a spatial resolution of 32 m. As expected, the largest errors were observed with the shoreline predicted from the hard classification method in which the shoreline was constrained to lie between pixels and had a jagged shaped. Moreover only, 54.4 %

of the shoreline predicted was within 2 m of the actual shoreline and the RMSE calculated along the 125 m test site was 3.16 m for the simulated 16 m spatial resolution imagery. The results indicated that shoreline prediction based on sub-pixel analyses produces smoother and more accurate shorelines than that derived from hard classification.

The shorelines generated from the application of the contouring, wavelet interpolation and two-point histogram methods were accurate, but the contouring method produced the most visually realistic representation of the shoreline with 89.6% of the shoreline prediction positioned within 2 m of the actual shoreline. Although the estimated accuracy of the shoreline derived from contouring method was better than that derived from other methods, the proportion information from soft classification was not maintained. A method that maintains this information, the two-point histogram method, however was only able to predict the shoreline to within an RMSE of 1.20 m. This could be attributed to inaccuracies in the soft classification and the generalization process during contouring (for the contouring method) reposition the shoreline prediction closer to the actual shoreline in comparison to the prediction from the two-point histogram method. The prediction generated from the wavelet interpolation method was not as accurate as two-point histogram and contouring method with an RMSE of 1.74 m and only 74.4 % of the shoreline prediction positioned within 2 m of the actual shoreline.

6.5.2.2 Area II (Linear along pixel orientation)

In Area II where the shoreline was linear but oriented nearly parallel with the column of the pixel grid, the accuracy varied greatly between the methods used. The shoreline prediction from the hard classification was again the least accurate and that derived from two-point histogram the most accurate. The two-point histogram method

produced shoreline position prediction with an RMSE of 1.34 m for the 16 m imagery with 89.0 % of the shoreline within 2 m of the actual shoreline. The shoreline prediction derived from contouring the soft classification method was not as accurate as in Area I. Although the shoreline from the contouring method was smooth and linear but it was positioned a few metres to the east of the actual shoreline. Here the generalization of proportion values required when fitting the contour (hence modifying pixel proportion values) introduces error when positioning the shoreline prediction, resulting in an RMSE of 4.72 m with only 32.8 % of the shoreline within 2 m of the actual shoreline. The accuracy of shoreline prediction derived with the wavelet interpolation method relies on the orientation of the shoreline and the wavelet function selected, in this case a Haar wavelet function (Donoho, 1992). From visual observation of the wavelet interpolation method shoreline prediction, it could be deduced that generally accuracy increases when the shoreline was aligned exact parallel to the column of the pixel grid and decreases even with a slight change in alignment. As shoreline in this area was not exactly aligned to the column of the pixel grid, accuracy of shoreline prediction from the wavelet interpolation method were not as accurate as two-point histogram method with only 52.0 % of the shoreline located within 2 m of the actual shoreline in comparison to 89.0 % for two-point histogram method.

6.5.2.3 Area III (Slightly curved).

In Area III, two-point histogram again produced the most accurate prediction of the shoreline position, followed closely by contouring of the soft classification with RMSE of 1.15 m and 1.29 m respectively for 16 m imagery. These two methods rely on the accuracy of the soft classification to predict the shoreline location, however inaccurate proportion information affect the two-point histogram more as the proportion information was maintained. The contouring method modified these values to fit a

contour to the shoreline which could result in increased accuracy (such as in Area I) or decreased accuracy. With accurate proportion information the two-point histogram method was able to accurately predict the shoreline with 94.4 % of the shoreline positioned within 2 m of the actual shoreline. Contouring of the soft classification produced similar accuracy but as contouring linearly divides pixels in two at the predicted shoreline position the shoreline produced was visually unrealistic. An example of this process was shown in Figure 6.13. Moreover only 89.6 % lies within 2 m of the actual shoreline which was lower than the accuracy achieved by two-point histogram method. In this area wavelet interpolation produces curved shoreline prediction similar to Area II. The method obtained an RMSE of 2.97 m with only 48.8 % of the shoreline positioned within 2 m of the actual shoreline. The hard classification method produced the worst prediction with an RMSE of 3.67 m with only 42.2 % positioned within 2 m of the actual shoreline.

6.5.2.4 Area IV (Sharply curved)

In Area IV, shoreline predictions from the four methods were not as accurate as in the other areas. The shoreline prediction derived from the wavelet interpolation method was the most accurate followed closely by two-point histogram method. Prediction from two-point histogram was not as accurate as before because the proportion information for this particular area was not as accurate as in area I, II and III. The correlation coefficient derived for the relationship of predicted against actual land image in the soft classification differed between the areas (16 m imagery); Area 1 = 0.986, Area II = 0.960 Area III = 0.980 and Area IV 0.940. Even though the difference is not large the shoreline prediction accuracy generally increases when the correlation between the actual and predicted coverage of a class from soft classification is accurate (Table 6.1 and 6.2). The two-point histogram method was,

however still within an RMSE of 2.08 m with 74.4 % located within 2 m of the actual shoreline. The wavelet interpolation method does not rely on results from soft classification when predicting the shoreline position, thus its shoreline prediction were the most accurate with an RMSE of 1.32 m and 90.4 % of the shoreline located within 2 m of the actual shoreline. As with Area III the contouring method predictions were visually unrealistic and positioned a few metres to the west of the actual shoreline position. This could again be attributed to contouring modifying the proportion values when allocating shoreline position resulting in an RMSE of 2.82 m.

6.5.2.5 Effects of spatial resolution.

In all of the areas the effect of spatial resolution was very similar. The accuracy of the shoreline prediction decreased with a coarsening of spatial resolution. For the shoreline prediction derived from hard classification the errors generally doubled at the 4 training sites when the spatial resolution was decreased. This was expected as the spatial resolution was decreased from 16 m to 32 m, increasing the pixel size. With an increase of pixel size, more pixels along the shoreline would have a mixed class composition (land and water). When these pixels are classified to either land or water, the shoreline prediction were derived along the pixels edges resulting in more errors in comparison to the prediction derived from the 16 m spatial resolution simulated imagery.

In the wavelet interpolation method accuracy seems to be affected more by the shape of the shoreline mapped than spatial resolution. But generally accuracy does decrease with coarser spatial resolution. Similarly to wavelet interpolation, there was no general trend observed in the results of the contouring method. Although the accuracy of shoreline prediction generally did decrease at coarser spatial resolution the shape of shoreline and accuracy of the proportion information from soft classification

had a greater effect. In Area I where the correlation coefficient derived for the relationship of predicted against actual land image in the soft classification were better for 32 m imagery than 16 m imagery, contouring produced an accurate result at 32 m spatial resolution.

In the two-point histogram method errors in shoreline prediction in Area I and Area III increased by approximately 40 % when the spatial resolution was changed from 16 to 32 m. In Area II and IV the error in the predicted shoreline positions nearly doubled. The differences in errors could be attributed to the accuracy of the proportion information derived from the soft classification as the correlation between the predicted proportion and actual proportion decreased when the spatial resolution was decreased to 32 m.

6.6 Conclusions

The shoreline cannot be represented appropriately in a conventional approach to thematic mapping based on a hard classification. However, by predicting the thematic composition of a pixel by applying a soft classification may help locate the shoreline position at a sub-pixel scale. This allows super-resolution mapping, mapping at scale finer than the spatial resolution of the data used, which can provide more accurate and realistic thematic representations. This was illustrated with the mapping of the shoreline from 16 and 32 m spatial resolution data. The conventional hard classification provided a visually poor and inaccurate representation of the shoreline. A superior representation, in terms of visual appearance and RMSE, was derived from each of the three super-resolution mapping approaches used. The two-point histogram approach generally gave the most accurate prediction of the shoreline with an RMSE of below 2.10 m for 16 m imagery and 5.11 for 32 m imagery. This method produce

accurate prediction of the shoreline irrespective of its shape but the accuracy decreased with increasing curvature of the shoreline.

To further increase the accuracy of the shoreline prediction this research looks at methods of increasing the accuracy of the soft classification. To predict the class composition within a pixel this research used four land and four water training sites (Figure 6.4) which were selected throughout the image. The average (Global) statistics from these sites were later used to define the end point of the sigmodial function used in the soft classification process. To increase the accuracy of the soft classification further analysis was conducted, based on these training sites a localised approach for soft classification was explored. This approach is explained in chapter 7.

These results indicate the considerable potential of super-resolution mapping techniques for accurate mapping of the shoreline from simulated coarse resolution satellite sensor imagery. However, to apply these methods to actual satellite sensor imagery such as images from Landsat TM and SPOT HRV several additional considerations need to be addressed. These considerations include the errors inherent in the transforming or geo-referencing the coarse spatial resolution data to the Malaysia RSO projection. Further research needs to be done to quantify the effect of image transformation on the accuracy of the predictions. This was not done in this thesis due to time limitations.

7 Localised soft-classification for Sub-pixel mapping

7.1 Introduction

In chapter 4 and 6 techniques for mapping the shoreline from coarse spatial resolution satellite sensor imagery were introduced. The results showed that by applying a soft classification to a coarse spatial resolution imagery to predict the class composition within a pixel and applying super-resolution techniques to position these classes geographically, an accurate prediction of the shoreline was possible. But the accuracy varied based on shoreline orientation and could be attributed to inaccuracies in the class composition prediction. Therefore, there is a need to increase the accuracy of the soft classification.

This chapter introduces a soft classification approach based on localised training statistics to increase the class composition prediction and ultimately the accuracy of the shoreline predictions. Another super resolution approach was also introduced to complement the two-point histogram method. The simulated 16 m spatial resolution imagery derived in chapter 5 was used as the base for this analysis.

In chapter 6 the soft classification process used global statistics to define the sigmodial class membership function used to classify the data. These global statistics were derived by averaging the statistics obtained from 4 homogenous land and 4 homogenously water sites (Figure 6.4). Here, the application of local training statistics was examined. Thus, for a specific portion of the shoreline only the closest land and

water training sites were used to define the sigmodial class membership function used to classify the data.

7.2 Methods and analysis

This section describes a soft classification approach based on local training statistics and a super-resolution mapping technique based on pixel swapping. Other methods such as contouring and two-point histogram were already discussed in chapter 4 and 6.

The analysis would compare super-resolution shoreline prediction results obtained by using localised and global training statistics.

7.2.1 Soft classification

To increase the accuracy of the thematic class composition this work implements a soft classification that uses localised training statistics. It needs to be pointed out the soft classification function (sigmodial) and training sites used are the same as in chapter 6.

The soft classification approach applied in chapter 6 used the conventional approach where all the training sites for a class were used to define a single global description of the class. The use of such global training statistics yielded an accurate soft classification, with a correlation coefficient between predicted and actual class cover of 0.95 ($p < 0.05$). For each class, it was apparent that the spectral response observed varied between the training sites (Table 7.1). Given this spectral variation, the global training statistics may provide an inappropriate description of each class locally. Therefore a soft classification approach based on localised training statistics were required.

Here, a localised approach was assessed in which the training statistics from the four training areas for each class were used separately in soft classification. For

this, individual land and water training sites were used in classifying a specific pixel (Figure 7.1). Thus, for a specific portion of the shoreline only the closest land and water training sites were used to define the sigmodial class membership function used to classify the data.

Table 7.1: Summary of average spectral response for each class at each training sites (Figure 7.1)

Training sites	Spectral response	
	Land	Water
Land 1 / Water 1	193.44	33.00
Land 2 / Water 2	184.33	37.78
Land 3 / Water 3	160.33	42.89
Land 4 / Water 4	147.33	16.22
Average	171.36	32.47
Std Dev.	21.25	11.56

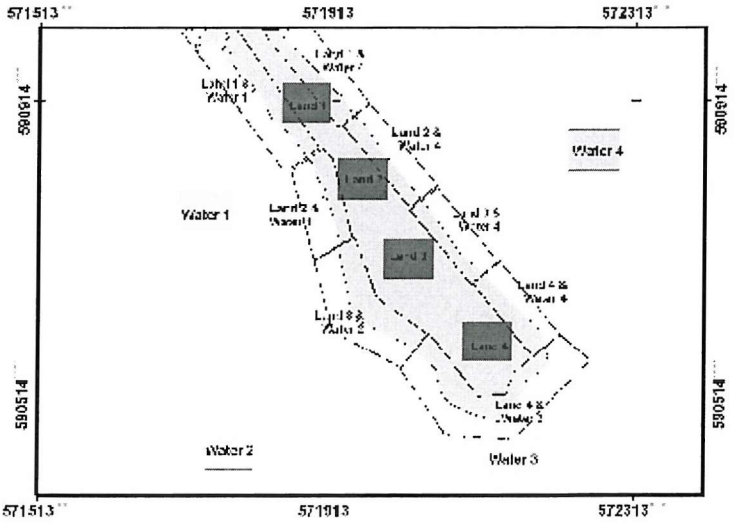

Figure 7.1 Division of shoreline by training sites used for localised soft classification.

Using a sigmodial function the coarse spatial resolution imagery was soft classified based on the localised training sites. The fraction image (land) obtained from the local soft classification is shown in Figure 7.2.

The accuracy of the soft classification was assessed through a comparison of the predicted coverage of a class with that derived from the ground data (Figure 6.5). The predicted coverage and ground data were correlated, with an r value of 0.98 ($p < 0.05$). This was larger than the estimate derived from a classification derived with global training sites which had an r value of 0.95 ($p < 0.05$) (chapter 5). The relationship between the predicted and actual fraction of land from soft classification derived using local statistics is shown in Figure 7.3.

Therefore, the soft classification derived with the use of local training statistics was more accurate than that derived from the use of global statistics.

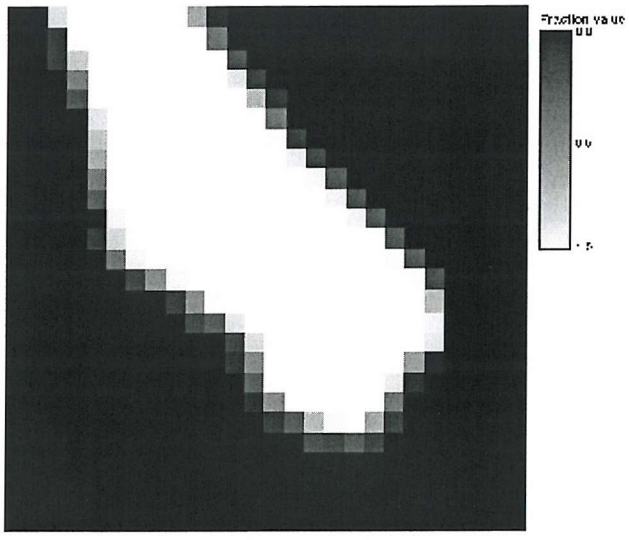

Figure 7.2: Soft classification output obtained from the use of localised training statistics. The greyscale shows the fraction of land.

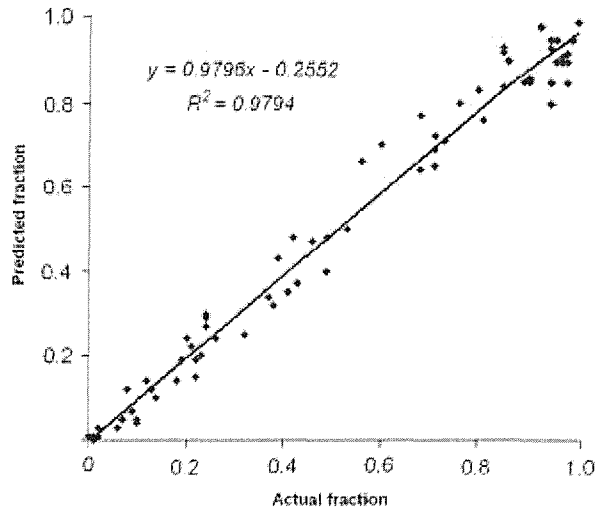

Figure 7.3: Relationship between the predicted and actual fraction of land from soft classification derived using local statistics.

7.2.2 Sub-pixel mapping

The outputs of the soft classification are fraction values representing the proportional cover of a class within each pixel. Since soft classification does not indicate where the sub-pixel components are located within each image pixel, sub-pixel scale approaches to locating the shoreline were investigated. In this analysis two methods of sub-pixel mapping were applied, the pixel swapping and two-point histogram methods. The two-point histogram approach would only be briefly explained here as it was already introduced in chapter 4 and 6. Soft classification results by using localised training sites and global training sites (derived in chapter 6) were used for the analysis.

7.2.2.1 Pixel-swapping

To complement the two point histogram method this chapter introduces a pixel-swapping algorithm (Atkinson, 2004). The objective of the algorithm is to vary the spatial arrangement of the sub-pixels in such a way that the spatial correlation between neighbouring sub-pixels is *maximized* given that the overall proportional composition within a pixel could not vary. The pixel-swapping algorithm comprised three basic

steps. First, for every sub-pixel the attractiveness A_i of the location is predicted as a distance weighted function of its neighbour:

$$A_i = \sum_{j=1}^{n} \lambda_{ij} z(u_j) \qquad 7\text{-}1$$

Where n is the number of neighbours, $z(u_j)$ is the value of the class z at the jth pixel location U_j and λ_{ij} is a distance-dependent weight predicted as :

$$\lambda_{ij} = \exp\left(\frac{-h_{ij}}{a}\right) \qquad 7\text{-}2$$

where h_{ij} is the distance between the pixel location i for which the attractiveness is desired u_i and the location j of the neighbour u_j, and a is the non-linear parameter of the exponential model.

Second, once the attractiveness of each sub-pixel location has been predicted based on the current arrangement of sub-pixel classes the optimization algorithm ranks the scores on a pixel-by-pixel basis. For each pixel, the least attractive location currently allocated to a '1' (i.e., a '1' surrounded mainly by '0's) is stored. Similarly, the most attractive location currently allocated to a '0' (i.e., a '0' surrounded mainly by '1's) is also stored. Third, sub-pixel classes are swapped if the attractiveness of the least attractive location is less than that of the most attractive location. If it is more attractive, no change is made.

The pixel-swapping was used to locate the sub-pixel components within each pixel for both the global and local soft classifications. In this method, as for the two-point histogram approach, the initial 16 m pixels were divided into 1 m sub-pixels and these randomly distributed throughout the pixels based on their fraction values. The three stage process described above was repeated such that a solution was approached

iteratively. This algorithm was applied for 40 iterations to both the global and local soft classified imagery to produce 1 m spatial resolution super-resolution images of the shoreline. A shoreline was later vectorised from both of the super-resolution images (*i.e.*, resulting from global and local soft classification).

7.2.2.2 Two-point histogram.

The two-point histogram method described in section 6.3.6.3 was applied to the soft classification outputs from both the global (Figure 6.8a) and local soft classifications (Figure 7.2). The training imagery was generated by fitting a contour of 0.5 membership of land to the soft classification proportions to represent the shoreline.

For both soft classifications, the initial 16 m pixels were divided into 1 m sub-pixels. Then each 1 m sub-pixel was allocated to a class based on the pixel-level soft proportions. The algorithm was run until there were no or minimal changes (70 iteration) to the imagery. A shoreline was later vectorised from both of the super-resolution images (*i.e.*, resulting from global and local soft classification).

7.3 Results

This section explains the results obtained from both sub-pixel mapping method that were applied to the soft classification outputs derived from local and global statistics.

7.3.1 Super-resolution mapping

For comparative purposes the soft classification derived from both the global and local training statistics were used in sub-pixel mapping of the shoreline. The shorelines generated by the two-point histogram and pixel-swapping method are shown in Figure 7.4 and Figure 7.5.

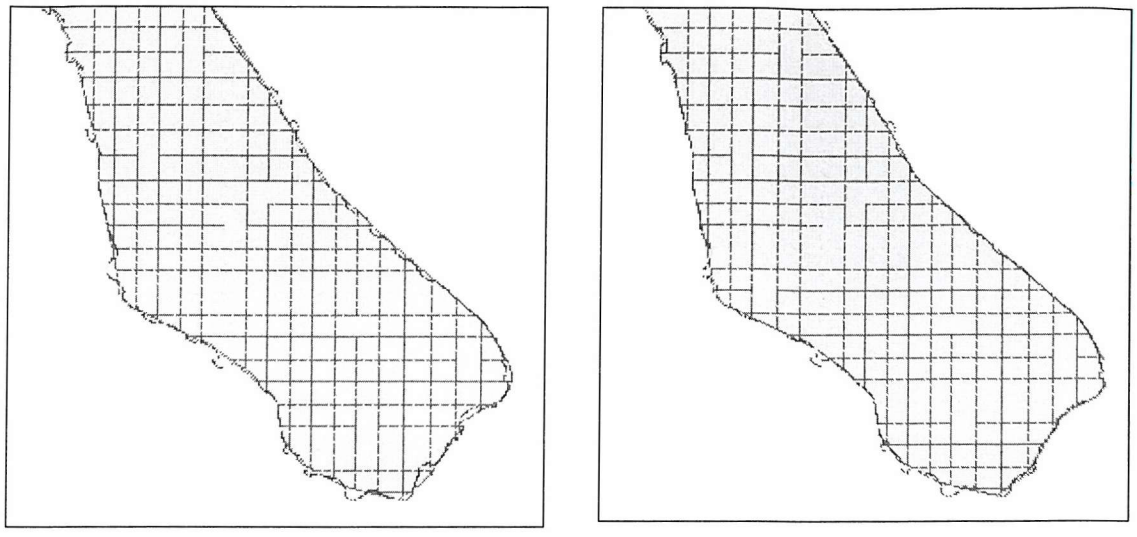

(a) (b)

Figure 7.4: Shoreline prediction generated using the pixel swapping algorithm based on soft classification using global (a) statistics and (b) local statistics. The actual shoreline is shown in black while the grid shows the actual pixel spatial resolution of 16 m.

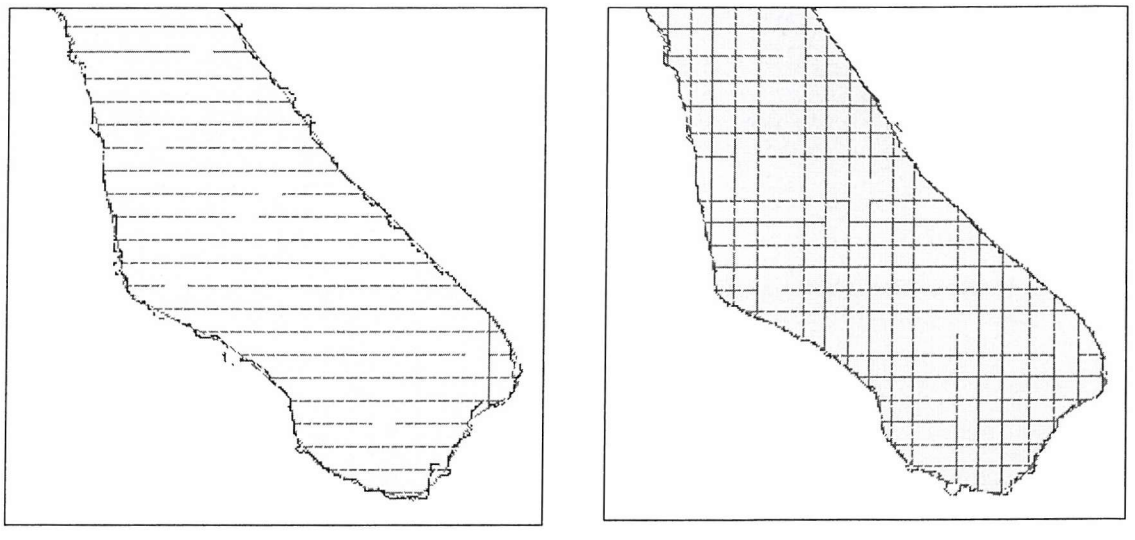

(a) (b)

Figure 7.5: Shoreline prediction generated using the two-point histogram algorithm based on soft classification using (a) global statistics and (b) local statistics. The actual shoreline is shown in black while the grid shows the actual pixel spatial resolution of 16 m.

The accuracy of the shoreline maps generated from the two-point histogram and pixel-swapping methods were analysed at 4 areas in the imagery (Figure 6.2). The accuracy of the shoreline prediction was determined by comparing the predicted location to the actual location determined from the ground data for each shoreline extract from each method for every metre of the shoreline (Table 7.2). The positional accuracy along the 125 m length of the shoreline for the four areas are shown in Figure 7.6 to Figure 7.9

The accuracy of shoreline prediction when using global statistics varied with location and orientation. The most accurate prediction was achieved from the linear shoreline (across pixel orientation) with an RMSE of 1.38 m for the pixel-swapping algorithm and 1.2 m for the two-point histogram algorithm when global training statistics were used. The use of local training statistics, however, increased the accuracy of the soft classification and ultimately shoreline prediction with the pixel swapping and two-point histogram method obtaining an RMSE of 0.99 m and 0.97 m, respectively (Table 7.2). The accuracy of the predictions at the 4 areas is given in Table 7.2.

Table 7.2: RMSE in shoreline prediction (m) from the 4 methods calculated at the 4 areas.

	Global training statistics		Local training statistics	
	Pixel-swapping	Two-point histogram	Pixel-swapping	Two-point histogram
Area I	1.38	1.20	0.99	0.97
Area II	2.13	1.34	1.51	1.10
Area III	1.46	1.15	1.23	1.05
Area IV	1.21	2.08	1.11	1.02

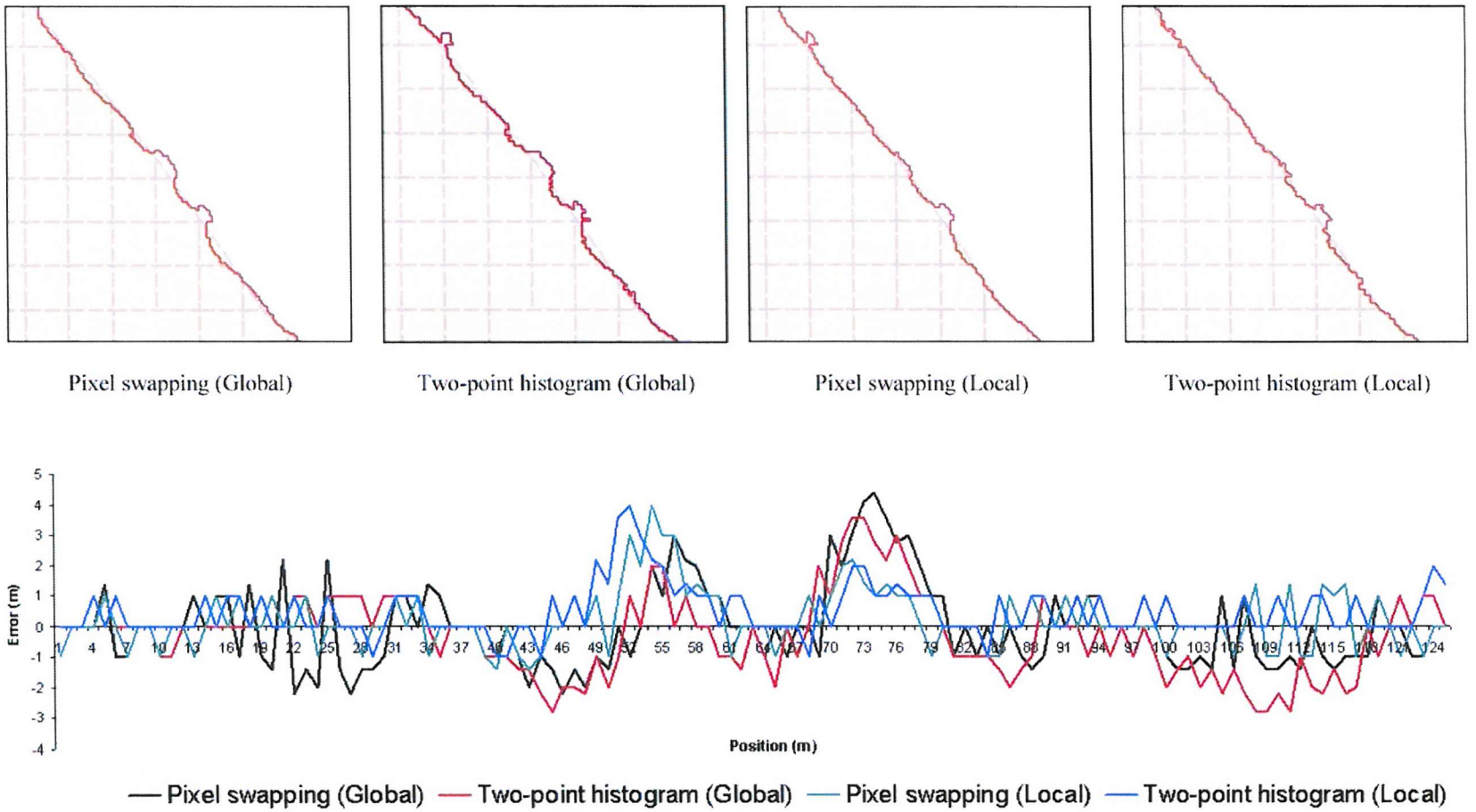

Figure 7.6: Positional accuracy for the 4 shorelines along a 125 m stretch of shoreline in Area I. The grid represents the spatial resolution of 16 m.

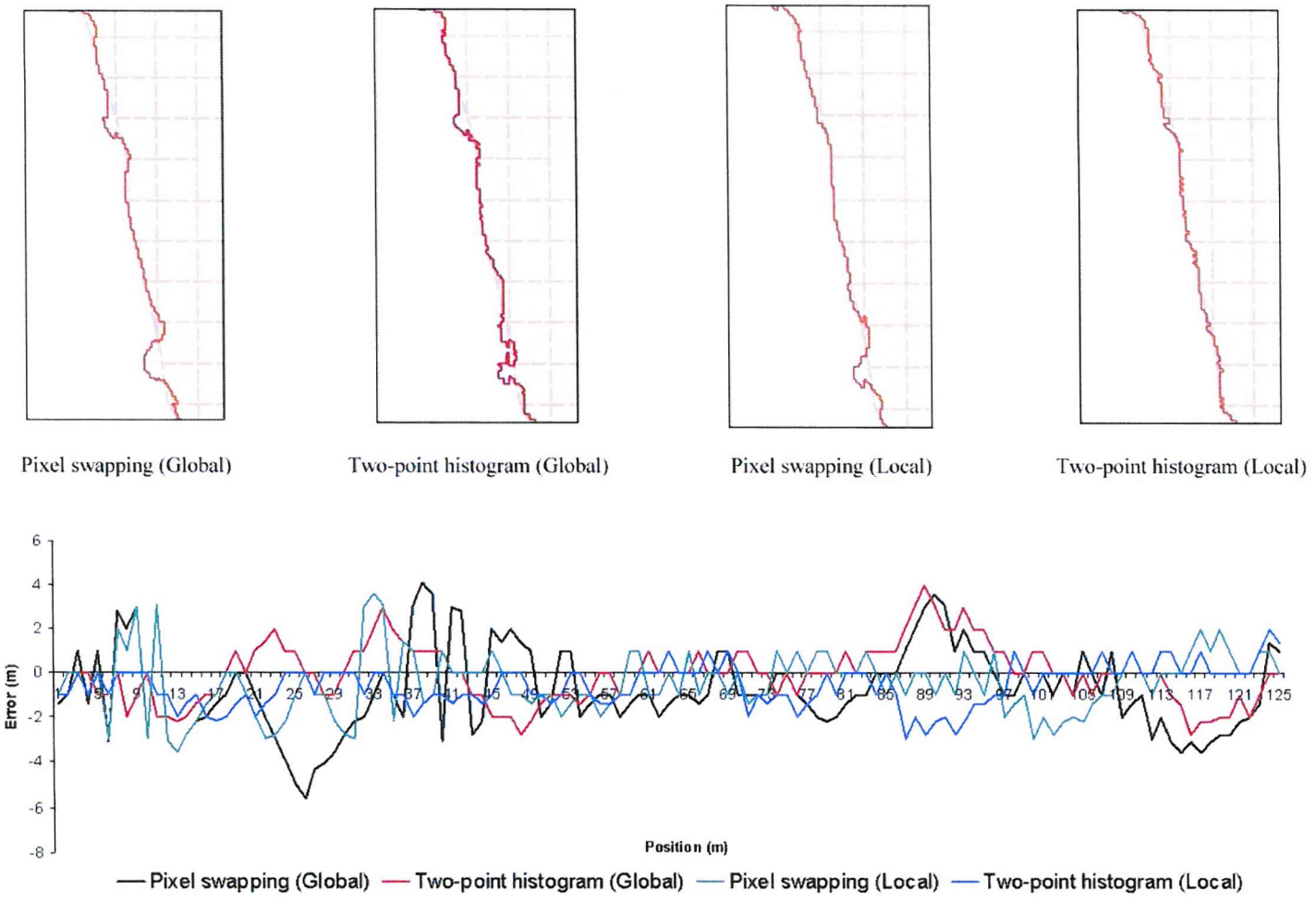

Figure 7.7: Positional accuracy for the 4 shorelines along a 125 m stretch of shoreline in Area II. The grid represents the spatial resolution of 16 m.

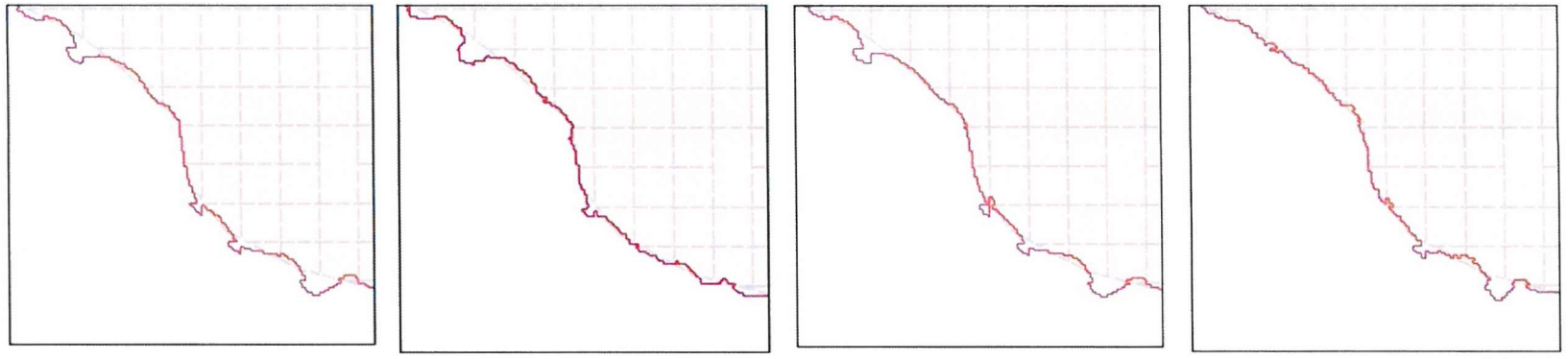

Pixel swapping (Global) Two-point histogram (Global) Pixel swapping (Local) Two-point histogram (Local)

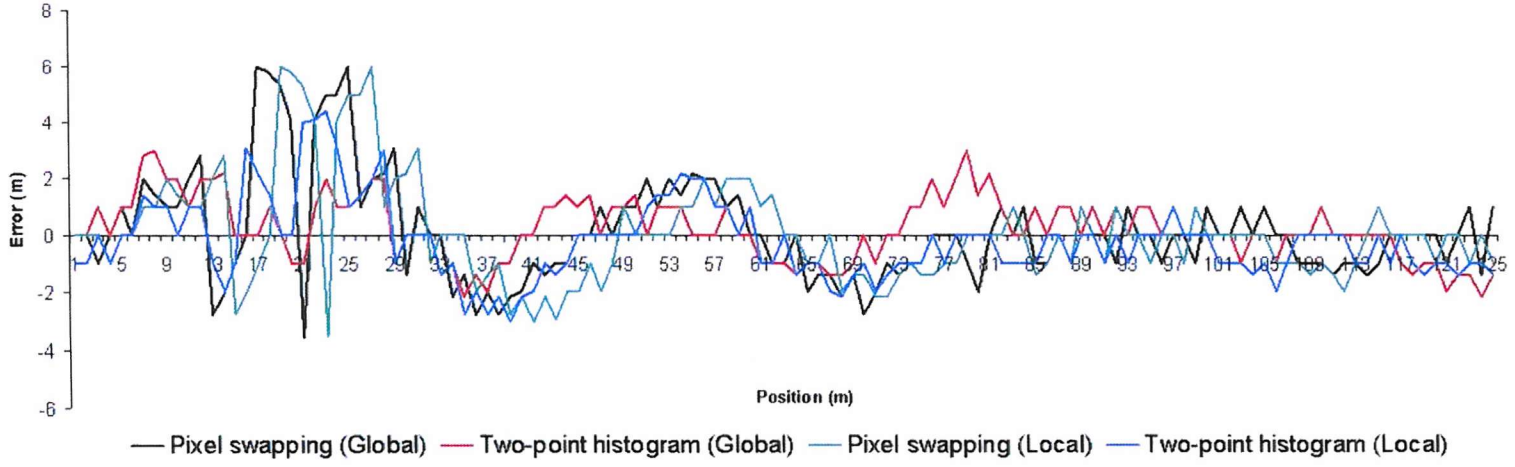

Figure 7.8: Positional accuracy for the 4 shorelines along a 125 m stretch of shoreline in Area III. The grid represents the spatial resolution of 16 m.

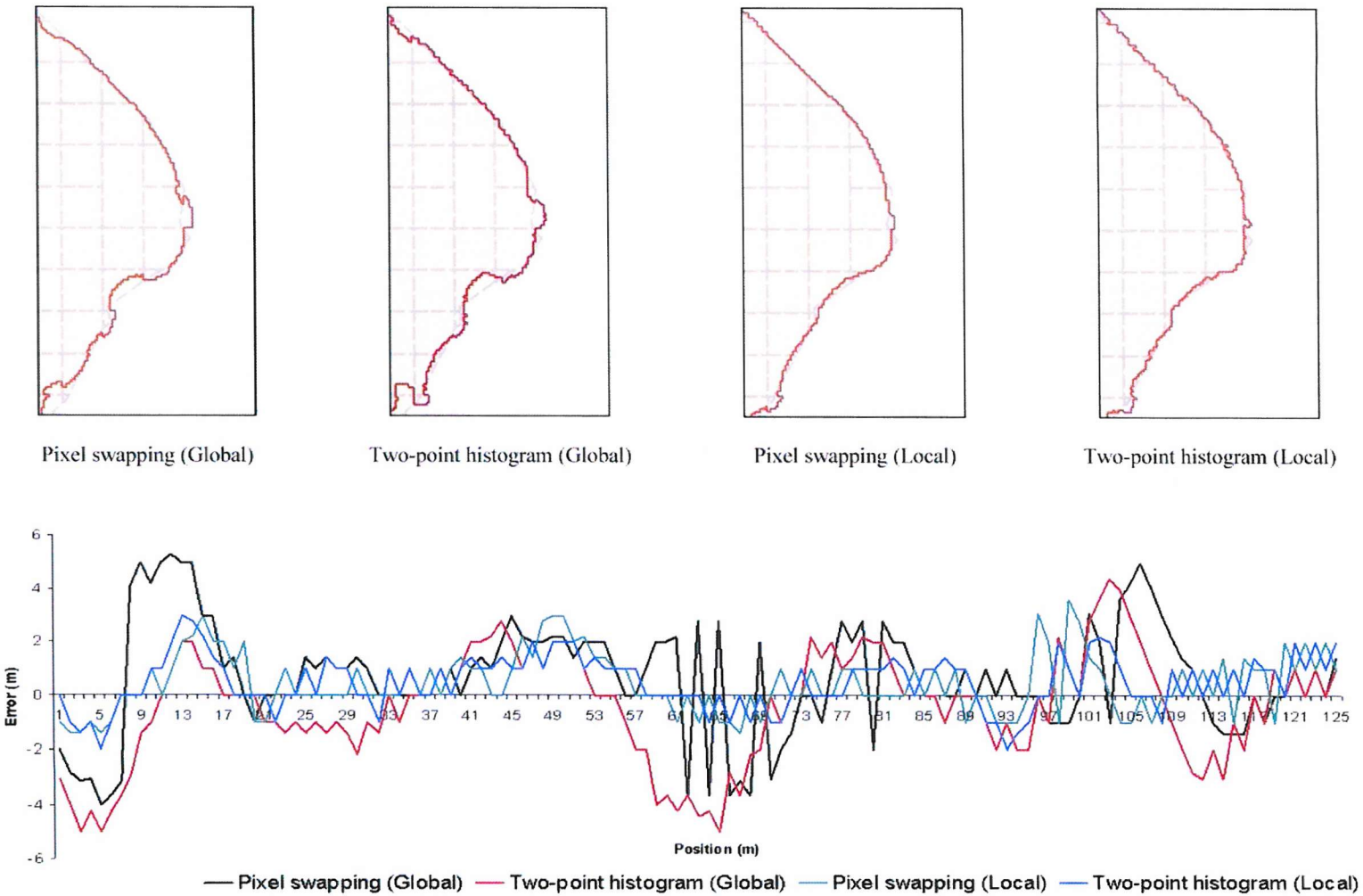

Figure 7.9: Positional accuracy for the 4 shorelines along a 125 m stretch of shoreline in Area IV. The grid represents the spatial resolution of 16 m.

7.4 Discussion

Analysis of the spectral response derived from the training sites indicate marked intra-class variation. This was expected, for example in water training sites, as the spectral response is a function of depth and quality of the water which are variable in space and time. Although the soft classification trained with global statistics produced an accurate prediction ($r = 0.95$) the global statistics did not represent local conditions accurately. To reduce error and produce a more accurate prediction of class proportion within a pixel, a soft classification approach based on utilising local training sites was proposed. Using the same training sites used in a global approach, local classification resulted in an increase in the r value from 0.95 to 0.98. The use of soft classification based on local training statistics would, therefore, be expected to yield a more accurate super-resolution prediction of shoreline position.

Two sub-pixel mapping algorithms were used to predict shoreline location within a pixel. The two methods were based on the two-point histogram and pixel-swapping algorithms. For all four areas and for both algorithms, the accuracy of shoreline prediction was larger when local rather than global training statistics were used. Results show that by using localised training sites the overall accuracy of shoreline prediction increased (RMSE of 1.51 m) relative to that achieved using global statistics (RMSE of 2.13 m). In addition, shoreline orientation had less effect on the prediction than when global statistics were used (Table 7.2). The result demonstrates that soft classification prediction provides a critical input to the super-resolution mapping process, with the accuracy of shoreline prediction related positively to the accuracy of the soft classification.

7.5 Conclusion

This research has indicated the potential of super-resolution techniques for mapping the shoreline at a sub-pixel scale using simulated satellite sensor imagery. The use of local statistics resulted in increased accuracy in soft classification in comparison to using global statistics. With increased accuracy in the prediction of class proportion within a pixel, sub-pixel mapping techniques were able to increase the accuracy of the shoreline location predictions.

Even though the results from this simulation study were encouraging, several additional factors need to be addressed before applying these methods to actual satellite sensor imagery.

8 Conclusion

Coastal areas are dynamic environments and constantly changing. The need to constantly monitor these changes has compelled researchers to develop methods of efficiently monitoring the shoreline. This thesis introduced methods of mapping the shoreline from satellite sensor imagery.

In chapter 2, the current status of Malaysia's shoreline was introduced with an overview of steps taken by the Malaysian government to address the issue of coastal erosion. These steps include the introduction of new government institution, financial allocation and regulatory measures. An overview of conventional and remote sensing methods for mapping the shoreline was provided to introduce how the shoreline has previously been mapped. The potential of remote sensing techniques to produce accurate maps was addressed leading to the aim of the study, the production of accurate shoreline maps from remote sensing satellite sensor imagery. This thesis examines the potential of using fine and coarse spatial resolution satellite sensor imagery in predicting the shoreline location. The data and study area for this thesis were described in chapter 3.

A pilot study examining the potential of mapping the shoreline from coarse spatial resolution satellite sensor imagery on a linear stretch of shoreline was discussed in chapter 4. The shoreline predicted from a conventional hard classification method was compared with those from several sub-pixel mapping methods. The pilot study showed that by combining soft classification and sub-pixel mapping methods accurate shoreline prediction was possible (RMSE = 2.25 m for the two-point histogram

method). But this result was only valid for linear shorelines and further analysis was needed to address the effect of different shoreline orientation. This issue was addressed later in chapter 6.

In chapter 5, fine spatial resolution satellite sensor imagery was used to map the shoreline. A shoreline prediction with an RMSE of 1.80 was obtained. But the use of fine spatial resolution imagery was impractical to map large stretches of shoreline at a national level. Therefore, methods of mapping the shoreline using coarse spatial resolution satellite sensor imagery were more practical.

Chapter 6 expanded the work in chapter 4, with emphasis given to the effect of shoreline orientation and on increasing the accuracy of the shoreline prediction. The sub-pixel mapping methods used included wavelet interpolation, contouring the soft classification and two-point histogram method. The two-point histogram method obtained the most accurate prediction with an average RMSE of 1.44 m followed by wavelet interpolation and contouring with an average RMSE of 2.14 m and 2.50 m, respectively. But the accuracy of the shoreline prediction varied depending on the orientation of the shoreline. The accuracy of the shoreline prediction could be increased by using a soft classification approach based on the use of local training statistics. The class composition predictions derived when using local training statistics were more accurate than those from global training statistics, with an increase in r, from 0.95 to 0.98 ($p < 0.05$). With increased accuracy, the use of soft classification based on local training statistics would, therefore, be expected to yield a more accurate super-resolution prediction of shoreline position. For the two-point histogram method, there was an increase in accuracy for all the shorelines, with the RMSE ranging from 0.97 m to 1.10 m when predicting from a 16 m spatial resolution image. Results show that shoreline orientation had less effect on the accuracy of the

prediction than when global statistics were used. The results demonstrated that soft classification prediction provides a critical input to the sub-pixel mapping process, with the accuracy of shoreline prediction related positively to the accuracy of the soft classification.

The value of sub-pixel mapping was apparent from the perspective of conventional mapping standards. Using the results from the two-point histogram method (16 m spatial resolution imagery) as an indicator of the achievable accuracy, the prediction satisfied the requirement of mapping at a 1: 1,500 scale. Using conventional methods, SPOT HRV sensor with a spatial resolution of 20 m only satisfies the requirement of a 1: 50,000 scale maps (Al-Rousan *et al.,* 1997). This research shows the potential of sub-pixel mapping method for mapping the shoreline at a sub-pixel scale using satellite sensor imagery such as Landsat TM, Landsat ETM+ and SPOT HRV. But when applying these methods to actual satellite sensor images, further research need to be done to address the affect of geo-referencing the images to the Malaysia RSO projection. The inaccuracies expected to be introduced and methods of addressing them would be addressed in future research.

The sub-pixel mapping methods proposed in this thesis are not limited to mapping the shoreline but have the potential to be applied to other boundary-type classification problems such as land cover mapping. When mapping the shoreline, sub-pixel mapping was relatively simple, as only two well-defined classes were being considered (water and land). Therefore, it remains to be seen how these methods would cope in more spatially complex landscapes, especially when more land cover classes occur at the sub-pixel scale. Further research addressing these issues needs to be conducted to be able to generalise these methods and make them applicable to other boundary-type classification problems. Obviously, other possibilities of improving the

algorithm exist. This includes automating the use of local training sites for soft classification by setting boundary conditions to enable the algorithm to select and utilise only sites fulfilling pre-determined conditions. Future research could also focus on generalising the methods to make them applicable to other boundary mapping applications.

Appendices

Appendix 1 : Header information for the IKONOS sensor data used in this thesis

Date	10th April 2002	1st July 2000	28th August 2002
Product Type :	Geo 1m + 4m bundle (Multi Spectral + Pan) + IGM	1-metre Pan-Sharpened Multispectral	1-metre Stereo Pan-Sharpened Multispectral + IGM
Map Projection:	Universal Transverse Mercator	Universal Transverse Mercator	Universal Transverse Mercator
UTM Parameters	Hemisphere: N Zone Number: 48	Hemisphere: N Zone Number: 48	Hemisphere: N Zone Number: 48
Datum:	WGS84	WGS84	WGS84
Product Order Pixel Size:	1.00 m (Pan) / 4.00 m (Multi spectral)	1.00 m	1.00 m
Sun Angle Azimuth:	81.4393 degrees	55.4660 degrees	76.4012 degrees
Sun Angle Elevation	68.13380 degrees	56.43733 degrees	68.81210
Acquisition Date/Time	2002-04-10 03:42 GMT	2000-07-01 03:14 GMT	2002-08-28 03:45 GMT
Product Map Coordinates	UL Map X (Easting): 286163.14 m UL Map Y (Northing): 598099.43 m	UL Map X (Easting): 253401.26 m UL Map Y (Northing): 620697.10 m	UL Map X (Easting): 286163.14 metres UL Map Y (Northing): 598099.43 m

Appendix 2 : RPC coefficient for the (a) left stereo image and (b) right stereo image

(a)

LINE_OFF: +008597.00 pixels
SAMP_OFF: +006206.00 pixels
LAT_OFF: +05.33020000 degrees
LONG_OFF: +103.14950000 degrees
HEIGHT_OFF: +0088.000 metres
LINE_SCALE: +008616.00 pixels
SAMP_SCALE: +006250.00 pixels
LAT_SCALE: +00.07880000 degrees
LONG_SCALE: +000.05640000 degrees
HEIGHT_SCALE: +0243.000 metres
LINE_NUM_COEFF_1: -8.015790460879763E-04
LINE_NUM_COEFF_2: +2.178622682118108E-03
LINE_NUM_COEFF_3: -1.011769649980722E+00
LINE_NUM_COEFF_4: -1.330176889963654E-02
LINE_NUM_COEFF_5: +1.219888840804130E-03
LINE_NUM_COEFF_6: +1.168241362165915E-05
LINE_NUM_COEFF_7: +6.193387652496905E-04
LINE_NUM_COEFF_8: -3.538944538391356E-05
LINE_NUM_COEFF_9: -1.343697662169847E-03
LINE_NUM_COEFF_10: +8.943706763229476E-06
LINE_NUM_COEFF_11: -1.969461521940275E-06
LINE_NUM_COEFF_12: -4.352652342039300E-08
LINE_NUM_COEFF_13: -3.425988224511912E-05
LINE_NUM_COEFF_14: -2.117075512873797E-08
LINE_NUM_COEFF_15: +3.818164163172455E-05
LINE_NUM_COEFF_16: -3.936778902318909E-05
LINE_NUM_COEFF_17: -2.829015317996647E-07
LINE_NUM_COEFF_18: +1.717311890757660E-06
LINE_NUM_COEFF_19: -6.114053814015430E-06
LINE_NUM_COEFF_20: -3.144209550132082E-09
LINE_DEN_COEFF_1: +1.000000000000000E+00
LINE_DEN_COEFF_2: -1.171297122436968E-03
LINE_DEN_COEFF_3: +1.327890963611945E-03
LINE_DEN_COEFF_4: -1.467246992524049E-03
LINE_DEN_COEFF_5: +3.398467622939111E-05
LINE_DEN_COEFF_6: +2.807995202840281E-06
LINE_DEN_COEFF_7: +7.491362145804603E-06
LINE_DEN_COEFF_8: -3.823133434583129E-05
LINE_DEN_COEFF_9: +3.890379284083888E-05
LINE_DEN_COEFF_10: +8.176329568243937E-07
LINE_DEN_COEFF_11: -1.417301916062796E-08
LINE_DEN_COEFF_12: -1.405394190498776E-09
LINE_DEN_COEFF_13: +3.101331878058564E-09
LINE_DEN_COEFF_14: -9.012681160945601E-10
LINE_DEN_COEFF_15: -2.532002959587352E-09
LINE_DEN_COEFF_16: +3.855470377029826E-09
LINE_DEN_COEFF_17: -3.325492335070448E-09
LINE_DEN_COEFF_18: +1.274772201659852E-08
LINE_DEN_COEFF_19: -2.941534098206556E-08
LINE_DEN_COEFF_20: -1.777496362565859E-10
SAMP_NUM_COEFF_1: -5.365250887172890E-03
SAMP_NUM_COEFF_2: +1.000484680928644E+00
SAMP_NUM_COEFF_3: +4.219770098547513E-03
SAMP_NUM_COEFF_4: -6.177058545830304E-04
SAMP_NUM_COEFF_5: +1.195719322853955E-03
SAMP_NUM_COEFF_6: -1.067775914962594E-03
SAMP_NUM_COEFF_7: +1.213001779249267E-04
SAMP_NUM_COEFF_8: -1.187516214410253E-03
SAMP_NUM_COEFF_9: +3.587305782641327E-05
SAMP_NUM_COEFF_10: +2.350444414402229E-06
SAMP_NUM_COEFF_11: +8.365749643280777E-06
SAMP_NUM_COEFF_12: -3.807003122182368E-05
SAMP_NUM_COEFF_13: +3.792129876125210E-05
SAMP_NUM_COEFF_14: +3.767512766913292E-07
SAMP_NUM_COEFF_15: +3.398009413464517E-05
SAMP_NUM_COEFF_16: +2.028306018110233E-07
SAMP_NUM_COEFF_17: -6.748417751803567E-08
SAMP_NUM_COEFF_18: +2.007369120900146E-06
SAMP_NUM_COEFF_19: -1.041086857938219E-06
SAMP_NUM_COEFF_20: -9.942412354259979E-10
SAMP_DEN_COEFF_1: +1.000000000000000E+00
SAMP_DEN_COEFF_2: -1.171297122436968E-03
SAMP_DEN_COEFF_3: +1.327890963611945E-03
SAMP_DEN_COEFF_4: -1.467246992524049E-03
SAMP_DEN_COEFF_5: +3.398467622939111E-05

(b)

LINE_OFF: +009486.00 pixels
SAMP_OFF: +005710.00 pixels
LAT_OFF: +05.32240000 degrees
LONG_OFF: +103.14960000 degrees
HEIGHT_OFF: +0088.000 metres
LINE_SCALE: +009450.00 pixels
SAMP_SCALE: +005798.00 pixels
LAT_SCALE: +00.08580000 degrees
LONG_SCALE: +000.05250000 degrees
HEIGHT_SCALE: +0243.000 metres
LINE_NUM_COEFF_1: +1.168330791267773E-03
LINE_NUM_COEFF_2: +1.838686643800731E-03
LINE_NUM_COEFF_3: -1.004473070864287E+00
LINE_NUM_COEFF_4: +2.247313951471594E-03
LINE_NUM_COEFF_5: +7.138606712661865E-03
LINE_NUM_COEFF_6: -1.129856466121717E-05
LINE_NUM_COEFF_7: -1.199754632965443E-03
LINE_NUM_COEFF_8: -3.908986245344519E-05
LINE_NUM_COEFF_9: +2.813701898460914E-02
LINE_NUM_COEFF_10: +2.439549121157181E-06
LINE_NUM_COEFF_11: +2.842682094128792E-06
LINE_NUM_COEFF_12: +1.365951095823415E-07
LINE_NUM_COEFF_13: -1.523222505873829E-04
LINE_NUM_COEFF_14: -1.373625179220041E-08
LINE_NUM_COEFF_15: +2.775423306408464E-05
LINE_NUM_COEFF_16: -3.814462211696524E-04
LINE_NUM_COEFF_17: +5.832369833462576E-07
LINE_NUM_COEFF_18: +9.372093412195353E-07
LINE_NUM_COEFF_19: -2.056769201469459E-06
LINE_NUM_COEFF_20: -1.367144597862590E-09
LINE_DEN_COEFF_1: +1.000000000000000E+00
LINE_DEN_COEFF_2: -7.129547814970496E-03
LINE_DEN_COEFF_3: -2.801379912935586E-02
LINE_DEN_COEFF_4: +2.367060941132691E-04
LINE_DEN_COEFF_5: +1.515505106826301E-04
LINE_DEN_COEFF_6: +2.481880476191763E-06
LINE_DEN_COEFF_7: +2.687900254731482E-05
LINE_DEN_COEFF_8: -2.725183863556567E-05
LINE_DEN_COEFF_9: +3.798438226324729E-04
LINE_DEN_COEFF_10: -1.538265355482507E-06
LINE_DEN_COEFF_11: -6.368298861627266E-08
LINE_DEN_COEFF_12: -1.064719461959987E-09
LINE_DEN_COEFF_13: +1.581381770001589E-08
LINE_DEN_COEFF_14: +5.605868171708611E-10
LINE_DEN_COEFF_15: +4.391419593884135E-09
LINE_DEN_COEFF_16: +8.606607346726961E-09
LINE_DEN_COEFF_17: -6.770126871700066E-09
LINE_DEN_COEFF_18: +6.654465706602339E-09
LINE_DEN_COEFF_19: -1.713598510377442E-07
LINE_DEN_COEFF_20: +5.437359867098021E-10
SAMP_NUM_COEFF_1: +4.063490175503958E-03
SAMP_NUM_COEFF_2: +1.003880523537400E+00
SAMP_NUM_COEFF_3: +4.849040778456582E-03
SAMP_NUM_COEFF_4: -5.652544098014657E-03
SAMP_NUM_COEFF_5: -2.829739152913578E-02
SAMP_NUM_COEFF_6: +6.743595539545685E-04
SAMP_NUM_COEFF_7: +3.383980858242207E-04
SAMP_NUM_COEFF_8: -7.172380385366849E-03
SAMP_NUM_COEFF_9: -9.7970873727040 2E-05
SAMP_NUM_COEFF_10: -3.755832700578262E-06
SAMP_NUM_COEFF_11: +1.402455669601033E-05
SAMP_NUM_COEFF_12: -2.711282360607431E-05
SAMP_NUM_COEFF_13: +3.845837149531081E-04
SAMP_NUM_COEFF_14: -1.302851671759722E-06
SAMP_NUM_COEFF_15: +1.534266775060973E-04
SAMP_NUM_COEFF_16: +7.585713745658501E-07
SAMP_NUM_COEFF_17: +1.684047669914581E-07
SAMP_NUM_COEFF_18: -6.304271485182397E-07
SAMP_NUM_COEFF_19: -6.778791352307466E-06
SAMP_NUM_COEFF_20: +6.927138825406827E-09
SAMP_DEN_COEFF_1: +1.000000000000000E+00
SAMP_DEN_COEFF_2: -7.129547814970496E-03
SAMP_DEN_COEFF_3: -2.801379912935586E-02
SAMP_DEN_COEFF_4: +2.367060941132691E-04
SAMP_DEN_COEFF_5: +1.515505106826301E-04
SAMP_DEN_COEFF_6: +2.481880476191763E-06

SAMP_DEN_COEFF_6: +2.807995202840281E-06
SAMP_DEN_COEFF_7: +7.491362145804603E-06
SAMP_DEN_COEFF_8: -3.823133434583129E-05
SAMP_DEN_COEFF_9: +3.890379284083888E-05
SAMP_DEN_COEFF_10: +8.176329568243937E-07
SAMP_DEN_COEFF_11: -1.417301916062796E-08
SAMP_DEN_COEFF_12: -1.405394190498776E-09
SAMP_DEN_COEFF_13: +3.101331878058564E-09
SAMP_DEN_COEFF_14: -9.012681160945601E-10
SAMP_DEN_COEFF_15: -2.532002959587352E-09
SAMP_DEN_COEFF_16: +3.855470377029826E-09
SAMP_DEN_COEFF_17: -3.325492335070448E-09
SAMP_DEN_COEFF_18: +1.274772201659852E-08
SAMP_DEN_COEFF_19: -2.941534098206556E-08
SAMP_DEN_COEFF_20: -1.777496362565859E-10

SAMP_DEN_COEFF_7: +2.687900254731482E-05
SAMP_DEN_COEFF_8: -2.725183863556567E-05
SAMP_DEN_COEFF_9: +3.798438226324729E-04
SAMP_DEN_COEFF_10: -1.538265355482507E-06
SAMP_DEN_COEFF_11: -6.368298861627266E-08
SAMP_DEN_COEFF_12: -1.064719461959987E-09
SAMP_DEN_COEFF_13: +1.581381770001589E-08
SAMP_DEN_COEFF_14: +5.605868171708611E-10
SAMP_DEN_COEFF_15: +4.391419593884135E-09
SAMP_DEN_COEFF_16: +8.606607346726961E-09
SAMP_DEN_COEFF_17: -6.770126871700066E-09
SAMP_DEN_COEFF_18: +6.654465706602339E-09
SAMP_DEN_COEFF_19: -1.713598510377442E-07
SAMP_DEN_COEFF_20: +5.437359867098021E-10

References

Adams, K. D. and Minor, T. B., 2002. Historic shoreline change at Lake Tahoe from 1938 to 1998 and its impact on sediment and nutrient loading. *Journal of Coastal Research*, 18: 637-651.

Al-Rousan, N., Cheng, P., Petrie, G., Toutin, T., and Zoej, M. J. V., 1997. Automated DEM extraction and orthoimage generation from SPOT Level 1B imagery. *Photogrammetric Engineering and Remote Sensing*, 63: 965-974.

Aplin, P. and Atkinson, P. M., 2001. Sub-pixel land cover mapping for per-field classification. *International Journal of Remote Sensing*, 22: 2853-2858.

Atanu, B. and Saxena, N. K., 1999. A Review of Shallow-Water Mapping Systems. *Marine Geodesy*, 22: 249-257.

Atkinson, P. M., 2003. Super resolution land cover classification using geostatistical optimization. In: GeoENV IV - Geostatistics for Environmental Applications. Dordrecht, Kluwer.

Atkinson, P. M., 1997. Mapping sub-pixel boundaries from remotely sense images. In: Innovation in GIS 4, Edited by Z.Kemp. Taylor and Francis, London, pp. 166-180.

Atkinson, P. M., 2004. Super Resolution Target Mapping From Soft-Classified Remotely Sensed Imagery. *Photogrammetrioc Engineering and Remote Sensing*, (In review).

Atkinson, P. M., Cutler, M. E. J., and Lewis, H., 1997. Mapping sub-pixel proportional land cover with AVHRR imagery. *International Journal of Remote Sensing*, 18: 917-935.

Bagheri, S., Stein, M., and Dios, R., 1998. Utility of hyperspectral data for bathymetric mapping in a turbid estuary. *International Journal of Remote Sensing*, 19: 1179-1188.

Baldwin, D. G., Emery, W. J., and Cheeseman, P. B., 1998. Higher resolution earth surface features from repeat moderate resolution satellite imagery. *IEEE Transactions on Geoscience and Remote Sensing*, 36: 244-255.

Balopoulos, E. T., Collins, M. B., and James, A. E., 1986. Satellite Images and their use in the numerical modelling of coastal processes. *International Journal of Remote Sensing*, 7: 905-919.

Baltsavias, E., Pateraki, M., and Li, Z. Radiometric and Geometric Evaluation of IKONOS Geo Images And Thier Use For 3D Building Mapping, Joint ISPRS

Workshop" High Resolution Mapping From Space 2001". 2001. Hannover, Germany. 19-9-2001.

Baltsavias, E. P., 1999. A comparison between photogrammetry and laser scanning. *ISPRS Journal of Photogrammetry and Remote Sensing*, 54: 83-94.

Benny, A. H. and Dawson, G. J., 1983. Satellite imagery as an aid to bathymetric charting in the Red sea. *The Cartographic Journal*, 20: 5-16.

Bhat, H. G. and Subrahmanya, K. R., 1993. Paleoshorelines and coastal processes in dakshina-kannada, karnataka, india - a study based on remotely-sensed data. *International Journal of Remote Sensing*, 14: 3311-3316.

Bierwirth, P. N., Lee, T. J., and Burne, R. V., 1993. Shallow sea-floor reflectance and water depth derived by unmixing multispectral imagery. *Photogrammetric Engineering and Remote Sensing*, 59: 331-338.

Blodget, H. W. and Taylor, P. T., 1990. Landsat MMS Monitoring of Nile Delta Shoreline Change. *IEEE Transactions on Geoscience and Remote Sensing*, ?: ?

Blodget, H. W., Taylor , P. T., and Raork, J. H., 1991. Shoreline changes along the rosetta nile promontory - monitoring with satellite-observations. *Marine Geology*, 99: 67-77.

Bohnestiehl, K. Create Accurate Orthophotos Using Softcopy Photogrammetry. 2001.

Bolstad, P. V. and Stowe, T., 1994. An evaluation of dem accuracy - elevation, slope, and aspect. *Photogrammetric Engineering and Remote Sensing*, 60: 1327-1332.

Borel, C. C. and Gerstl, S. A. W., 1992. Adjaceny-blurring effect of scenes modelled by radiosity method. *SPIE*, 1688: 620-624.

Bowman, D. and Pranzini, E., 2003. Reversed responses within a segmented detached breakwater, the Tuscany coast Italy - a case study. *Coastal Engineering*, 49: 263-274.

Brock, J. C., Wright, C. W., Sallenger, A. H., Krabill, W. B., and Swift, R. N., 2002. Basis and methods of NASA airborne topographic mapper lidar surveys for coastal studies. *Journal of Coastal Research*, 18: 1-13.

Brokelbank, D. C. and Tam, A. P., 1991. Stereo elevation determination techniques for spot imagery. *Photogrammetric Engineering and Remote Sensing*, 57: 1065-1073.

Bukata, R. P., Jerome, J. H., Kondratyev, K. Ya., and Pozdnyakov, D. V., 1995. Optical Properties and Remote sensing of Inland and Coastal Waters. CRC press, Boca Raton.

Byrnes, M. R., Cromwell, M., and Fowler, C., 2003. Special issue #38 - Shoreline mapping and change analysis; Technical considerations and management implications - Preface. *Journal of Coastal Research*, 1-4.

Camfield, F. E. and Morang, A., 1996. Defining and interpreting shoreline change. *Ocean & Coastal Management*, 32: 129-151.

Carvalho, L. M. T., Fonseca, L. M. G., Murtagh, F., and Clevers, J. G. P. W., 2001. Digital change detection with the aid of multiresolution wavelet analysis. *International Journal of Remote Sensing*, 22: 3871-3876.

Ceballos, J. C. and Bottino, M. J., 1997. The discrimination of scenes by principal components analysis of multi-spectral imagery. *International Journal of Remote Sensing*, 18: 2437-2449.

Cendrero, A. and Fischer, D. W., 1997. A procedure for assessing the environmental quality of coastal areas for planning and management. *Journal of Coastal Research*, 13: 732-744.

Cetin, H., Bal, Y., and Demirkol, C., 1999. Engineering and environmental effects of coastline changes in Turkey, northeastern Mediterranean. *Environmental & Engineering Geoscience*, 5: 315-330.

Chauvaud, S., Bouchon, C., and Maniere, R., 1998. Remote sensing techniques adapted to high resolution mapping of tropical coastal marine ecosystems (coral reefs, seagrass beds and mangrove). *International Journal of Remote Sensing*, 19: 3625-3639.

Chen, L. C. and Rau, J. Y., 1998. Detection of shoreline change for tideland areas using multi-temporal satellite images. *International Journal of Remote Sensing*, 19: 3383-3397.

Chen, L. C., Lo, C. Y., and Rau, J. Y., 2003. Generation of digital orthophotos from IKONOS satellite images. *Journal of Surveying Engineering-Asce*, 129: 73-78.

Chevrel, M., Courtois, M., and Weill, G., 1981. The SPOT satellite remote-sensing mission. *Photogrammetric Engineering and Remote Sensing*, 47: 1163-1171.

Church, R. L., Stoms, D. M., and Davis, F. W., 1996. Reserve selection as a maximal covering location problem. *Biological Conservation*, 76: 105-112.

Cicin-Sain, B. and Robert, W. K. Integrated Coastal and Ocean Management: Concept and Practices. Appendix 1: ICM Practices in Twenty-Two Selected Nations, Part II: Middle Developing Nations, Case Study on Malaysia. 373-380. 1998. Washington, D.C, *Island Press.*

Clark, C. D., Ripley, H. T., Green, E. P., Edwards, A. J., and Mumby, P. J., 1997. Mapping and measurement of tropical coastal environments with hyperspectral and high spatial resolution data. *International Journal of Remote Sensing*, 18: 237-242.

Clark, J. R., 1983. Coastal Ecosystem management : A technical manual for the conservation of coastal zone resources. Robert E. Krieger Publishing Company, Inc, Malabar, Florida.

Clark, R. K., Fay, T. H., and Walker, C. L., 1987. Bathymetry calculations with Landsat-4-TM imagery under a generalized ratio assumption. *Applied Optics*, 26: 4036-4038.

Clarke, T. A. and Fryer, J. G., 1998. The development of camera calibration methods and models. *Photogrammetric Record*, 16: 51-66.

Clavet, D., Lasserre, M., and Pouliot, J., 1993. Gps control for 1-50,000-scale topographic mapping from satellite images. *Photogrammetric Engineering and Remote Sensing*, 59: 107-111.

Cracknell, A. P., 1999. Remote sensing techniques in estuaries and coastal zones - an update. *International Journal of Remote Sensing*, 20: 485-496.

Cracknell, A. P. and Ibrahim, M., 1988. Bathymetry Studies On The Coastal Waters (Red-Sea) Of Jeddah, Saudi-Arabia, Using Shuttle Moms-01 Data. *International Journal of Remote Sensing*, 9: 1161-1165.

Cromwell, M., Leatherman, S. P., and Buckley, M. K., 1991. Historical shoreline change - error analysis and mapping accuracy. *Journal of Coastal Research*, 7: 839-852.

Curran, P. J. and Atkinson, P. M., 1998. Geostatistics and remote sensing. *Progress in Physical Geography*, 22: 61-78.

Curran, P. J. and Dungan, J. L., 1989. Estimation Of Signal-To-Noise - A New Procedure Applied To Aviris Data. *IEEE Transactions on Geoscience and Remote Sensing*, 27: 620-628.

David L, D., 1993. Smooth wavelet decompositions with blocky coefficient kernels. In: Larry L.Schumaker and Glenn Webb (Editor), Recent Advances in Wavelet Analysis. Academic Press.

Davies, C. H. and Wang, X. Planimetric Accuracy of IKONOS 1-m Panchromatic Image Products. CD-ROM (Unpaginated). 2001. St. Louis, Missouri, USA, *Proceeding of the ASPRS Annual Conference*. 23-4-2001.

Davis, R. A., Wang, P., and Silverman, B. R., 2000. Comparison of the performance of three adjacent and differently constructed beach nourishment projects on the gulf peninsula of Florida. *Journal of Coastal Research*, 16: 396-407.

Dekker, A. G., Malthus, T. J., Wijnen, M. M., and Seyhan, E., 1992. Remote-Sensing As A Tool for Assessing Water-Quality in Loosdrecht Lakes. *Hydrobiologia*, 233: 137-159.

Department of Defense. Mapping Carting and Geodesy Accuracy. MIL-STD-600001. 1990.

Department of Survey and Mapping Malaysia. A Country Report on the Geodetic and Tidal Activities in Malaysia. 2001. *Department of Survey and Mapping Malaysia.*

Deutsch, Clayton, V., and Andre G, J., 1998. Gslib: Geostatistical Software Library and User's Guide (Applied Geostatistics Series). Oxford University Press, Oxford.

Deutsch, C. V. and Wen, X. H., 1998. An improved perturbation mechanism for simulated annealing simulation. *Mathematical Geology*, 30: 801-816.

Dewidar, K. M. and Frihy, O. E., 2003. Thematic Mapper analysis to identify geomorphologic and sediment texture of El Tineh plain, north-western coast of Sinai, Egypt. *International Journal of Remote Sensing*, 24: 2377-2385.

Di, K. C., Ma, R. J., and Li, R. X., 2003. Rational functions and potential for rigorous sensor model recovery. *Photogrammetric Engineering and Remote Sensing*, 69: 33-41.

Donoho, D. L. Interpolating Wavelet Transforms. Technical Report 408. 1992. *Department of Statistics Stanford University.*

Donoho, D. L., 1993. Smooth wavelet decompositions with blocky coefficient kernels. In: Larry L.Schumaker and Glenn Webb (Editor), Recent Advances in Wavelet Analysis. Academic Press.

Dorota, A. G.-B. and Charles, K. T., 1999. AIM: An alternative tool for Coastal Mapping. *Marine Geodesy*, 22: 129-137.

Doucette, P. and Beard, K., 2000. Exploring the capability of some GIS surface interpolators for DEM gap fill. *Photogrammetric Engineering and Remote Sensing*, 66: 881-888.

Duffy, W. and Dickson, S. M. Using Grid and Graph to Quantify and Display Shoreline Change. 1998. *US, Maine geological Survey.*

Duggin, M. J., Sakhavat, H., and Lindsay, J., 1985. Systematic and Random Variations in Thematic Mapper Digital Radiance Data. *Photogrammetric Engineering and Remote Sensing*, 51: 1427-1434.

Dwivedi, R. S., 1997. The utility of multi-sensor data for mapping eroded land. *International Journal of Remote Sensing*, 18: 2303-2318.

El Asmar, H. M., 2002. Short term coastal changes along Damietta-Port Said coast northeast of the Nile Delta, Egypt. *Journal of Coastal Research*, 18: 433-441.

El Raey, M., El Din, S. H. S., Khafagy, A. A., and Zed, A. I. A., 1999. Remote sensing of beach erosion/accretion patterns along Damietta-Port Said shoreline, Egypt. *International Journal of Remote Sensing*, 20: 1087-1106.

Elraey, M., Nasr, S. M., Elhattab, M. M., and Frihy, O. E., 1995. Change detection of Rosetta Promontory over the last 40 years. *International Journal of Remote Sensing*, 16: 825-834.

Fanos, A. M., 1995. The impact of human activities on the erosion and accretion of the nile delta coast. *Journal of Coastal Research*, 11: 821-833.

Fleming, D. IKONOS DN Value Conversion to Planetary Reflectance. 2003. Geography department, University of maryland.

Fletcher, C., Rooney, J., Barbee, M., Lim, S. C., and Richmond, B., 2003. Mapping shoreline change using digital orthophotogrammetry on Maui, Hawaii. *Journal of Coastal Research*, 106-124.

Foody, G. M., 1998. Sharpening fuzzy classification output to refine the representation of sub-pixel land cover distribution. *International Journal of Remote Sensing*, 19: 2593-2599.

Foody, G. M., 1992. A Fuzzy-Sets Approach to the Representation of Vegetation Continua from Remotely Sensed Data - An Example from Lowland Heath. *Photogrammetric Engineering and Remote Sensing*, 58: 221-225.

Foody, G. M., 1996. Approaches for the production and evaluation of fuzzy land cover classifications from remotely-sensed data. *International Journal of Remote Sensing*, 17: 1317-1340.

Foody, G. M., 2002a. Status of land cover classification accuracy assessment. *Remote Sensing of Environment*, 80: 185-201.

Foody, G. M., 2002b. The role of soft classification techniques in the refinement of estimates of ground control point location. *Photogrammetric Engineering and Remote Sensing*, 68: 897-903.

Foody, G. M. and Cox, D. P., 1994. Sub-Pixel Land-Cover Composition Estimation Using A Linear Mixture Model and Fuzzy Membership Functions. *International Journal of Remote Sensing*, 15: 619-631.

Foody, G. M., Jackson, R. G., and Quine, C. P., 2003. Potential improvements in the characterisation of forest canopy gaps caused by windthrow using fine spatial resolution multispectral data: comparing hard and soft classification techniques. *Forest Science*, 444-454.

Forbes, V. L., 1998. Malaysia's maritime space : an analytical atlas of environments and resources. Maritime Institute of Malaysia (MIMA).

Fraser, C. S., Baltsavias, E., and Gruen, A., 2002a. Processing of Ikonos imagery for submetre 3D positioning and building extraction. *ISPRS Journal of Photogrammetry and Remote Sensing*, 56: 177-194.

Fraser, C. S. and Hanley, H. B., 2003. Bias compensation in rational functions for Ikonos satellite imagery. *Photogrammetric Engineering and Remote Sensing*, 69: 53-57.

Fraser, C. S., Hanley, H. B., and Yamakawa, T., 2002b. Three-dimensional geopositioning accuracy of Ikonos imagery. *Photogrammetric Record*, 17: 465-479.

Friedman, R. M., Dunn, S. V., and Merrell, W. J., 2002. Summary of the Heinz Center report on coastal erosion and the National Flood Insurance Program. *Journal of Coastal Research*, 18: 568-575.

Frihy, O. E., Debes, E. A., and El Sayed, W. R., 2003. Processes reshaping the Nile delta promontories of Egypt: pre- and post-protection. *Geomorphology*, 53: 263-279.

Frihy, O. E. and Dewidar, K. M., 2003. Patterns of erosion/sedimentation, heavy mineral concentration and grain size to interpret boundaries of littoral sub-cells of the Nile Delta, Egypt. *Marine Geology*, 199: 27-43.

Frihy, O. E., Dewidar, K. M., Nasr, S. M., and El Raey, M. M., 1998. Change detection of the northeastern Nile delta of Egypt: shoreline changes, Spit evolution, margin changes of Manzala lagoon and its islands. *International Journal of Remote Sensing*, 19: 1901-1912.

Ganas, A., Lagios, E., and Tzannetos, N., 2002. An investigation into the spatial accuracy of the IKONOS 2 orthoimagery within an urban environment. *International Journal of Remote Sensing*, 23: 3513-3519.

Gavin, J. and Jennison, C., 1997. A subpixel image restoration algorithm. *Journal of Computational and Graphical Statistics*, 6: 182-201.

Geman, S. and Geman, D., 1984. Stochastic relaxation, Gibbs distributions, and the bayesian restoration of images. *IEEE Transaction on pattern analysis and Machine intelligence*, Pami-6: 721-739.

Gibsob, P. J. and Dorothy, M. J., 2003. Environmental Applications of Geophysical Surveying Techniques. Nova Science Publishers, Inc.; New York.

Gibson, P. J., 2000. Introductory Remote Sensing : Principles and Concepts. Routledge.

Giles, P. T. and Franklin, S. E., 1996. Comparison of derivative topographic surfaces of a DEM generated from stereoscopic SPOT images with field measurements. *Photogrammetric Engineering and Remote Sensing*, 62: 1165-1171.

Gobbett, D. J. and Hutchison, C. S., 1973. Geology of the Malay Peninsula: West Malaysia and Singapore. John Wiley & Sons, Geological Society Of Malaysia.

Gorman, L., Morang, A., and Larson, R., 1998. Monitoring the coastal environment; Part IV: Mapping, shoreline changes, and bathymetric analysis. *Journal of Coastal Research*, 14: 61-92.

Gould, R. W. and Arnone, R. A., 1997. Remote sensing estimates of inherent optical properties in a coastal environment. *Remote Sensing of Environment*, 61: 290-301.

Grodecki, J. IKONOS Stereo Feature Extraction- RPC Approach, Proceeding, ASPRS Annual Conference 2001 (on CD-ROM). 2001. St. Louis, *American Society for Photogrammetry and Remote Sensing*. 23-4-2001.

Grodecki, J. and Dial, G. IKONOS Geometric Accuracy. *Proceedings of Joint Workshop of ISPRS Working Group I/2. I/5 and IV/7 on High Resolution Mapping From Space 2001*. 2001. University of Hannover, Hannover, Gernamy. 19-9-2001.

Hancock, G. and Willgoose, G., 2001. The production of digital elevation models for experimental model landscapes. *Earth Surface Processes and Landforms*, 26: 475-490.

Hanley, H. B. and Fraser, C. S., 2001. Geopositioning accuracy of Ikonos imagery: Indications from two dimensional transformations. *Photogrammetric Record*, 17: 317-329.

Harakunarak, A. Malaysia : ICM Country Profile. *Intergrated Cosatal Management* . 2000.

Haralick, R. M., Shanmugan, K., and Dinstein, I., 1973. Textural Features for Image Classification. *IEEE Tr. on Systems, Man, and Cybernetics*, SMC-3: 610-621.

Hoffman, C., Stennocher, K., Kasanko, M., Toutin, T., and Cheng, P., 2001. Urban Mapping with High resolution satellite imagery : IKONOS and IRS Data put to the test. *Geoinformatics*, 4: 34-37.

Honeycutt, M. G., Cromwell, M., and Douglas, B. C., 2001. Shoreline-position forecasting: Impact of storms, rate- calculation methodologies, and temporal scales. *Journal of Coastal Research*, 17: 721-730.

Honeycutt, M. G. and Krantz, D. E., 2003. Influence of the geologic framework on spatial variability in long-term shoreline change, Cape Henlopen to Rehoboth Beach, Delaware. *Journal of Coastal Research*, 147-167.

Horgan, G., 1998. Wavelets for SAR image smoothing. *Photogrammetric Engineering and Remote Sensing*, 64: 1171-1177.

Hotine, M. The Projection Tables for Malaya. 1947. *The Department of Survey and Mapping Malaysia.*

Ibrahim, M. and Cracknell, A. P., 1990. Bathymetry Using Landsat MSS Data Of Penang Island In Malaysia. *International Journal of Remote Sensing*, 11: 557-559.

Jensen, J. R., 1996. Introductory Digital Image Processing. Prentice-Hall, Inc, New Jersey.

Jensen, J. R., 2000. Remote sensing Of The Environment: an Earth Resource Perspective. Prentice-Hall Inc., New Jersey.

Jerlov, N. G., 1976. Marine Optics. Elsevier, Amsterdam.

Jeroen, C. J. H. A. and Gerard, B. M. H., 2002. Using simulated Annealing for resource allocation. *International Journal of Geographical Information Science*, 16: 571-587.

Ji, W., Civco, D. L., and Kennard, W. C., 1992. Satellite remote bathymetry - a new mechanism for modeling. *Photogrammetric Engineering and Remote Sensing*, 58: 545-549.

Jill ,M.M., 2001. Close-Range Hyperspectral And Broad Band
Satellite Remote Sensing Of Coral Reef Structures. Geography University of Nebraska.

John, R. C., 1983. Coastal Ecosystem Management – A Technical Manual For The Conservation Of Coastal Zone Resources. Robert E Krieger Publishing Company Malabar, Florida.

Judge, E. K. and Overton, M. F., 2001. Remote sensing of barrier island morphology: Evaluation of photogrammetry-derived digital terrain models. *Journal of Coastal Research*, 17: 207-220.

Kanellopoulos, I., Varfis, A., Wilkinson, G. G., and Megier, J., 1992. Land-Cover Discrimination in Spot Hrv Imagery Using An Artificial Neural Network - A 20-Class Experiment. *International Journal of Remote Sensing*, 13: 917-924.

Kenward, T., Lettenmaier, D. P., Wood, E. F., and Fielding, E., 2000. Effects of digital elevation model accuracy on hydrologic predictions. *Remote Sensing of Environment*, 74: 432-444.

Kim, T., 2000. A study on the epipolarity of linear pushbroom images. *Photogrammetric Engineering and Remote Sensing*, 66: 961-966.

Kim, T., Shin, D., and Lee, Y. R., 2001. Development of a robust algorithm for transformation of a 3D object point onto a 2D image point for linear pushbroom imagery. *Photogrammetric Engineering and Remote Sensing*, 67: 449-452.

Kirkpatrick, S., Gelatt, C. D., and Vecchi, M. P., 1983. Optimization by Simulated Annealing. *Science*, 220: 671-680.

Krupnik, A., 2000. Accuracy assessment of automatically derived digital elevation models from SPOT images. *Photogrammetric Engineering and Remote Sensing*, 66: 1017-1023.

Lane, S. N., James, T. D., and Crowell, M. D., 2000. Application of digital photogrammetry to complex topography for geomorphological research. *Photogrammetric Record*, 16: 793-821.

Langley, S. K., Alexander, C. R., Bush, D. M., and Jackson, C. W., 2003. Modernizing shoreline change analysis in Georgia using topographic survey sheets in a GIS environment. *Journal of Coastal Research*, 168-177.

LaValle, P. D. and Lakhan, V. C., 2000. An assessment of lake-level fluctuations on beach and shoreline changes. *Coastal Management*, 28: 161-173.

Leatherman, S. P., 2003. Shoreline change mapping and management along the US East Coast. *Journal of Coastal Research*, 5-13.

Lee, C., Theiss, H. J., Bethel, J. S., and Mikhail, E. M., 2000. Rigorous mathematical modeling of airborne pushbroom imaging systems. *Photogrammetric Engineering and Remote Sensing*, 66: 385-392.

Lee, J.-B., Huh, Y., Seo, B., and Kim, Y. Improvement the Positional Accuracy of the 3D Terrain Data Extracted From IKONOS-2 Satellite Imagery. 2002. Graz, Austria , *ISPRS Commission III, Symposium 2002*. Photogrammetric Computer Vision.

Lee, J., Snyder, P. K., and Fisher, P. F., 1992. Modeling The Effect Of Data Errors On Feature-Extraction From Digital Elevation Models. *Photogrammetric Engineering and Remote Sensing*, 58: 1461-1467.

Lemmens, M. J. P. M., 2001. Structure-Based Edge Detection: Delineation of Boundariesin Aerial and Space Images. Delft University Press, Delft.

Leow, R. H. D., Tan, Y., Wan , C. Y., and Melsheimer, C. Observing Intertidal Zones Using Satellite Imagery. 2000. *Asian Conference for Remote Sensing 2000.*

Li, R., Liu, J., and Felus, Y., 2001. Spatial modelling and analysis for shoreline change detection and coastal erosion monitoring. *Marine Geodesy*, 24: 1-12.

Li, R., Ma, R., and Di, K. C., 2002. Digital tide-coordinated shoreline. *Journal of Marine Geodesy*, 25: 27-36.

Li, R., Zhou, G., Gonzalez, A., Liu, J. K., Ma, F., Felus, Y., Lapine, L., Lockwood, M., Schmidt, N. J., and Fowler, C. Coastline Mapping and Change Detection Using One-Meter Resolution Satellite Imagery. Project Annual Report. 1998. *Department of Civil and Environmental Engineering and Geodetic Science,The Ohio State University, Columbus, OH.* 1998.

Li, R., Zhou, G., Gonzalez, A., Liu, J. K., Ma, F., Felus, Y., Lapine, L., Lockwood, M., Schmidt, N. J., and Fowler, C. A Study Of The Potential Attainable Geometric Accuracy Of Ikonos
Satellite Imagery. Working Group IV/6. 2000. Amsterdam, *19th International Society for Photogrammetry and Remote Sensing.* 16-7-2000.

Li, R. X., 1998. Potential of high-resolution satellite imagery for national mapping products. *Photogrammetric Engineering and Remote Sensing*, 64: 1165-1170.

Liang, S. L., Fang, H. L., and Chen, M. Z., 2001. Atmospheric Correction of Landsat ETM+ Land Surface Imagery—Part I: Methods. *IEEE Transactions on Geoscience and Remote Sensing*, 39: 2490-2498.

Lillesand, T. M. and Kiefer, R. W., 2000. Remote sensing and image interpretation. John Wiley & Sons, Inc., New York.

Lockwood, C. and Moore, T., 1993. Harvest Scheduling with Spatial Constraints - A Simulated Annealing Approach. *Canadian Journal of Forest Research-Revue Canadienne de Recherche Forestiere*, 23: 468-478.

Lohani, B. and Mason, D. C., 1999. Construction of a Digital Elevation Model of the Holderness Coast using the waterline method and Airborne Thematic Mapper Data. *International Journal of Remote Sensing*, 20: 593-607.

Lyzenga, D. R., 1978. Passive remote sensing technigues for mapping water depth and bottom features. *Applied Optics*, 17: 379-383.

Lyzenga, D. R. Shallow Water Reflectance Modeling With Applications to Remote Sensing of the Ocean Floor. Proc.13th Int'l.Symposium on Remote Sensing of Environment. 583-602. 1979. Ann Arbor, MI.

Lyzenga, D. R., 1985. Shallow-Water Bathymetry Using Combined Lidar And Passive Multispectral Scanner Data. *International Journal of Remote Sensing*, 6: 115-125.

Lyzenga, D. R. and Tanis , F. J., 1981. Monte-Carlo Calculation Of Radiation Reflectance For Highly Turbid Waters. *Journal of the Optical Society of America*, 71: 1643-1644.

Madani, M. Real-Time Sensor Independant Positioning by Rational Functions. *Proceeding of ISPRS Workshop on Direct Versus Indirect Methods of Sensor Orientation*. 64-75. 1999. Barcelona. 25-11-1999.

Malaysian Meteorological Service. Climate Summary. 2001. Kuala Lumpur, *Malaysian Meteorological Service*. 2001.

Malaysian Meteorological Service. 2002 Climate Summary. 2002. *Malaysian Meteorological Service*.

Malthus, T. J. and Karpouzli, E., 2003. Integrating field and high spatial resolution satellite-based methods for monitoring shallow submersed aquatic habitats in the Sound of Eriskay, Scotland, UK. *International Journal of Remote Sensing*, 24: 2585-2593.

Malthus, T. J. and Mumby, P. J., 2003. Remote sensing of the coastal zone: an overview and priorities for future research. *International Journal of Remote Sensing*, 24: 2805-2815.

Mather, P. M. and Tso, B., 2001. Classification Methods for Remotely Sensed Data. Taylor & Francis, London & New York.

McCarthy, F., Cheng, P., and Toutin, T. Case Study of Using IKONOS Imagery in Small Manucipalities. *Earth Observation Magazine* 10[11], 13-16. 2001.

McKenna, J., O'Hagan, A. M., MacLeod, M., Power, J., and Cooper, A., 2003. Obsolete maps and coastal management: Case studies from northwest Ireland. *Coastal Management*, 31: 229-246.

Mertens, K. C., Verbeke, L. P. C., Ducheyne, E. I., and De Wulf, R. R., 2003. Using genetic algorithms in sub-pixel mapping. *International Journal of Remote Sensing*, 24: 4241-4247.

Metropolis, N., Rosenbluth, A., Rosenbluth, M., Teller, A., and Teller, E., 1953. Equation of state calculation by fast computing machines. *Journal of Chemical Physics*, 21: 1087-1092.

Mikhail, E. M., 1999. Is photogrammetry still relevant? *Photogrammetric Engineering and Remote Sensing*, 65: 740-+.

Ministry of Agriculture, M. Guidelines On Erosion Control for Development Projects in the Coastal Zone. 1997. Kuala Lumpur, *Department of Irrigation Drainage, Coastal Engineering Division*.

Morton, R. A., Leach, M. P., Paine, J. G., and Cardoza, M. A., 1993. Monitoring beach changes using GPS surveying techniques. *Journal of Coastal Research*, 9: 702-720.

Mumby, P. J. and Edwards, A. J., 2002. Mapping marine environments with IKONOS imagery: enhanced spatial resolution can deliver greater thematic accuracy. *Remote Sensing of Environment*, 82: 248-257.

Nanu, L. and Robertson, C., 1993. The effect of suspended sediment depth distribution on coastal water spectral reflectance - theoretical simulation. *International Journal of Remote Sensing*, 14: 225-239.

NASA. Landsat 7 Science Data Users Handbook. 2003.

National Ocean Service. Computer Applications to Tides in the National Ocean Survey. Supplement to the "Manual of Harmonic Analysis and Prediction of Tides. National Oceanic and Atmospheric Administration. 1982. *U.S.Department of Commerce*.

Norcross, Z. M., Fletcher, C. H., and Merrifield, M., 2002. Annual and interannual changes on a reef-fringed pocket beach: Kailua Bay, Hawaii. *Marine Geology*, 190: 553-580.

Omnistar. Omnistar. *Http://Www.Omnistar.Com* . 2001.

Ooi, J., 1974. The climate of west Malaysia and Singapore. Oxford University Press.

Pajak, M. J. and Leatherman, S., 2002. The high water line as shoreline indicator. *Journal of Coastal Research*, 18: 329-337.

Pala, V. and Pons, X., 1995. Incorporation of Relief in Polynomial-Based Geometric Corrections. *Photogrammetric Engineering and Remote Sensing*, 61: 935-944.

Parker, B. B., 2003. The difficulties in measuring a consistently defined shoreline - The problem of vertical referencing. *Journal of Coastal Research*, 44-56.

Philpot, W. D., 1989. Bathymetric mapping with passive multispectral imagery. *Applied Optics*, 28: 1569-1578.

Polcyn, F. C., Brown, W. L., and Sittinger, I. J. The Measurement of Water Depth by Remote Sensing Techniques. Report 8973-26F. 8973-26F. 1970. Ann Arbor, Willow Run Laboratories, *University of Michigan*.

Rao, P. P., Nair, M. M., and Raju, D. V., 1985. Assessment of the role of remote-sensing techniques in monitoring shoreline changes - a case-study of the Kerala Coast. *International Journal of Remote Sensing*, 6: 549-558.

Richards, J. A., 1993. Remote sensing digital image analysis: An introduction. Springer-Verlag, Berlin.

Roberts, A. C. B. and Anderson, J. M., 1999. Shallow water bathymetry using integrated airborne multi- spectral remote sensing. *International Journal of Remote Sensing*, 20: 497-510.

Ruggiero, P., Kaminsky, G. M., and Gelfenbaum, G., 2003. Linking proxy-based and datum-based shorelines on a high-energy coastline: Implications for shoreline change analyses. *Journal of Coastal Research*, 57-82.

Sandidge, J. C. and Holyer, R. J., 1998. Coastal bathymetry from hyperspectral observations of water radiance. *Remote Sensing of Environment*, 65: 341-352.

Saw, H. S. Arah Tuju Masa Depan Program Dan Struktur Ofganisasi Bahagian Kejuruteraan Pantai. 2000. Langkawi, Malaysia, *Persidangan tahunan pengurus kanan JPS Malaysia 2000.*

Shaghude, Y. W., Wannas, K. O., and Lunden, B., 2003. Assessment of shoreline changes in the western side of Zanzibar channel using satellite remote sensing. *International Journal of Remote Sensing*, 24: 4953-4967.

Shanmugan, K. S. and Breipohl, A. M., 1988. Random signals: Detection, Estimation and Data Analysis. Wiley, Chichester.

Shoshany, M. and Degani, A., 1992. Shoreline detection by digital image-processing of aerial- photography. *Journal of Coastal Research*, 8: 29-34.

Siegel, S. and Castellan, N. J., 1988. Nonparametric Statistics for the Behavioral Sciences. McGraw-Hill, New York.

Simhadri, K. K., Iyengar, S. S., Holyer, R. J., Lybanon, M., and Zachary, J. M., 1998. Wavelet-based feature extraction from oceanographic images. *IEEE Transactions on Geoscience and Remote Sensing*, 36: 767-778.

Simons, R. and Hollingham, S. Marine Aggregate Dredging: A Review Of Current Procedures for Assessingcoastal Processes and Impact of the Coastline. 57-60. 2001. Civil and Environmental Engineering Department, *University College London.*

Smith, M. S. and Curran, P. J., 1999. Methods for estimating image Signal-to-Noise Ratio (SNR). In: P.M.Akinson and N.J.Tate (Editors), Advances in remote sensing and GIS analysis. John Wiley & Sons Ltd, pp. 61-74.

Song, C., Woodcock, C. E., Seto, K. C., Lenney, M. P., and Macomber, S. A., 2001. Classification and change detection using Landsat TM data: when and how to correct atmospheric effects? *Remote Sensing of Environment*, 75: 230-244.

Space Imaging. Space Imaging Catalog of Product and Services. 1999. Thorton, *Space imaging,inc.*

Space Imaging. Space Imaging Awarded License to Provide Half-Meter Resolution Commercial Satellite Imagery. *Press Release* . 2001.

Space Imaging. IKONOS Imagery Product and Product Guide. ver 1.3. 2003a.

Space Imaging. Space Imaging Document Number SE-REF-016, Rev. N/C. 2003b.

Stanley consultants Inc., Moffatt and Nichols Engineers, and Jurutera Konsultants (S.E.A) Sdn.Bhd. National Coastal Erosion Study. 1985. Kuala Lunpur, Malaysia, *Jabatan Perdana Menteri.*

Stauble, D. K., 2003. The use of shoreline change mapping in coastal engineering project assessment. *Journal of Coastal Research*, 178-206.

Stumpf, R. P., Holderied, K., and Sinclair, M., 2003. Determination of water depth with high-resolution satellite imagery over variable bottom types. *Limnology and Oceanography*, 48: 547-556.

Tanaka, S. and Sugimura, T., 2001. A new frontier of remote sensing from IKONOS images. *International Journal of Remote Sensing*, 22: 1-5.

Tao, C. V. and Hu, Y., 2002. 3D reconstruction methods based on the rational function model. *Photogrammetric Engineering and Remote Sensing*, 68: 705-714.

Tatem, A. J., Lewis, H. G., Atkinson, P. M., and Nixon, M. S., 2001. Super-resolution target identification from remotely sensed images using a Hopfield neural network. *IEEE Transactions on Geoscience and Remote Sensing*, 39: 781-796.

Tatem, A. J., Lewis, H. G., Atkinson, P. M., and Nixon, M. S., 2003. Increasing the spatial resolution of agricultural land cover maps using a Hopfield neural network. *International Journal of Geographical Information Science*, 17: 647-672.

Tebbens, S. F., Burroughs, S. M., and Nelson, E. E., 2002. Wavelet analysis of shoreline change on the Outer Banks of North Carolina: An example of complexity in the marine sciences. *Proceedings of the National Academy of Sciences of the United States of America*, 99: 2554-2560.

Toutin, T., 2003a. Error tracking in Ikonos Geometric processing using a 3D parametric model. *Photogrammetric Engineering and Remote Sensing*, 69: 43-51.

Toutin, T., 2003b. Impact of terrain slope and aspect on radargrammetric DEM accuracy (vol 57, pg 228, 2002). *ISPRS Journal of Photogrammetry and Remote Sensing*, 58: 124-125.

Toutin, T., 2004. Geomatric processing of remote sensing images: models, algorithms and methods. *International Journal of Remote Sensing*, 20: 1893-1924.

Toutin, T. and Cheng, P. Demystification of IKONOS. 2000.

Toutin, T., Chenier, R., and Carbonneau, Y. 3D Geometric Modelling of IKONOS Geo Images. 2001. Hannover, Germany, *ISPRS Joint Workshop "High Resolution Mapping from Space"*. 19-9-2001.

Toutin, T., Chenier, R., and Carbonneau, Y. 3 D Models For High Resolution Images: Examples With Quickbird, IKONOS and EROS. 34[4], 547-551. 2002. Ottawa. ISPRS Commission IV Symposium, Joint International Symposium on Geospatial Theory, Processing and Applications.

U.S.Geological Survey. Map Accuracy Standards. 1999. *U.S. Department of the Interior.*

Vassilopoulou, S., Hurni, L., Dietrich, V., Baltsavias, E., Pateraki, M., Lagios, E., and Parcharidis, I., 2002. Orthophoto generation using IKONOS imagery and high-resolution DEM: a case study on volcanic hazard monitoring of Nisyros Island (Greece). *ISPRS Journal of Photogrammetry and Remote Sensing*, 57: 24-38.

Wolf, P. R., 1983. Elements of Photogrammetry. McGraw-Hill.Inc., New York.

Wrigley, R. C., Card, D. H., Hlavka, C. A., Hall, J. R., Mertz, F. C., Archwamety, C., and Schowengerdt, R. A., 1984. Thematic Mapper Image Quality - Registration, Noise, and Resolution. *IEEE Transactions on Geoscience and Remote Sensing*, 22: 263-271.

Yuhas, R. H., Boardman, J. W., and Geotz A.F.H. Determination of Semi-Arid Landscape Endmembers and Seasonal Trends Using Convex Geometry Spectral Unmixing Techniques, In: Summaries of the Fourth Annual JPL Airborne Geoscience Workshop. 1. 1993. Washington D.C.

Zadeh, L. A., 1965. Fuzzy sets. *Information and Control*, 8: 338-353.

Zhang, J. and Foody, G. M., 1998. A fuzzy classification of sub-urban land cover from remotely sensed imagery. *International Journal of Remote Sensing*, 19: 2721-2738.

Zhou, G. Q. and Li, R., 2000. Accuracy evaluation of ground points from IKONOS high- resolution satellite imagery. *Photogrammetric Engineering and Remote Sensing*, 66: 1103-1112.

Zhu, C. Q. and Yang, X. M., 1998. Study of remote sensing image texture analysis and classification using wavelet. *International Journal of Remote Sensing*, 19: 3197-3203.

Zuzek, P. J., Nairn, R. B., and Thieme, S. J., 2003. Spatial and temporal considerations for calculating shoreline change rates in the Great Lakes Basin. *Journal of Coastal Research*, 125-146.

Anon, 1984. Shore Protection Manual. U.S Army Corp of Engineers.

Anon, 1993. Engineering and Design:Photogrammetric Mapping. U.S Army Corp of Engineers.